Non-Canonical functions of ATG16L1 in immunity and infection

By Benjamin Bone
Norwich Medical School
University of East Anglia
September 2021

ABSTRACT

ATG16L1 has many non-canonical roles outside its classical role in autophagy. It plays a vital role in the innate immune response LC3-associated phagocytosis (LAP). Furthermore, it has been recently shown to be involved in lysosomal fusion to the plasma membrane (PM), which is necessary for cholesterol transport to the PM. Our group developed a mouse model (ΔWD) that expresses an ATG16L1 protein truncated at position E230, lacking the WD domain. This mouse has increased susceptibility to the influenza A virus (IAV), with increased viral replication in the mouse, in addition to a lethal cytokine storm. The aim of this thesis was to investigate the mechanism by which the WD domain protects mice from lethal IAV infection.

Initially, I investigated differences in tissues and mouse embryonic fibroblast (MEF) cell lines isolated from wild type (WT) and ΔWD mice. I found that cholesterol was reduced in the PM of ΔWD brain and lung tissue as well as ΔWD MEFs.

I then investigated whether modulation of the membrane cholesterol would affect IAV fusion. IAV fused more efficiently to the PM of ΔWD MEFs, when infected by acid bypass, that allows the virus to fuse directly with the PM.

IAV endocytosis and fusion in ΔWD MEFs were measured using a differential immunostaining assay and FACs respectively. Increased endocytosis and fusion were seen in ΔWD MEFs. I showed that IAV replicated to higher levels in ΔWD MEFs and in precision cut lung slices. Additionally, interferon and ISG expression were higher in infected ΔWD MEFs and lung slices, mimicking the cytokine storm seen in the mutant mice. Overall, this thesis demonstrates that the WD domain of ATG16L1 has a role in cholesterol transport to the PM, a WD deficiency resulting in IAV entering cells more efficiently and replicating to higher levels and causing elevated cytokine expression.

Access Condition and Agreement

Each deposit in UEA Digital Repository is protected by copyright and other intellectual property rights, and duplication or sale of all or part of any of the Data Collections is not permitted, except that material may be duplicated by you for your research use or for educational purposes in electronic or print form. You must obtain permission from the copyright holder, usually the author, for any other use. Exceptions only apply where a deposit may be explicitly provided under a stated licence, such as a Creative Commons licence or Open Government licence.

Electronic or print copies may not be offered, whether for sale or otherwise to anyone, unless explicitly stated under a Creative Commons or Open Government license. Unauthorised reproduction, editing or reformatting for resale purposes is explicitly prohibited (except where approved by the copyright holder themselves) and UEA reserves the right to take immediate ‘take down’ action on behalf of the copyright and/or rights holder if this Access condition of the UEA Digital Repository is breached. Any material in this database has been supplied on the understanding that it is copyright material and that no quotation from the material may be published without proper acknowledgement.

TABLE OF CONTENTS

Abbreviations

25HC - 25-hydroxycholesterol
ATG - Autophagy
BafA - Bafilomycin A
BCA - Bicinchoninic acid
BMDM - Bone marrow derived macrophage
BSA - Bovine serum albumin
CCD - Coiled-coil domain
CCP - Clathrin-coated pit
CCV - Clathrin-coated vesicle
cGAS - GMP-AMP synthase
CLR - C-type lectin receptor
CRM1 - Chromosome region maintenance 1
cRNA - Complementary ribonucleic acid
cRNP - Complementary ribonucleoprotein
DAPI - 4’-6’diamidino-2-phenylindole
DEAF-1 - Deformed epidermal autoregulatory factor 1
DFCP1 - Double FYVE domain-containing protein
DiOC18 - 3,3’-dioctadecyloxacarbocyanine
DMEM - Dulbecco’s modified eagles medium
DMSO - Dimethyl sulfoxide
DNA - Deoxyribonucleic acid
dNTP - deoxynucleoside triphosphate
dsRNA - Double-stranded ribonucleic acid
DTT - Dithiothreitol
EDTA - Ethylenediaminetetraacetic acid
EEA1 - Early endosome antigen 1
EGTA - Ethylene glycol-bis(β-aminoethyl ether)-N,N,N’,N’-tetraacetic acid
EM - Electron microscopy
ER - Endoplasmic reticulum
FBS - Foetal bovine serum
FFAT - Two phenylalanines in an acidic tract
FIP200 - FAK family kinase-interacting protein of 200 kDa (alt. RB1-inducible coiled-coil protein 1)
GFP - Green fluorescent protein
GPI - Glycosylphospatidyl inositol
HA - Haemagglutinin
HBSS - Hanks Balanced Salt Solution
HEPES - 4-(2-hydroxyethyl)-1-piperazineethanesulfonic acid
HPI - Hours post infection
IAV - Influenza A virus
IFIT1 - Interferon-induced protein with tetratricopeptide repeats 1
IFITM - Interferon-induced transmembrane protein

IFN - Interferon

Ig - Immunoglobulin

IKK - IϰB kinase

IPS-1 - IFN-β promoter stimulator (alt. MAVS - Mitochondrial antiviral-signalling protein)

IRAK1/4 - Interleukin-1 receptor associated kinase 1/4

IRF3/7 - Interferon regulatory factor 3/7

ISG - Interferon stimulated gene

LANDO - LC3-associated endocytosis

LAP - LC3-associated phagocytosis

LBD - Ligand binding domain

LC3 - Microtubule-associated protein light chain 3

LDL - Low density lipoprotein

LRR - Leucine rich repeat

LTP - Lipid transport protein

M1 - Matrix protein 1

M2 - Matrix protein 2

MβCD - methyl-β-cyclodextrin

MCSF - Macrophage colony stimulating factor

MDCK - Madin Darby Canine Kidney cell

MEF - Mouse embryonic fibroblast

MEM - Minimal essential medium

MERS - Middle Eastern respiratory syndrome

MHC - Major Histocompatibility Complex

MOI - Multiplicity of infection

MTOC - Microtubule organising centre

mRNA - Messenger ribonucleic acid

MyD88 - Myeloid differentiation primary response 88

NA - Neuraminidase

NAP1 - NF-kappa-B-activating kinase-associated protein 1

NEMO - NF-kappa-B essential modulator

NES - Nuclear export signal

NF-ϰB - Nuclear factor kappa-light-chain-enhancer of activated B cells

NLS - Nuclear localisation signal

NOX2 - NADPH oxidase 2

NP - Nucleoprotein

NPC - Nuclear pore complex

NPC2 - Niemann-Pick C2

NS1 - Non-structural protein 1

NS2/ NEP - Non-structural protein

Opti-MEM - Opti-Minimal Essential Medium

ORD - Core lipid binding ORP domain

OSBP - Oxysterol-binding protein

PA - Polymerase acidic subunit 2/Nuclear export protein

PAMP - Pathogen-associated molecular pattern

PB1 - Polymerase basic subunit 1

PB2 - Polymerase basic subunit 2

PBS - Phosphate buffered saline

PCR - Polymerase chain reaction

pDCs - Plasmacytoid dendritic cells

PE - Phosphatidylethanolamine

PFA - Paraformaldehyde

PFU - Plaque forming unit

PH - Pleckstrin homology

PI3K - Phosphatidylinositol-3 kinase

PMSF - Phenylmethylsufonyl fluoride

Poly I:C - Polyinosinic:polycytidylic acid

PM - Plasma membrane

PRR - Pattern recognition receptor

PR8 - IAV A/Puerto Rico/8/1934

PS - Phosphatidylserine

PVDF - Polyvinylidene fluoride or polyvinylidene difluoride

qPCR - Quantitative PCR

R18 - Octadecyl rhodamine B

RNA - Ribonucleic acid

RdRp - Ribonucleoprotein dependent ribonucleic acid polymerase

RE - Recycling endosome

RIG-I - Retinoic acid-inducible gene I

RIP-1 - Receptor interacting protein 1

RNP - Ribonucleoprotein

ROS - Reactive oxygen species

RPMI - Roswell Park Memorial Institute

SARS - Severe acute respiratory syndrome

SDS - Sodium dodecyl sulfate

SNP - Single nucleotide polymorphism

SOC - Super optimal broth with catabolite repression

SSC - Side scatter

ssRNA - Single-stranded ribonucleic acid

svRNA - Small viral ribonucleic acid

STING - Stimulator of interferon genes

TAK1 - Transforming growth factor beta-activated kinase 1

TANK - TRAF family member-associated NF-kappa-B activator

TBK1 - TANK-binding kinase 1

TBST - Tris-buffered saline +Tween 20

TCID$_{50}$ - Tissue Culture Infectious Dose$_{50}$

TIM - TRAF-interacting motif

TIR - Toll/IL-1 receptor

TLR - Toll-like receptor

TPCK - N-tosyl-L-phenylalanine chloromethyl ketone

TRAF3/6 - TNF receptor-associated factor 3/6

TRIF - TIR-domain-containing adaptor-inducing interferon-β

VAPA - Vesicle-membrane-protein-associated protein A

VLDL - Very Low density lipoprotein

VSV - Vesicular stomatitis virus

vRNA - Viral ribonucleic acid

vRNP - Viral Ribonucleoprotein

WGA - Wheat germ agglutinin

WIPI2 - WD repeat domain phosphoinositide-interacting protein 2

WT - Wildtype

ΔWD - WD domain deficient

X31 - IAV A/X-31

List of Figures and Tables

CHAPTER 1: Introduction

CHAPTER 2: Materials and Methods

CHAPTER 3: Replication of IAV in ΔWD and WT cells.

CHAPTER 4: IAV entry kinetics in WT and ΔWD MEFs

CHAPTER 5: Replication of IAV and cytokine signalling in ΔWD and WT MEFs

CHAPTER 5: Discussion

Figure 6.1: The WD domain of ATG16L1 has a role in the transport of cholesterol to the plasma membrane.

CHAPTER 1

Introduction

1.1 LC3-Associated Phagocytosis (LAP) and Endocytosis (LANDO)

1.1.1 Overview

Macroautophagy, hereafter autophagy, is a highly-conserved fundamental cell mechanism of degrading cellular contents by directing them to lysosomes for destruction. All cells accumulate debris from catabolic processes and waste materials which can be toxic. It is autophagy (derived from Greek which means ‘self-eating’) that compartmentalises these waste materials and destroys them (1). Waste removal is one reason but another reason for this mechanism is to recycle nutrients during periods of starvation, however it is becoming clearer and clearer that this process has roles in the adaptive and innate immune systems (2,3). The execution of autophagy involves a pathway not dissimilar from the ubiquitination method of cargo degradation, with the cargo being tagged for destruction. Portions of the cytosol are compartmentalised by an isolation membrane, creating a double membraned vesicle called an autophagosome. This structure then fuses with a lysosome (4). Several autophagy (ATG) proteins also play a role in another similar but functionally different innate immune process: LC3-associated phagocytosis (LAP).

LAP uses elements from two conserved pathways: autophagy and phagocytosis, perhaps originating at the branching point between their two evolutionary pathways. Crucial autophagy components are recruited to the phagosome during phagocytosis so that some of the autophagy mechanisms are harnessed (5,6).

Both autophagy and LAP share one crucial mechanic between their processes, and that is the conjugation of microtubule-associated protein light chain 3 (LC3) to membranes. The most characterised of the LC3 protein subfamilies is the LC3B protein (7,8). This protein is conjugated to vesicles containing cargo to be degraded and both autophagy and LAP utilise it as a marker for their autophagosomes or LAPosomes respectively (7). A fundamental difference between autophagy and LAP is that autophagosomes are double membraned structures, whereas LAPosomes are single membraned structures (9,10).

Initiation of LAP does not require the activation of a pre-initiation complex; also it does not require mTOR (11,12). It is initiated by receptors on the plasma membrane. These receptors recognise a wide variety of ligands including PAMPs and phosphatidylserine (PS) (6). Receptors that activate LAP include Toll Like Receptors (TLRs), C-type lectin receptors (CLRs), Immunoglobulin (Ig) receptors and TIM4 receptors (6,13–15). Once ligands have bound, an unknown process then activates a variety of LAP effectors which are recruited to the phagosome.

A key component that needs to be recruited to the phagosome is the class III Phosphatidylinositol-3 kinase (PI3K). In autophagy there are several PI3K complexes, similar apart from the Beclin-1 interacting protein that associates to the complex. Autophagy is positively regulated by two PI3K complexes: the ATG14L, Beclin-1, Vps34, Vps15 complex (which aids autophagosomal formation) and the UVRAG, Beclin-1, Vps34, Vps15 complex (which aids endosome maturation) (16,17). A third complex includes UVRAG as well as the other shared components, but also incorporates Rubicon. Rubicon is also a Beclin-1 binding protein and its involvement in the class III PI3K transforms the complex into an inhibitor of autophagy (17–19). However, it is this class III PI3K complex which is vital for LAP with Rubicon being translocated to the membrane of the LAP-engaged phagosome (LAPosome) and then recruiting the rest of the class III PI3K complex, stabilising it (Figure 1.1). The recruited PI3K then produces phosphatidylinositol-3-phosphate (PI3P) (5,12). Additionally, Rubicon has another role in initiating LAP. LAP-activating receptor engagement with ligands also triggers the assembly of cytosolic NADPH oxidase 2 (NOX2) components ($p40^{phox}$, $p47^{phox}$, $p67^{phox}$, Rac1) at the LAPosome. These components assemble and interact with the membrane bound $p22^{phox}$ and $gp91^{phox}$ (alternatively known as NOX2). Rubicon binds to p22phox and stabilises it (Figure 1.1) (12,20,21). Rubicon recruitment to the LAPosome occurs first, stabilising the class III PI3K so that it produces PI3P which aids recruitment of $p40^{phox}$ to the LAPosome membrane (22).

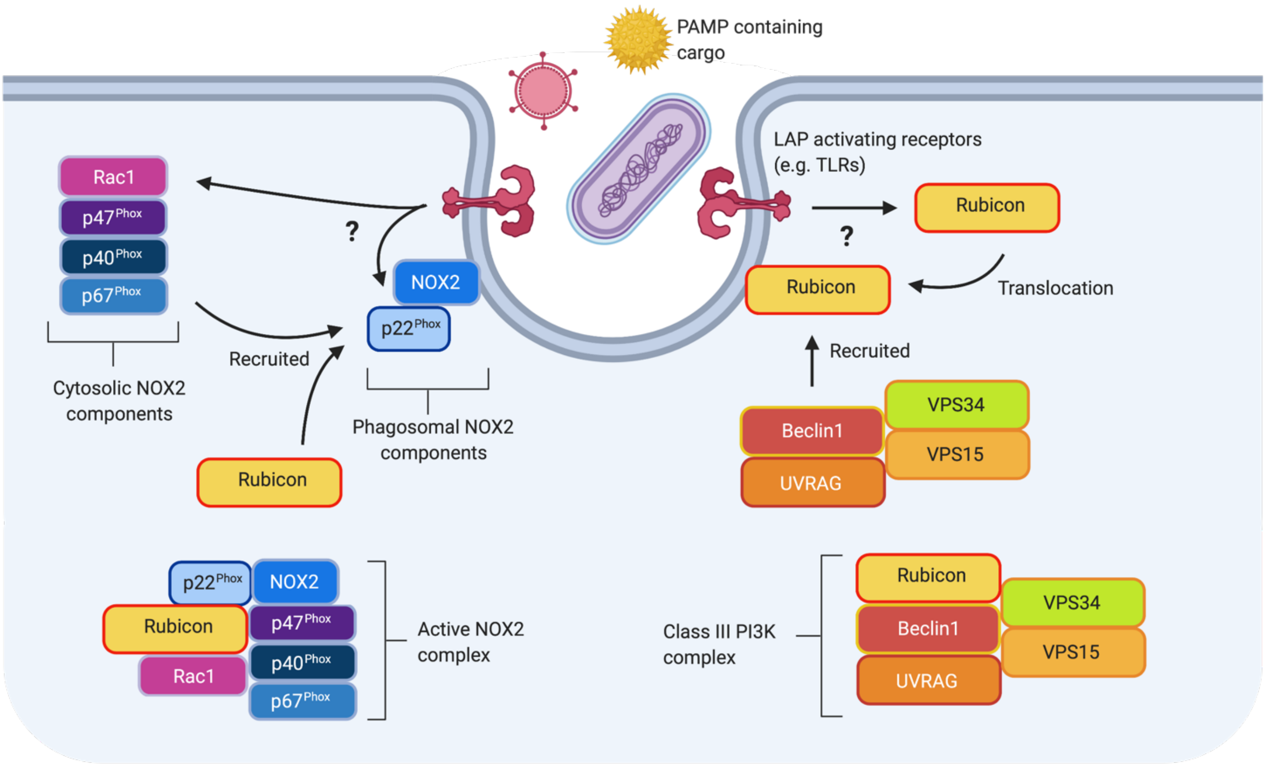

Figure 1.1: The initiation of LAP at the phagosome. LC3-associated phagocytosis (LAP) is initiated by ligand binding to LAP-activating receptors such as Toll Like Receptors (TLRs). Ligands are recognised by these receptors which leads to the recruitment of rubicon to the plasma membrane. This, in turn, results in the assembly of the Class III PI3K complex for PI3P production. Additionally, receptor activation leads to the formation of the NOX2 complex from cytosolic and phagosomal components. Adapted from (23,24). Produced using Biorender.

Following the recruitment of the NOX2 components to the LAPosome, the active NOX2 complex generates reactive oxygen species (ROS) inside the phagosome from cytosolic NADPH. These ROS are needed for the activation of downstream ubiquitin-like conjugation systems that both autophagy and LAP use to conjugate LC3 to the target vesicle's membrane (Figure 1.2). ROS have been shown to oxidise lipids with this phenomenon leading to altered biological characteristics of the membranes (5,25,26). It is ROS that induces the recruitment of the conjugation machinery during LAP.

For the contents of autophagosomes or LAPosomes to be successfully degraded, the vesicle must fuse with a lysosome. This is mediated by LC3. LC3 needs to be conjugated to the membrane of a target vesicle for lysosomal fusion to occur which is facilitated by the ATG5-ATG12 and the LC3-PE conjugation systems, two ubiquitin-like conjugation systems. These processes are both required for autophagy as well as LAP.

For the ATG5-ATG12 system, Atg12 is activated by the E1-like enzyme ATG7, a thioester bond generating between ATG12's C-terminal glycine residue and ATG7's cysteine residue (27). This catalyses the transfer of ATG12 and formation of a thioester bond to the ATG10 E2-like enzyme (28,29). ATG10 then catalyses the conjugation of ATG12 to ATG5, an isopeptide bond forming between the two (27). So far, this process has mirrored ubiquitination, with the degradation signal ubiquitin being activated by an E1 enzyme before being transferred to an E2 enzyme and then being conjugated to the target (30). The ATG12-ATG5 complex is essential for the LC3-PE conjugation system (31) but first the ATG12-bound ATG5 interacts non-covalently with the coiled-coiled protein ATG16L1. ATG16L1 isn't needed for the initial ATG12-ATG5 conjugation, but instead aids recruitment of the complex to the LAPosome (32). ATG16L1 naturally forms homodimers, with the entire complex forming a hetero-tetrameric complex (33,34).

Conjugation of phosphatidylethanolamine (PE) to LC3 is preceded by LC3 being primed via the ATG4 cysteine protease. LC3 is cleaved at its C-terminus (35,36) exposing a glycine residue which is essential for PE conjugation. ATG4 also acts as a deconjugating

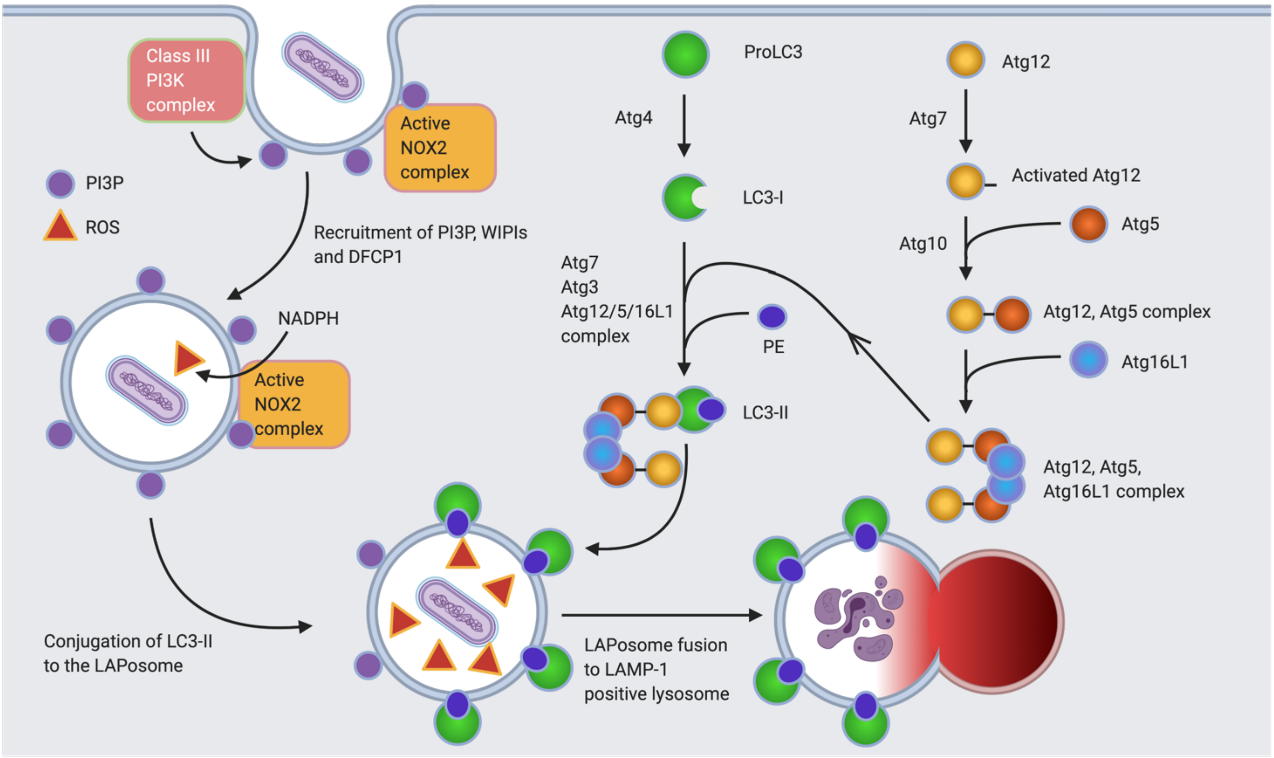

Figure 1.2: The destruction of cargo via LAP. Following initiation of LC3-associated phagocytosis by pattern recognition receptors, the active class III PI3K complex is recruited, decorating the LAPosome's membrane with PI3P. This stabilises the NOX2 complex which is also recruited, producing ROS in the LAPosomal lumen. Both PI3P and ROS activate the downstream conjugation systems, with ATG12 forming a complex with ATG5 and ATG16L1. Concurrently, ProLC3 is cleaved to its active form, LC3-I. LC3-I is then conjugated to PE via the action of several ATG proteins including the ATG12-ATG5+ATG16L1 complex, forming LC3-II. This is then conjugated to the LAPosome via the action of the ATG12-ATG5+ATG16L1 complex. LC3-II positive LAPosomes are fused to LAMP-I positive lysosomes and the contents degraded. Adapted from (23,37). Produced using Biorender.

enzyme, recycling PE and LC3 after the LAPosome fuses to a lysosome. It is believed that ROS may regulate ATG4, inhibiting the protease to prevent deconjugating during moments of cellular stress when LC3 is needed for autophagy and perhaps even LAP (38). With LC3 primed (designated LC3-I), the exposed glycine binds to ATG7's cysteine residue (the same residue used in the ATG12-ATG5 conjugation system) (39,40). ATG7 acts once again as an E1-like enzyme, transferring LC3-I to the E2-like enzyme ATG3 (41). The ATG12-ATG5 complex possesses E3-like enzyme activity, with ATG12 interacting with ATG3 and catalysing the transfer of LC3-I to PE, generating LC3-II. The complete ATG12-ATG5+ATG16L1 complex is needed to correctly localise and conjugate LC3-II to the LAPosome membrane. Specifically it is ATG16L1 which facilitates this localisation, doing so through its WD domain. ROS induces the WD domain to bind to the LAPosome membrane. With the conjugation machinery correctly localised, LC3-II is conjugated to the target LAPosome. Successful LC3-II attachment is a prerequisite for LAPosomal expansion, maturation and eventual lysosomal fusion to the LAPosome and destruction of the cargo (5,12,42,43).

Another process, independent of phagocytosis, also facilitates cargo uptake in association with LC3 and that is LC3-associated endocytosis or LANDO. This process was first noticed when endosomal markers such as Rab5 and clathrin as well as LC3 associated to single membraned endosomes when phagocytosis was inhibited. The mechanism may be used to recycle cell receptors and certainly seems to play a role in the clearance of toxic β-amyloid within the brain (44). Very little is known about the exact mechanism of LANDO however as the LAP mechanism is specific to conjugating LC3 to single membraned vesicles, it is likely that the similar mechanism is used for LANDO.

1.1.2 LC3-associated phagocytosis functions

A functioning LAP system is necessary for a wide range of cellular behaviours (Figure 1.3). One of the main functions of LAP is the engulfment and destruction of pathogens. Acidic hydrolases degrade the phagocytosed/endocytosed material and transmembrane pumps recover nutrient molecules and pass them to the cytosol for recycling. LAP has been shown to provide genuine defence against the pathogens *Listeria monocytogenes* and *Legionella dumofii* (45,46). Furthermore, this defence role of LAP was explored by knocking out LAP in mice and infecting with the fungus *Aspergillus fumigatus*, an infection which was unable to be cleared in LAP^{-} mice (5,47). LAP is also proposed to be utilised by the commensal bacteria *Bacteroides fragilis,* the bacteria using this mechanism to deliver immunomodulatory compounds into the cells to protect them from inflammatory bowel disease (IBD) (48).

LAP plays a role in another immune response mechanism: efferocytosis. This process oversees the removal of apoptotic cells, being conducted by macrophages. These apoptotic cells could be themselves infected, therefore this process plays an important role in pathogen clearance. A characteristic of efferocytosis is that it is ‘immunologically silent’ (23), meaning it doesn’t trigger any immune response and pro-inflammatory cytokines are inhibited from being expressed (49–51). This immunological silence is facilitated by LAP. A LAP deficiency in mice was seen to result in an accumulation of apoptotic bodies in immune cells and tissue (52) and the development of an autoimmune lupus-like condition, characterised by extreme inflammation (14,23).

LAP not only contributes to the capturing and degradation of pathogens and apoptotic cells, but also cooperates with the adaptive immune system. Activation of LAP via the non-TLR pattern recognition receptor dectin-1 (53) leads to a promotion of Major Histocompatibility Complex (MHC) class II presentation. Dectin-1 signalling triggers phagocytosis and formation of LC3-II. Furthermore, dectin-1 directs the conjugation of LC3-II to the LAPosomal membrane. A deficiency in LC3-II resulted in a dysfunctional MHC class II system, whereby MHC class II molecules couldn’t be recruited to phagosomes and the antigens concomitantly presented (9,13,54). This dysfunctional MHC class II system present when LAP is absent could explain why mice with a LAP deficiency have reduced capabilities at clearing infection (23,55,56).

In addition to enhanced MHC class II presentation, LAP also aids the immune response by promoting type I interferon expression. LAP activation leads to type I interferon expression through TLRs signalling through IRF7 (57,58), a regulatory factor paramount to the immune response. Type I interferons, which include IFNα and IFNβ, have the ability to induce an antiviral state by signalling through the JAK-STAT pathway, making them essential in fighting disease (59). LAP leads to enhanced TLR signalling, likely due to TLRs being trafficked into LC3 marked vesicles (58,60,61). This would lead to sustained ligand-TLR interaction and signalling, concomitantly leading to a strong immune response.

In addition to the immune response to infection and preventing inflammatory responses, LAP is also believed to have a role in the vision cycle. LAP may aid in the clearance of photoreceptor outer segments, which allows for the renewal of photoreceptor disks (23,62).

These functions cannot just be attributed to LAP alone, with LANDO possibly contributing to a functioning immune system in conjunction. Both LAP and LANDO utilise LC3 as a marker on their vesicles meaning that LC3-associated endosomes or ‘LANDOsomes’ would be targeted for maturation and degradation as well.

LAP and LANDO are novel pathways requiring further research due to their novel means at pathogen removal. The majority of recent literature looks at the efficiency these mechanisms have at clearing bacterial and fungal pathogens as well as β-amyloid (44). In my work I have investigated the role of the LAP and the ATG16L1 protein in viral infection.

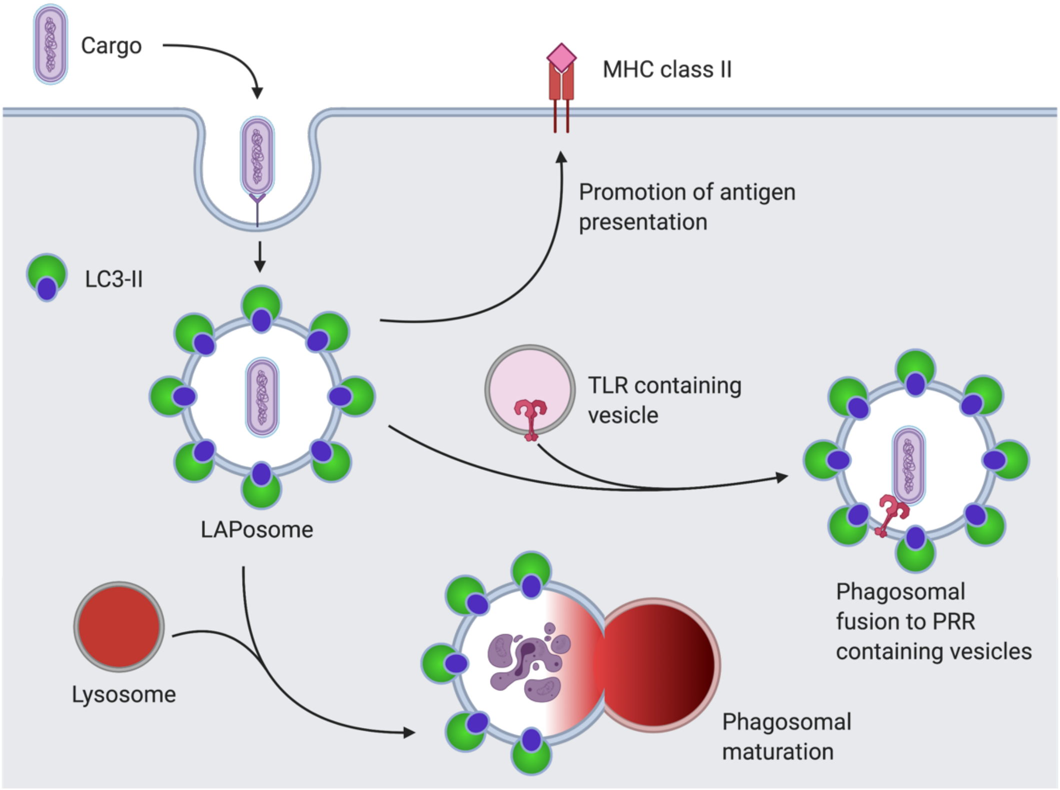

Figure 1.3: From destruction to presentation, how LAP processes its phagocytosed cargo. Cargo phagocytosed by LAP can be processed in multiple ways. LAPosomes decorated in LC3-II may fuse to LAMP1 positive lysosomes and the cargo be degraded. Alternatively, the LAPosome may fuse to pattern recognition receptor (PRR) containing vesicles, for example TLR containing vesicles. This would lead to the expression of type I interferons. Otherwise, degradation of the cargo would allow antigens to be recruited by MHC class II proteins and be expressed by the cell, allowing for recognition by the immune system. Adapted from (2). Produced using Biorender.

1.2 The ATG16L1 protein

1.2.1 ATG16L1 and LAP/LANDO

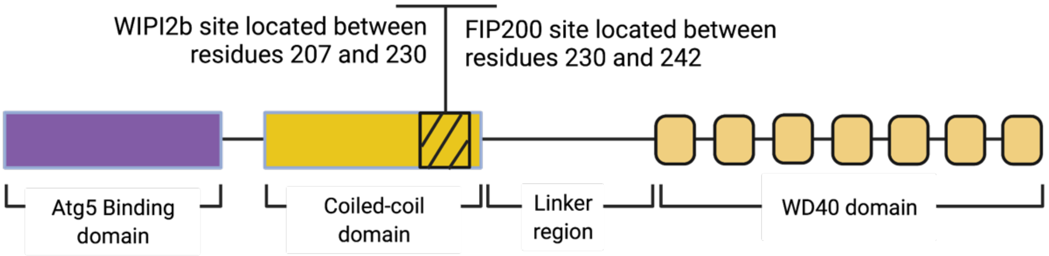

Figure 1.4: ATG16L1 domain layout. ATG16L1 is a 68 kDa protein arranged into four main regions, an ATG5 binding domain, a coiled-coil domain, a linker region and a WD40 domain made up of seven WD40 repeats. Adapted from (63), binding site information from (64). Produced using Biorender.

A protein crucial to the successful targeting of LC3-II to autophagosomes and LAPosomes is the coiled-coil protein called ATG16L1. It is a core component in the E3-ligase ATG12-ATG5+ATG16L1 needed to catalyse LC3-I lipidation. One of the main reasons for this is that it binds to the phagosomal membrane following the production of ROS by NOX2. This secures the complex to the membrane and allows it to direct LC3-II to the membrane.

ATG16L1 is a 607 amino acid, 68 kDa protein (Figure 1.4) which is comprised of three domains. The N-terminal binds to ATG5 and is responsible for complexing with ATG12-ATG5. Adjacent to the ATG5 binding domain is the coiled-coil domain (CCD). This domain possesses two overlapping but distinct binding sites: a binding site to WD repeat domain phosphoinositide-interacting protein 2 (WIPI2) and a binding site to FAK family kinase-interacting protein of 200 kDa (FIP200) which is a protein inhibitor for focal adhesion kinase (64–66). The WIPI2 site is essential for canonical autophagy, with WIPI2 interacting with PI3P on membranes and anchoring the conjugation complex. It is here where the dimerization occurs with a second ATG16L1 protein, producing the hetero-tetrameric complex. Overall, the CCD is essential for recruitment of ATG16L1 due to its intrinsic lipid binding activity (67).

The CCD is followed by a linker region that links it to the WD domain, which is made up of seven WD40 β-propeller repetitions (forty repetitions of tryptophan and aspartate residues). The function of this region is uncertain. Unlike the CCD, It is not necessary for canonical autophagy in unicellular organisms such as yeast, as they simply do not possess it (68). It also does not appear to be necessary for canonical autophagy in mammalian cells, as an autophagy deficiency can be corrected with an ATG16L1 protein that does not possess the WD domain (64,69). Studies have shown that the WD domain possesses protein binding characteristics, interacting with the transmembrane proteins TMEM59 and TMEM166/EVA1A (70,71). TMEM59 is involved in controlling β-amyloid precursor protein secretion and Wnt signalling which is crucial for stem cell maintenance (72,73). TMEM166/EVA1a's interaction with ATG16L1 promotes ATG12-ATG5+ATG16L1 recruitment to phagosomes, implicating it in autophagy activation. Furthermore, the C-terminal region, which includes the WD domain, has been shown to be membrane binding. While it is dispensable for autophagy, it is involved in lipidation and has been shown to sustain LC3 lipidation even in the absence of a WIPI2 binding site. Interestingly, this membrane binding region is only present in the β-isoform of ATG16L1, suggesting that different isoforms can utilise different lipidation mechanisms under varying cellular conditions (74).

With these membrane and protein binding affinities, the WD domain was further investigated to see whether it has a role in LAP, with it indeed having a role in the process. Fletcher *et al*. (2018) demonstrated that the WD domain was required for LAP, with a deletion of the domain resulting in less ATG16L1 recruited to phagosomes (66). This was not due to a failure for the protein to form the E3-like ATG5-ATG12+ATG16L1 complex, as both WD deficient and full length ATG16L1 were seen to form the E3-like complex. Specific sites on the WD domain were seen to be fundamental for ATG16L1 recruitment to membranes, these being N453, F467 and K490. Due to this inability for ATG16L1 to recruit to membranes, LC3 was unable to conjugate to phagosomes encapsulating apoptotic cells. Additionally, using bone marrow derived macrophages (BMDMs) from our lab, Fletcher *et al.* (2018) demonstrated that lack in the WD domain (E230) was seen to impair antigen presentation through the MHC class II pathway. These data heavily implicate the WD domain as being important for a functional LAP system (66).

Our lab has spent the last 10 years generating mice with mutations in the WD domain of ATG16L1. Rai *et al.* (2019) generated mice expressing the E230 mutation through homologous recombination in embryonic stem cells. A targeting vector installed two stop codons at the end of the CCD, immediately following the E230 glutamate residue (63). The N-terminal was translated as usual, allowing for autophagy, and the mouse survived. However residues post E230 were missing, such as the FIP200 binding region, the linker region and the WD domain. In our lab, Rai *et* al (2019) showed that in E230 mice, the ATG5-binding and coiled-coil domains of ATG16L1 maintained autophagy and tissue homeostasis in mice independently of the WD domain required for LAP. E230 mice were shown to not have any defects in liver, brain, kidney or muscle tissue homeostasis; with similar levels of autophagosomes detected as were seen in littermate controls. The FIP200 domain is described as being crucial for autophagy (64), however it is clear from these mice that autophagy is still functional without the intact domain. This could be due FIP200 being able to bind to other regions of the coiled-coil domain. Regardless, the ability to induce autophagosome formation in this E230 mouse suggests autophagy is still functional. In another mouse, an unexpected recombination resulted in a STOP codon being introduced earlier and loss of the E230 glutamate residue required for WIPI2 binding. This more severe truncation at position E226, impaired the WIPI2 binding site as it requires both the E226 and E230 glutamate residues, consequently generating an autophagy deficiency. This mouse was designated E226. The E226 mouse survived the postnatal lethality seen with other autophagy deficient ATG16L1 KO mice, however these mice grow to be smaller than their littermate controls. The E226 mouse model saw decreased survivability (average life span of 5-7 months) and increased tissue defects, such as neurological impairment. In the E230 mouse model, LAP was not functional, supporting the WD domain’s role in LAP (63) (Figure 1:5). This LAP deficient mouse, hereafter the ΔWD mouse, is a fantastic model for investigating LAP/LANDO further and observing the pathologies of diseases when this innate immune system is knocked out. LAP has never been shown before to be an antiviral mechanism and this was a focus of my thesis project.

A point mutation in ATG16L1 is a risk allele for Crohn's disease (75). This single nucleotide polymorphism (SNP) at position T300A is thought to be responsible for defects in autophagic processes and attenuated antibacterial defence (76,77). Furthermore this mutation is found in the linker region of the protein, upstream of the WD domain. This mutation is implicated in a dysfunctional WD domain (75) through the insertion of a caspase 3 cleavage site. Caspase 3 is activated following inflammation and apoptosis and upon activation would cleave the ATG16L1 protein, removing its WD domain. This implies that individuals with the T300A mutation may suffer from a LAP deficiency through the lack of a WD domain; but this has never been shown. This could contribute to the increased inflammation seen with Crohn's disease. Our lab recently generated a T300A mouse model which is an important disease model and will be used to investigate whether this mutation induces LAP deficiency.

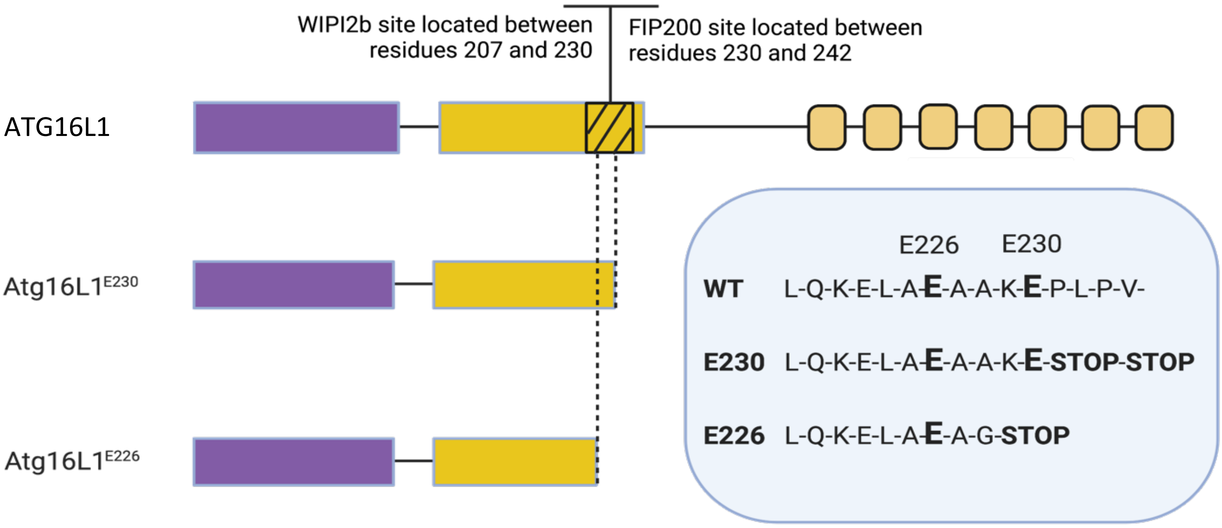

Figure 1.5: The positions of STOP codons to create the different ATG16L1 truncations. Mouse models lacking either LAP or autophagy and LAP were generated via the insertion of stop codons either following the E226 glutamate residue or the E230 glutamate residue. Two stop codons were introduced following the E230 glutamate residue to generate the ATG16L1^{E230} (ΔWD) mouse. This mouse did not have a functioning LAP system but autophagy was preserved. A stop codon was introduced following the E226 residue, removing the E230 residue and impairing the WIPI2 binding site, removing autophagy function as well as LAP. Adapted from (63). Produced using Biorender.

1.2.2 LAP is an important anti-viral mechanism

With it established that LC3-associated phagocytosis is an innate immune response to bacteria, we asked if it was important in virus infection. The E230 mouse model was used in our lab to investigate the role of LAP in viral infection. In work from our lab (Wang *et al.* 2021), we showed that the WD domain is vital in limiting the infection of the influenza A virus (IAV) *in vivo* and protects mice from lethal infection (78). The mice with systemic loss of the WD domain: ΔWD (LAP deficient) were sensitive to low pathogenicity IAV, that is IAV that causes mild disease in mice. Infection of the ΔWD mouse resulted in the mice suffering a severe cytokine storm, with elevated inteferon and inflammatory cytokine expression. There was a greater infiltration of the lungs with neutrophils and the mice just after five days following infection, whereas the littermate controls survived (Figure 1.13). These are significant results as it demonstrates for the first time that LAP is an antiviral mechanism. Deletion of this mechanism results in elevated interferon (IFN) and interferon stimulated gene (ISG) expression, cytokine storm and death (78).

In this paper my work involved characterising the severe cytokine storm, resulting from elevated IFN and inflammatory cytokine expression. In Wang *et al.* (2021) I collaborated with Dr Yohei Yamauchi to produce figure 6, which showed increased fusion and endocytosis of IAV in ΔWD cells (see Appendix 1). However, I have expanded my work for this paper in this thesis where I have investigated the mechanism of this cytokine storm following IAV infection in cells and tissues derived from the E230 mice *in vitro*. Recently several non-canonical functions of ATG16L1 have been published, which may be important in susceptibility to IAV.

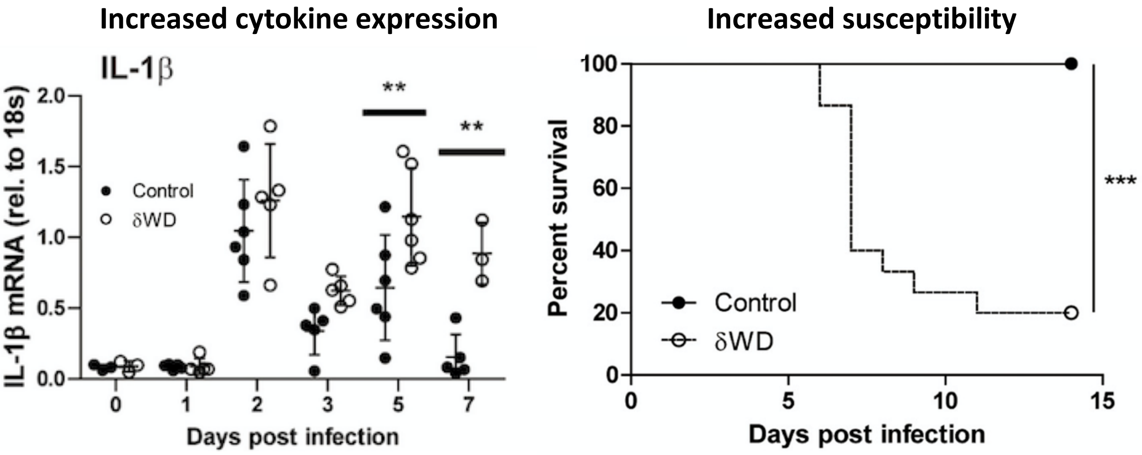

Figure 1.13: Increased inflammatory cytokine expression (IL-1β) discovered in δWD/ΔWD mice as well as increased mortality of δWD/ΔWD mice following influenza infection. Data taken from figures 2 and 3 of Wang *et al.* 2021 (79).

1.2.3 Non-canonical functions of ATG16L1

ATG16L1 is involved in LC3 conjugation to endosomes (44) and macropinosomes (80). In addition, ATG16L1 has many other non-canonical functions (Figure 1.6). Recent literature also suggests a role of ATG16L1 in lysosome biogenesis with a ATG16L1 deficiency causing irregular lysosomes (81). ATG16L1 has also been shown to interact with heavy-chain clathrin, possibly stabilising clathrin mediated endocytosis (82).

My work has contributed to a publication showing that ATG16L1 as having a pro-viral role and demonstrated that ATG16L1 is involved in the efficient phosphorylation of eukaryotic translation initiation factor 2α (EIF2α) in response to Sindbis virus infection, promoting infection (83). I demonstrated that there is a potentiation in IFNβ and ISG expression in ATG16L1 knock out (KO) cells following Sindbis virus infection (see Appendix 2).

The lack of the WD domain could attenuate the ATG161's other non-canonical functions, such as its role in cholesterol homeostasis which is described in more detail in the next section. Recently, Tan *et al.* showed that ATG16L1 and its binding partners ATG5 and ATG12, are involved in facilitating plasma membrane repair (84,85). This plasma membrane repair function of ATG16L1 was shown to be via a non-canonical route and independent of autophagy. ATG16L1 was shown to be necessary for lysosomal exocytosis, a cell mechanism needed for efficient membrane repair. Defects in this protein, such as the T300A mutation, resulted in intracellular cholesterol accumulation and limited transport of cholesterol to the plasma membrane. This implicates the WD domain in cholesterol transport. These plasma membrane repair roles were examined during *Listeria monocytogenes* infection. It was observed that full-length ATG16L1 was crucial in countering *L. monocytogenes* infection, by limiting the membrane damage caused by its pore forming toxin: Listeriolysin O (84). This shows the importance of ATG16L1 in cholesterol transport and since cholesterol has a role in virus uptake and release; could this be a mechanism why the WD domain suppresses IAV infection?

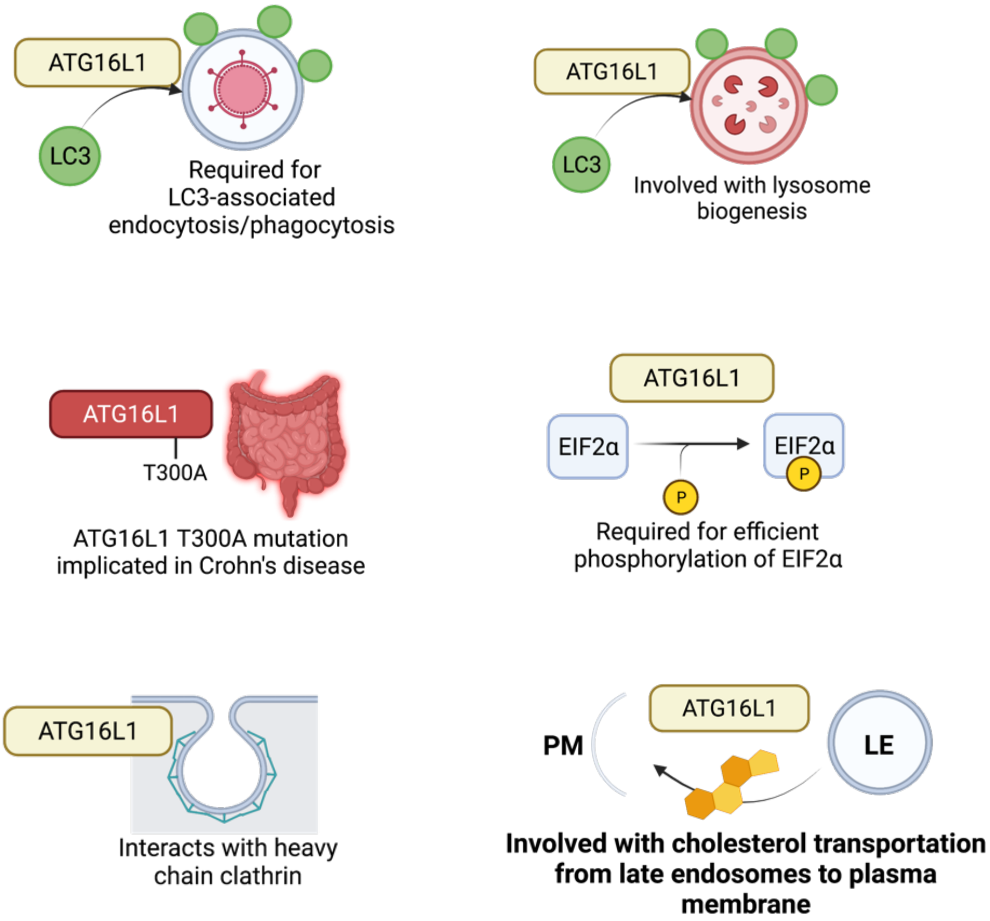

Figure 1.6: Non-canonical functions of ATG16L1. ATG16L1 is involved in LAP, recruiting LC3 to LAPosomes. Additionally, ATG16L1 has a role in lysosome biogenesis. The T300A mutation in ATG16L1 is a risk allele for Crohn's disease. ATG16L1 is required for efficient phosphorylation of EIF2α during Sindbis virus infection and interacts with heavy chain clathrin. ATG16L1 also has a role in cholesterol homeostasis. Produced using Biorender.

1.2.4 The role of cholesterol in virus uptake and release

Cholesterol is a sterol fundamental to the dynamic properties of membranes, contributing to their ability to remain fluid but preventing ‘leakiness’. Cholesterol is embedded in the biological membranes of animals, with its polar hydroxyl group interacting with surrounding water molecules and its hydrocarbon tail integrated into the membrane (Figure 1.7 A). Biological membranes, while inherently fluid, sit in an equilibrium between ordered and disordered states (Figure 1.7 B) (86).

This equilibrium is facilitated by cholesterol, which in biological membranes associates with sphingolipids to form liquid ordered regions. Cholesterol poor regions tend to form liquid disordered regions (87). Liquid ordered zones rich in cholesterol and sphingolipids in the outer leaflet of the bilayer form a micro domain which is slightly thicker than the membrane proper. These zones, or lipid rafts, were first described in 1997 by Simons & Ikonen (88). Lipid rafts are small (approx. 50 nm), and enriched with an array of distinct protein classes, including: glycosylphospatidyl inositol (GPI) anchored proteins and transmembrane proteins. (Figure 1.7 C) (89,90). Rafts are proposed to be self-assembled structures that float in liquid disordered regions of the membrane (91,92).

These lipid rafts are vital in many cellular functions including signal transduction (93) but they are also manipulated by viruses to hijack exocytic machinery and bud from host cells. One virus well characterised in its association with lipid rafts is the Influenza virus. This virus utilises lipid raft domains to concentrate viral proteins, such as haemagglutinin and neuraminidase during the budding process (90,94). This leads to the promotion of infectious virus particle release. Additionally, the membranes of Influenza viruses seem to be heavily enriched with lipid rafts, likely due to the raft-viral protein association. HA and NA clustering causes deformation of the target membrane and eventual budding (95–97,90). Disruption of lipid rafts within the membrane concomitantly yields a greater release of influenza viruses from host cells through budding. Cholesterol was depleted from cellular membranes and lipid rafts disrupted by the drug methyl-β-cyclodextrin (MβCD) (98) and

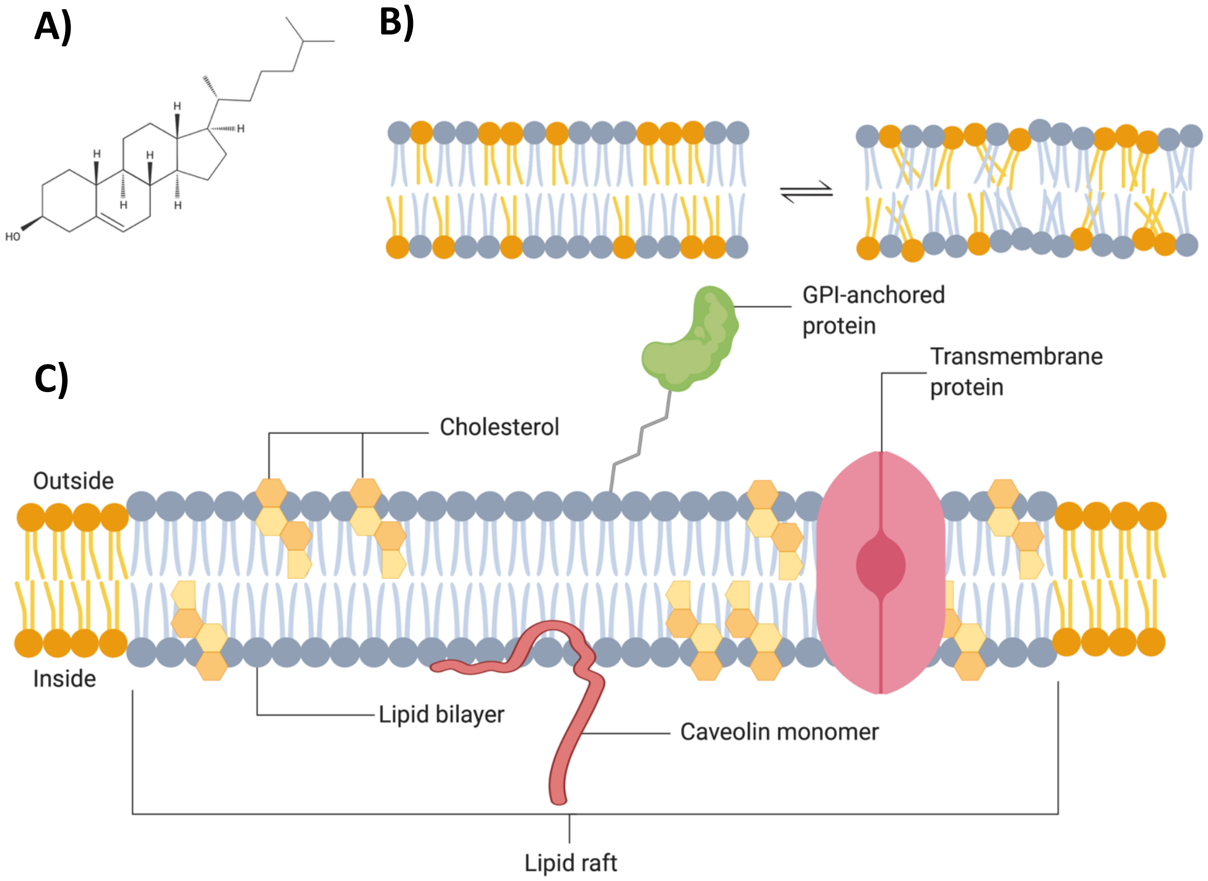

Figure 1.7: Cholesterol and its role in the membrane.

A) Chemical structure of cholesterol.

B) A representation of the two extreme states a lipid bilayer can exist in, the Liquid Ordered state (L_O) state and the Liquid Disordered state (L_D). Conventional bilayers exist in an equilibrium between the two. In the L_O state, phospholipids have regular geometry and arrangement whereas in the L_D state the phospholipids have little to no organisation. Adapted from (87).

C) Schematic of a membrane/lipid raft. Cholesterol condenses sphingolipids into stable and ordered micro domains known as rafts. These rafts exist in the outer leaflet of the lipid bilayer and are enriched with proteins, such as transmembrane and GPI-anchored proteins. Adapted from (87,89). Produced using Biorender.

viral release was measured using plaque forming units, a protein assay and negative stain EM. All three assays demonstrated that the release of influenza viruses increased when cholesterol was depleted. To ensure cholesterol's role in this, MβCD treated cells were exposed to exogenous cholesterol which reduced the amount of virus released (99).

While these results seem clear, further literature has been published which contradicts these results. One such study examined the action of the interferon-inducible protein viperin which disrupts lipid rafts (100,101). Viperin expression was found to inhibit influenza virus release (102) which conflicts with the finding that cholesterol depletion increases virus budding. An explanation for this could be the method used to determine raft disruption and that rafts weren't completely disrupted in the viperin experiment (97).

Lipid rafts are not just necessary for viral budding but also viral endocytosis. The endocytosis of adenovirus Type 2 into epithelial cells was found to be dependent on cholesterol. This virus relies on clathrin-mediated endocytosis. When cholesterol was reduced in cells via MβCD treatment, infection was reduced four-fold; suggesting cholesterol has a role in clathrin-mediated endocytosis (103). Influenza also utilises clathrin-mediated endocytosis and therefore it is possible that a similar cholesterol depletion could affect its uptake into cells. Similar assays have been conducted to remove cholesterol from the plasma membrane and inhibit clathrin-mediated endocytosis however unlike with adenovirus Type 2, the uptake into cells was unaffected. Interestingly, further blocking of the caveolae uptake pathway (which also depends on cholesterol) also resulted in unaffected endocytosis, suggesting there is a clathrin/caveolin-independent pathway influenza can use (104). Cholesterol is certainly required in virus membranes. Depletion of it through MβCD treatment significantly attenuated virus fusion (105).

Cholesterol is biosynthesised as well as acquired through dietary means. Biosynthesis of cholesterol occurs in the endoplasmic reticulum (ER), but is mostly limited to the liver: hepatocytes producing it via a four stage process beginning with acetyl-CoA (87). The majority of cholesterol is then transported away from the liver in the blood as cholesterol esters within the cores of Low Density Lipoprotein (LDL) particles. LDLs are secreted as precursor very low-density lipoproteins (VLDLs) before undergoing exchange reactions with other lipoproteins to reduce their size and produce LDLs (106,107). LDLs express apoB-100 which bind to LDL receptors, targeting the cholesterol to clathrin-coated pits whereby it is endocytosed via receptor-mediated endocytosis. Acidic conditions caused by an influx of protons cause dissociation of apoB-100 from the receptors and, following fusion to a lysosome, the LDLs are broken down (108).

Cholesterol egress from lysosomes is mediated by Niemann-Pick C2 (NPC2) protein which carries cholesterol to the membrane bound NPC1 protein. Cholesterol then ends up at one of two structures: the plasma membrane for storage and support, or the endoplasmic reticulum for re-esterification (109–111) (Figure 1.8). From the membrane, cholesterol dissociates and is chaperoned to different destinations, such as the endocytic recycling compartment (ERC) for storage (112,113) or to the inner mitochondrial membrane (114).

Additionally, cholesterol can be stored in lipid droplets (112). Lipid droplets consist of a amphipathic phospholipid monolayer surrounding a cargo of triglycerides, diacylglycerols and esterified cholesterol. The lipids are stored until required for energy generation (115,116). Lipid droplets are found ubiquitously in the cytoplasm of eukaryotic cells, including mammalian cells and are known to interact with various organelles, including the nucleus and peroxisomes as well as endosomes and lysosomes (117). Cholesterol within lipid droplets is thought to aid IAV infection. A recent study examined the cellular responses of cells experiencing ER stress due to IAV infection. They noticed that cells infected with IAV produced significantly more lipid droplets in the cytoplasm. These lipid droplets were clearly important to viral replication as blocking their formation through atorvastatin, which inhibits HMG-CoA reductase (responsible for cholesterol biosynthesis) (118,119), resulted in a 90-95% reduction in viral reduction. How lipid droplets are vital for IAV replication is the subject of much research (119).

Viral fusion to the endosomal membrane is preceded by a hemifusion intermediate stage whereby the outer leaflets of the two membranes merge, creating a stalk like structure. This intermediate structure eventually collapses and a fusion pore is formed which allows entry of the capsid or, in the case of IAV, its viral ribonucleoproteins. Development of this intermediate hemifusion structure and breakdown into a fusion pore is reliant on several biochemical properties of the membranes and the environment, including cholesterol. High concentrations of cholesterol in eukaryotic cell membranes promote the formation of a fusion pore by SNARE mediated fusion, whereas less

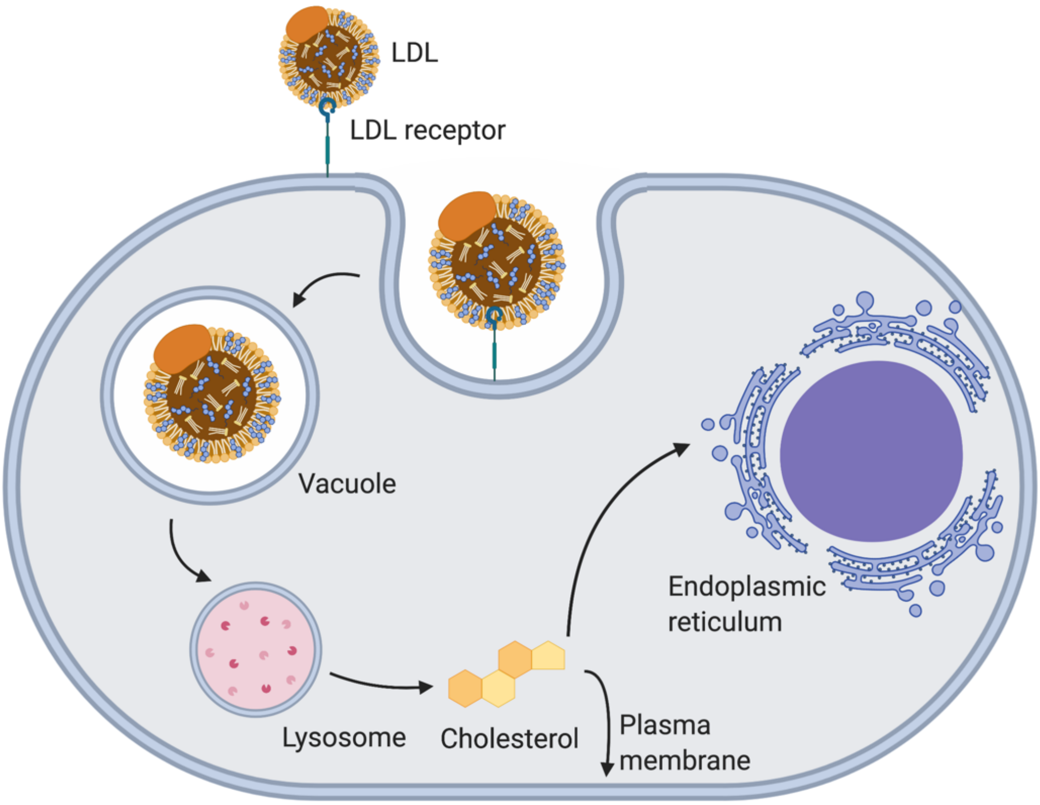

Figure 1.8: Cholesterol's pathway into cells via Low Density Lipoprotein (LDL). LDLs are endocytosed into vacuoles or endosomes and the contents broken down through the fusion with lysosomes. Cholesterol is then transported to either the plasma membrane or endoplasmic reticulum via the Niemann-Pick 2 protein. Produced using Biorender.

cholesterol in the membranes prolong the hemifusion intermediate (120). This is also seen for influenza: high membrane cholesterol levels promote more complete fusion events whereas cholesterol deficient environments promote hemifusion, less complete fusion and even rupture of the stalk intermediate structure (121). This does not necessarily mean that fusion cannot occur in cholesterol absent environments, just that it is not energetically favourable.

It has also been reported that cholesterol is vital for fusion to membranes, but only if the membranes are zwitterionic (122). If membranes are negatively charged, or the environment is sufficiently acidic (positively charged) then that would overpower the requirements for membrane bending and cholesterol (123). For other viruses, such as flaviviruses, both the addition and removal of cholesterol effectively blocked viral entry; suggesting that a fine balance in the cholesterol composition of the cell is required for viral entry (124).

However, viral entry is inhibited by an accumulation of cholesterol. The interferon-induced transmembrane (IFITM) proteins are a family of interferon stimulated genes (ISGs). One of these proteins is IFITM3 which has been demonstrated to combat a number of viruses including HIV-1, Zika virus, vesicular stomatitis virus, West Nile virus, dengue virus and IAV (125–128). IFITM3 expression is induced by both type I and type II interferons (129,130) and it has a particular role in modulating IAV virus infection with research finding enhanced viral replication when the gene was silenced and knocked out (128,131). This is accomplished through its interaction with vesicle-associated membrane protein (VAMP)-associated protein A (VAP-A). VAP-A interacts with oxysterol binding protein (OSBP) which possesses three binding domains: the Pleckstrin homology (PH) domain, the FFAT (two phenylalanines in an acidic tract) domain and the core lipid binding ORP domain (ORD). The PH binds phosphatidylinositol-4-phosphate (PI4P). This interaction is important as OSBPs transport PI4P to the ER to facilitate the counter transport of phosphatidylserine (PS) (132), a phospholipid required in the plasma membrane for cell signalling (133). The PH also aids the protein’s recruitment to membranes such as the Golgi (134,135). The FFAT interacts with VAP-A, targeting the protein to the ER (136), with the C-terminal ORD extracting sterols from the membrane. The VAPA-OSBP interaction allows OSBP to transfer cholesterol from the endoplasmic reticulum to organelles (137). When this interaction is inhibited, cholesterol accumulates in the ER. This leads to a build-up of cholesterol in multi-vesicular bodies and late endosomes that originate from the ER, these organelles being used by viruses for escape into the cytoplasm (135,138). In addition, IFITM3 also causes enlargement of these cholesterol-rich endocytic compartments. This late endosomal cholesterol accumulation correlates with decreased IAV entry (138).

The drug U18666A is an NPC1 inhibitor and like IFITM3, causes an accumulation of cholesterol in lysosomes/late endosomes. U18666A interacts with a binding site, independent of the cholesterol binding site, called the sterol-sensing domain. This results in NPC1 being unable to transport cholesterol (139).

In addition, specific oxysterols present in the endosomal membrane restrict virus entry. The ISG cholesterol oxidase (CH25H) catalyses the oxidation of cholesterol to 25-hydroxycholesterol (25HC) an oxysterol thought to be involved in the response to enveloped viruses such as HIV. 25HC modulates cholesterol in cholesterol-containing membranes, altering its position and orientation in the membrane, moving it to the water interface. This makes cholesterol more accessible to external receptors for its removal, decreasing available cholesterol within the membrane for use by viruses (140). Additionally, 25HC orients itself differently within the membrane, having an off-parallel arrangement that increases the space between phospholipid head groups. Furthermore, this membrane expansion, hydrophilic interactions between the 25-hydroxyl groups of 25HC may cause aggregation within the membrane which could inhibit viral fusion (141).

Possible reasons why cholesterol has this antiviral effect have been suggested. Late endosomal cholesterol accumulation disturbs the back fusion of intralumenal vesicles within the limiting endosomal membrane. This disturbance was enough to reduce infection of vesicular stomatitis virus, meaning that cholesterol accumulation disrupts intra-endosomal membrane dynamics (142); this could also be the same reason as to why IAV fusion is inhibited. Alternatively, excess endosomal cholesterol could move into the membrane of IAV, which would reduce the proximity of the viral and endosomal membranes due to the cholesterol enriched membranes being thicker, therefore the cooperation between haemagglutinins wouldn’t be as enhanced and they would be less effective at generating fusion pores (143,144).

Research on lipid transfer proteins (LTPs) such as OSBPs and NPC1 is applicable to a clinical environment. Functional LTPs are needed for efficient viral replication, with inhibition of them potentially stalling entry. The drug U18666A interacts with the luminal loop of NPC1 which perturbs cholesterol transport from late endosomes (145). This causes an accumulation of endosomal membrane cholesterol similar to the effects of IFITM3, which would inhibit virus fusion. These LTPs are therefore an attractive target for novel antiviral therapeutics.

1.3 The Influenza A virus (IAV)

1.3.1 Overview

Influenza is a widespread disease which is characterised by the rapid onset of fever, dry cough, malaise, sore throat, headaches and joint/muscular pain. These symptoms can be severe and generally last for multiple weeks before recovery, however the disease is culpable for 290,000 to 650,000 deaths all around the world (146). In the US alone there are 3000-49,000 respiratory deaths relating to influenza annually (147,148). The effects of seasonal influenza are not just limited to clinical concerns, but also cause broader economic consequences (149).

The causative agent of influenza is the influenza virus, which belongs to the Orthomyxoviridae family of viruses. There are many genera of influenza viruses, but of main concern are the influenza A viruses (IAV). Constant surveillance of IAV is needed to monitor the antigenic drift of the virus, which is the cause of regular outbreaks of seasonal influenza. Antigenic drift is when a small mutation induces variation in the glycoprotein receptors of influenza (150–152). Of more concern is antigenic shift: the replacement of influenza glycoproteins with novel subtypes that haven't been present in human populations for a long time, via significant genetic alterations (153,154). This generally occurs when the virus passes through an animal reservoir such as a swine or avian host, before infecting humans (155). Antigenic shift was the cause behind the emergence of the Highly Pathogenic H5N1 Influenza virus, more commonly known as avian influenza. This lineage is thought to have arisen from multiple reassortments between H5 viruses in migratory birds and N1 viruses in terrestrial poultry (156). This virus has enhanced virulence (157) and the threat of it causing an epidemic is an example of why surveillance and research into the influenza viruses is always essential.

Influenza A viruses share several common structural elements. Influenza A virions are either spherical or filamentous, their spherical forms being approximately 100 nm in diameter. The core of an IAV is a viral Ribonucleoprotein (vRNP) complex. These complexes comprise of the viral RNA (vRNA) bound with nucleoprotein (NP). The NP binds without any sequence specificity to the vRNA, with an association frequency of approximately one NP to 24 nucleotides. NP binds at a high affinity to the phosphate sugar backbone of vRNA, leaving the bases exposed for replication. The ends of the vRNA are not associated with NP but instead fold back on itself and coil in a double helix configuration. The viral polymerase complex binds to the 5' and 3' ends, with these terminal sequences acting as a promoter region (158–160) (Figure 1.9).

IAV possesses a genome comprised of eight negative sense vRNA segments. They are numbered according to their decreasing length, with segment 1 being the largest. Segment 1 codes for the polymerase basic 2 subunit (PB2), with segment 2 coding for the polymerase basic 1 subunit (PB1). Segment 3 codes for the polymerase acidic subunit (PA), all three subunits of which form the heterotrimeric polymerase complex that associates with each vRNP (161). Segment 4 codes for one of the key glycoproteins utilised in IAV infection, haemagglutinin (HA) (162) while segment 5 codes for the main structural player in vRNPs: NP (163). Segment 6 codes for neuraminidase (NA), another significant glycoprotein for IAV (162). Segments 7-8 code for more than one protein each, with segment 7 coding for the M1 and M2 structural proteins and segment 8 coding for NS1 and NS2 (164) (Figure 1.9). These segments arrange themselves in a ring-like structure, with seven segments on the outside and one in the centre (165).

Also contained within the virion core is the Nuclear Export protein (NEP), otherwise known as NS2. This protein's main function is to facilitate the export of newly synthesised vRNPs from the nucleus (166). Surrounding the genome and NS2 protein is a matrix of M1 proteins which forms the protein capsid. M1 is necessary for maintaining the structural integrity of the viral structure and also binds the vRNPs within core (167). Surrounding the M1 protein layer is a host cell derived lipid membrane which is studded with several significant glycoproteins: haemagglutinin, neuraminidase as well as the M2 channel protein (168) (Figure 1.9).

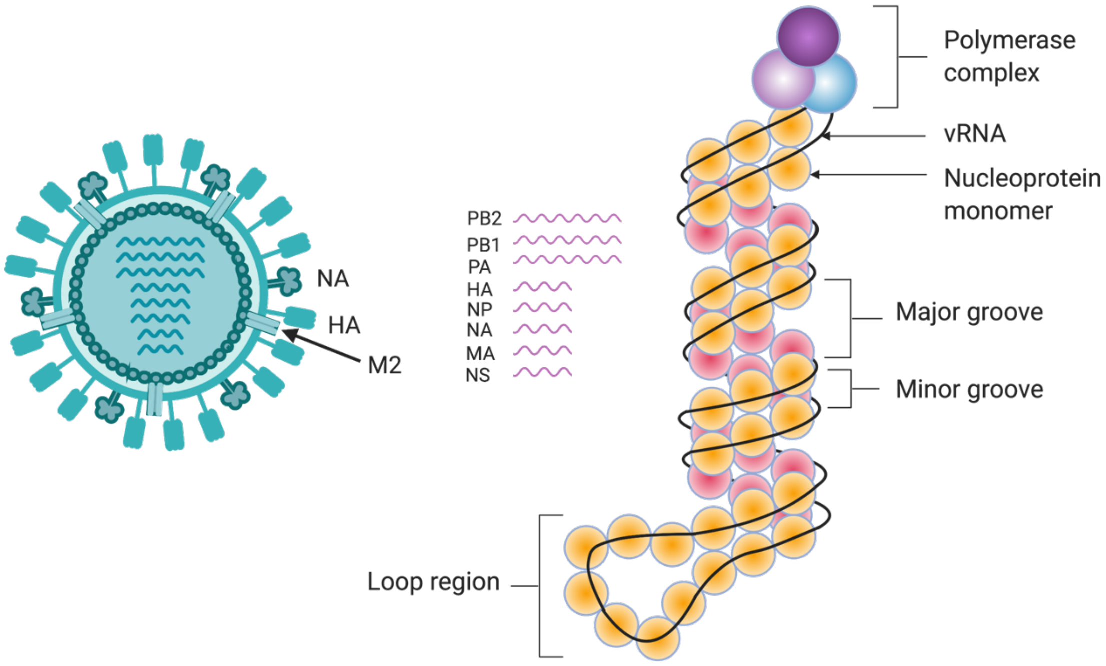

Figure 1.9: Overview of the basic structure of IAV (left). The genetic material of IAV (vRNA) (middle) is complexed with nucleoprotein to form viral ribonucleoproteins (vRNPs) (right). The vRNA within vRNPs takes a double helical form, binding terminally to a polymerase complex comprised of PA, PB1 and PB2. The genome of IAV is contained within a capsid made of the M1 protein which is surrounded by a lipid membrane. Studding this membrane are two glycoproteins: haemagglutinin (HA) and neuraminidase (NA) as well as the transmembrane channel: M2. vRNP schematic adapted from (159). Produced using Biorender.

1.3.2 Replication cycle of IAV

The replicative cycle (Figure 1.10) of human IAV begins with haemagglutinin (HA) interacting with sialic acid with a α-2,6-linkage to galactose. This type of expressed sialic acid is common on the surface of tracheal epithelium (169). For avian IAV strains, the sialic acid target differs in that it possesses an α-2,3-linkage (170,171) and is more abundant in the avian gut. Once HA binds to sialic acid, the virus is internalised via endocytosis. The exact uptake mechanism varies, with IAV utilising both receptor-mediated and clathrin-mediated endocytosis as well as macropinocytosis (172–174).

Sialic acid binding to haemagglutinin (Figure 1.10 A) appears to be the trigger for the *de novo* synthesis of clathrin coated pits (CCPs) around the bound virus, an unorthodox mechanism as usually receptors are initially targeted to CCPs. Once these CCPs form they evolve into clathrin coated vesicles (CCVs) and the virus is internalised (175). Once endocytosed (Figure 1.10 B), the influenza virus would find itself within an early endosome which soon matures to a late endosome. Endocytosed biological cargo has two fates. The first is to be recycled back to the plasma membrane. Otherwise, the material (often including invading pathogens) migrates further into the cell to the perinuclear region via microtubule assistance (176,177). It is here that influenza conducts its escape from endosomal confinement.

Acidic conditions are required for late endosomal escape (178). Within the late endosome IAV encounters a low pH (approx. 5-6) which causes large-scale irreversible conformational change to the haemagglutinin glycoprotein, converting it from its prefusion state to a low pH hairpin structure. Consequently, its fusion peptide is exposed (170,179). This fusion peptide interacts with the endosomal membrane, mediating a merger between the virion membrane and it. This generates a fusion pore in the membrane of the late endosome (180,181).

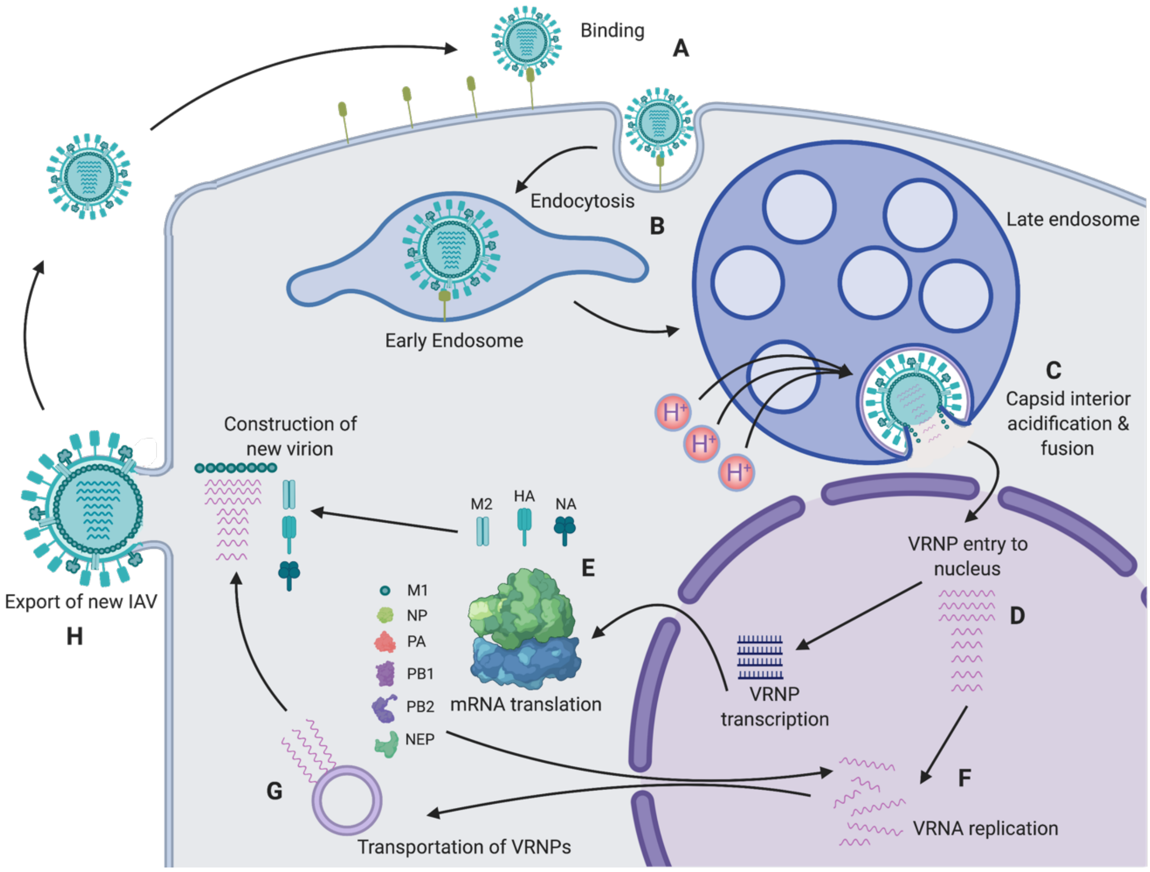

Figure 1.10: The replication cycle of the Influenza A virus (IAV). Upon random interaction, IAV binds to sialic acid (**A**) via its haemagglutinin glycoprotein receptor, initiating receptor-mediated endocytosis which can be clathrin dependent or independent (**B**). IAV enters the cell in an early endosome which matures to a late endosome. Acidic conditions within the endosome allow IAV to fuse with the endosome membrane, the vRNPs within thereby escape into the cytosol (**C**). The vRNPs are transported to the nucleus (**D**) where they are transcribed for protein translation (**E**) and replicated for new vRNPs (**F**). All the components are eventually shuttled back to the cell membrane (**G**) and a new virus exits the cell by budding (**H**). Produced using Biorender.

Prior to HA activation though is another important step in IAV's replication. Endosomal acidic conditions prime the viral core for uncoating, by opening the M2 channel proteins. When the endosomal pH reaches approximately 6 the channels open, allowing protons and potassium ions to flow into the capsid interior (182). This renders the viral core uncoating competent (183,184). A characteristic of this is that the membrane envelope of the virion undergoes structural change, become more pliable and predisposed for fusion as the interaction between the M1 protein layer and the membrane weakens (185). Acidification also weakens the M1 protein's ability to interact with itself and vRNPs. The pH drop to approximately 5.5 results in an irreversible softening of the protein core, a process that can be blocked by inhibiting M2 with amantadine, proving it is due to internal acidification (186,187). An influx of potassium ions likely then weakens M1-vRNP interactions, as potassium ions have been seen to influence the secondary structures of single stranded RNA (188). Now that the vRNPs have dissociated from their tether, the integrity of the M1 coat compromised and successful HA mediated fusion between the endosomal and virus membrane, the vRNPs gain access the cytosol (189,190) (Figure 1.10 C).

Access to the nucleus is restricted with acceptable cargo possessing nuclear localisation signals which enable translocation. These signals direct cellular proteins to shuttle cargo into the nucleus. It is here that the NP, which provides the skeleton for the vRNPs, plays a considerable role in aiding IAV in establishing infection. vRNPs alone surpass the maximum size for passive transport into the nucleus. Proteins belonging to the family known as karyopherins recruit cargo tagged with nuclear localisation signals (NLS) and chaperone them across the nuclear membrane (191). While all the proteins in the vRNP complex possess NLSs, it is the NLSs on NP which appear to significantly aid the complex's movement into the nucleus (192). NP possesses two NLSs, one at the N-terminus and one at the middle of the protein, with some evidence pointing to a possible third NLS (193). NP interacts with two karyopherins via these NLSs: karyopherin α1 and karyopherin α2. These proteins are NLS-binding proteins, conventionally recognising 'classical' NLSs, which are likely to be two clusters of basic residues, and binding to them (191,194,195). However, karyopherin α1 predominantly interacts with the N-terminal NLS which is considered a nonclassical NLS (196). Karyopherin α1 then interacts with karyopherin β, forming a trimeric complex which interacts and docks at the nuclear pore complex (NPC) (197).

Following NPC docking, translocation of the vRNP into the nucleus is facilitated by p10 which is a cytosolic nuclear transport factor and the GTPase Ran which is a regulator of protein transport (198) (Figure 1.10 D).

Replication of influenza within the nucleus begins with the generation of mRNA from the negative sense vRNA. The vRNA cannot itself be used directly as mRNA for translation and must be transcribed first. Synthesis of mRNA from vRNA is conducted by the RNA-dependent RNA polymerase (RdRp) which is comprised of the PA, PB1 and PB2 subunits (168,181). Transcription (Figure 1.11 (1)) is initiated via a process known as 'cap snatching' whereby the polymerase subunits cannibalise host cell mRNAs. The PB2 subunit recognises 5' terminal methylated caps (cap 1 structures) and binds them, with the PA subunit possessing the endonuclease activity needed to cleave the 10-14 nucleotide stretch off (199–202). These mRNA fragments behave as primers to initiate mRNA synthesis. The RdRp would then transcribe the vRNA, transcribing a poly(A) tail on the mRNA via a chain of five to seven uracil residues already encoded on the vRNA (203). Finally, host cell splicing machinery is utilised to splice the viral mRNA. For segments 7 and 8, this allows two proteins to be translated; segment 7 coding for both M1 and M2 and segment 8 coding for NS1 and NS2, depending on whether the spliced or unspliced mRNA is read (204). Transcription of the vRNA occurs at quite a high rate early in infection however at later time points (post 3.5 hpi) the transcription rate slows down considerably while vRNA replication remains high, however export rates of either RNA type are unaffected (205). Export of the mRNA is facilitated by the NS1 protein which is thought to interact with the NXF1 export apparatus. This apparatus is used to export its late gene transcripts (206,207). Additionally, the hnRNP proteins have a role in mRNA export. These are abundant in the nucleus and shuttle rapidly between the nucleus and cytosol. These proteins bind mRNA and pre mRNA, including viral mRNA, and possess nuclear export signals (NESs) needed to vacate the nucleus (208,209).

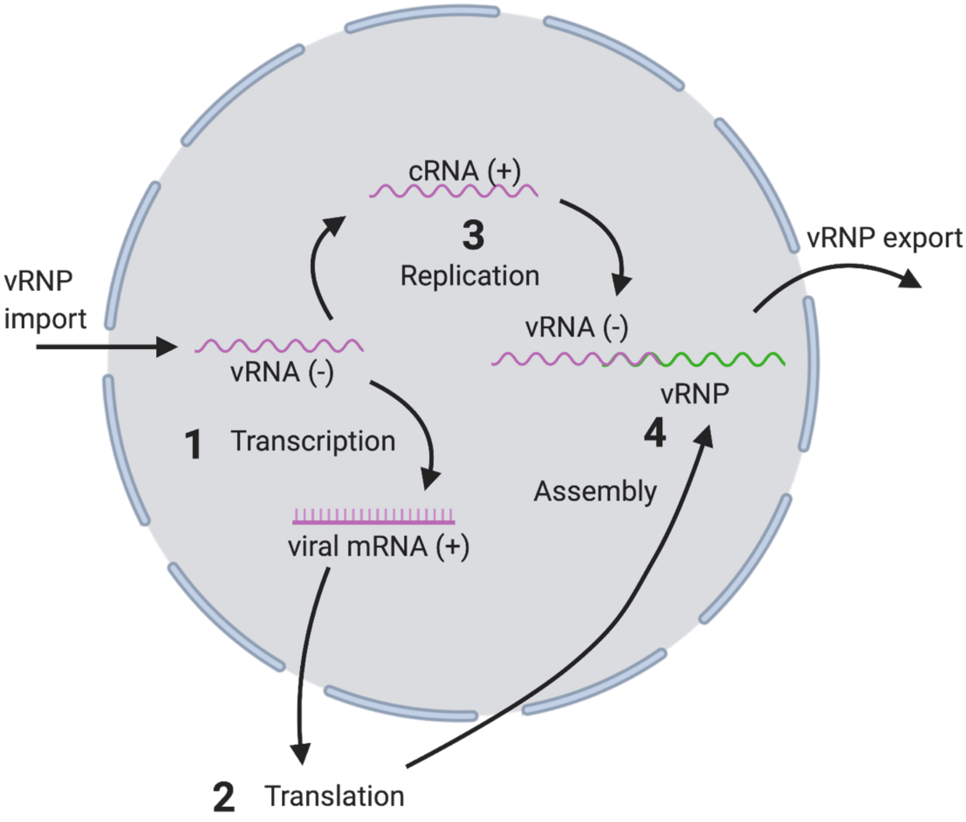

Figure 1.11: IAV genome replication in the nucleus. After vRNP import the vRNA is transcribed into viral mRNA (**1**) which is then exported from the nucleus and translated by cellular ribosomes (**2**). The original vRNA template is replicated via a cRNA intermediate to form more vRNA of a (-) sense (**3**) with the assembly of the vRNP occurring simultaneously to vRNA synthesis (**4**). Adapted from (210). Produced using Biorender.

There is a dramatic change in translation following the infection of a cell with IAV. Viral mRNA leaving the nucleus is translated by ribosomes (Figure 1.10 E) (Figure 1.11 (2)) but in infected cells, host cell mRNA translation appears to be inhibited while viral mRNA translation seems to be upregulated. Investigation into this has found that it is not due to a ribosomal preference to the 5' untranslated region that IAV mRNAs possess (211) but could be due to the NS1 protein. The NS1 protein, encoded by the unspliced segment 8, not only appears to reduce host mRNA translation but also amplifies the synthesis of several viral proteins. NS1 has been shown to amplify the translation of both NP and M1 (212) possibly due to the presence of specific regulatory sequences on these mRNAs which NS1 interacts with (213). IAV also inhibits host cell mRNA translation, interfering with the initiation and elongation steps of translation (214). Additionally, NS1 interacts with several proteins to inhibit host mRNA polyadenylation which would lead to an inability for the mRNA to be exported and eventually translated (215). With host cell translation impaired, translation is optimised for IAV with the PB1, PB2, PA NP, NS1, NS2 and M1 proteins all being produced in the cytosol for vRNP assembly. The envelope proteins: HA, NA and M2 are all produced by ribosomes bound to the ER. These newly synthesised envelope proteins are inserted into the ER, glycosylated and delivered to the Golgi for further post-translational modification. Following that they are transported to the membrane of the host cell (210).

At some point in the replicative cycle, a switch occurs from transcription to genome replication in the nucleus (Figure 1.10 F) (Figure 1.11 (3)). Genome replication involves producing vRNA copies of the original vRNAs via a complementary RNA (cRNA) intermediate. This process is a two-stage primer independent process, unlike transcription (216). This switch is thought to be due to small viral RNAs (svRNAs) which are believed to be generated by the RdRp, with these svRNAs interacting with the replicative machinery to transition it from transcription to replication (217).

The RdRp initiates replication just in from the 3' terminus of the vRNA to generate a primer which realigns with the 3' terminus. The cRNA product then assembles into a vRNP like structure, known as a complementary ribonucleoprotein (cRNP) complex. Just like vRNPs, the viral RdRP is bound to the 5' and 3' termini and NP associates with the cRNA strand (218). Replication of the cRNA then proceeds however, unlike with the first stage of replication, a second polymerase in addition to the complexed polymerase needs to be present. Interestingly, this polymerase doesn't need to be functionally active meaning that it is *trans*-activating. Possibly this second polymerase induces a conformational change in the complexed RdRp which allows efficient initiation of replication at the cRNA's 3' terminus (216,218). These polymerases are bridged by the host protein ANP32A, which stabilises the polymerase dimer and promotes template realignment (219). With the two stages of replication complete, a perfect copy of the original vRNA should result.

Following vRNA replication, new vRNPs need to be constructed and exported from the nucleus (Figure 1.11 (4)). The matrix protein M1 appears to be a significant driving force in this process, with the protein interacting with newly synthesised vRNPs. M1 then aids vRNP export from the nucleus and prevents the import of them back into the nucleus (192,220). Nuclear import of the M1 protein following its synthesis in the cytosol appears to terminate vRNA replication (221) however M1's presence appears to support the assembly of NP and vRNA into a helical configuration not dissimilar from a completed vRNP (222). M1 interacts with completed vRNPs directly, the exact nature of which is uncertain due to conflicting literature. Studies have shown that the N-terminal of M1 interacts with NP (223) however it has also been shown that the C-terminal domain of M1 binds to vRNPs (221). Regardless, this interaction alone is not sufficient for nuclear export, with the vRNPs relying on another protein in influenza's arsenal: the NS2 protein otherwise known as the nuclear export protein (NEP). This protein is highly important due to it possessing a leucine rich nuclear export signal (NES) which is identified by the NPC for translocation out of the nucleus. This nuclear export activity was found to be heavily dependent on the chromosome region maintenance 1 (CRM1) protein mediated pathway, which aids in shuttling the complex (224,225). The NS2 protein binds to M1 via its C-terminal domain, and the whole complex is transported (226,227).

Recently exported vRNPs are prevented from being imported back into the nucleus via the action of the M1 and NP proteins. M1 is a known inhibitor of vRNP import, hence why its dissociation from the original virion's vRNPs is necessary for nuclear import. Because of this, and its collated export from the nucleus with new vRNPs, it would likely prevent them from being translocated back. M1 does this by inhibiting interactions between vRNPs and NPCs (228,229).

NP has been shown to bind to actin and this interaction is thought to facilitate a second method of cytoplasmic retention. RNPs interacting with F-actin would likely be unable to then be imported back into the nucleus, allowing them to continue to the cell membrane and be assembled into a new virion (230).

With all IAV components now having been produced by the cell, they all need to be brought to a single point at the plasma membrane for assembly (Figure 1.10 G). vRNPs loitering in the perinuclear region after recent nuclear export will localise at the recycling endosome (RE) which is adjacent to the proximally located microtubule organising centre (MTOC). These recycling endosomes are the platforms which IAV then uses to deposit its components at the plasma membrane (231–233) (Figure 1.12). An interaction between vRNPs and the REs is required for IAV to hijack the transport system, with Rab11 being the facilitator of this. Rab11 is a GTPase and marks the envelopes of vesicles operating in the recycling endosome pathway. These recycling endosomes deliver endocytosed cargo, or cellular cargo, to the perinuclear recycling endosome compartment before it is sent to the plasma membrane for removal (234).

The PB2 subunit of the vRNPs is what interacts specifically with Rab11 (231). This interaction impairs the function of the recycling endosome due to PB2 directly competing with cellular host factors that also need to bind. A result of this is that there is clustering of single and double membraned vesicles in the cytosol which creates hotspots of vRNPs (235). These hotspots could arise due to the collision of Rab11 vesicles and may be sites where vRNPs can interact via RNA-RNA interactions to assemble themselves so that all eight vRNPs are present (236,237).

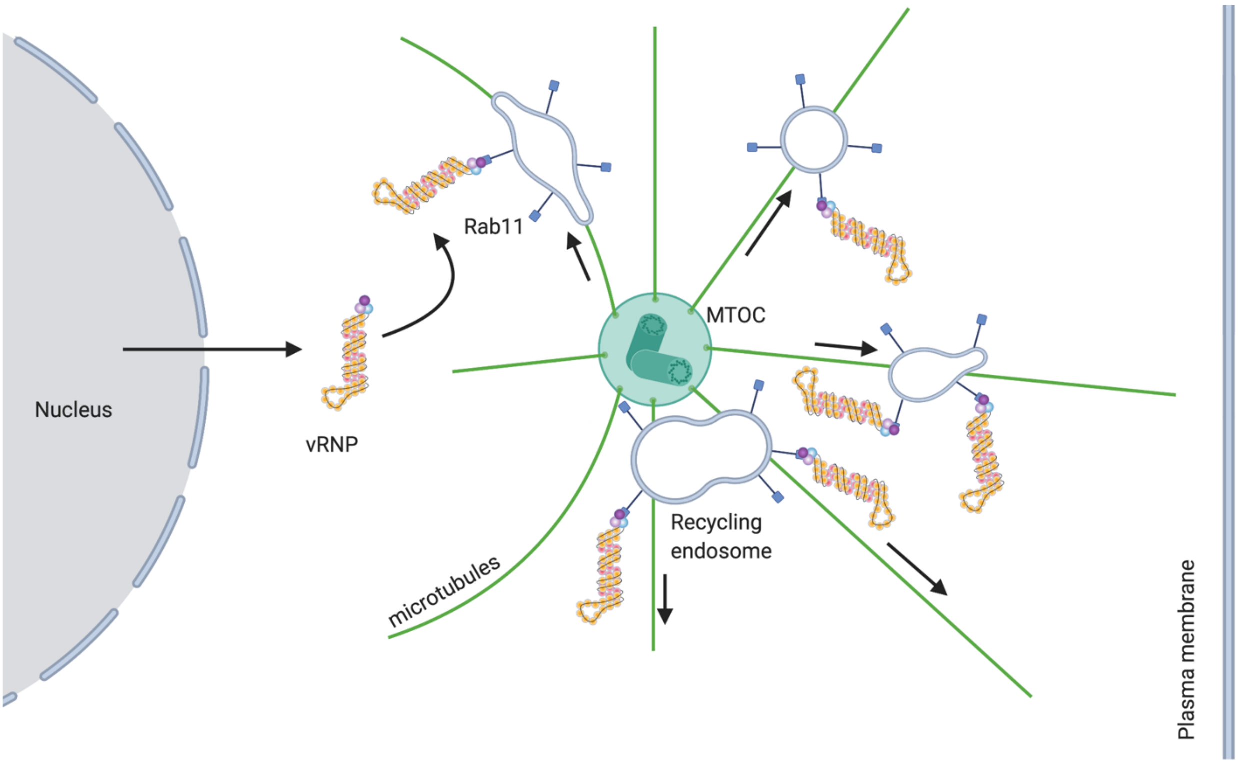

Figure 1.12: vRNPs transportation from the perinuclear region after nuclear export via recycling endodomes (REs). These compartments express Rab11 and are shuttled to the plasma membrane. vRNPs interact with Rab11 via their PB2 subunit and they 'piggyback' their way to the cell periphery. Adapted from (231). Produced using Biorender.

The final part of IAVs replicative cycle is genome packaging and the assembly of a new virion (Figure 1.10 H). Post-translational modification of the envelope proteins NA and HA appear to be the possible means for the proteins to target sites of budding (238,239). Not just any region of the plasma membrane is suitable for budding. The envelopes of IAV particles require high concentrations of cholesterol (240) which leads to IAV assembly at cholesterol rich membrane domains known as lipid rafts (96,241). HA and NA are directly targeted to these lipid rafts, embedding themselves in the plasma membrane at raft sites. HA's transmembrane domain associates with the lipid rafts, its binding to the membrane initiating the budding process. This is because HA appears to modulate plasma membrane curvature (242). Removal of HA doesn't completely abolish this (243), which suggests NA plays a role in this as well and may explain why they are both recruited at this initiation stage.

M1 recruitment into the developing virion is then the next step. Both the cytoplasmic tails of NA and HA facillitate this, with there likely being a dual redundancy in their methods of interaction due to how important the interaction is for virion assembly (244). With M1 recruited, the high concentrations of the protein allows it to mulitmerise (167); this recruitment conveniently influencing membrane curvature and virion overall morphology (245). M1 also plays a role in binding the assembled vRNPs and NS2, binding to NP and grouping them together at the bud site (96).

M2 is recruited to the boundaries of budding sites via binding between its cytoplasmic tail and the already recruited M1 protein (246). Its incorporation is not its only action here, it may also aid membrane scission (247) (the act of severing a budding structure's membrane and re-sealing the membranes of the now two structures). M2 possesses an amphiphilic α-helix which induces negative membrane curvature. This facilitates neck formation on the budding virus and concomitant scission (248).

With the virus now having budded, it has only one final obstacle to overcome: which incidently is sialic acid, the receptor that granted IAV initial access. NA possesses sialidase activity, catalysing the hydrolysis of the glycosidic link which attaches sialic acid to galactose. With NA removing proximal sialic acid residues, the virus is free to detach without problematic HA-sialic acid interaction (249). In the airways of its host, proteases would then cleave HA, converting it from its precursor (HA0) state to its cleaved (HA1/HA2) state, allowing it to participate in fusion and enabling the virion to be infectious (250).

1.3.3 IAV and cytokine storms

In humans, severe influenza is uncommon. Complications in influenza disease progression usually arise from the hyperinduction of proinflammatory cytokines. This response is initiated in the respiratory cell targets of influenza. IAV proliferates in respiratory cells and then invade neighboring cells such as alveolar macrophages. Eventually these cells die from necrosis or apoptosis and inflammatory responses are triggered due to the release of death factors (251). Blood flow to the affected site is increased, raising the local temperature and bathing the site in leukocytes. Additionally, the induction of pro-inflammatory cytokines and chemokines expression occurs.

Cytokines are a diverse group of proteins which regulate cell proliferation, differentiation and chemotaxis. They also regulate angiogenesis and inflammatory responses. Within this group of cytokines are inteferons and interleukins, but the largest group are chemokines. Chemokine expression results in the recruitment of pro-inflammatory cells such as neutrophils and macrophages, which further increase cytokine expression but also invades and damages tissue. Interferons, interluekins and chemokines are all contributors to cytokine storms. A cytokine storm occurs when localised inflammation overflows into systemic circulation. Inflammatory cells and cytokines are circulated to other sites causing sepsis, hypotension and attenuated temperature homeostasis. Multi-organ dysfunction can occur in extreme cirucmstances. Understanding what causes cytokine storms is important (251).

1.4 Signalling pathways

1.4.2 TLR Signalling

Virus infection is countered by the innate immune system which utilises various signalling mechanisms to achieve this. Viruses can be detected by a range of receptors expressed by cells, but by far the most utilised would be the Toll-like receptors (TLRs). These receptors, originally identified in *Drosophila* (252), are found in many organisms including mammals. These receptors are essential at initiating an immune response to pathogens, with a range of different TLRs recognising an array of pathogen associated molecular patterns (PAMPs). The vast amount of research conducted into these receptors show that while most signal through a common adaptor protein, several do not and they all seem to elicit unique responses to the PAMPs they recognise (253). TLRs are type I membrane proteins, with there being thirteen different TLRs in mammals. These receptors are found ubiquitously in cells, including on the cell surface and within endosomes. Their unique structure comprises a leucine rich repeat (LRR) ectodomain which is vital for PAMP recognition, and a cytoplasmic domain necessary for downstream signalling. This domain is homologous to the interleukin-1 (IL-1) receptor family, resulting in the domain being designated the Toll/IL-1 receptor (TIR) domain (253–256) (Figure 1.14).

TLRs are employed by both innate immune cells (255) as well as other cells such as epithelial cells and fibroblasts (257–259), making them an effective detection system for foreign particles and pathogens. They also recognise a variety of PAMPs, with these target ligands generally being based on where the specific TLR is found. All TLRs are generated in the ER (260) but are then transported to their location of function and proteolytically cleaved to enable them to optimally detect PAMPs (261,262). One key function of TLRs are as activators of LAP. Pathogens are recognised by TLRs, following which they would be taken up by phagocytosis and the LAPosome decorated with PI3P which preceeds LC3 conjugation (263).

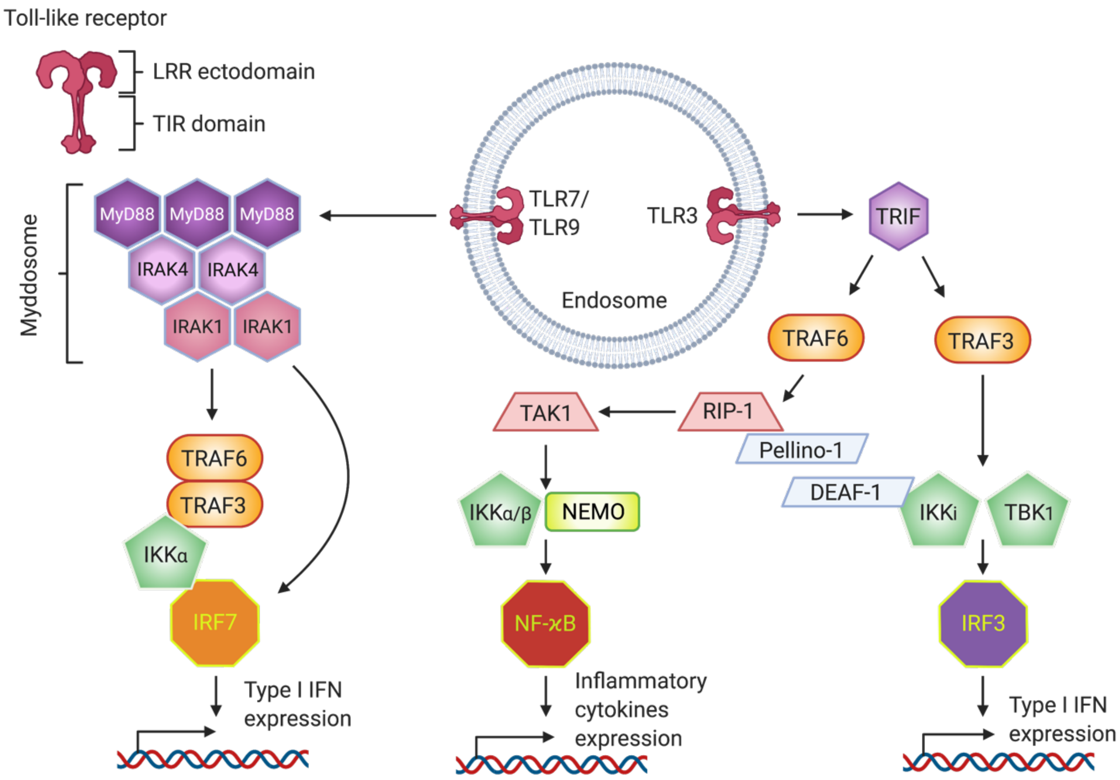

Figure 1.14: TLR signalling pathways in response to viral infection. Inflammatory cytokine and Type I IFN expression is triggered in response to viral infection by TLR3 (recognising dsRNA) or TLR7 and TLR9 (recognising ssRNA and DNA unmethylated at CpG motifs respectively) in pDCs. These three TLRs localise to endosomes. TLR7 and TLR9 signal through the traditional MyD88 adaptor protein. MyD88 is recruited following TLR engagement and following IRAK4 recuitment to MyD88. This MyD88 complex also recruits IRAK1 to form the Myddosome, which either directly or indirectly recruits IRF7. Once IRF7 is recruited, it is phosphorylated and enters the nucleus to modulate Type I IFN expression. TLR3 is unique to TLRs in that it solely signals through the TRIF adaptor protein. TRIF activates both TRAF6 and TRAF3, TRAF6 interacting with RIP-1 which goes on to interact with the TAK1 complex. This leads to activation of NF-ϰB and inflammatory cytokine expression. TRAF3, on the other hand, interacts with IKKi and TBK1. These aid in phosphorylating IRF3 which leads to Type I IFN expression. Adapted from (264). Produced using Biorender.

The location of TLRs specifies which subfamily it belongs to, these being whether they localise to the cell surface or are intracellular. TLRs on the cell surface include: TLR1, TLR2, TLR4, TLR5, TLR6 and TLR10 with these recognising adjuvants such as lipids and proteins. Intracellular TLRs include: TLR3, TLR7, TLR8, TLR9, TLR11, TLR12 and TLR13, with these recognising nucleic acids. The most important for virus detection would be TLR3 (recognising dsRNA), TLR7 (recognising ssRNA) and TLR9 (recognising dsDNA unmethylated at CpG motifs); all of which localise to endosomes (255,265,266). While TLR3 is specific for dsRNA, it has been shown to sense some ssRNA viruses, such as West Nile virus (267), Cytomegalovirus (268) and IAV (269,270).

TLRs recruit adaptor proteins to facillitate signal transduction (Figure 1.14). These adaptor proteins contain a TIR domain which interacts with the TLR TIR domain. All TLRs, except TLR3, recruit the MyD88 adaptor protein. MyD88 goes on to activate the transcription factor NF-ϰB, which in turn leads to inflammatory cytokine production (271,272). However in plasmacytoid dendritic cells (pDCs) the virus-sensing TLR7 and TLR9 proteins signal through MyD88 to trigger type I Interferon (IFN) production (264,273–276).

TLR3 recognises dsRNA and when engaged by an adjuvant, recruits the TRIF adaptor protein instead of MyD88. TRIF interacts with either the TRAF6 or TRAF3 kinases, with those kinases going on to activate either inflammatory cytokine expression or type I IFN expression respectively. TRAF3 interacts TBK and IKKi, IKK-related kinases which phosphorylate IRF3. Following that, IRF3 forms a dimer which enters the nucleus and upregulates type I IFN gene expression. In contrast to TRAF3, TRAF6 interacts with RIP-1, a kinase involved in the inflammatory signalling pathway. RIP-1 interacts with TAK1, an upstream kinase of NF-ϰB. This interaction leads to NF-ϰB's activation and subsequent inflammatory cytokine expression (255,264,265). The pellino-1 E3 ubiquitin ligase promotes both the inflammatory and type I IFN expression pathways. Pellino-1 recuits RIP-1, aiding NF-ϰB activation as well as binding to DEAF-1, a transcription factor that mediates IRF3-DNA binding (264,277–279).

TLR7 or TLR9 recruit MyD88. The kinase IRAK4 is firstly recruited to MyD88, with the complex being recruited to the TIR domain of the activated TLR. MyD88 forms a larger complex, referred to as a Myddosome, upon IRAK1 kinase recuitment. During the formation of the Myddosome, IRAK4 activates IRAK1 leading to IRAK1 autophosphorylating

(264,280) concomitantly causing it to either directly interact with Interferon regulatory factor 7 (IRF7) or indirectly interact through the TRAF6/TRAF3 kinases. IRF7 is then phosphorylated by IKKα kinase if indirectly recruited to the MyD88 complex via TRAF6 and TRAF3, or directly by activated IRAK1. IRF7 then enters the nucleus and binds to type I IFN promoters to upregulate gene expression (264,281).

Type I IFNs, an example being IFNβ, are secreted cytokines which bind to IFN receptors and trigger an immune response in cells which generates an antiviral state. This 'antiviral state' encompasses a range of different protein expressions and cellular effects that limit viral propagation (282). Genes upregulated that produce proteins necessary for this antiviral state are known as interferon stimulated genes (ISGs) and include ISG15 and ISG56 (IFIT1). ISG15 directly antagonises infection by partipating in ISGylation, a process whereby the protein binds to newly translated viral proteins and impairs their function (283). IFIT1 has RNA binding characteristics, binding to mRNA to prevent the binding of eukaryotic translation inititaion factors and preventing translation (284).

1.4.2 cGAS-STING-mediated type I IFN response

LAP is also connected to another pathogen recognition receptor pathway, the cyclic GMP-AMP synthase (cGAS) - stimulator of interferon genes (STING). The cGAS-STING pathway detects foreign DNA, with cGAS binding to double stranded DNA (dsDNA) which produces the STING agonist 2,3' cyclic GMP-AMP (cGAMP) (285). STING comprises of a cytosolic N-terminal segment, a transmembrane domain that spans the membrane four times, a connector region and a C-terminal cytosolic ligand binding domain (LBD). At the ER, STING forms homodimers and cGAMP binds to the LBD. This binding results in conformational change including a 180° untwisting of the LBD before inwardly rotating. Finally, the LBD is covered by an ordered β-sheet. Altogether, this restructuring supports oligomerisation of adjacent STING dimers. Disulphide bridges form between the dimers, and exposed cysteine residues covalently tagged with fatty acids by palmitoylation. This completes the transition of STING dimers into the activated STING unit. The activated

STING unit is liberated from the ER, being incorporated into coatomer protein complex II (COPII) vesicles. These pass through the endoplasmic reticulum-golgi complex, with the C-terminal of STING recruiting TANK-binding kinase I (TBKI). TBKI phosphorylates a serine residue (Ser366) at the C-terminal of STING, which allows it to recruit IRF3. TBKI then phosphorylates IRF3. This then leads to the expression of type I IFNs (286). LAP is involved in engulfing and destroying apoptotic cells (efferocytosis). This method is an efficient way of disposing of extracellular DNA and prevents the activation of cGAS-STING pathways, preventing unwanted cytokine expression. A deficiency in LAP promotes cGAS-STING activation in myeloid cells and the expression of pro-inflammatory genes. This aids the regulation of tumours, with a LAP deficiency creating a tumour suppressive environment (23,287). This demonstrates that LAP has both detrimental and advantageous roles in the innate immune system.

1.4.4 RIG-I Signalling

Viruses are also detected within the cytoplasm, with many receptors on stand-by to detect viral genomes. One of these receptors is retinoic acid inducible-gene-1 (RIG-I), which is an RNA helicase whose activation by ssRNA and dsRNA triggers downstream kinases, IRF3 and IRF7 phosphorylation and eventual type I IFN production (281). RIG-I, like TLRs, is found in dendritic cells and fibroblasts (288,289). To discriminate from host ssRNA, RIG-I detects ssRNA with a 5’-triphosphate, preventing any autoimmune reactions to host mRNA (290,291). Virus recognition by the immune system relies heavily on RIG-I just as it does on TLRs, with numerous viruses being detected by the helicase, including IAV, Japanese encephalitis virus, Sendai virus as well as the SARS and MERS coronaviruses (292–295).

The multidomain structure of RIG-I is conserved among vertebrates (296). At the N-terminal end of RIG-I are two caspase activation and recruitment domain (CARD) repeats. These CARDs are essential for initiating the signalling cascade that leads to type I IFN expression (297) (Figure 1.15). Following the tandem CARD signalling domain is the RNA binding helicase domain, terminating with a repressor domain at the C-terminus. This repressor is implicated in RIG-I autorepression, interacting with both the signalling and helicase domains (298,299). This repressor domain maintains RIG-I in a ‘closed’ structure whereby it is inactive. The CARD signalling domain is masked in this conformation, preventing downstream signalling (298,300).

The C-terminal RNA-binding domain recognises cytoplasmic viral RNA. This binding site-RNA interaction and ATP binding leads to a conformational change in the protein. An ATP-driven switch causes the structure to ‘open’ revealing the CARD signalling domain (301,302). Additionally, RNA binding promotes polyunbiquitination of RIG-I (303) and subsequent multimerisation of the protein (304). With RIG-I CARDs now exposed, they are free to interact with another CARD expressing protein, interferon β promoter stimulator 1 (IPS-1) also labelled mitochondrial antiviral signalling (MAVS) protein. IPS-1 is found expressed on the outer membrane of mitochondria, a location required for some of the cell responses it modulates (305,306). Evidence suggests that the interaction between both RIG-I and IPS-1 is facilliated by their CARDs, even proposing that there is significant oligomerisation of their respective CARDs to aid IPS-1 nucleation to form a filament, enabling downstream signalling (307).

Further to the CARDs interaction, IPS-1 concomitantly activates TRAF3 via its TRAF-interacting motif (TIM) for subsequent IFN expression (308). IPS-1 can also signal for inflammatory cytokine production by instead interacting with TRAF6 (309). TRAF3 signals to downstream TBK1 and IKKi which activates them and leads to IRF3/7 phosphorylation. This signalling facillitated by TANK, NAP1 and NEMO, which play a role in the TBK1/IKKi activation of IRFs (310–312). IRF3/7 is then phosphorylated and forms homodimers or heterodimers and enter the nucleus for type I IFN upregulation (313,314).

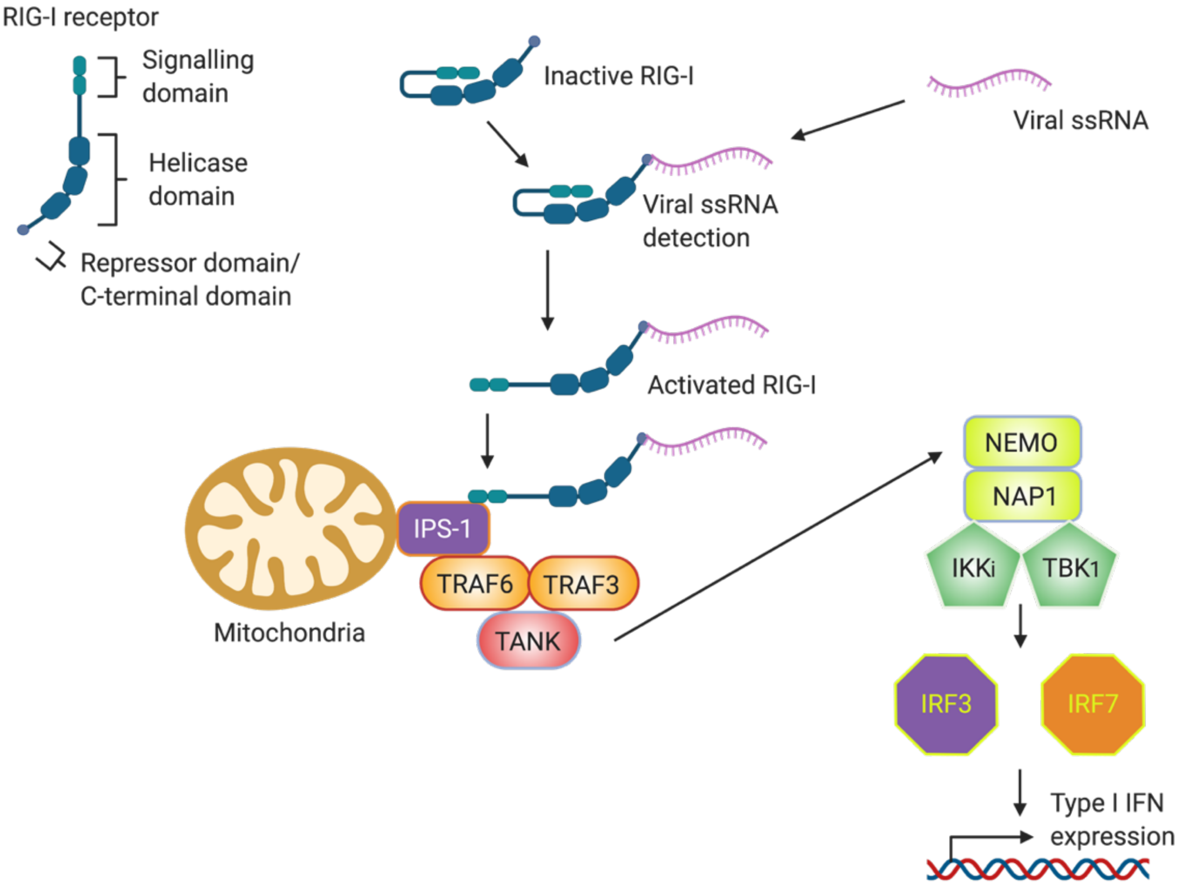

Figure 1.15: RIG-I signalling pathway in response to viral infection. Cytoplasmic viral sensors include the RIG-I, which recognises dsRNA and 5’-triphosphate ssRNA. The C-terminus of RIG-I interacts with RNA to cause conformational change that opens the CARD signalling domain to be revealed for downstream signalling. These CARDs interact with the CARD containing IPS-1 protein. IPS-1 signals through either TRAF6 (for the inflammatory response) or TRAF3, which is needed for IFN expression. Adapted from (314). Produced using Biorender.

1.5 Specific Aims

Investigate the role of the WD domain of ATG16L1 in cholesterol transportation to the plasma membrane in cells and tissue from mutant mice.

- The cholesterol content in the plasma membranes of wild-type (WT) cells and WD deficient cells will be investigated. Cholesterol will be assayed from subcellular membrane fractions using a biochemical fluorometric assay.
- Cholesterol will be localised in WT cells and WD deficient cells by bioimaging using probes such as filipin III and D4H mCherry, which specifically bind to cholesterol.

Investigate the mechanism of the WD domain of ATG16L1 in limiting fusion of IAV with cell plasma membranes using an acid bypass assay.

- By inhibiting cholesterol transport to the PM in WT and WD deficient cells with U18666A (an NPC1 inhibitor) and measuring IAV NP entry into the cytoplasm by immunostaining.

Investigate the entry of IAV into WD deficient cells by endocytosis and fusion.

- Using antibody staining that distinguishes between internal and external virus.
- Using IAV labelled with R18/SP-DioC18 to monitor fusion.

Investigate the role of the WD domain in suppressing viral replication and cytokine storms in MEFs and a 3D lung organ model.

- By titrating IAV secreted from MEFs and lung slices by $TCID_{50}$, qPCR and plaque assay.
- By measuring IFN and ISG expression by qPCR.
- By inhibiting IFN signal transduction through TLR3 inhibition.
- By inhibiting IFN signal transduction through Rig-I knock out.

CHAPTER 2

Materials and Methods

2.1 Tissue Culture

2.1.1 Primary cell line preparation

Wildtype (WT) and ∆WD mouse embryonic fibroblasts (MEFs) were obtained from embryos harvested from WT and ∆WD mice grown in the University of East Anglia Biomedical Research Centre Disease Modelling Unit. Embryos were macerated before being placed through a cell-strainer into Dulbecco's Modified Eagles Medium with GlutaMAX (DMEM) (Gibco) with 1% penicillin/streptomycin (p/s) (Gibco), kanamycin and 10% Foetal bovine serum (FBS) (Gibco). Cells were spontaneously immortalised through aggressive passaging to create MEF cell lines. Cells were incubated at 37°C 5% CO_2 unless otherwise stated.

WT and ∆WD mouse bone marrow derived macrophages (BMDMs) were obtained from the bone marrow of mouse femurs. Mouse leg bone marrow was flushed through a cell-strainer with Roswell Park Memorial Institute (RPMI) medium (Gibco). BMDMs were then plated in RPMI with 1% p/s and 10% FBS and 25 ng/mL macrophage colony stimulating factor (M-CSF) (Cell Signaling Technology) and incubated at 37°C 5% CO_2 for 7 days.

Madin Darby Canine Kidney cells (MDCKs) were obtained from the European Collection of Authenticated Cell Collections. MDCKs were grown in DMEM with 1% penicillin/streptomycin and 10% FBS and incubated at 37°C 5% CO_2.

Table 2.1: Cell seeding numbers for tissue culture plates.

Tissue culture vessel	Growth area (cm^2)	Cell density (per well)	Total well/plate media (mL)
96-well plate	0.5	5000	0.1
24-well plate	2	20000	0.5
6-well plate	9.5	250000	2
100mm plate	44	1000000	7

2.1.1.1 RIG-I KO MEF preparation

WT and ΔWD RIG-I KO cell lines were created using custom CRISPR gRNA lentivirus transduction particles (Sigma Aldrich) (Table 2.2). WT and ΔWD MEFs were seeded and infected with the CRISPR gRNA lentiviruses in Opti-Minimal Essential Medium (Opti-MEM) at an MOI of 1, to introduce the KO sequence. To increase the possibility of a successful transformation, a flask was infected with each construct as well as a double construct infection. Cells were incubated with the virus and 16 µg/mL hexadimethrine bromide (Sigma Aldrich) for two days before removing the infection media and replacing with DMEM + 10% FBS. Cells were grown to confluency and then selected for with 10 µg/mL puromycin, which selects for cells expressing the KO sequence. Transformed cells were passaged in puromycin-containing DMEM three times before growing again in DMEM + 10% FBS + 1% (p/s) to confluency. Successful gene knock out was investigated by Western blotting using the Rabbit RIG-I/DDX58 antibody (Abcam).

Table 2.2: Custom CRISPR gRNA lentiviral transduction particle information.

Vector	Clone ID	Plasmid sequence verified
LV05	MMPD0000132807	GCATCTCCAACGCCGACGG
LV05	MMPD0000132808	CCGCAAATGTGATGTGTAC

2.1.2 Lung Slice preparation and culture

The protocol for developing lung slices was adapted from Lui *et al.* (2014) (315). WT and ΔWD mouse lungs were harvested and inflated with 1% low melting point agarose (Thermofisher) in Hanks Balanced Salt Solution (HBSS) (Gibco) to inflate them. Lungs inflated with agar in DMEM F12 (Gibco) were allowed to set before being cast in 2% agarose blocks in HBSS for sectioning with a vibrating microtome. Slices were cut at a thickness of 300 µm and incubated in DMEM F12 + penicillin/streptomycin + kanamycin, overnight at 37°C 5% CO_2.

2.1.3 Tissue Culture Media and Additives

DMEM and Opti-MEM were used to culture WT and ∆WD cells and tissue in various experiments. Final working concentrations of chemicals used are detailed in Table 2.3.

Table 2.3: Tissue culture additives and their working concentrations. * prepared in dH_2O, ** prepared in ethanol, *** prepared in DMSO, **** prepared in PBS.

Compound/drug/additive	Manufacturer	Catalogue #	Working concentration
Penicillin/streptomycin	Gibco	15070063	1%
Foetal bovine serum	Gibco	10082147	10%
Kanamycin *	Sigma Aldrich	60615	100 µg/mL
M-CSF *	Invitrogen	RP-8615	25 ng/mL
TPCK-treated Trypsin *	Sigma Aldrich	4370285	0.5 µg/mL
Puromycin *	Sigma Aldrich	P8833	10 µg/mL
Hexadimethrine bromide *	Sigma Aldrich	H9268	16 µg/mL
TLR9 ligand ODN 1585 *	InvivoGen	Tlrl-1585	5 µM
U18666A *	Sigma Aldrich	U3633	3 µg/mL
Cholesterol **	Sigma Aldrich	C8667	80 µM
25-hydroxycholesterol **	Sigma Aldrich	H1015	5 µM
Dynasore ***	Sigma Aldrich	324410	80 µM
Bafilomycin A1 ***	Sigma Aldrich	B1793	50 nM
TLR3 inhibitor ***	Sigma Aldrich	614310	100 µM
Poly I:C****	Sigma-Aldrich	P1530	10 µg/mL

2.2 Antibodies and fluorescent compounds

Table 2.4: Antibodies and their working dilutions.

Antibody	Clone	Manufacturer	Catalogue #	Working Dilution
Mouse anti-IAV NP	AA5H	Abcam	Ab20343	1:1000
Mouse anti-IAV NP	AA5H	GeneTex	GTX40343	1:500
Rabbit anti-HA (PINDA)	-	Yamauchi lab	-	1:500
Mouse anti-HA1	-	Yamauchi lab	-	1:100
Donkey anti-mouse IgG Alexa Fluor® 488	-	Abcam	Ab150105	1:1000
Goat anti-rabbit IgG Alexa Fluor 594	-	Abcam	Ab150080	1:1000
Rabbit anti-sodium potassium ATPase	EP1845Y	Abcam	Ab76020	1:1000
Rabbit anti-ERP60	-	Wileman lab	-	1:1000
Mouse anti-β-actin	AC-15	Sigma Aldrich	A5441	1:10000
Rabbit anti-Rig-I/DDX58	-	Abcam	Ab45428	1:500
IRDye 680 Donkey anti-Mouse	-	Li-cor	925-68072	1:10000
IRDye 800 Donkey anti-Mouse	-	Li-cor	925-32212	1:10000
Mouse anti-Cadherin-1	36/E-cadherin	BD Biosciences	610181	1:1000

Table 2.5: Fluorescent compounds and their working concentrations.

Compound	Manufacturer	Catalogue #	Working concentration
Filipin III	Sigma Aldrich	F4767	0.5 mg/mL
WGA 647	Invitrogen	W32466	5 µg/mL
DAPI	Thermo Scientific	D1306	0.2 µg/mL

2.3 *Influenza A virus*

2.3.1 *IAV strains*

Infection of cells were with either of two mouse-adapted Influenza A viruses: A/Puerto Rico/8/1934 (PR8 (316)) and A/X-31 (H3N2) (X31 (317)). PR8 belongs to the H1N1 IAV subtype, with X31 expressing the NA and HA proteins of H3N2 in the genetic background of PR8. High titre virus stocks were kindly provided by John McCaulay at The Crick Institute but also grown in-house in eggs and MDCK cells. X31 virus for endocytosis and fusion assays was kindly provided by Yohei Yamauchi while collaborating at the University of Bristol. PR8 and X31 stocks were 10^8 ml^{-1} and 10^9 ml^{-1} respectively.

2.3.2 *Growing IAV*

IAV was harvested both from egg allantoic fluid and cell media. For growing IAV in eggs, fertilised eggs were incubated for 9-10 days. The airspaces of the eggs were injected (using a sterile 18G needle) with 100 µL 10^3 ml^{-1} PR8/X31 (diluted in phosphate buffered saline (PBS) before being resealed with candle wax. Eggs were incubated at 37°C 0% CO_2 for 72 hours for viral growth. Following incubation, eggs were euthanised by chilling at 4°C overnight. Allantoic fluid was then collected and frozen (-80°C) for titration.

For growing IAV in cells, MDCK cells were grown to confluency in a T175 flask with DMEM supplemented with 10% FBS and 1% penicillin/streptomycin. Cells were incubated overnight. At confluency, cells were washed and infected with 2 mL PR8/X31 (diluted in PBS) for 1 hour. Cell infection media was then made up to 15 mL with Opti-MEM with 0.5 µg/mL N-tosyl-L-phenylalanine chloromethyl ketone (TPCK)-treated trypsin and incubated for 72 hours post infection (hpi) under usual conditions. Media was then carefully removed, cell debris pelleted via a 1000 xg spin for 5 min and supernatant frozen (-80°C) for titration.

2.4 IAV replication experiments

2.4.1 IAV challenges

WT and ΔWD MEFs were seeded onto 24-well plates to ensure confluency the following day. Plates were incubated overnight. Cells were washed with PBS then infected at an approximate multiplicity of infection (MOI) of 0.1 in Opti-MEM supplemented with 0.5 µg/mL TPCK-treated trypsin. Cell challenges were incubated for various time points (24 hpi, 48 hpi and 72 hpi) before the cell media was collected and frozen (-80°C) for titration. Two methods of titration were employed for determining virus concentration: Tissue Culture Infectious Dose$_{50}$ (TCID$_{50}$) and plaque assay.

For lung slice challenges, each slice was infected with 5 x 10^4 X31 particles; determined from plaque assay of stocks, and suspended in DMEM F12 for 2 hours. Following this, infection media was removed and slices were washed in PBS before being incubated in fresh DMEM F12 + TPCK-treated trypsin, for various time points (24hpi, 48hpi, 72hpi). At each timepoint, media was removed and frozen (-80°C). Virus concentration in each sample was determined by plaque assay.

2.4.2 IAV Titration: $TCID_{50}$ assay

For the $TCID_{50}$ assay, MDCKs were seeded onto a 96-well plate and grown to a confluent monolayer. Wells were infected with a serial 10-fold dilution of the collected cell secreted virus and incubated for 48 hours. Afterwards, cells were washed with PBS and fixed with 4% paraformaldehyde (PFA) before the cells were washed again and blocked in blocking buffer (5% goat serum (Gibco), 0.3% Triton^{TM} x100 (Sigma-Aldrich), 1xPBS) for 30 min. Anti-Influenza A virus nucleoprotein antibody (GeneTex) was diluted in blocking buffer and used to stain the infected MDCKs for 2 hours at room temperature (RT). Plates were then washed with PBS + 0.5% Tween® 20 (PBST) (Sigma-Aldrich). Donkey anti-mouse IgG-Alexa Fluor 488 (Abcam) was then diluted in blocking buffer and used to stain the MDCKs. Cells were incubated at RT for two hours, in the dark. Cells were washed one final time with PBST and then viewed using a Zeiss Axiovert 40 CFL with x20 magnification. Viral titre was determined from the dilution of the last well where fluorescence is detected and determined using the Spearman Kärber formula and the following calculator (318).

2.4.3 IAV Titration: Plaque assay

For the plaque assay, MDCKs were seeded onto 6-well plates and grown to a confluent monolayer. A 10-fold dilution series was made up of the virus samples and 1 mL of the dilutions 10^{-1}–10^{-6} were used to infect the MDCKs for one hour at 37°C 5% CO_2. Following this infection, inoculum was removed and cells carefully overlaid with 4 mL overlay media (2.4% Avicel (Sigma-Aldrich) is mixed 1:1 with plaque maintenance media. 50 mL plaque maintenance media consists of 10 mL 10x MEM (Sigma-Aldrich), 2 mL 1M HEPES (Gibco), 1 mL 200mM L-glutamine (Gibco), 1 mL 75% $NaHCO_3$ (Gibco), 1 mL p/s, and 70 mL H_2O. TPCK-treated trypsin was added at a concentration of 0.5 µg/mL). Infections were incubated for 72 hours. Afterwards, overlays were removed, cells carefully washed with PBS before fixing in ice-cold 60:40 acetone/methanol solution. Fixed monolayers were then stained with crystal violet (Sigma-Aldrich) to reveal plaques. Viral titre was then determined from the stock sample via the following equation (319):

$$PFU/mL = \frac{Avg.\#\, of\ plaques}{D\ x\ V}$$

$$D = Dilution \quad V = Volume\ of\ diluted\ virus\ added\ to\ plate$$

2.5 Cytokine analysis

2.5.1 Poly I:C transfection

WT and ΔWD MEFS were seeded onto P100 plates, to provide a confluent monolayer the next day.

Polyinosinic:polycytidylic acid (Poly I:C) (Roche) was dissolved in PBS and sheared through a 25G needle to 200-800 bp fragments. Cells were transfected with Poly I:C using Lipofectamine LTX with Plus reagent (Invitrogen) according to the manufacturer's instructions. In brief, separate mixtures of OptiMEM + Lipofectamine LTX and OptiMEM + Poly I:C + Plus reagent were created and then combined and incubated at RT for 5 min. The transfection mixture was placed on cells in media and incubated for 4 hours. After 4 hours, cells were processed to isolate RNA.

2.5.2 IAV challenge

Cells were infected with X31 at a MOI of 2. Cells were infected in OptiMEM + 0.5 µg/mL TPCK-treated trypsin and incubated for various time points (4 hpi, 6 hpi, 8 hpi, 12 hpi). Plates were processed for RNA isolation after incubation time elapsed.

For lung slices, each slice was infected with 5 x 10^4 X31 particles suspended in DMEM F12 for two hours before removing infection media and replacing with DMEM F12 for 16 hours. Dissociation of cells from slices was achieved through an adapted protocol published by Niehof *et al.* (2017) (320). Slices were incubated in a digestion solution (DMEM + 1% p/s, 100 U/mL DNase I (Roche), 2.4 U/mL Dispase II (Roche), 150 U/mL collagenase III (Roche)) for 30 minutes at 37°C at 300 rpm. Slices were rinsed through a 70 µm cell strainer with ice-cold PBS, spun by centrifugation for 3 min at 1000 x g to pellet cells before 1 mL TRIzol® was added and an RNA extraction was carried out identically to cell RNA extraction protocol.

2.5.3 RNA extraction, cDNA synthesis and quantitation by qPCR.

RNA was extracted by lysing cells in TRIzol® (Thermofisher). Chloroform was added to TRIzol® lysate, vortexed and then incubated at RT for 10 min before being separated by centrifugation at (15 min/9660 xg/4°C). The upper phase was then removed and RNA precipitated from it using isopropanol on ice for 10 min. RNA was pelleted via centrifuging (10 min/9660 xg/4°C) and the pellet re-suspended in 1 mL 75% ethanol and vortexed briefly before centrifuging (5 min/3875 xg/4°C). Supernatant was discarded and pellet air dried before being dissolved in H_2O. A separate clean-up step was then performed with an RNeasy MinElute Cleanup kit (Qiagen) according to the manufacturer's instructions. Final concentration of eluted RNA was measured using a Nanodrop spectrophotometer.

Reverse transcription was used to synthesise cDNA. RNA (1 µg) in 10 µL dH_2O was incubated with 1 µL aliquots of 10mM dNTPs (Invitrogen), 3 µg/µL random primers (Invitrogen) and RNase OUT (Invitrogen). Primers were annealed at 65°C for 5 min before adding 4 µL 1X FS buffer (Invitrogen), 2 µL 0.1M DTT (Invitrogen) and 0.5 µL Superscript™ II reverse transcriptase (Invitrogen). The reaction was incubated for 2 hours at 42°C and then incubated for 15 min at 70°C to denature the RNA/enzymes. The reaction volume was made up to 200 µL to make a final cDNA concentration of 5 ng/µL and stored at -20°C.

Quantitative PCR (qPCR) was carried out on a QuantStudio 3. For one 20 µL reaction, the following mixture was made: 10 µL 2X Bioline Immomix™ (Meridian Bioscience), 2 µL 10 mg/mL bovine serum albumin (BSA) (New England Biolabs), 0.2 µL $MgCl_2$ (Meridian Bioscience), 0.4 µL ROX Reference dye (Invitrogen), 0.12 µL SYBR green and 0.28 µL dH_2O. To this, 2 µL primer (see Table 2.4) and 5 µL 1 ng/µL cDNA was added before sealing and analysing by qPCR using the standard curve thermal cycle protocol. Relative quantity of gene mRNA was determined using the Pfaffl method (321) and normalised to the 18S values for each sample.

Table 2.6: List of primers used in qPCR analysis. All primers were prepared in dH_2O.

Gene/target	Catalogue #	Geneglobe ID	Company
18S	249900	QT02589300	Qiagen
IFNβ1	249900	QT00249662	Qiagen
IFIT1	249900	QT01161286	Qiagen
ISG15	249900	QT00322749	Qiagen
IFITM3	249900	QT00140189	Qiagen
IL-6	249900	QT00098875	Qiagen
Ddx58	249900	QT00123515	Qiagen
Primer	**Sequence**		**Company**
IAV M2 segment forward	GACCRATCCTGTCACCTCTGAC		Sigma Aldrich
IAV M2 segment reverse	AGGGCATTYTGGACAAAKCGTCTA		Sigma Aldrich

2.6 MEF IAV entry experiments

2.6.1 Endocytosis assay

Purified X31 was used for this assay at MOI: 10. WT and ΔWD MEFs were seeded onto coverslips prior to infection and grown to 75% confluency. Dynasore, a dynamin inhibitor, was used to pre-treat the cells as an endocytosis control. Dynasore (Sigma Aldrich) (80 µM), in infection medium (DMEM, 50 mM HEPES, pH 6.8, 0.2% BSA (VWR Life Science)), was used to pre-treat the cells 30 min before the bind warm up stage. All cells were then infected with purified X31 diluted in infection medium and incubated on ice (4°C) for 1 hour. Unbound particles were removed in a wash stage with ice cold infection medium before bound virus was allowed to internalise through a treatment of warm (37°C) infection medium. Dynasore containing infection media was also used to treat cells after bind warm up until fixation.

After a 30 min incubation at 37°C, cells were fixed in 4% paraformaldehyde (PFA). Plasma membranes were stained with wheat germ agglutinin (WGA 647) before cells were washed and blocked for 30 min (Blocking solution: 1% BSA, 5% FCS, 1 x PBS). External influenza HA epitopes were immunostained with the primary antibody PINDA (named for the rabbit it was raised in) (Yamauchi lab) (1:500) in blocking solution and incubated overnight at 4°C. PINDA was then stained with the secondary antibody anti-rabbit IgG-Alexa Fluor 594 (Abcam) (1:1000) in blocking solution for 1 hour at RT, in the dark. Cells were fixed again in 4% PFA and washed before being permeabilised (Permeabilisation solution: 0.1% Triton™X100, 1% BSA, 5% FCS, 1 x PBS). They were then incubated for 2 hours at RT with the HA1 antibody (Yamauchi lab) (1:100), a mouse monoclonal also specific to the HA epitope. As PINDA will have bound external HA, HA1 will be able to bind internal HA. Cells were washed and stained with the donkey anti-mouse IgG Alexa Fluor 488 (1:1000) in permeabilisation solution for 1 hour at RT. Cell nuclei were stained with DAPI (1:5000) before coverslips were mounted onto slides using Fluoromount-G® (SouthernBiotech). Slides were viewed using a Zeiss Axio Imager 2 microscope with the x63 oil objective. Internalised and external IAV could be distinguished and internalised IAV were counted.

2.6.2 Fusion assay

Purified X31 was dual-labelled with fluorescent dyes 3,3’-dioctadecyloxacarbocyanine (DiOC18: ex. 480 nm em. 510 nm) and octadecyl rhodamine B (R18: ex. 558 nm em. 586 nm), protocol adapted from (322). DiOC18 and R18 in ethanol were mixed at respective concentrations of 33 µM and 67 µM. This mixture was added to 100 µg X31 protein suspended in 1 mL PBS and the reaction mixture mixed for 1 hour before passing through a 0.22 µm pore filter (Millipore).

WT and ∆WD MEFs were seeded onto 24-well plates prior to infection and grown to 90% confluency. Bafilomycin A (BafA) (a viral fusion inhibitor) was used to pre-treat the MEFs as a fusion control. Infection medium (DMEM, 50 mM HEPES, pH 6.8, 0.2% BSA) with BafA (50 nM) was used to pre-treat the MEFs 30 min prior to infection. Labelled X31 was diluted in infection medium and aliquoted onto cells so that each well received approximately 3.3 µg X31 protein. Cells were incubated on ice (4°C) for 1 hour to bind the virus, then internalised via the addition of warm (37°C) infection medium and incubated at 37°C; the fusion control medium containing 50 nM BafA.

At 30 and 60 min post infection, cells were washed with PBS and incubated with trypsin. After a couple of minutes incubation, cells were liberated and suspended in DMEM + 10% FCS. This cell solution was fixed in 4% PFA for 20 min. Cells were spun down (419 xg, 4 min) and then re-suspended in 100 µL fluorescence-activated cell sorting (FACS) buffer (1 X PBS 1% BSA). This was then added to a optical 96-well FACS plate (Thermofisher) and cells sorted using a Novocyte Advanteon flow cytometer. Data was analysed using FlowJo software, with cell distribution gates being determined from the non-infected controls.

2.6.3 Nuclear entry assay

PR8 was used in this assay (MOI: 4) and diluted in OptiMEM. WT and ∆WD MEFs were seeded onto coverslips and grown to 75% confluency. OptiMEM PR8 mixture was added to wells and cells were incubated on ice (4°C) for 1 hour to enable the virus to bind. Virus was allowed to internalise through incubating at 37°C. Cells were fixed in 4% PFA at the following time points: 2, 3, 4 and 5 hpi. Cells were permeabilised with 0.1% triton x100 before blocking in 0.1M glycine and 2% BSA solutions. Coverslips were then immunostained with mouse anti-IAV NP (Abcam) in 2% BSA blocking solution overnight at 4°C. Coverslips were then washed with PBS before being stained with donkey anti-mouse IgG Alexa Fluor® 488 in 2% BSA blocking solution for 2 hours at RT. Cells were stained with DAPI for 10 min before being mounted in Fluoromount on slides. Coverslips were viewed using a Zeiss Axio Imager 2 microscope with the x20 objective. NP positive nuclei were counted.

2.7 IAV acid bypass experiments

The protocol for synchronising the fusion of the viral membrane to the cell plasma membrane (hereafter acid bypass) has been adapted from Banerjee *et al.* (2014) and Miyake *et al.* (2019) (323,324). WT and ΔWD MEFs were seeded onto coverslips (NP entry assay) or 6-well plates (IFNβ assay) and grown to 75% confluency or 100% confluency respectively. X31 was used in these assays, at an MOI of 100 for the NP entry assay and 10 for the IFNβ assay. Virus was bound to pre-cooled MEFs for 1 hour on ice (4°C), unbound virus being washed off in cold infection medium (DMEM, 50 mM HEPES, pH 6.8, 0.2% BSA). Cells were incubated for 2 min in FUSION medium (DMEM, 50mM citric buffer adjusted to pH 5.0) before being cooled, washed in cold infection medium and incubated at 37°C in STOP medium (DMEM, 50mM HEPES, 20mM NH_4Cl, pH 7.4) for the appropriate time points.

2.7.1 Acid bypass NP assay

Purified virus was used to infect MEFs. MEFs were fixed in 4% PFA at 10, 30 and 50 min post infection. Cells were permeabilised in 0.1% Triton X100 before being blocked in 0.1M glycine and 2% BSA blocking solutions. Cells were immunostained with mouse anti-IAV NP (Abcam) in 2% BSA blocking solution overnight at 4°C. Cells were then washed with PBS before staining with donkey anti-mouse IgG Alexa Fluor® 488 in 2% BSA blocking solution for 2 hours at RT. Coverslips were then washed with PBS before finally being stained with DAPI for 10 min and mounted onto slides with Fluoromount. Coverslips were viewed using a Zeiss Axio Imager 2 with the x40 oil objective. Puncta were counted and sized using ImageJ software. Images are representative of three independent experiments.

2.7.2 Acid bypass IFNβ assay

MEFs were lysed and RNA extracted as described in 2.5.3 via TriZOL at 10, 30 and 50 min post infection. RNA was converted to cDNA via reverse transcription and analysed via qPCR as described in 2.5.3; 18S and IFNβ1 being targeted for amplification using the appropriate primers. Non-infected MEFs were also analysed for IFNβ expression, and these basal levels were subtracted from the total relative quantity of IFNβ expression.

2.8 Plasma membrane isolation and cholesterol quantification

2.8.1 Plasma membrane isolation

Brains and lungs from WT and ∆WD mice were weighed and then minced using a razor blade and the pieces re-suspended for 1 min in ice-cold hypotonic buffer (10 mM tris/HCl in dH_2O, pH 7.4) to induce osmotic swelling of cells. Cells were then disrupted in homogenisation buffer (10 mM tris/HCl, 1 mM EGTA, 0.5 mM EDTA, 0.25 M sucrose, 1 x cOmplete™ ULTRA, Mini Easypack protease inhibitor cocktail tablet (Roche), pH 7.4) on ice, via a Dounce homogeniser (approx. 20 passes with each A and B pestles). Lysates was sonicated twice for 20 seconds each. Whole cells and nuclei were pelleted at 67 xg for 10 min at 4°C. Fatty residue above supernatant was discarded and the post nuclear supernatant (PNS) salvaged. The PNS was sonicated twice for 20 seconds each.

A Nycodenz® (Progen) gradient was made up from a 50% stock (50% Nycodenz® in 10 mM tris 1 mM EDTA). A 1.2 mL aliquot of PNS was layered on the bottom of a 14 x 95 mm polypropylene Beckman Coulter® ultracentrifuge tube and a step gradient from 25% to 0% Nycodenz® was layered on top. Tubes were placed into a SW 40.1 rotor and membranes were then fractionated at 86578 xg at 4°C for 1.5 hours in a Beckman Coulter ultracentrifuge. Fractions of 2 mL were then stored at -80°C for analysis.

2.8.2 SDS-PAGE and Western Blot

Fractions were made up in 1X Laemlli sample preparation buffer (6X stock: 8 mL 1.5 tris, 0.4% SDS pH 6.8; 6 mL glycerol; 2 g SDS; 1.2 mg bromophenol blue; 60 mL 2-mercaptoethanol; make up to 100 mL with dH_2O) and boiled at 93°C for 4 min. Samples were loaded onto Bolt 4-12% Bis-Tris plus gels (Invitrogen) and ran in 1X Nupage running buffer at 150 V for 90 min. Protein was transferred to an Immobilon® PVDF membrane via wet transfer in 1X transfer buffer (39 mM glycine, 48 mM tris, 1.3 mM SDS , 20% methanol in dH_2O) at 200 mA for 1 hour at 4°C. Membranes were then blocked for 1 hour in 0.5% milk in tris buffered saline (50 mM tris, 150 mM NaCl, pH 7.5) + 0.5% Tween 20 (TBST). Blots were immunostained with rabbit anti-sodium potassium ATPase (Abcam), mouse anti-E-cadherin (BD Biosciences), rabbit anti-ERP60 and mouse anti-actin overnight at 4°C. Blots were then washed thoroughly in TBST before staining with rabbit 800 and mouse 670 in 0.5% milk TBST for 2 hours at 4°C. Blots were washed in TBST before viewing on a Licor Odyssey CLx imaging system using the 785 nm and 685 nm lasers.

2.8.3 Cholesterol quantification

Protein concentrations of fractions were measured using a Pierce™ BCA protein assay kit (Thermo Scientific™) according to the manufacturer's instructions.

Cholesterol concentrations of fractions were measured using a Amplex® Red cholesterol assay kit (Invitrogen). This assay consisted of mixing the cholesterol fraction with a working Amplex® red solution (300 µM Amplex® red reagent, 2 U/mL horseradish peroxidase, 2 U/mL cholesterol oxidase and 0.2 U/mL cholesterol esterase). Amplex Red® reagent reacts with H_2O_2 to make fluorescent resorufin. Mixtures were then incubated for 30 min at 37°C before the resorufin fluorescence was measured on a SpectraMax M2 microplate reader (excitation: 545 nm, emission: 590 nm). These cholesterol quantifications were then normalised to both the protein concentration of the sample and the mass of the organ post harvesting.

For total cell cholesterol quantification, MEFs were grown to confluency in P100 plates before washing with ice-cold PBS. Cells were lysed in ice-cold lysis buffer (50 mM

Tris-HCl, 150 mM NaCl, 1 mM EDTA, 1% TritonX-100 + protease inhibitor tablet and phenylmethylsufonyl fluoride (PMSF)). Lysates were then measured using the Amplex® Red cholesterol assay kit.

2.9 Cholesterol localisation using D4H mCherry probe and filipin

2.9.1 D4H mCherry plasmid purification

D4H mCherry pGEX plasmid was a kind gift from Gregory D. Fairn. Plasmid was chemically transformed into competent *Escherichia coli* (DH5α) by incubating plasmid and bacteria together at 4°C before briefly heat shocking at 42°C for 30 seconds. Bacteria and plasmid were then returned to 4°C for 5 minutes. Bacterial mixture was then added to super optimal broth with catabolite repression (SOC) medium and incubated at 37°C for 30 minutes at 250rpm. Bacteria were plated onto LB + Ampicillin plates overnight at 37°C to select for transformed bacteria. A transformed colony was grown in LB + Ampicillin overnight at 37°C at 250rpm. Bacteria were pelleted at 6000 x g at 4°C for 15 minutes. Plasmid was purified using a NucleoBond® Xtra Midi prep kit (Machery Nagel). Firstly cells were resuspended in buffer RES before lysing with buffer LYS at RT for 5 minutes. Buffer LYS was neutralised using buffer NEU, mixing until the lysates became colourless. Lysates were then loaded onto equilibrated NucleoBond® Xtra column filters and washed with buffer EQU. Filters were removed and columns washed with buffer WASH. Plasmid was then eluted from column using buffer ELU. DNA was precipitated using isopropanol before centrifuging (15000 x g, 4°C, 30 minutes). DNA pellet was washed with 70% ethanol before centrifuging (15000 x g, RT, 5 minutes) before air drying for 15 minutes. Pellet was reconstituted in dH_2O to 1 µg/mL and stored at -20°C.

2.9.2 D4H mCherry transfection and microscopy

D4H mCherry was transfected into WT and ΔWD MEFs on a 24-well plate using Lipofectamine 2000. Lipofectamine reagent was added to OptiMEM medium at a 1:1 dilution with plasmid DNA and incubated at RT for 5 minutes. DNA-lipofectamine complex was then added to MEFs and incubated at 37°C for 24 hours. Cells were then fixed using 4% PFA for 20 minutes, before permeabilising in 0.1% Triton X100 for 10 minutes and blocking in 0.1M glycine and 0.5% BSA solutions for 20 and 30 minutes respectively. Transfected cells were stained with either anti-Rab7, anti-LAMP1 or anti-EEA1 to visualise late endosomes, lysosomes or early endosomes at 4°C overnight. Antibodies were stained with IgG 488 before mounting with fluoromount and visualising using a Zeiss M2 Imager using oil immersion with the x63 lens. Images were processed on ImageJ, correlation between D4H mCherry and the antibodies was measured using the JACoP plug-in, which generates a Pearson correlation coefficient. The closer the coefficient is to 1.0, the more colocalised the datasets are. Images are representative of three independent experiments.

2.9.3 Lung slice/MEF filipin staining and confocal microscopy

Lungs were covered in optimal cutting temperature compound (OCT) and snap frozen in liquid nitrogen chilled isopentane for 30 seconds. Frozen tissue was kept at -80°C. Samples were fixed to the pre-chilled cryostat chuck using OCT. Specimen temperature was set to -24°C, cryostat blade was set to -26°C and placed into a cryostat. Specimens were sliced to a thickness of 10 µm. Samples were mounted onto a microscope slide and allowed to air dry for 2 hours before washing in PBS and staining. Slides were fixed in 4% PFA and stained with 0.5 mg/mL filipin III (Sigma-Aldrich) in PBS + 1% BSA for 2 hours at RT. Lung slices were also stained with anti-rab7 (Abcam).

MEFs were fixed with 4% PFA and stained in 0.5 mg/mL filipin III in PBS + 1% BSA for 2 hours at RT. Coverslips were mounted with fluoromount and visualised using oil immersion on the x63 lens of a Zeiss LSM980-Airyscan confocal microscope with the 405 nm laser. Images were processed on ImageJ.

2.10 Statistics

Statistical analysis was conducted either on SPSS statistics or ImageJ. Where possible, the more conservative statistical test, the Mann Whitney U test, was used to compare the ranks between two data groups. Otherwise an independent samples t-test was performed to compare the mean averages. Where more than one group was being compared, a two-way ANOVA test was performed.

CHAPTER 3

The WD domain of ATG16L1 modulates cholesterol in the plasma membrane

3.1 Introduction

Cellular cholesterol is synthesised in the endoplasmic reticulum or internalised in low density lipoprotein (LDL). Once LDL is endocytosed, the cholesterol is released from the lipoprotein in lysosomes via lipolysis where it is then redistributed within the cell. It is transported to the plasma membrane and then onwards to endoplasmic reticulum. At the ER, internalised cholesterol can regulate the cholesterol synthesis pathway, preventing over-production of cholesterol and subsequent steroid hormones. The pathway cholesterol takes to the plasma membrane and then onwards to the ER involves the proteins NPC1 and NPC2. Liberated cholesterol in lysosomes is bound to the iso-octyl group of NPC2. NPC2 then transfers the cholesterol molecules to the N-terminal domain of NPC1 which shuttles the cholesterol to the lipid bilayer of membranes (325). Mutations in these proteins result in lysosomes overloaded with cholesterol.

Cells contain esterified cholesterol and unesterified cholesterol. Esterified cholesterol does not participate in membrane formation. It is, however, the predominant form of cholesterol found within lipoproteins such as LDL. Unesterified cholesterol is found in membranes, such as the plasma membrane (326), and can be stained for using filipin (327).

The enzyme PTDSS1 is thought to have a role in cholesterol transport. PTDSS1 synthesises phosphatidylserine (PS). Knocking out the gene has been shown to reduce cholesterol movement to the ER from the plasma membrane, resulting in a cholesterol-laden plasma membrane (328). Tan *et al.* (2018) demonstrated that cholesterol is also delivered to the membrane through lysosomal exocytosis, with the cholesterol rich lysosomal membrane fusing with the plasma membrane via the action of autophagy proteins such as ATG16L1. Defects in this protein, such as through the T300A mutation, have resulted in attenuated plasma membrane repair; with deficiencies of ATG16L1 resulting in cholesterol being held up in lysosomes (84). In this thesis the action of ATG16L1 and its WD domain, with respect to cholesterol homeostasis, have been investigated. This chapter aims to investigate the cholesterol content of membranes in WT and ΔWD cells. Tan *et al.* (2018) showed that ATG16L1 has a role in cholesterol homeostasis and membrane repair, with the T300A mutation inhibiting this process. This implicates the WD domain in cholesterol transport. I investigated whether cholesterol transport is modulated within ΔWD MEFs. WT and ΔWD MEFs immortalised MEF cell lines were used for these experiments. A truncated and dysfunctional ATG16L1 protein may reduce cholesterol trafficking to the plasma membrane (Figure 3.1).

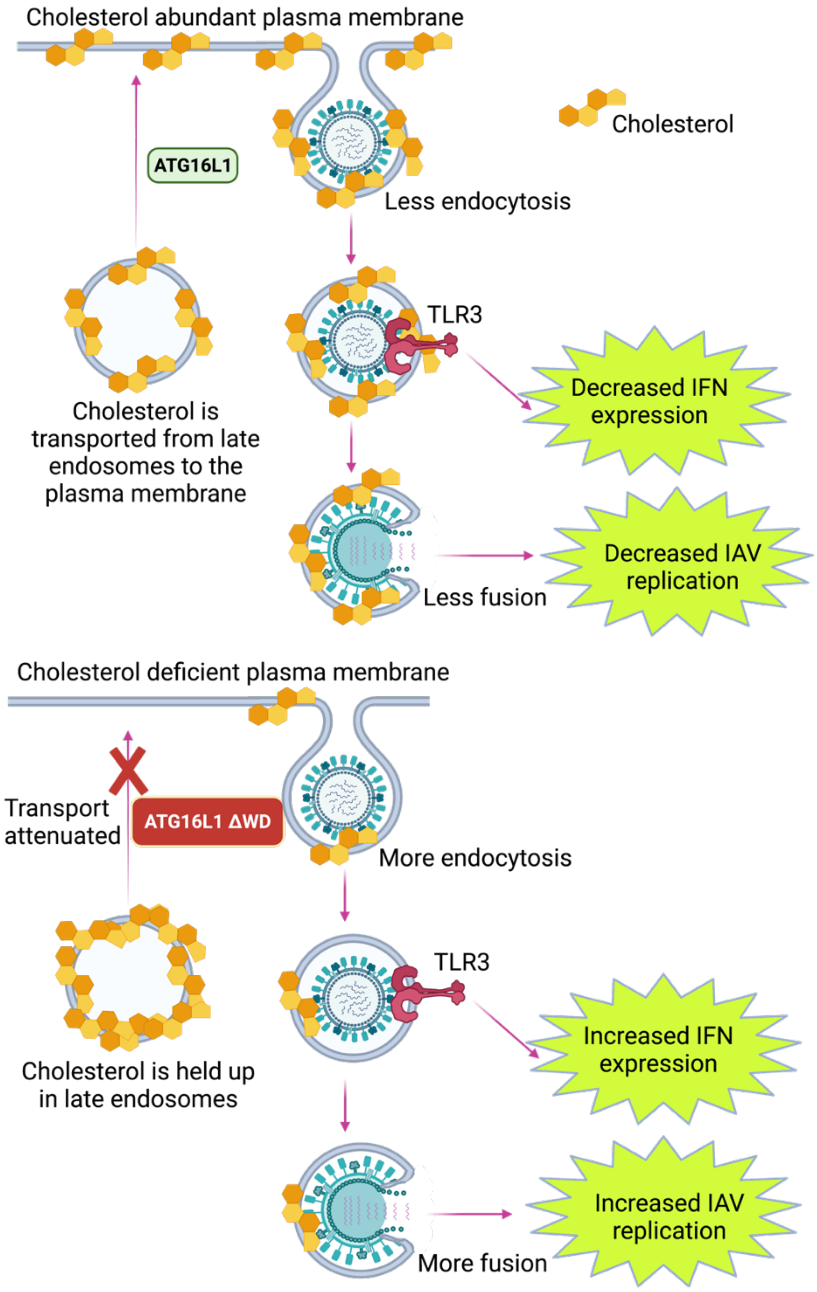

Figure 3.1: Graphical hypothesis- the WD domain has a role in cholesterol transport. The WD domain of ATG16L1 is required for lysosomal fusion-mediated transport of cholesterol from late endosomes/ lysosomes to the plasma membrane (PM). Removal of the WD domain attenuates cholesterol transport to the PM, resulting in less cholesterol in the endosome when IAV infects. This reduced cholesterol promotes IAV fusion, resulting in increased IAV replication. Increased viral entry results in increased receptor activation and greater cytokine expression, explaining the cytokine storms seen in Wang *et al.* (2021). Produced using Biorender.

3.2 Aims

- Investigate the role of the WD domain of ATG16L1 in cholesterol transportation to the plasma membrane (PM) in cells and tissue by subcellular fractionation.
    - The cholesterol content of WD deficient cells and the PMs of WT and WD deficient cells will be investigated. A fractionation protocol will be developed to isolate the PM subcellular membrane fraction and the cholesterol content of it will be measured by the Amplex red biochemical fluorometric assay.
    - Cholesterol will be localised in WT and WD deficient cells by bioimaging using cholesterol binding probes such as filipin III and D4H mCherry which specifically bind to cholesterol.

3.3 Results

3.3.1 Measurement of total cell cholesterol in WT and ΔWD MEFs.

The Amplex Red cholesterol assay was used to measure cholesterol in WT and ΔWD cell lysates. This assay relies on the oxidation of cholesterol to form cholest-4-en-3-one and hydrogen peroxide. This hydrogen peroxide then oxidises the Amplex Red reagent in the presence of horseradish peroxidase to make fluorescent resorufin. Resorufin has a specific absorption and fluorescence emission maxima at 571 nm and 585 nm respectfully, and this fluorescence is proportional to the cholesterol present. The addition of cholesterol esterase in the reaction allows for the detection of esterified cholesterol, which is found in lipid droplets. In this initial experiment, the total cholesterol content of cells was quantified.

There was no difference seen in the total cholesterol (esterified + unesterified) between the two cell lines, with both lysates having cholesterol concentrations of approximately 40-42 ng/mL (Figure 3.2). However, for unesterified cholesterol, significantly more was detected in ΔWD MEFs compared to WT MEFs. Unesterified cholesterol was measured at approximately 33 ng/mL in ΔWD MEFs in contrast to only 28 ng/mL in WT MEFs. These data suggests that either more unesterified cholesterol is synthesised or more accumulates in these cells. Overall, these data suggests the WD domain has a role in cholesterol homeostasis.

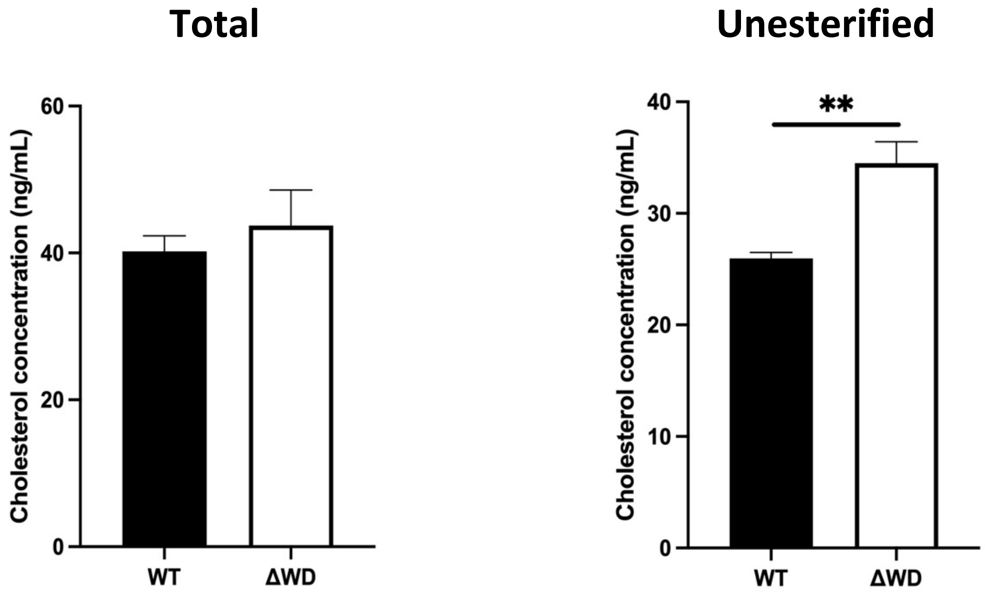

Figure 3.2: Total cell cholesterol and unesterified cholesterol in WT and ΔWD MEFs

WT and ΔWD MEFs were lysed and total cell cholesterol and cell unesterified cholesterol levels were measured by Amplex Red cholesterol assay (+SD). Cholesterol values were normalised to 1 µg sample protein. Mann Whitney U test shows ranked increase in unesterified cholesterol in ΔWD cells: ** = p<0.01, n=6 (technical replicates).

3.3.2 Unesterified cholesterol is decreased in brain, lung and MEF plasma membranes lacking the WD domain of ATG16L1.

This experiment aimed to isolate the plasma membranes of WT and ΔWD brain and lung tissue as well as MEFs to see if cholesterol transport to the plasma membrane is attenuated in mice lacking the WD domain of ATG16L1. WT and ΔWD mice brains and lungs were harvested and homogenised. WT and ΔWD MEFs were grown in T175 flasks (ten flasks per cell line), pelleted and homogenised. Tissue and cell homogenates were fractionated on a Nycodenz step gradient. This Nycodenz step gradient is a density gradient and was used due to its non-toxic nature, its ability to easily dissolve into solution and because it does not interfere with the assays afterwards. The samples were separated on the Nycodenz gradient using ultracentrifugation and six fractions were collected and analysed by Western blot: using plasma membranes and endoplasmic reticulum (ER) markers, to identify the membrane-containing fractions. The plasma membrane was found within fractions of 5-10% Nycodenz using the marker Na/K ATPase in brain and MEFs. E-cadherin was used as a marker for lung PMs. Figure 3.3 shows the fractionation process, with a 113 kDa Na/K ATPase band in fractions 3 and 4 in all brain and MEF homogenates, showing that these fractions contain the plasma membrane. The E-cadherin 105 kDa band was seen in fractions 3-6 in lung homogenates, which indicates a less successful fractionation. The ER marker ERP60, at 60 kDa, was mainly found in fractions 5 and 6, and very little in fractions 3 and 4. Due to the lack of ER contamination in fraction 3 of all homogenates, this fraction was used for analysis.

Fraction 3 was analysed for tissue and MEFs using the Amplex Red cholesterol biochemical assay. Figure 3.4 demonstrates decreased total and unesterified cholesterol in the ΔWD plasma membrane fractions of brains, lungs and MEFs. This difference was significant in all measurements. For brains and MEFs, WT unesterified cholesterol was approximately 2-fold greater than ΔWD. These data provide clear evidence that the WD domain of ATG16L1 has a role in cell cholesterol transport.

Western blot representative of brain and MEF fractions (Na/K ATPase) and Lung fractions (E-cadherin).

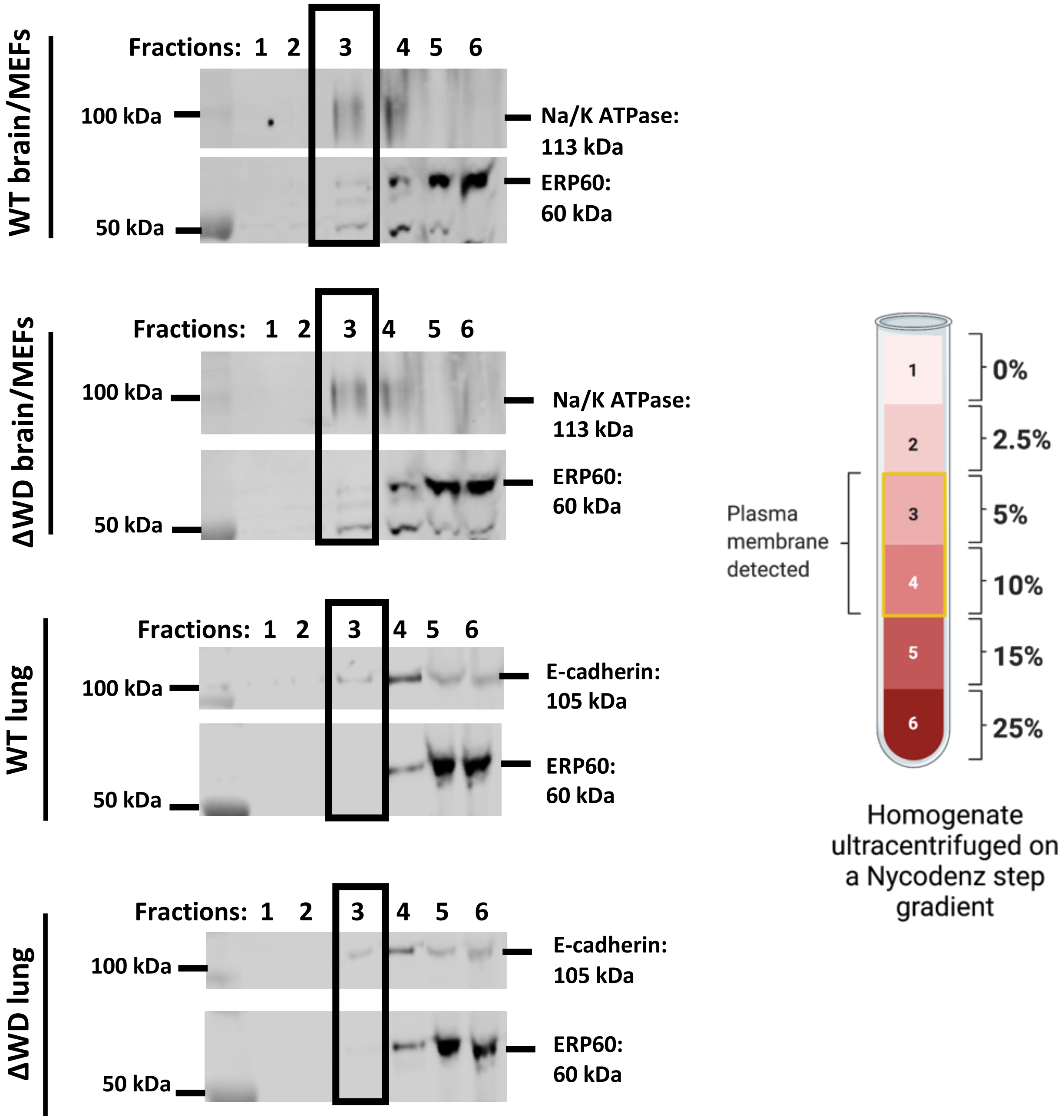

Figure 3.3: Brain, lung and MEF cell membranes were fractionated using a Nycodenz step gradient and plasma membrane fractions were validated by Western blot. Brain and lung tissue, and MEFs, were homogenised and fractionated by ultracentrifugation on a Nycodenz step gradient. A Na/K ATPase antibody was used to identify plasma membrane fractions for the brain and MEFs where as an E-cadherin antibody was used for the lung fractions. An ERP60 antibody was used to identify the endoplasmic reticulum fractions.

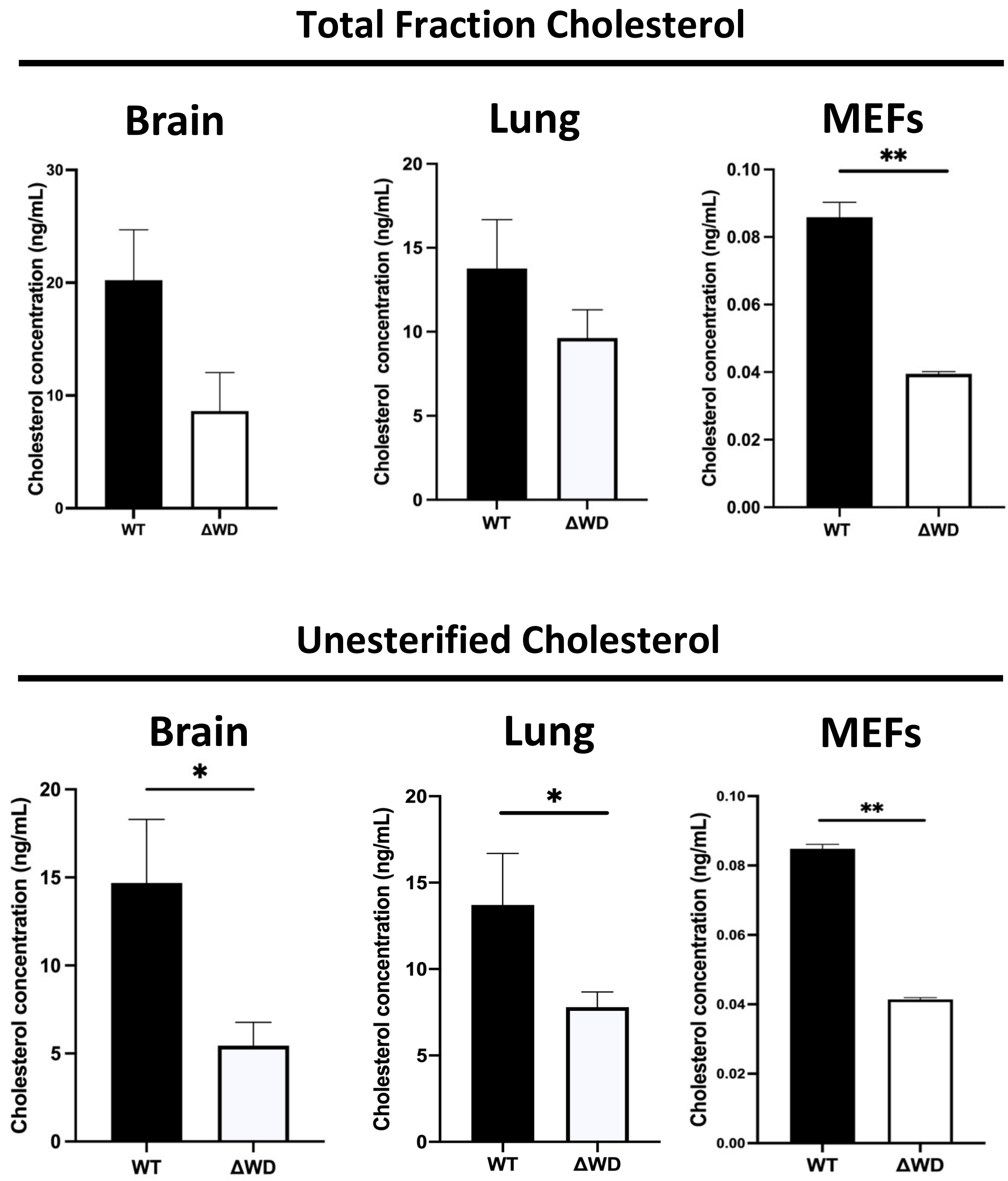

Figure 3.4: Decreased total fraction and unesterified cholesterol concentration in the plasma membranes of brain, lung and MEFs from ΔWD mice. Plasma membrane fractions for brain, lung and MEFs were analysed using an Amplex red cholesterol assay for total cholesterol and unesterified cholesterol. Cholesterol was normalised to 1 µg protein and 1 mg original organ/pellet weight. Concentrations are presented (+SEM) and a Mann Whitney U test was conducted: * = $p<0.05$, ** = $p<0.01$, n=6 (biological replicates for tissue, experimental replicates for MEFs).

3.3.3 Intracellular cholesterol aggregates detected in ∆WD MEFs compared with WT MEFs when visualised with filipin.

The cellular localisation of cholesterol in ∆WD and WT MEFs was investigated using filipin III and examination using confocal microscopy. Filipin III is a fluorescent polyene antibiotic which binds to unesterified cholesterol within membranes. It does not binds to esterified cholesterol, as found in lipid droplets.

WT MEFs had filipin/cholesterol localisation at the plasma membrane (annotated with arrow on Figure 3.5) which could not be clearly seen in ∆WD MEFs. Small cytoplasmic puncta of cholesterol were seen in WT MEFs, however in ∆WD MEFs larger cytoplasmic filipin-positive aggregates were seen (annotated with arrows in figure 3.5). Immunohistochemistry was used to investigate the subcellular localisation of these puncta.

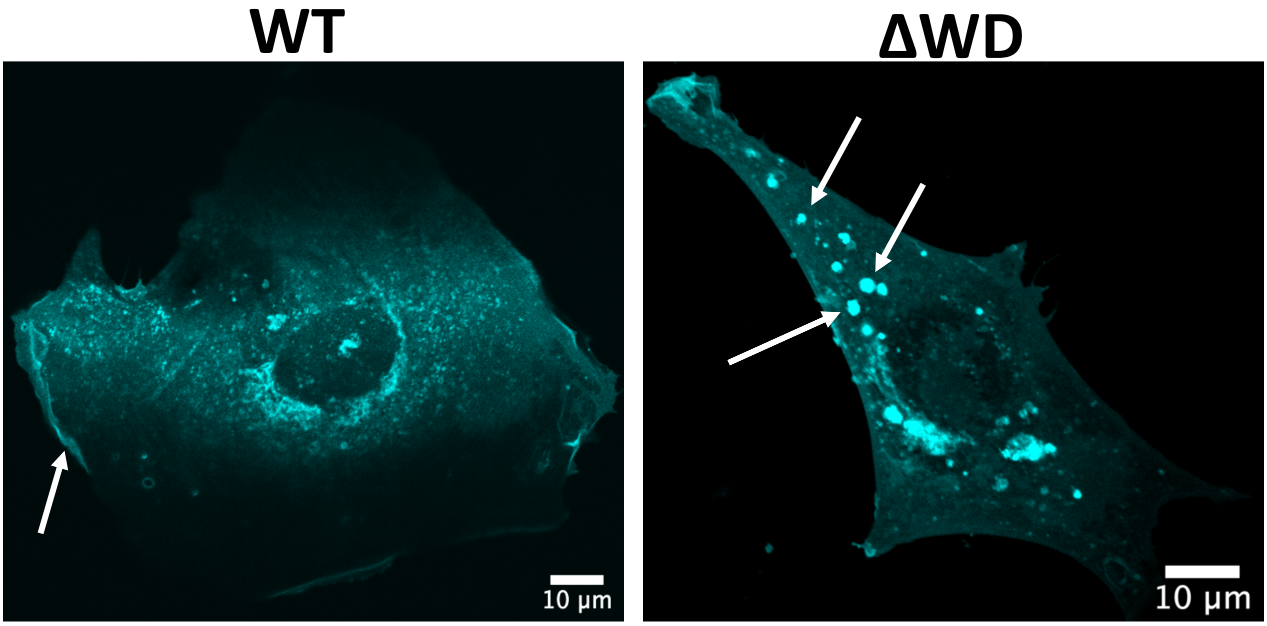

Figure 3.5: Increased size and frequency of cholesterol aggregations in ΔWD MEFs compared with WT MEFs. WT and ∆WD MEFs were fixed and stained with filipin III before cells were viewed using a Zeiss LSM980-Airyscan confocal microscope.

3.3.4 Localisation of cholesterol with Rab7 (late endosomes) in WT and ΔWD slices.

As the previous experiments demonstrated that cholesterol is reduced in ΔWD lung plasma membranes, I investigated the cholesterol localisation within ΔWD lungs to see if there was any alteration. WT and ΔWD lungs were removed, frozen in liquid nitrogen-cooled isopentane and sliced into 10 µm slices before fixing.

Slices were stained with either filipin III or Rab7 and DAPI to see if cholesterol or late endosome distribution across the native cells of the lung was altered in ΔWD tissue compared to WT tissue. No clear difference was noted between WT and ΔWD lung cholesterol (Figure 3.6) or late endosome (Figure 3.7) distribution. Lung slice structures showed possible morphological differences between WT and ΔWD lung tissue over three individual mice, with alveolar spaces appearing to be more constricted in ΔWD, however this could be an artifact of the slice preparation procedure. Overall, more investigation is needed into the cholesterol distribution in WT and ΔWD lung slices.

As it was not possible to use immunohistochemistry with filipin staining to investigate the subcellular localisation of puncta further work was conducted to investigate cholesterol localisation in cells. Cells were transfected with the fluorescent probe D4H mCherry which binds specifically to cholesterol (329) and then immunostained with organelle specific antibodies.

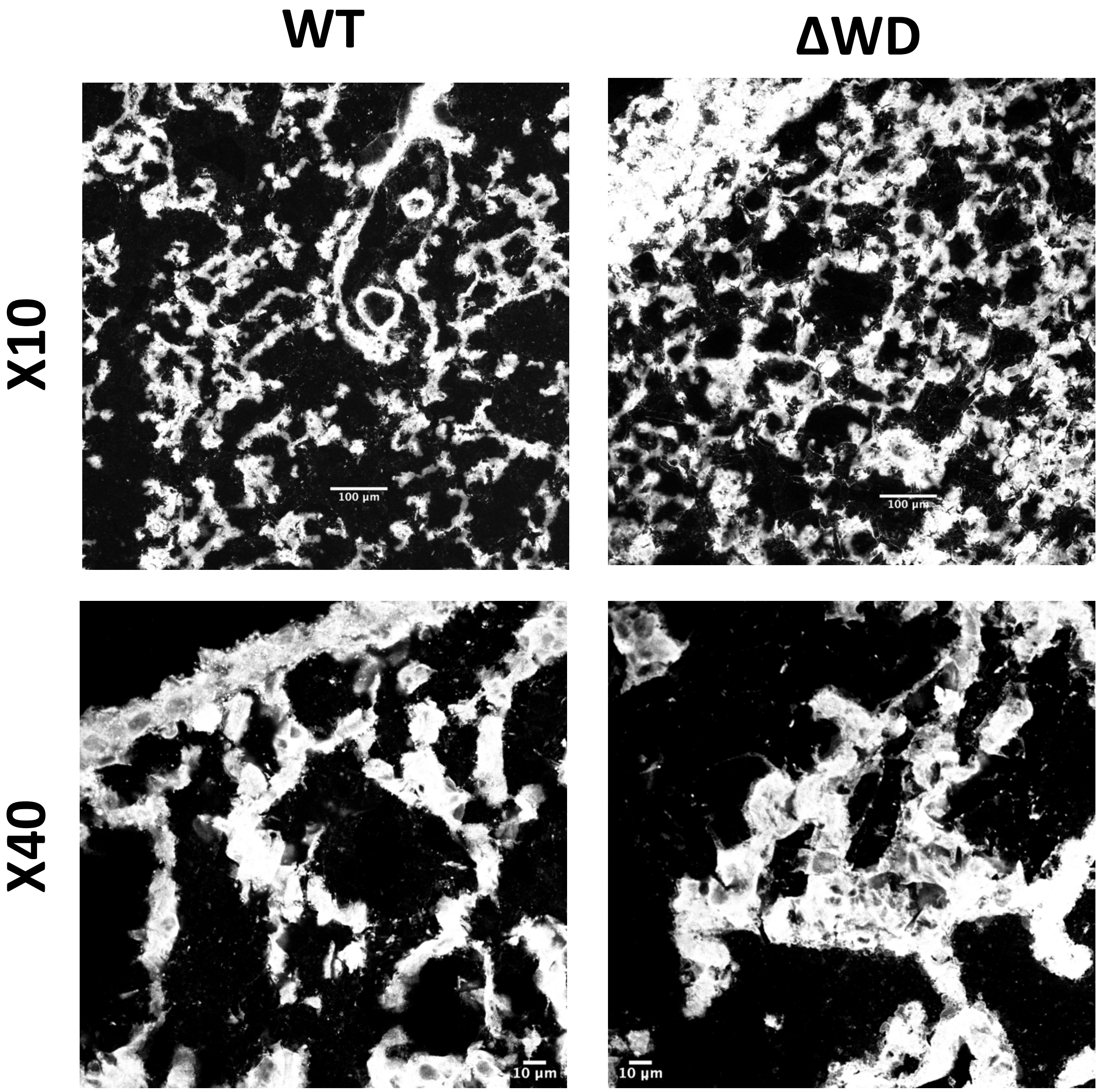

Figure 3.6: Cholesterol localisation in WT and ΔWD lung slices. WT and ΔWD lungs were frozen and sliced using a cryostat. Slices were stained with filipin to localise cholesterol. Slices were viewed using a Zeiss LSM980-Airyscan confocal microscope.

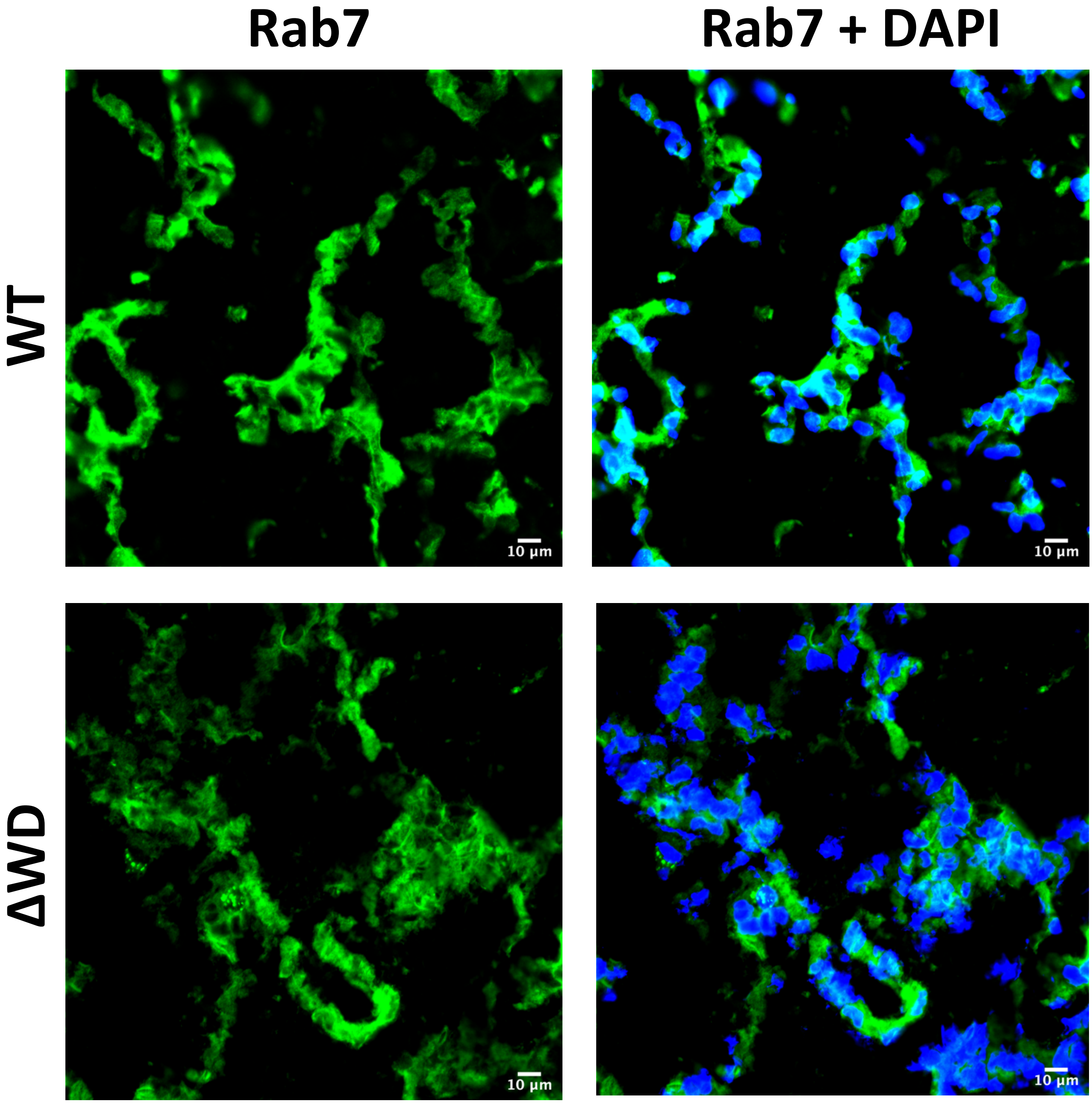

Figure 3.7: Late endosomal (Rab7) localisation in WT and ΔWD lung slices. WT and ΔWD lungs were frozen and sliced using a cryostat. Slices were stained with anti-rabbit rab7 antibodies and visualised with anti-rabbit Alexa Fluor 488 (green) to stain for late endosomes. Nuclei were stained with DAPI. Slices were examined using a Zeiss LSM980-Airyscan confocal microscope.

3.3.5 There is increased colocalization of cholesterol to late endosomal membranes in ΔWD MEFs compared with WT MEFs.

Filipin III is a fluorescent polyene antibiotic widely used as a cholesterol stain. However it suffers from an impracticality in that it is easily photobleached which makes microscopy difficult. Another protein that can be used to localise cholesterol in cells is domain 4 (D4) of perfringolysin O, a theta-toxin produced by *Clostridium perfringens* (330). This domain has lipid binding properties, binding the hydroxyl group at position 3 of cholesterol. Scientists have produced an array of cholesterol biosensors using D4, increasing its affinity for cholesterol such as with D4H, a modified D4 protein that is able to bind cholesterol within intracellular membranes (329).

WT and ΔWD MEFs were transfected with the D4H mCherry plasmid. After 24 hours, cells were fixed and stained with either anti-EEA1 (early endosomes), anti-LAMP1 (lysosomes) or anti-Rab7 (late endosomes). Antibody was visualised with a secondary antibody labelled with Alexa Fluor 488. D4H mCherry was seen in vesicle-like structures in both WT and ΔWD cells (Figure 3.8 A, B, C). This organelle colocalised significantly more with Rab7/late endosomes and LAMP1/lysosomes than EEA1/early endosomes (Figure 3.8 D). D4H mCherry was seen to colocalise significantly more to Rab7/late endosomes in ΔWD MEFs than WT MEFs, indicating that cholesterol accumulated more in late endosomes in ΔWD MEFs (Figure 3.8 E). While not statistically significant, greater colocalization of D4H mCherry to LAMP1 stained lysosomes and EEA1 stained early endosomes was also seen in ΔWD MEFs (Figure 3.8 F, G).

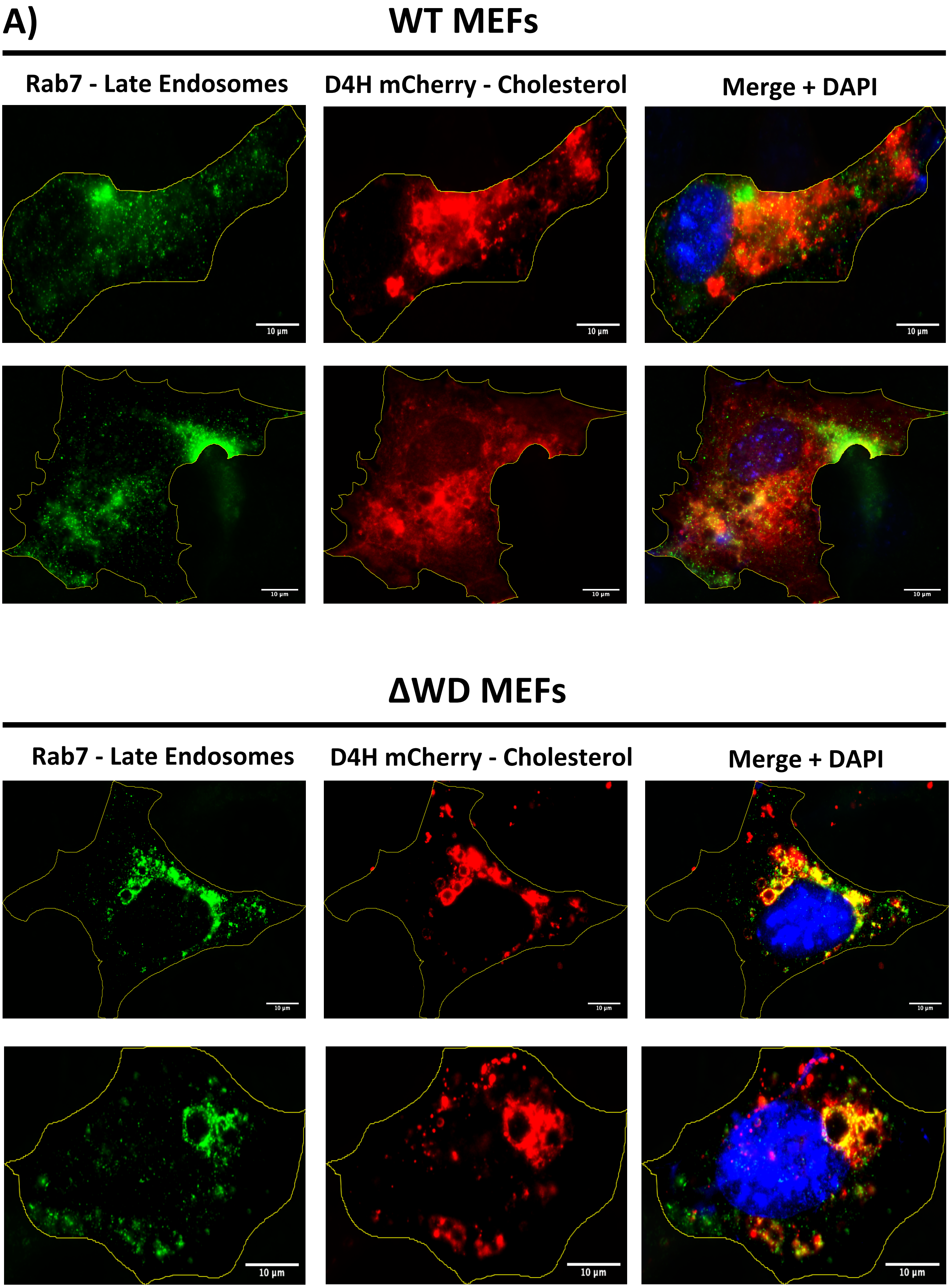
A)
WT MEFs
Rab7 - Late Endosomes
D4H mCherry - Cholesterol
Merge + DAPI
10 µm
10 µm
10 µm
10 µm
10 µm
10 µm
ΔWD MEFs
Rab7 - Late Endosomes
D4H mCherry - Cholesterol
Merge + DAPI
10 µm
10 µm
10 µm
10 µm
10 µm
10 µm

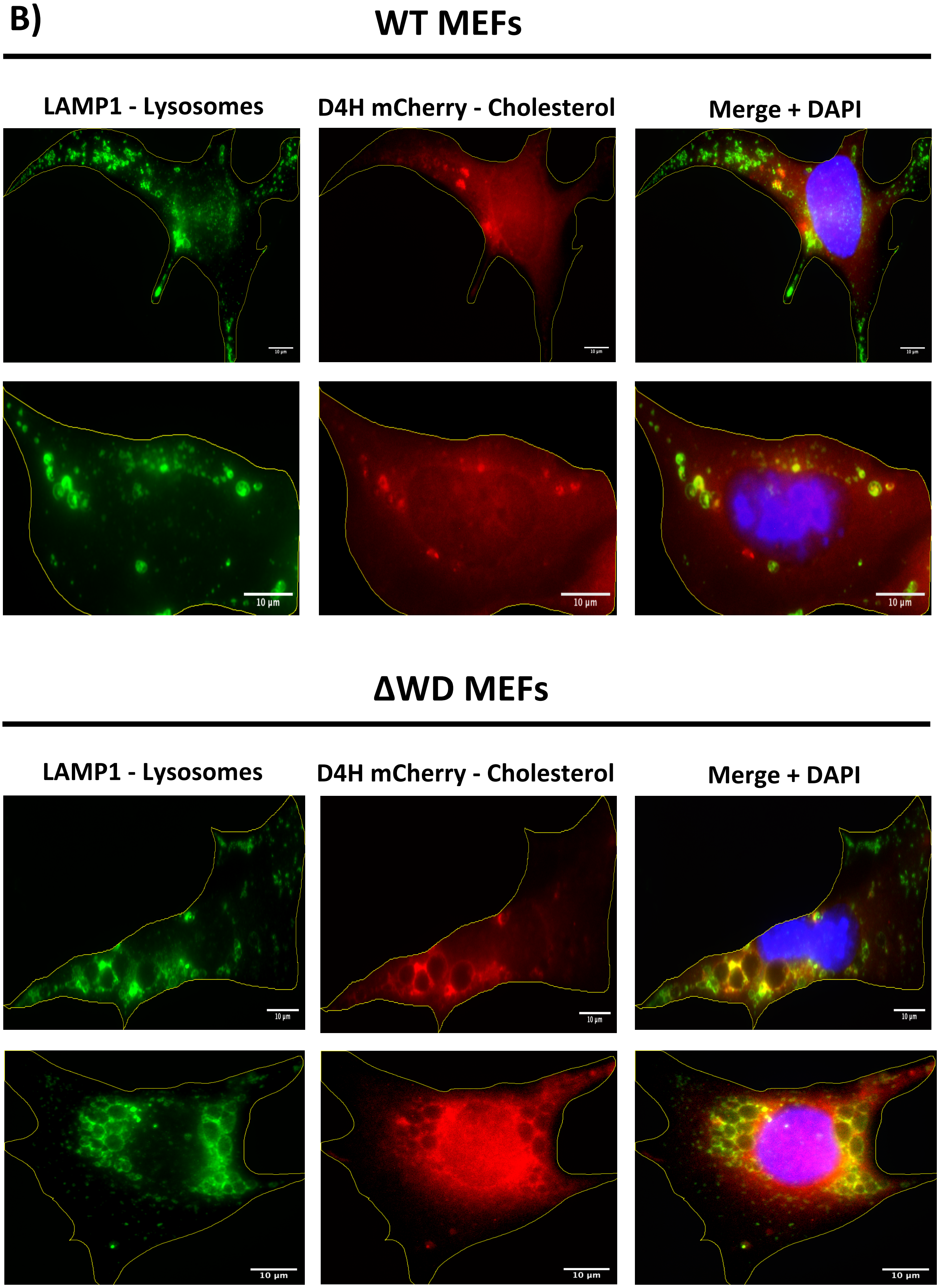
B)
WT MEFs
LAMP1 - Lysosomes
D4H mCherry - Cholesterol
Merge + DAPI
10 µm
ΔWD MEFs
LAMP1 - Lysosomes
D4H mCherry - Cholesterol
Merge + DAPI
10 µm

C)

WT MEFs

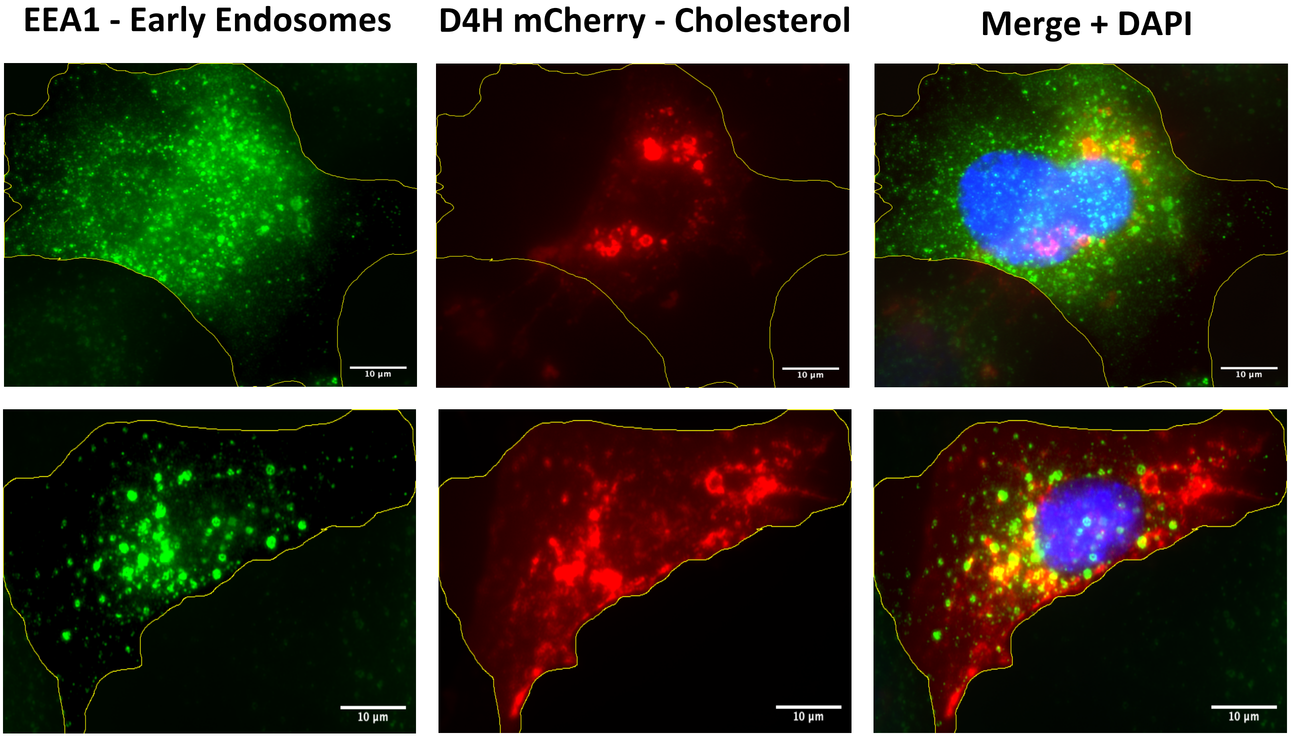

ΔWD MEFs

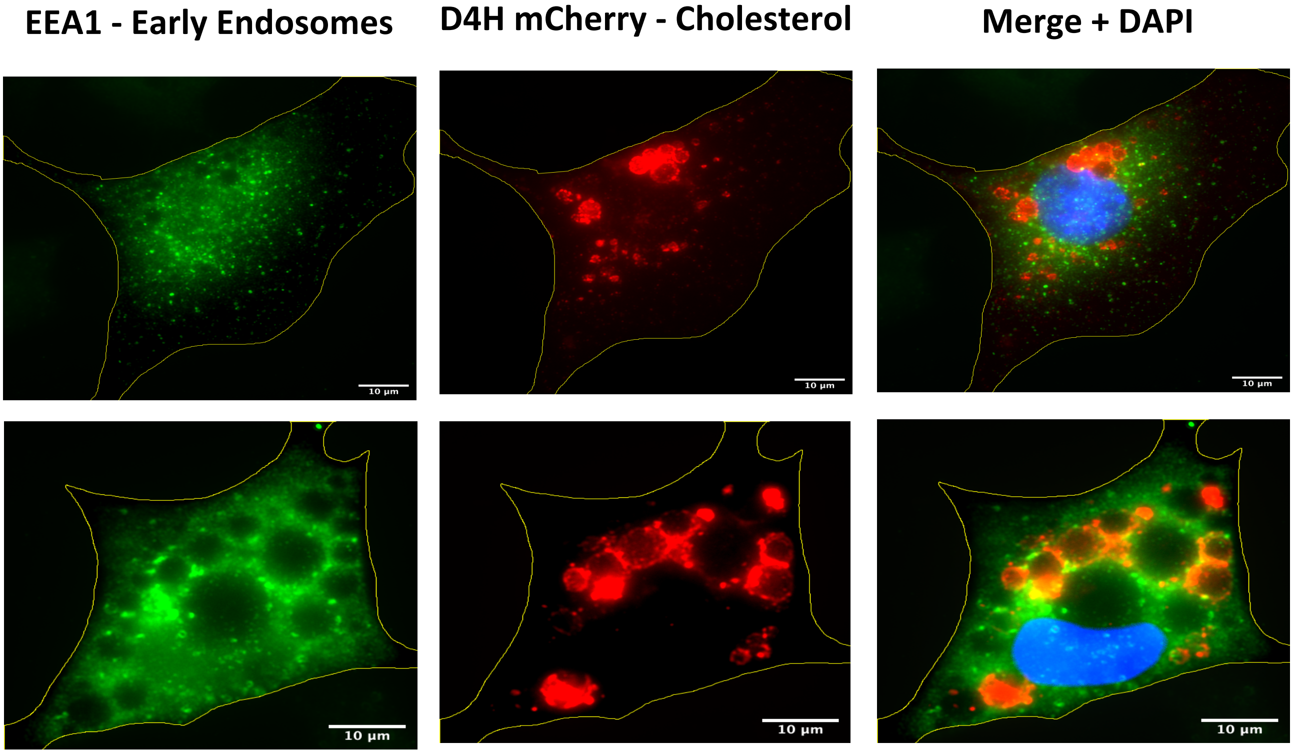

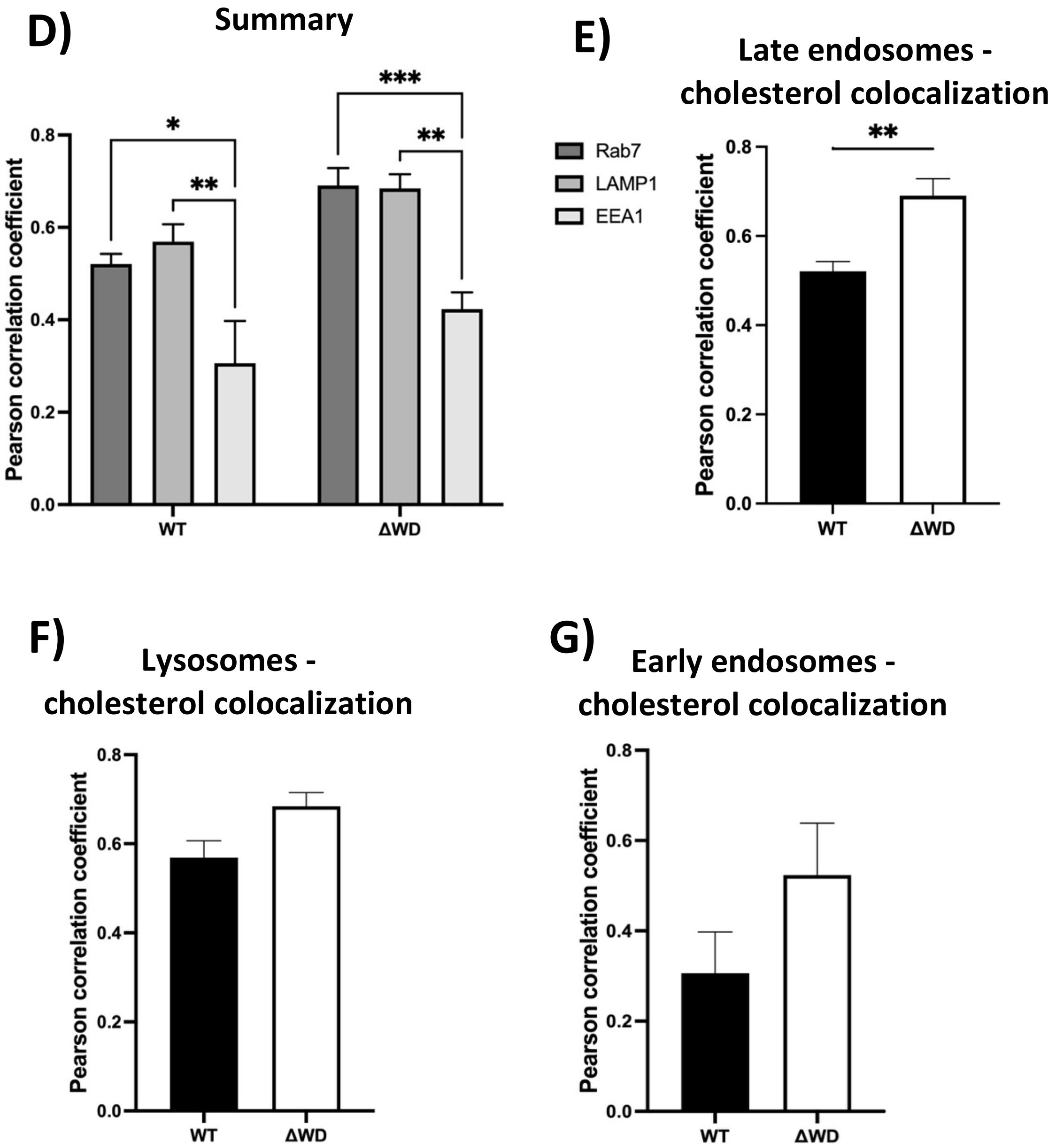

Figure 3.8: There is increased cholesterol colocalization in late endosomes in ΔWD MEFs compared to WT MEFs. WT and ΔWD MEFs were transfected with D4H mCherry for 24 hours before staining with either anti-Rab7 (A - Late endosomes), anti-LAMP1 (B - Lysosomes) or EEA1 (C - Early endosomes). Images of D4H mCherry and antibody datasets were correlated using a Pearson correlation and the average Pearson coefficients are presented (+SEM) (D). A two-way ANOVA with Bonferroni corrections was conducted for the summary graph: * = $p<0.05$, ** = $p<0.01$, *** = $p<0.001$. Panels E-G demonstrate the differences in cholesterol co-localisation between WT and ΔWD with Mann Whitney U tests: ** = $p<0.01$, n=15 over 3 coverslips.

3.4 Discussion

In order to investigate the role of the WD domain in cholesterol localisation this chapter used a biochemical assay to quantify cholesterol in subcellular fractions and cholesterol-specific probes to image it in cells and tissue. Firstly the total cell cholesterol was measured for WT and ΔWD MEFs, with higher levels of unesterified cholesterol detected in ΔWD MEFs (Figure 3.2). This suggested that there is more cholesterol localised in membranes within ΔWD MEFs, however the replicates for this experiment were technical, which does limit this conclusion. The localisation of this cholesterol was further investigated with the plasma membranes being successfully isolated from brain and lung tissue as well as MEFs (Figure 3.3). Total and unesterified cholesterol were again measured for the plasma membrane fractions and it was shown that there were lower levels of unesterified cholesterol found in ΔWD brain, lung and MEF plasma membranes (Figure 3.4). This was in contrast to the cell unesterified cholesterol levels, which were higher in ΔWD MEFs. The fractionation data show the plasma membrane alone, suggesting that cholesterol may be distributed elsewhere in ΔWD cells. Cholesterol would be found within lysosomal or late endosomal membranes before it is transported to the plasma membrane.

Cholesterol localisation within cells was visualised using cholesterol probes such as filipin III and D4H mCherry. When filipin was used to stain for cholesterol in MEFs, cholesterol was found to localise to the plasma membrane in WT MEFs and found aggregating into large cytoplasmic structures in ΔWD MEFs (Figure 3.5). Within lung slices, no clear difference in cholesterol distribution could be seen between WT and ΔWD tissue (Figure 3.6) or late endosome distribution (Figure 3.7).

Cholesterol localisation was further investigated using D4H mCherry which is a cholesterol-binding probe. Cholesterol was found to localise with late endosomes and lysosomes more than early endosomes. Additionally, cholesterol localised to late endosomes significantly more in ΔWD MEFs than in WT MEFs. While not significant, it also was seen to localise more to lysosomes in ΔWD MEFs than WT MEFs (Figure 3.8). This explains the high cholesterol content of ΔWD MEFs. Cholesterol enters cells through the endocytic pathway of LDL, but lysosomal exocytosis is blocked due to the absence of the

WD domain, therefore less cholesterol is able to reach the plasma membrane. In addition, less cholesterol is able to reach the endoplasmic reticulum and switch off cholesterol synthesis pathways. This would lead to an accumulation of cholesterol within ∆WD cells, but also results in decreased levels of cholesterol at the plasma membrane.

ATG16L1 has many non-canonical functions, with Tan *et al*. (84) demonstrating that a deficiency in the protein prevents lysosomal exocytosis and a failure in cholesterol to supplement the plasma membrane. This chapter has shown that the WD domain of ATG16L1 has a role in cholesterol transportation, with a build-up of cholesterol within ∆WD MEFs. Cholesterol is held up in the membranes of late endosomes and lysosomes, with this cholesterol unable to be transported to the plasma membrane. The conjugation of LC3 to single membranes is crucial for them to fuse with lysosomes. For LAP this process relies on the WD domain of ATG16L1 (66), and it is required to conjugate LC3 to other single membraned organelles. This conjugation may well be needed to support lysosomal-plasma membrane fusion, which allows for effective transport of cholesterol from the late endosome/lysosome to the plasma membrane. In these unique experiments I have shown that this does not occur in ∆WD cells and there is decreased cholesterol in the plasma membrane. ∆WD mice are very susceptible to IAV (78) and this could be because IAV is able to more efficiently enter ∆WD cells. Cholesterol homeostasis may be the mechanism as to why the WD domain is able to suppress infection. This thesis will investigate whether IAV can more efficiently fuse with cholesterol deficient membranes in ∆WD cells. The subsequent chapter will investigate if IAV can enter cells by endocytosis and fusion more efficiently due to the biochemical differences in cells lacking cholesterol in their membranes.

CHAPTER 4

The WD domain of ATG16L1 limits the entry and fusion of IAV in MEFs

4.1 Introduction

In Chapter 3 the results demonstrated that the plasma membrane (PM) of ΔWD MEFs contain less cholesterol than WT MEF PMs. In this chapter I investigate how alteration in PM cholesterol affects fusion and endocytosis of IAV into cells. Banerjee *et al.* (2013) developed assays for quantifying seven sequential events in the early infection of IAV (331). These steps are: virus binding, endocytosis, acidification of HA, fusion, nucleocapsid uncoating, nuclear import and expression of nucleoprotein. In this chapter I have used three of these assays to measure the efficiency of virus entry between WT and ΔWD MEFs. The first measures endocytosis using two antibodies that compete for HA, thereby when used before and after permeabilisation can discriminate between external and internal IAV: PINDA and HA1. Cells are infected with IAV for 30 min and then fixed in PFA. The HA epitopes of the external virus are masked with PINDA, a rabbit polyclonal antibody. Following this, the cells were fixed again and permeabilised. Internalised viruses were then stained with HA1, a mouse monoclonal antibody. PINDA and HA1 were then stained with Alexa Fluor 594 and 488 respectively (Figure 4.1).

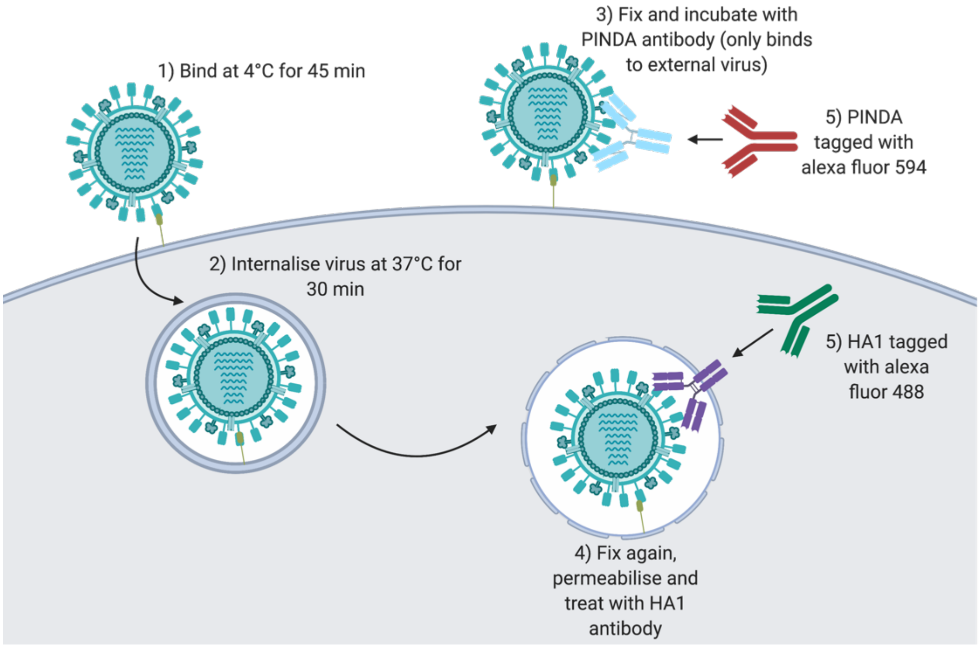

Figure 4.1: Schematic of the endocytosis assay. Produced using Biorender.

In a second series of experiments, IAV was labelled with two lipophilic fluorescent dyes: R18 (red) and SP-DiOC18 (green). The fluorescence of SP-DiOC18 is attenuated by self-quenching and through fluorescence resonance energy transfer (FRET) to R18, but only when in close proximity to it. R18, on the other hand, is only slightly suppressed by self-quenching when in close proximity. IAV is labelled with this dye combination and used to infect cells. When fusion occurs, the lipophilic dye is spread across the membrane of the late endosome the virus fuses to, as well as the original virus membrane. This separates the dyes, dequenching SP-DiOC18 and allowing for green fluorescence. Fusion events would then be quantified using fluorescence activated cell sorting (FACS) by measuring the shift from red to green fluorescence (Figure 4.2).

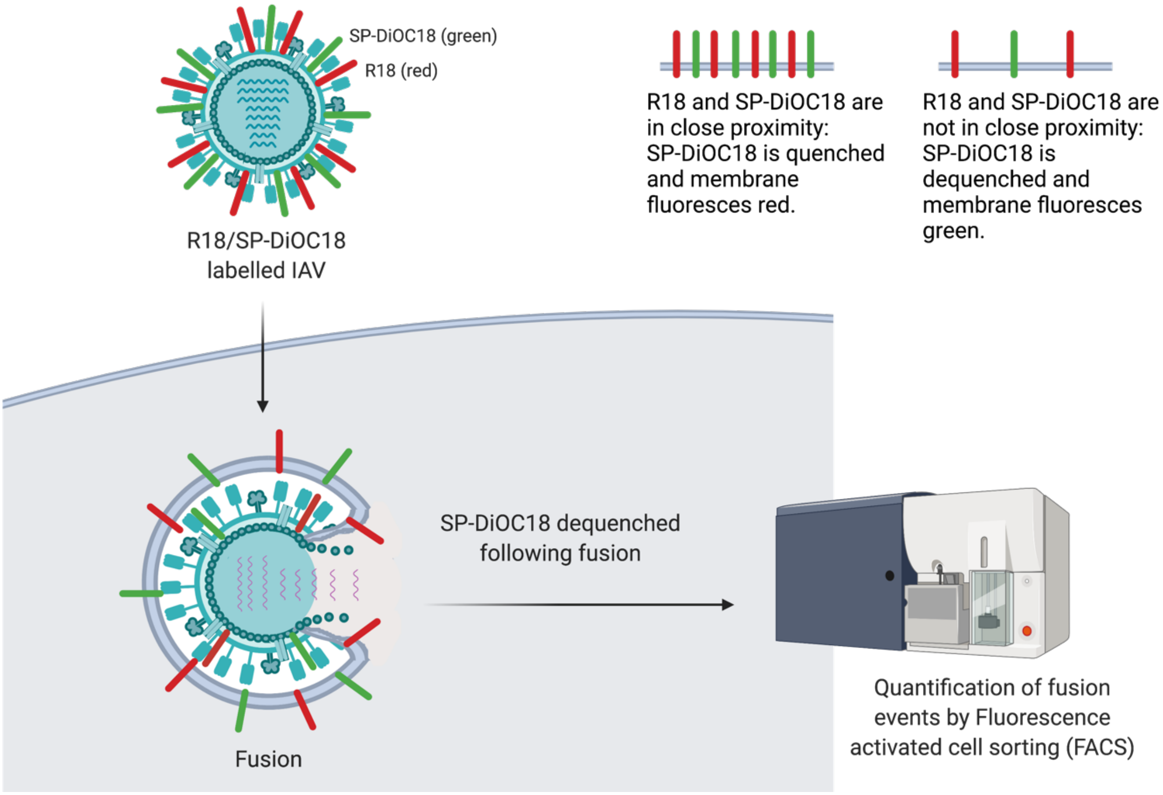

Figure 4.2: Schematic of the fusion assay. Produced using Biorender.

The third assay I used was the nuclear entry assay. This assay relies on monitoring the migration of NP to the nucleus, which would be measured using an anti-NP antibody. When NP is stained with a secondary antibody (Alexa Fluor 488), the nucleus will fluoresce green.

Entry of IAV into cells can be categorised into four distinct phases: binding to sialic acid, endocytosis, acidification of IAV's core and viral membrane fusion to the endosomal membrane. Furthermore, the genome then migrates to the nucleus for successful gene delivery and infection. The primary route for IAV to enter the cell, is by clathrin-mediated endocytosis, although IAV can also enter by clathrin-independent entry mechanisms such as macropinocytosis (173).

Once in the cell, the low pH of the late endosome activates the M2 protein of IAV and causes conformational change to the HA protein. Two fundamental pre-fusion events then occur allowing for fusion. The first concerns HA, where lowering the pH of the endosome causing conformational change to the protein that exposes its fusion peptide. When near the endosomal membrane, the fusion peptide inserts itself into the membrane. The second event involves M2, M2 being an envelope embedded ion-channel that, upon activation, allows entry of protons into the capsid core. This lowers the pH causing the interactions between the M1 protein (which lines the inside of the capsid) and the capsid membrane to weaken and M1 to dissociate: liberating the vRNPs (188,332).

The endosomal membrane IAV fuses to during its fusion stage may have a similar constitution to the PM due to the PM donating the membrane by invagination during endocytosis. The previous chapter demonstrated that there is a reduction in unesterified cholesterol within the plasma membranes of ΔWD MEFs, brains and lungs. Additionally, monitoring of intracellular cholesterol showed that there is a build-up of cholesterol in late endosomes and lysosomes in ΔWD MEFs. Therefore the WD domain has a role in cholesterol transport, with a potential lack of lysosomal exocytosis preventing cholesterol reaching the plasma membrane.

In this chapter, the effect of cholesterol on IAV fusion is studied using a process known as acid mediated bypass, or acid bypass (Figure 4.3). This is where reducing the pH of the extracellular environment forces the insertion of the fusion peptide of IAV into the plasma membrane resulting in viral fusion and entry of IAV's nucleoproteins directly into the cytoplasm, effectively bypassing endocytosis of the virus. This work asks if entry of IAV by fusion at the plasma membrane is altered in ΔWD cells due to the changes in cholesterol content described in Chapter 3.

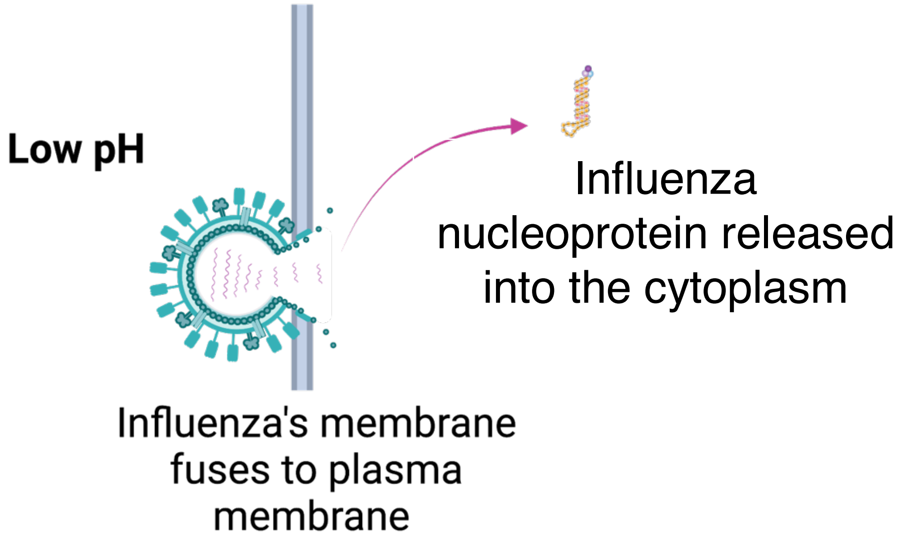

Figure 4.3: Fusion between the membrane of IAV and host plasma membrane to deliver the genome directly to the cytoplasm. Produced using Biorender.

4.2 Aims

- Investigate the mechanism of the WD domain of ATG16L1 in limiting fusion of IAV with cell plasma membranes using acid bypass. Does inhibiting cholesterol transport to the PM with U18666A treatment affect IAV fusion?
    - I set out to determine whether cholesterol and IAV fusion were linked, forcing fusion at the PM using acid bypass infection and measuring entry of IAV NP by immunostaining and microscopy. Using U18666A (an NPC1 inhibitor), the cholesterol content of the PM in cells was reduced to see the effect on fusion.
- Investigate the role of the WD domain in limiting IAV entry using an antibody staining assay that discriminates between internalised and external IAV.
- Investigate the role of the WD domain in limiting IAV fusion using IAV labelled with R18/SP-DioC18, a lipophilic dye that fluoresces when fusion occurs.

4.3 Results

4.3.1 Increased IFNβ mRNA expression following IAV uptake by acid bypass.

I first investigated whether the cholesterol content of membranes affects the efficiency of viral fusion to them. IAV infection by acid bypass allows for the infection process to bypass the endocytosis stage, forcing acid-mediated fusion at the plasma membrane (PM). The ability to fuse at the membrane was investigated. I next investigate the differences in IAV entry during normal infection at the endocytosis, fusion and nuclear entry stages.

WT and ΔWD MEFs were infected on ice with IAV PR8 for one hour before pulsing with warm medium at pH 5 or 7 for 3 minutes. Cells were then incubated in STOP medium for 10, 30 and 50 minutes and RNA was extracted and reverse transcribed to form cDNA. IFNβ mRNA levels in samples was quantified by qPCR using specific primers and normalised to 18S and with the negative controls. Increased levels of IFNβ were observed in ΔWD MEFs at all three time points (Figure 4.4), this difference being significant at 30 and 50 minutes post infection. At 30 and 50 minutes post infection, cells where the WD domain was deleted expressed approximately 20-fold higher IFNβ levels. These values were lower than in the control seen during normal infection in Chapter 5 because of the early time course. Alternatively, the difference could be due to the isolate used. This difference is not due to differences in the ability of IAV to bind to WT and ΔWD cells. IAV binding to WT and ΔWD MEFs has been performed prior and no significant difference was detected (Appendix 1 Figure 6B).

These elevated IFNβ transcript levels could be due to increased receptor activation in ΔWD MEFs which could be due to increased IAV entering cells and triggering cell viral receptors such as TLR3 or Rig-I. IAV hasn’t been mentioned directly in this assay, however the next experiment measures IAV entry directly and supports these data.

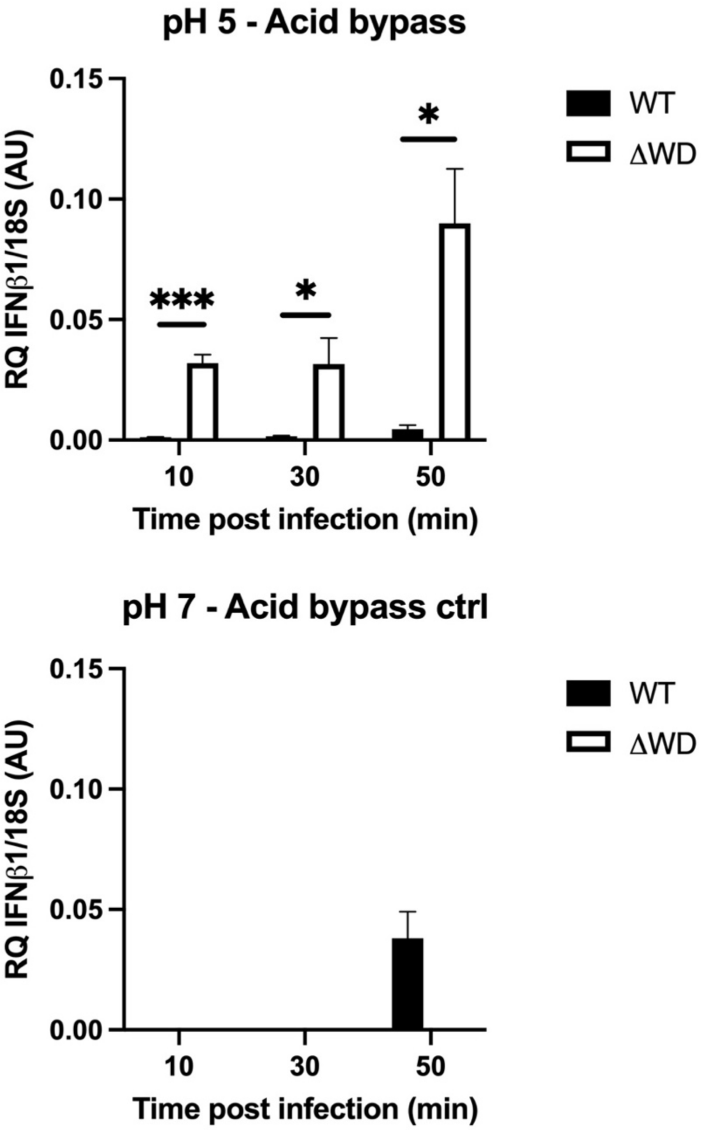

Figure 4.4: Increased IFNβ1 mRNA detected by qPCR at 10, 20 and 50 minutes post infection of ΔWD MEFs compared with WT MEFs by acid bypass.

WT and ΔWD MEFs were infected with influenza (MOI: 10) at 4°C before pulsing with warm media at pH 5.0 (acid bypass) and infecting for 10, 30 and 50 minutes. At each time point, cells were lysed and RNA isolated, reverse transcribed and IFNβ1 transcripts measured by qPCR using specific primers. Transcript levels relative to 18S are shown on the top chart (+SEM). An independent samples t-test was conducted: * = $p<0.05$, *** = $p<0.001$, n=3 technical replicates.

Control cells were also infected as normal, IFNβ1 transcript levels relative to 18S are shown on the bottom chart (+SEM).

4.3.2 Increased frequency of IAV PR8 nucleoprotein (NP) in ΔWD MEFs on infection by acid bypass.

In this experiment, the entry of IAV nucleoprotein (NP) was measured using fluorescence microscopy. WT and ΔWD MEFs were infected by acid bypass and cells were fixed at 10, 30 and 50 minutes post infection. IAV PR8 NP was visualised using a mouse anti-NP and stained with IgG 488 anti-mouse. Cells were viewed using a Zeiss Axio.M2 imager and NP puncta counted. Figure 4.5 demonstrates a significant increase in frequency of cytoplasmic NP puncta of ΔWD MEFs as well as an increased size of the puncta, at all 3 time points. At 30 and 50 minutes post infection, ΔWD NP puncta were two-fold more frequent than WT NP puncta. In addition, ΔWD MEF NP puncta were, on average, three-fold greater in size compared with WT NP puncta. An increased frequency of NP puncta suggests more IAV PR8 was able to enter ΔWD MEFs by direct fusion with the plasma membrane. This is also supported by the data in figure 4.4, with more IAV NP leading to an increased pathogen recognition receptor activation and activating the IFN signalling pathway. The increased size of NP puncta also supports the greater frequency.

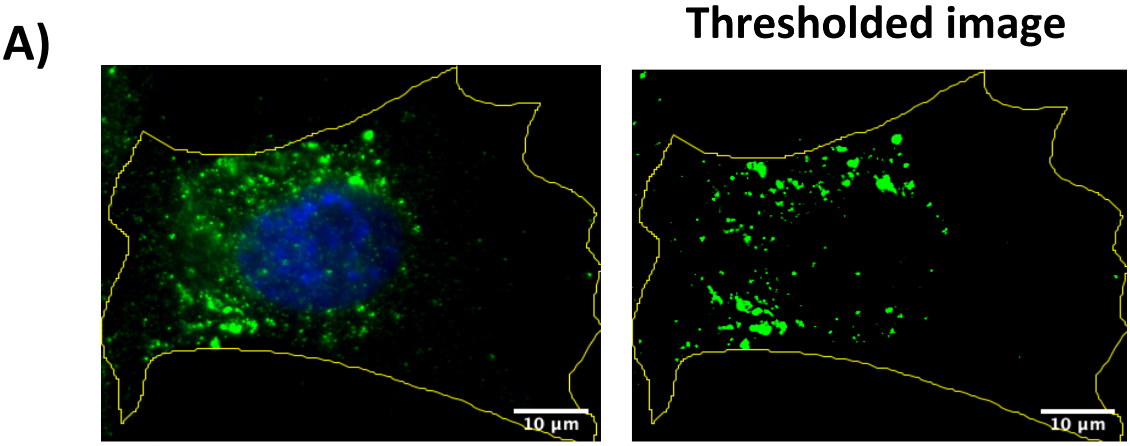

Count	Average size
180	0.317

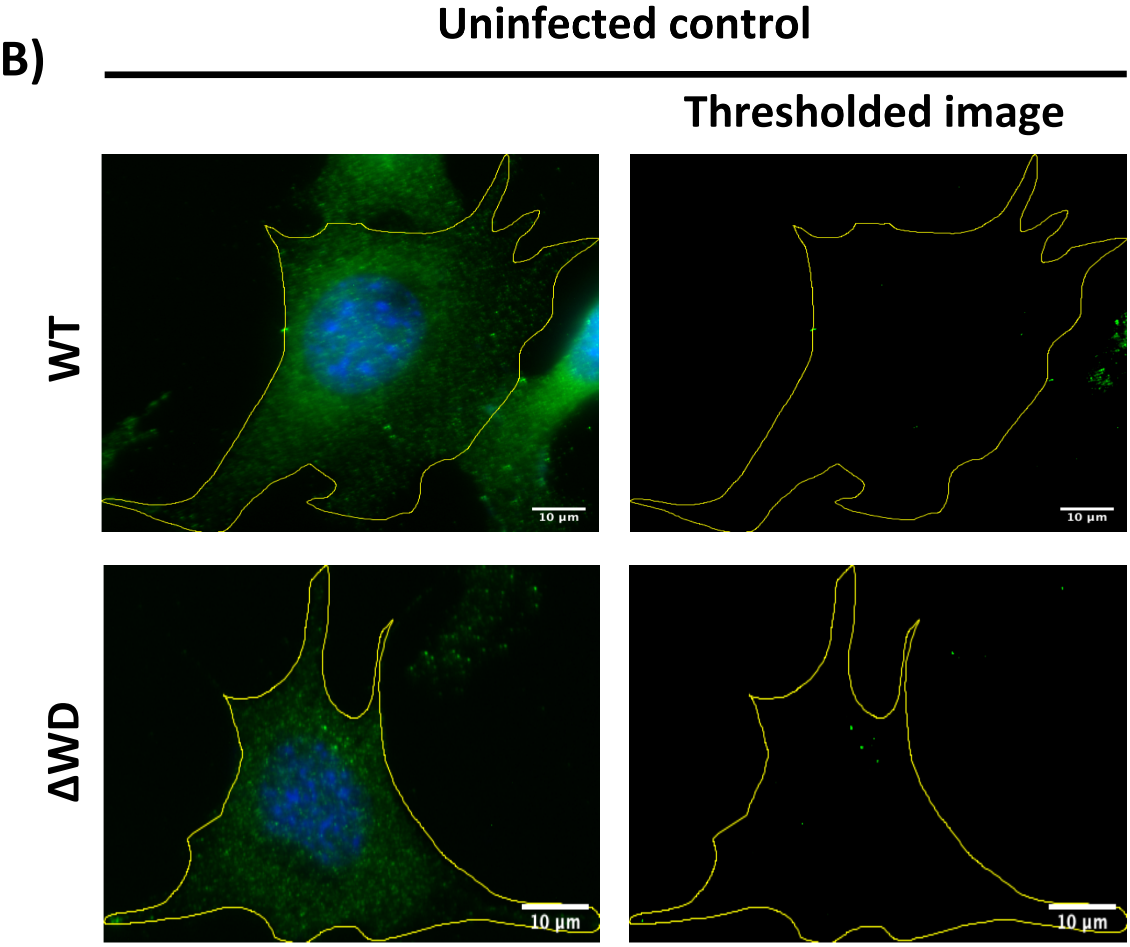

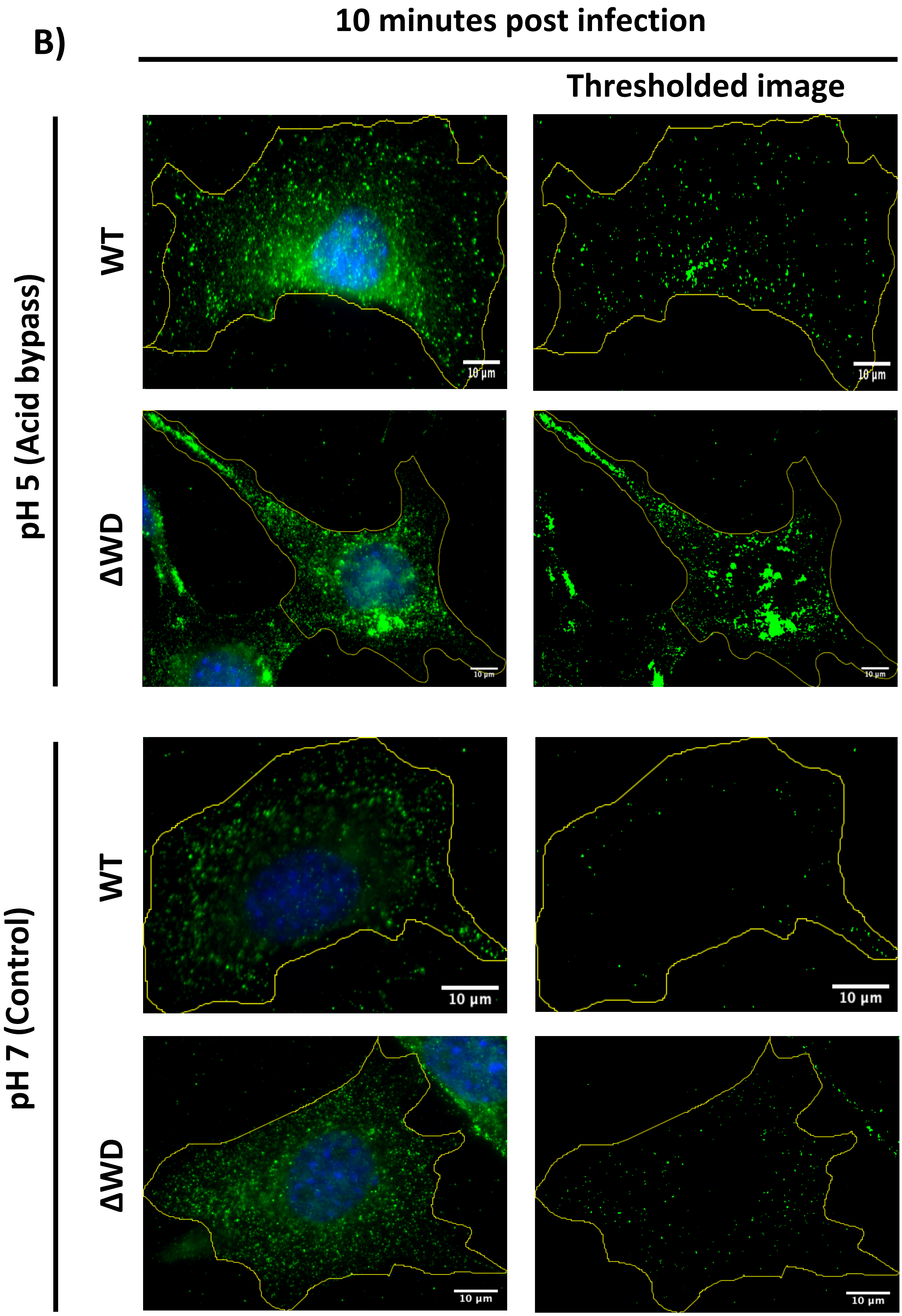
B)
10 minutes post infection
Thresholded image
pH 5 (Acid bypass)
WT
ΔWD
pH 7 (Control)
WT
ΔWD
10 µm

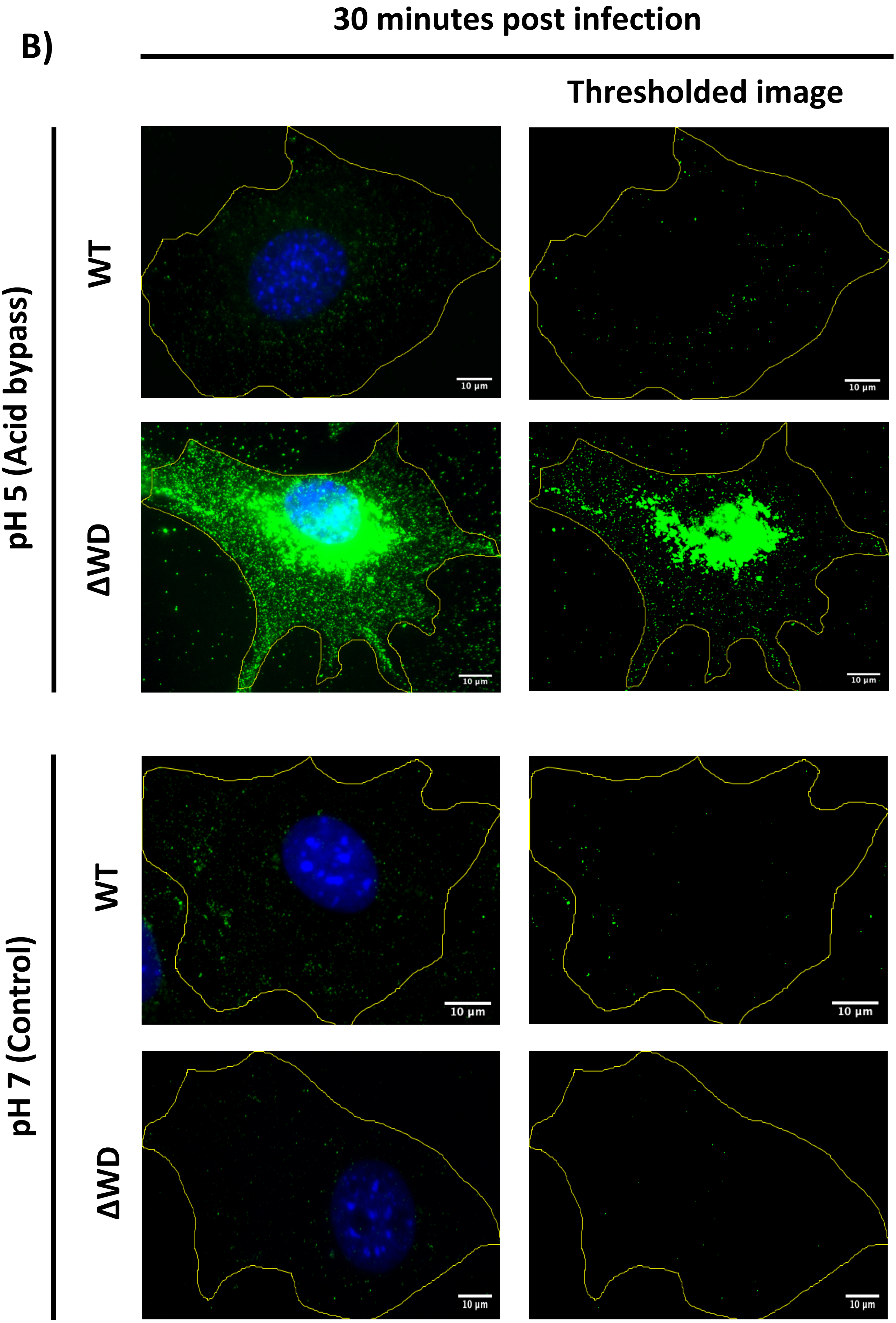
B)
30 minutes post infection
Thresholded image
pH 5 (Acid bypass)
WT
ΔWD
pH 7 (Control)
WT
ΔWD
10 µm

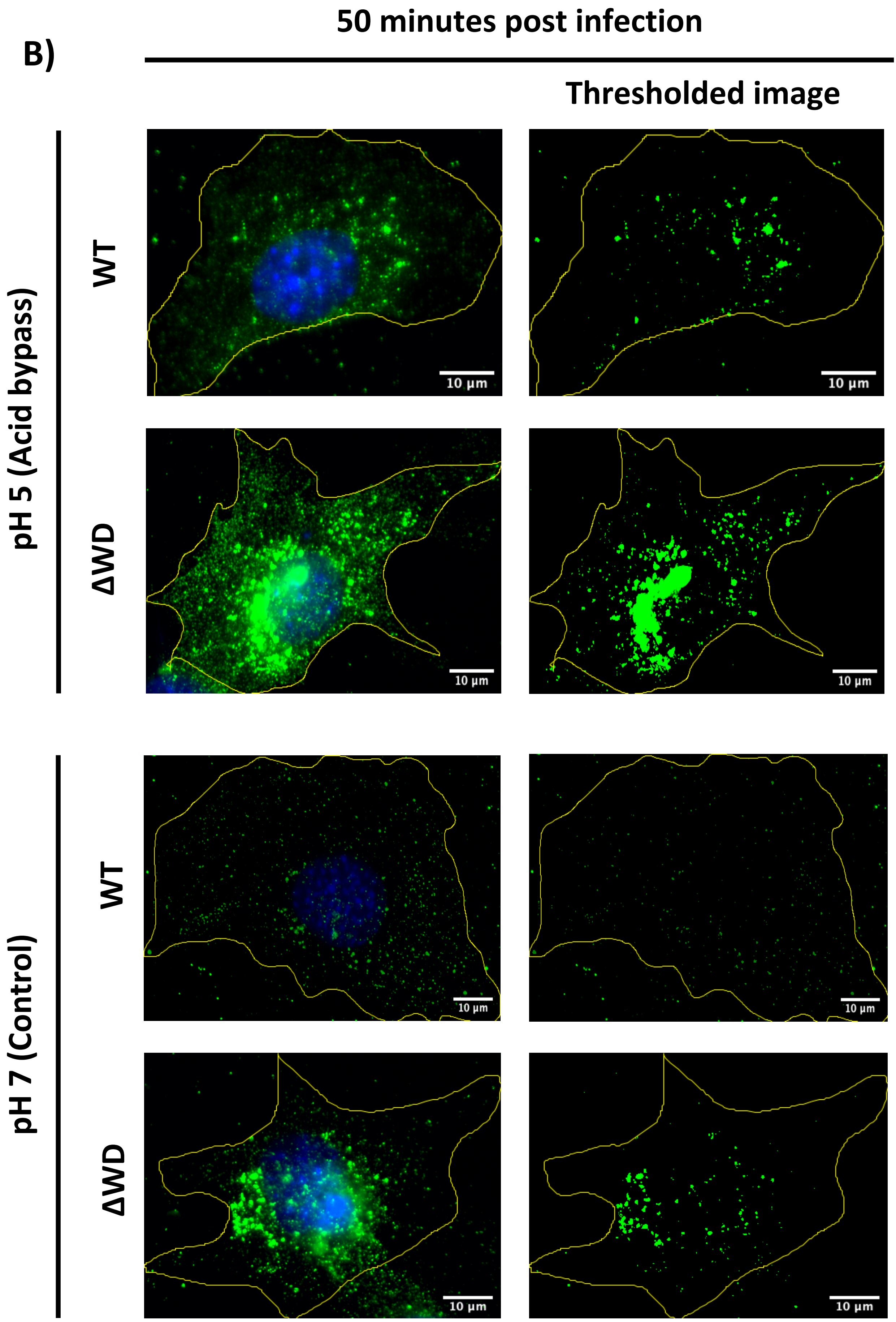
B)
50 minutes post infection
Thresholded image
pH 5 (Acid bypass)
WT
ΔWD
pH 7 (Control)
WT
ΔWD
10 µm

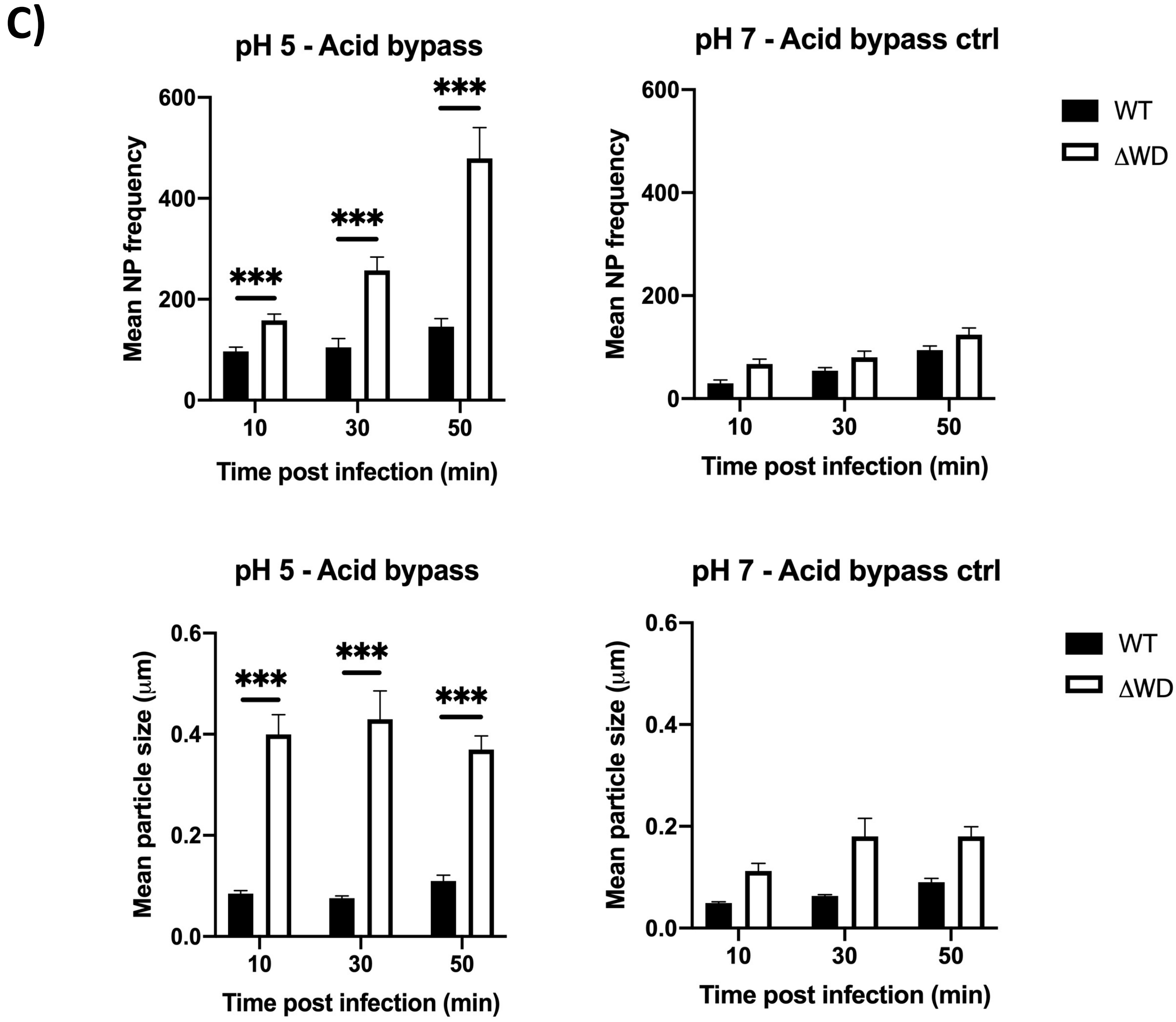

Figure 4.5: Increased frequency and size of IAV NP puncta detected at 10, 30 and 50 minutes post infection, using fluorescence microscopy.

WT and ΔWD MEFs were infected with influenza on ice before pulsing with warm acidic media (acid bypass) and allowing to infect for 10, 30 and 50 minutes. Cells were fixed and stained with a mouse anti-NP antibody to view IAV NP.

A) Cells were viewed using a Zeiss Axio.M2 Imager with the contrast increased and particles counted and sized using Image J.

B) IAV NP size and frequency was counted for 10, 30 and 50 min post infection. A control at pH: 7 was also used.

C) NP particle frequency and size displayed (+ SEM). A Mann Whitney U test was conducted: *** = p<0.001 n=50 per coverslip; three coverslips.

4.3.3 Increased frequency of IAV PR8 NP in MEFs treated with U18666A but not in MEFs treated with cholesterol or 25HC.

Cholesterol transport from lysosomes to the PM is perturbed using the cationic sterol U18666A (333). U18666A directly inhibits NPC1 by binding to its sterol-sensing domain. Cholesterol egress from lysosomes therefore does not occur (139). WT and ΔWD MEFs were pre-treated with either U18666A (24 hours), 25HC (16 hours) or cholesterol (12 hours) before infecting with IAV at pH 5. Cells were fixed at 90 minutes post infection. IAV PR8 NP was immunostained for using mouse anti-NP and stained with IgG 488 anti-mouse. Cells were viewed using a Zeiss Axio.M2 imager and NP puncta counted. For both WT and ΔWD MEFs, U18666A treatment significantly increased IAV NP frequency seen within cells (Figure 4.6). In contrast, 25HC treatment significantly reduced IAV NP frequency seen in cells. This is interesting as 25HC is known to reduce available cholesterol in membranes to viruses, yet viral reduced entry is seen. This could be due to 25HC having other effects on cell membranes. 25HC inserts itself into membranes at unorthodox angles, increasing the space between phospholipid molecules and effecting the stability of these membranes (334).

Interestingly, cholesterol treatment reduced IAV NP frequency in both WT and ΔWD, but this reduction was significant only for ΔWD MEFs. This supports the data in Figure 4.4 and 4.5 that IAV fuses more efficiently with PMs containing decreased cholesterol. IAV NP entry was inhibited by supplementing cell membranes with exogenous cholesterol or 25HC. These data suggest that fusion of IAV is more efficient at the PM of ΔWD MEFs. During normal infection IAV enters via endocytosis, the IAV-containing endosome is formed from the invaginating PM. The endosomal membrane would have a similar constitution to the PM, meaning that IAV is able to fuse more efficiently to them.

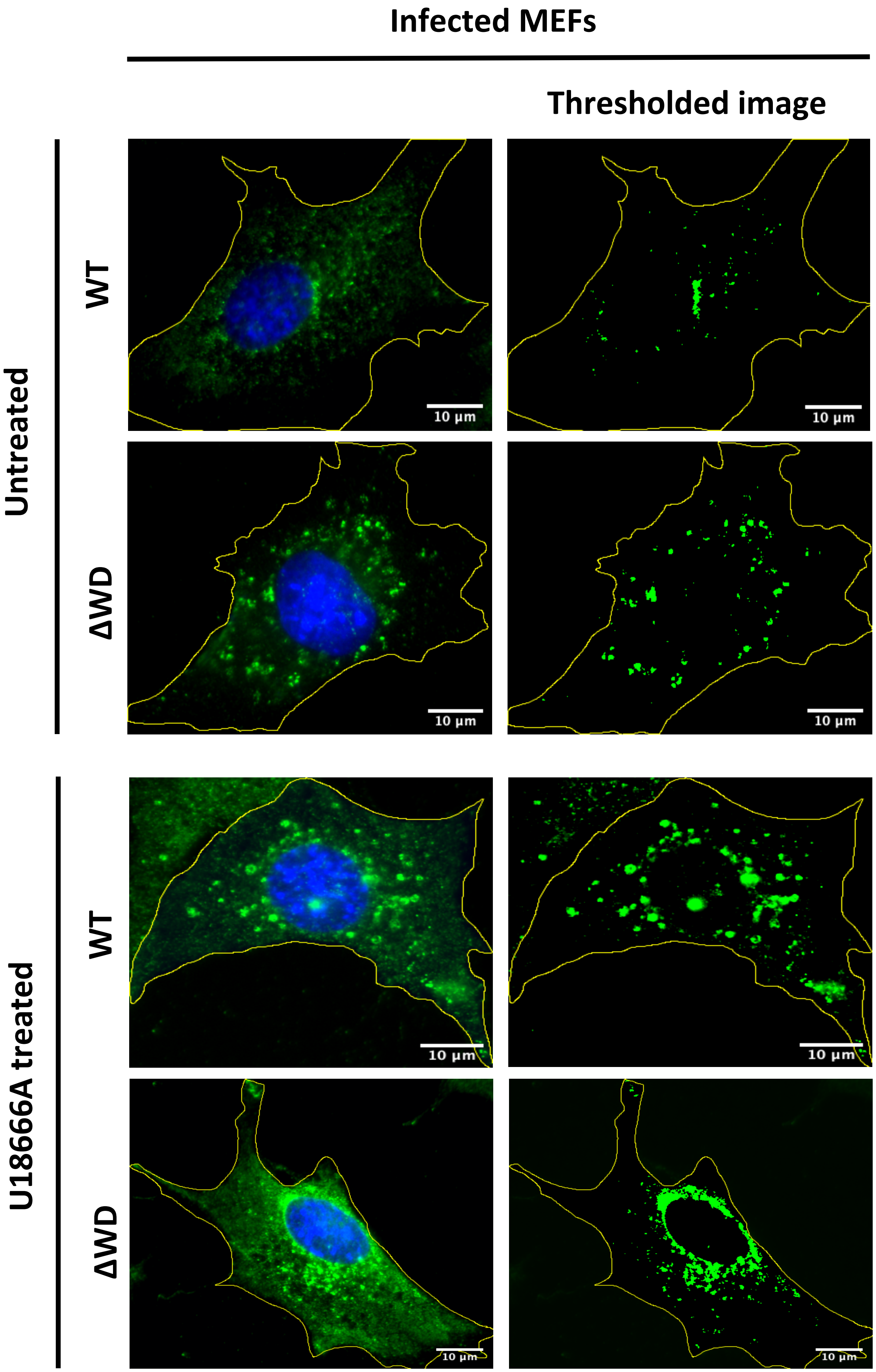
Infected MEFs
Thresholded image
Untreated
WT
ΔWD
U18666A treated
WT
ΔWD
10 μm
10 μm
10 μm
10 μm
10 μm
10 μm
10 μm
10 μm

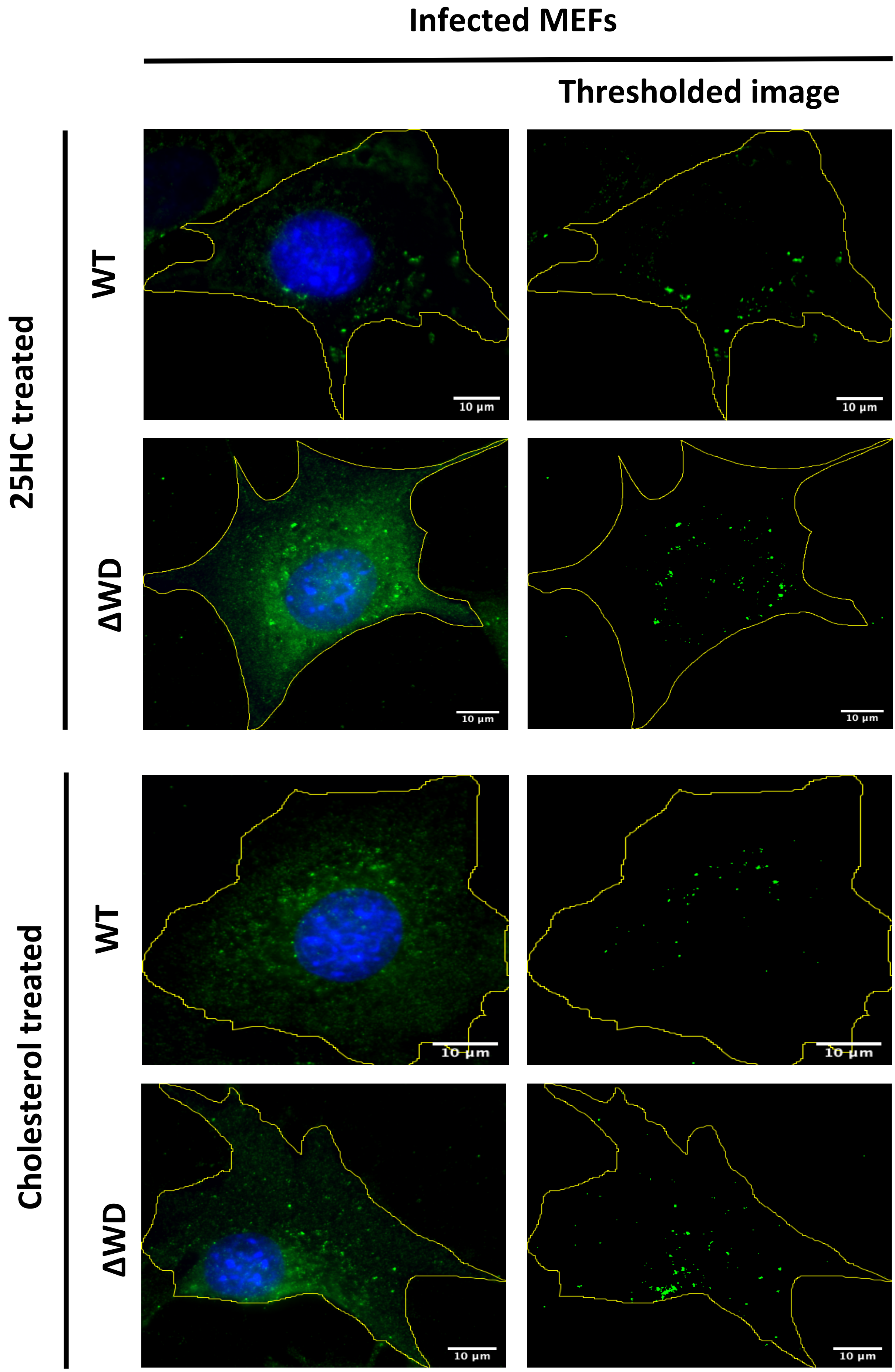
Infected MEFs
Thresholded image
25HC treated
WT
ΔWD
Cholesterol treated
WT
ΔWD
10 µm

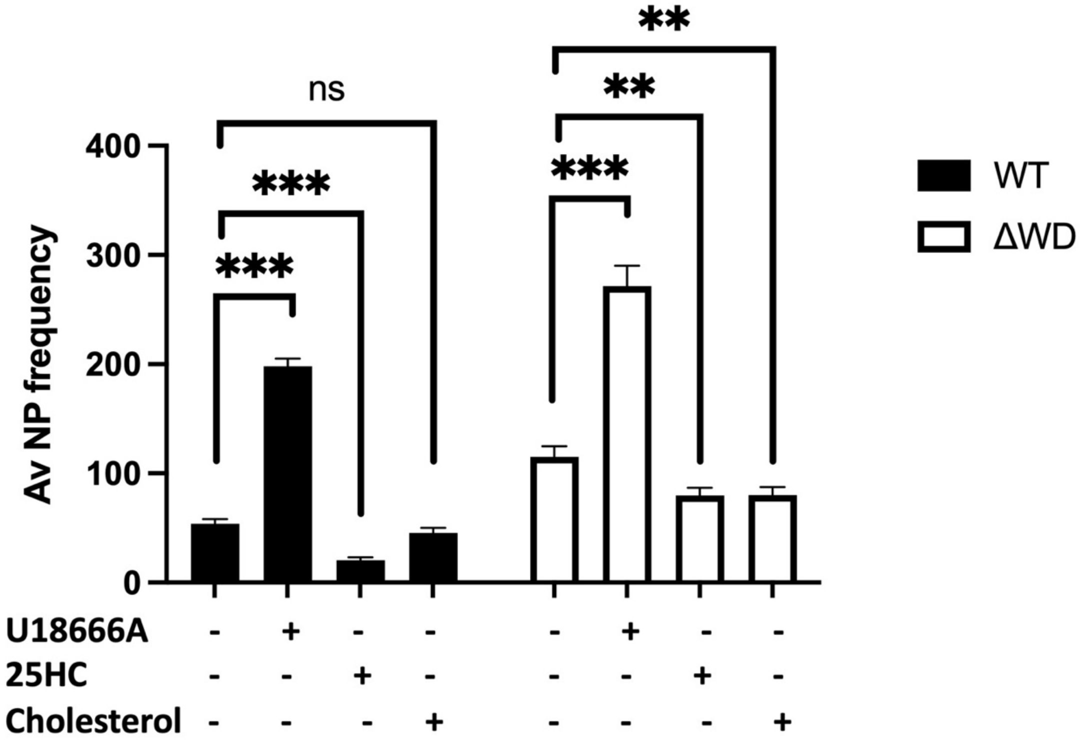

Figure 4.6: Increased frequency of IAV NP in cells treated with U18666A. Decreased NP detected in cells treated with 25-hydroxycholesterol (25HC) and cholesterol for both WT and ΔWD MEFs.

WT and ΔWD MEFs were treated with U18666A, 25HC and cholesterol prior to infecting with IAV on ice before pulsing with warm media at pH 5 and infection for 90 minutes. Cells were fixed and stained with a mouse anti-NP antibody and visualised with an IgG488 anti-mouse antibody. IAV NP puncta were counted using Image J and presented (+SEM). A Mann Whitney U test was performed: ** = p<0.01, *** = p<0.001, n=50 per coverslip; three coverslips.

4.3.4 Increased endocytosis of IAV in ΔWD MEFs compared with WT MEFs.

Chapter 3 demonstrated that the WD domain has a role in cholesterol homeostasis and Figures 4.4-4.6 showed that the cholesterol content of the PM affected IAV entry. These next three experiments aimed to investigate whether the WD domain of ATG16L1 has a role in the entry of IAV under normal infection, as opposed to acid bypass. Firstly, the endocytosis of IAV was monitored using an assay that relies on two IAV Haemagglutinin (HA) antibodies that discriminate between external and internal IAV.

IAV X31 was bound to WT and ΔWD MEFs for 60 minutes on ice before internalising and incubating at 37°C to internalise virus for 30 minutes. Cells were fixed and stained with PINDA, which binds and masks HA epitopes on external virus. Cells were then fixed again and permeabilised before staining with HA1, which binds to HA epitopes on internal virus. PINDA and HA1 were stained with the secondary Alexa Fluor 594 and 488 antibodies respectively. Additionally, cells were counterstained with WGA647 (purple) and DAPI (nuclei) to stain for cell membranes and nuclei respectively. Red and yellow puncta (coloured yellow due to both PINDA and HA1 colocalising to external virus) represent external viruses and were counted. Green puncta, which represent internal virus were counted, see white arrows on figure 4.7 A. Dynasore is a drug that inhibits dynamin and effectively attenuates endocytosis (335). Uninfected cells and cells treated with Dynasore for 30 minutes, were used as controls. In the uninfected control panels, no virus puncta were seen. In the Dynasore controls no green (internalised) puncta were observed, which suggests that PINDA has effectively bound all external virus and that the green puncta seen in the experimental conditions is due to endocytosis of the virus (Figure 4.7B).

The internalised virus was counted and presented as a percentage of the total virus that was used to infect the cell (Figure 4.7C). As can be seen from the chart, the WT MEFs mean average of virus internalised by the cell was 13.5% whereas for the ΔWD MEFs, 17.5% of the virus was internalised. This is an increase of 4% which is also statistically significant. This increase suggests that IAV more efficiently enters ΔWD MEFs by endocytosis.

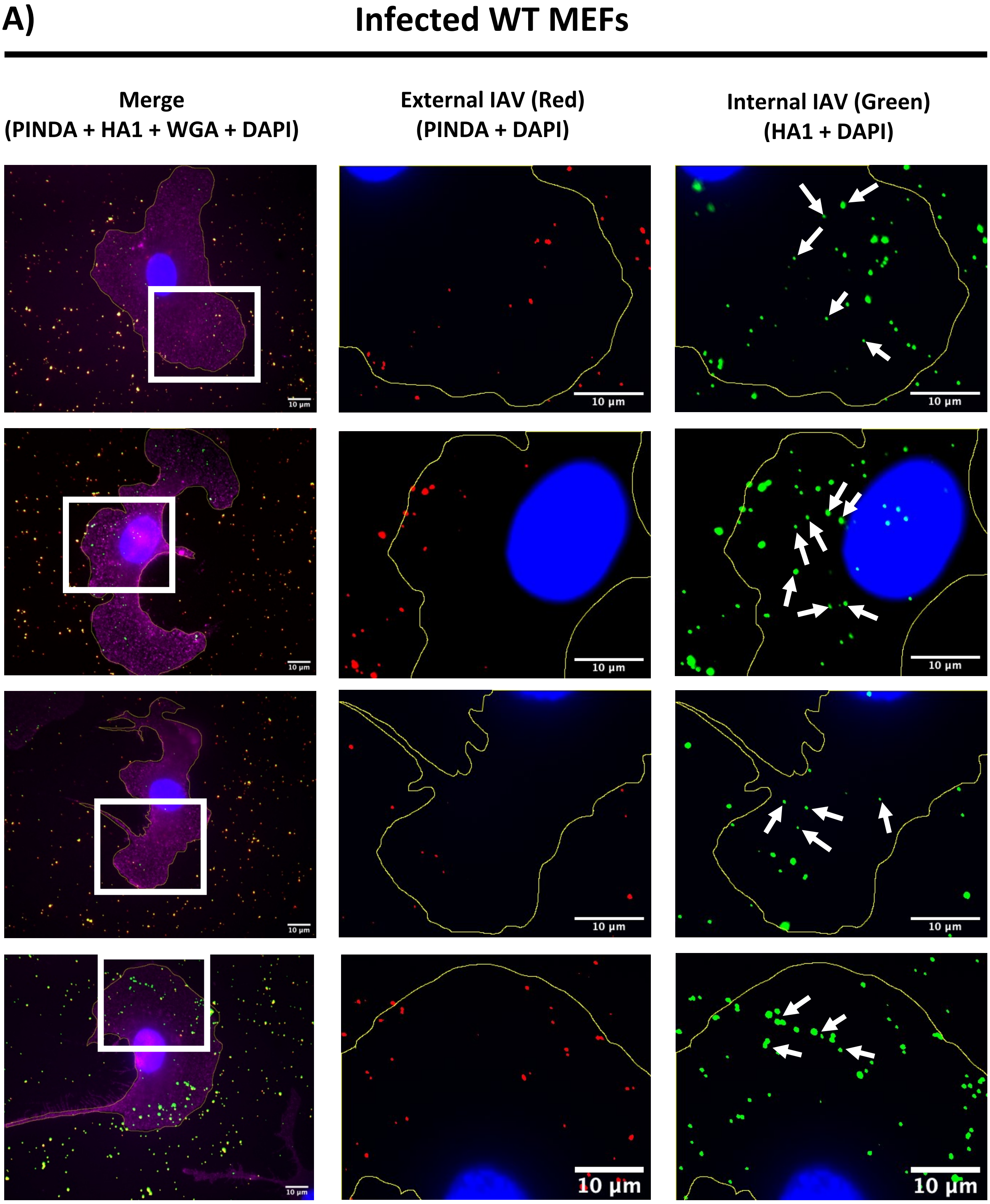
A)
Infected WT MEFs
Merge
(PINDA + HA1 + WGA + DAPI)
External IAV (Red)
(PINDA + DAPI)
Internal IAV (Green)
(HA1 + DAPI)
10 µm

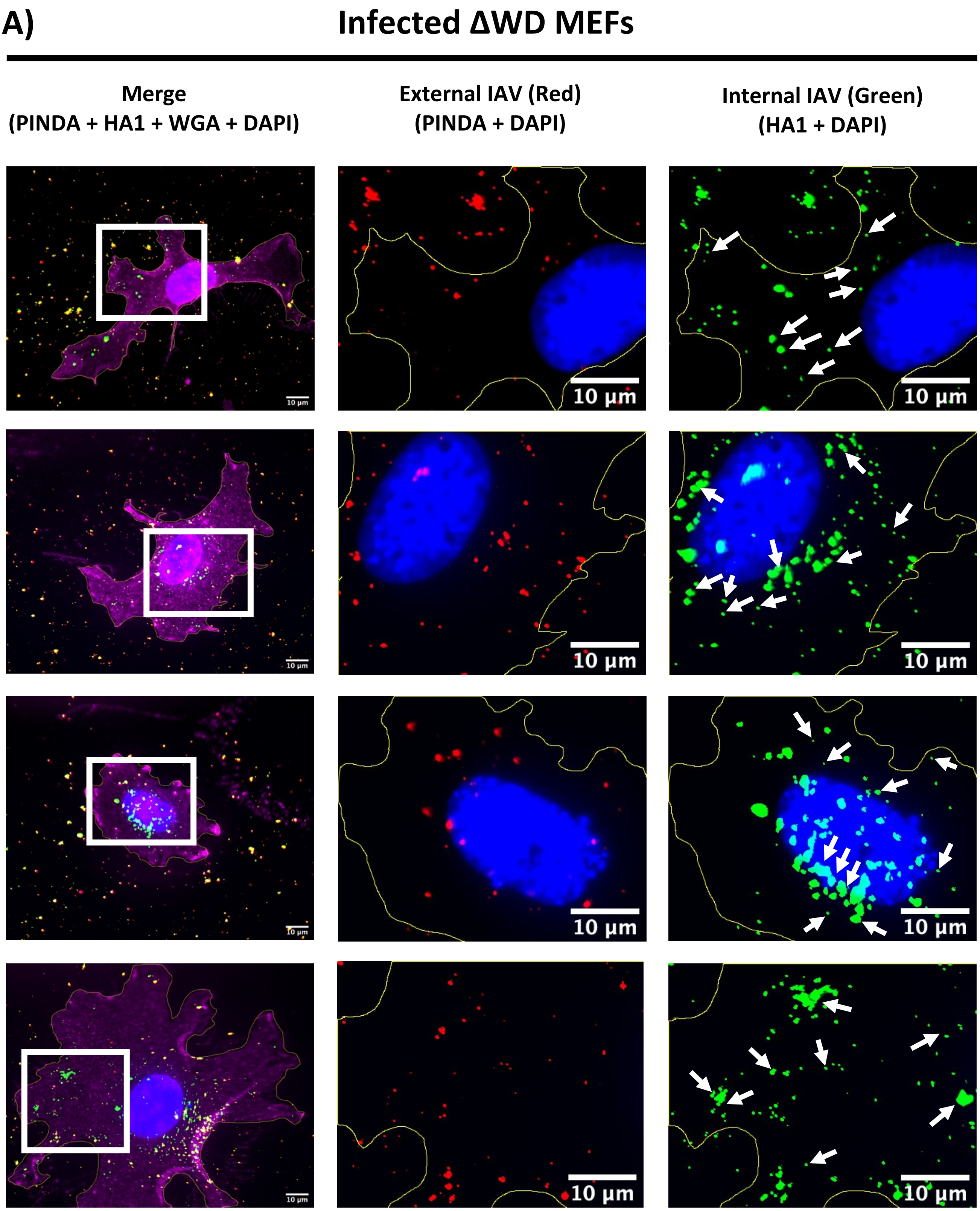
A)
Infected ΔWD MEFs
Merge
(PINDA + HA1 + WGA + DAPI)
External IAV (Red)
(PINDA + DAPI)
Internal IAV (Green)
(HA1 + DAPI)
10 µm

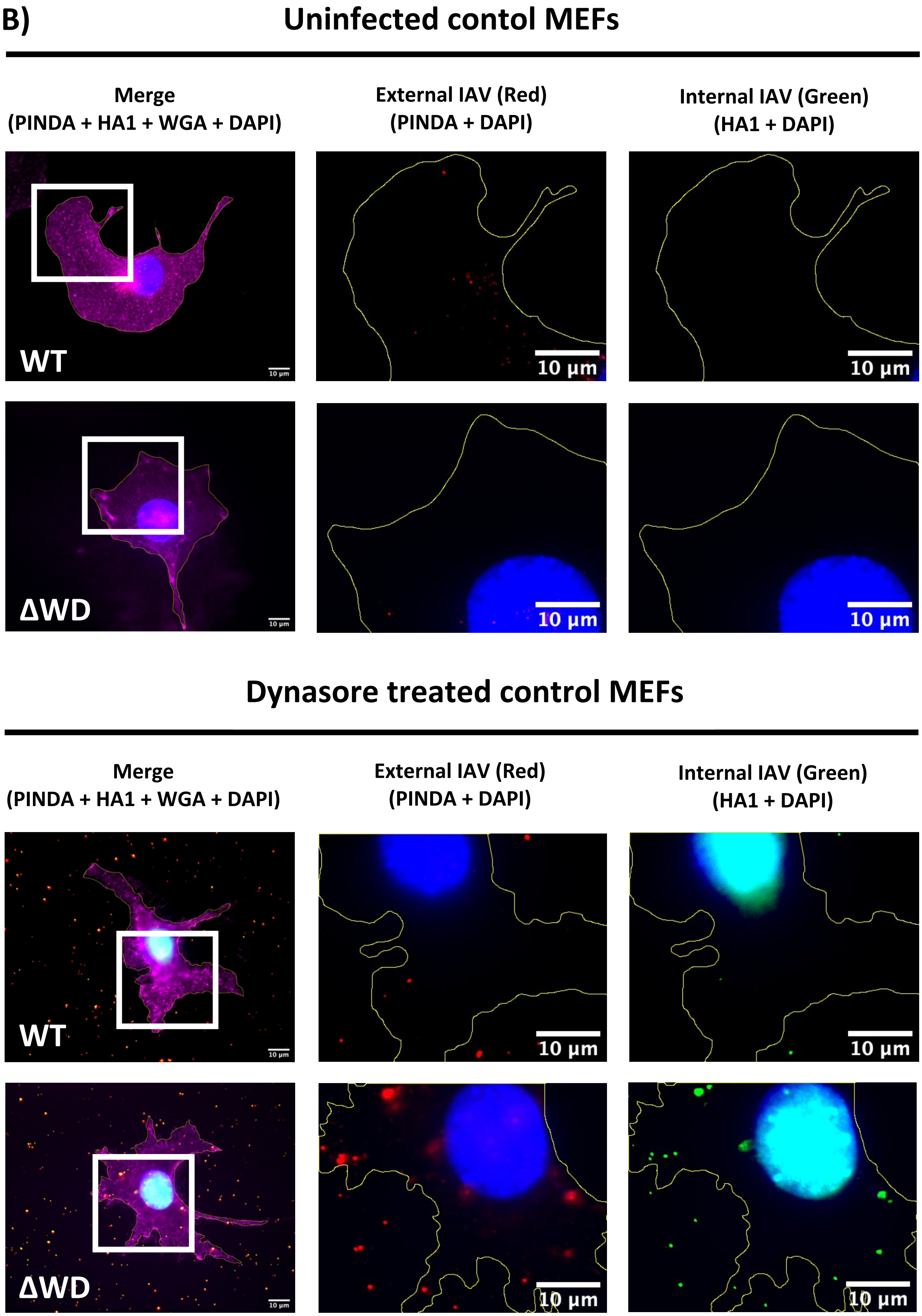
B)
Uninfected contol MEFs
Merge
(PINDA + HA1 + WGA + DAPI)
External IAV (Red)
(PINDA + DAPI)
Internal IAV (Green)
(HA1 + DAPI)
WT
10 µm
10 µm
10 µm
ΔWD
10 µm
10 µm
10 µm
Dynasore treated control MEFs
Merge
(PINDA + HA1 + WGA + DAPI)
External IAV (Red)
(PINDA + DAPI)
Internal IAV (Green)
(HA1 + DAPI)
WT
10 µm
10 µm
10 µm
ΔWD
10 µm
10 µm
10 µm

C)

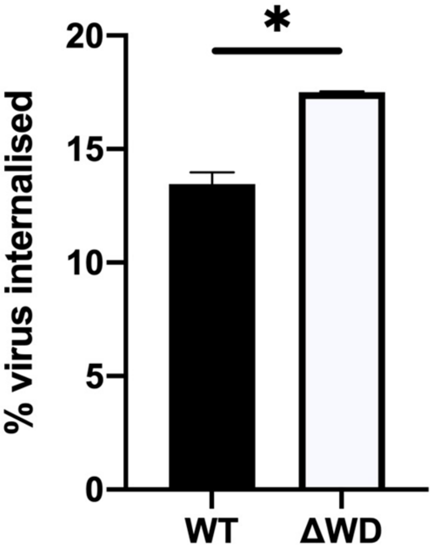

Figure 4.7: Increased endocytosis of IAV X31 in ΔWD MEFs compared with WT MEFs.

A) WT and ΔWD MEFs were infected with IAV X31 and incubated for 30 min before fixing and immunostaining external influenza haemagglutinin (HA) using the PINDA antibody. Cells were then permeabilised and fixed again and internal influenza HA were immunostained. Primary antibodies were then secondary Ab stained, PINDA with Alexa-Fluor 594 (red) and HA1 with Alexa-Fluor 488 (green). Cells were also stained with WGA647 and DAPI. Cells were visualised using a Zeiss M2 Imager on a x63 oil objective. Internalised virus can be seen as green puncta that do not co-localise to red external virus puncta. White arrows point to these internalised virus puncta.

B) Uninfected controls for WT and ΔWD MEFs were used to demonstrate the effectiveness of the assay at visualising virus. Dynasore controls were set up by pre-treating cells with Dynasore for 30 minutes and were used to demonstrate that the assay measures endocytosis.

C) The percentage of virus infecting a cell that are internalised is presented (+SEM). A Mann-Whitney U test was conducted: * = $p<0.05$ n=6 experiments of 50 cells.

4.3.5 Increased fusion of IAV in ∆WD MEFs compared with WT MEFs when measured by the fusion assay.

The fusion of IAV to the endosomal membrane during normal infection was investigated next. This was measured using a lipophilic dye called R18/SP-DiOC18 that emits a green signal when fusion occurs.

X31 was labelled with the lipophilic dyes: R18 (red) and SP-DiOC18 (green). Labelled X31 was bound to WT and ∆WD MEFs on ice for 60 minutes before internalising the virus at 37°C for 30 and 60 minute time points. Cells were then fixed and analysed via FACS. Cells with fusion events fluoresce green and side-scatter (SSC Y-axis) was plotted against the dequenching of SP-DiOC18 (X-axis) to visualise the infected population. Side scatter was plotted instead of forward scatter to identify cells based on internal complexity, side scatter height (SSC-H) being plotted to discriminate between single cells and doublets. R18 fluoresces red and would give an indication of infected cells, but this was not measured for this experiment as an uninfected control was used to demonstrate the results were due to infection. Gates were placed using the uninfected controls to see the shifts in populations. As can be seen in figure 4.8A, more cells were fluorescing green due to more dequenched SP-DiOC18 across both WT and ∆WD conditions and at both time points. This is seen by the increased amount of cells in the gate set-up in the uninfected controls. At the 30 minute time point, 41.4% of WT and 61.8% of ∆WD had a fusion event occurring within them, with a difference of 20.4%. At the 60 minute time point, the percentage of cells with fusion events increased to 60.4% in WT and 76.8% in ∆WD, with a difference of 16.4% between them. These differences are statistically significant (Figure 4.8C).

Bafilomycin A (BafA) controls were set-up to inhibit virus fusion. BafA inhibits vacuoloar-type H^+-ATPase, preventing the endosome from becoming acidified. With BafA, the percentage of cells with fusion events occurring was reduced, with an average of 17.9% in WT and 11.32% in ∆WD (Figure 4.8B). BafA did not entirely stop fusion with fusion levels not being as low as the uninfected control. This could be due the BafA stocks themselves possibly being poor quality.

The population count (Y-axis) was plotted against the dequenching SP-DiOC18 (X-axis), the resulting histograms were used to determine the median fluorescence intensity (MFI) of the two cell lines. Figure 4.8D presents these findings, with ΔWD having a higher MFI compared with WT. This corresponds to more fusion events occurring in each cell in ΔWD MEFs. This increase in IAV fusion in ΔWD MEFs suggests that IAV escapes the endosome more efficiently in WD deficient cells, which supports the acid bypass experiments shown earlier in this chapter.

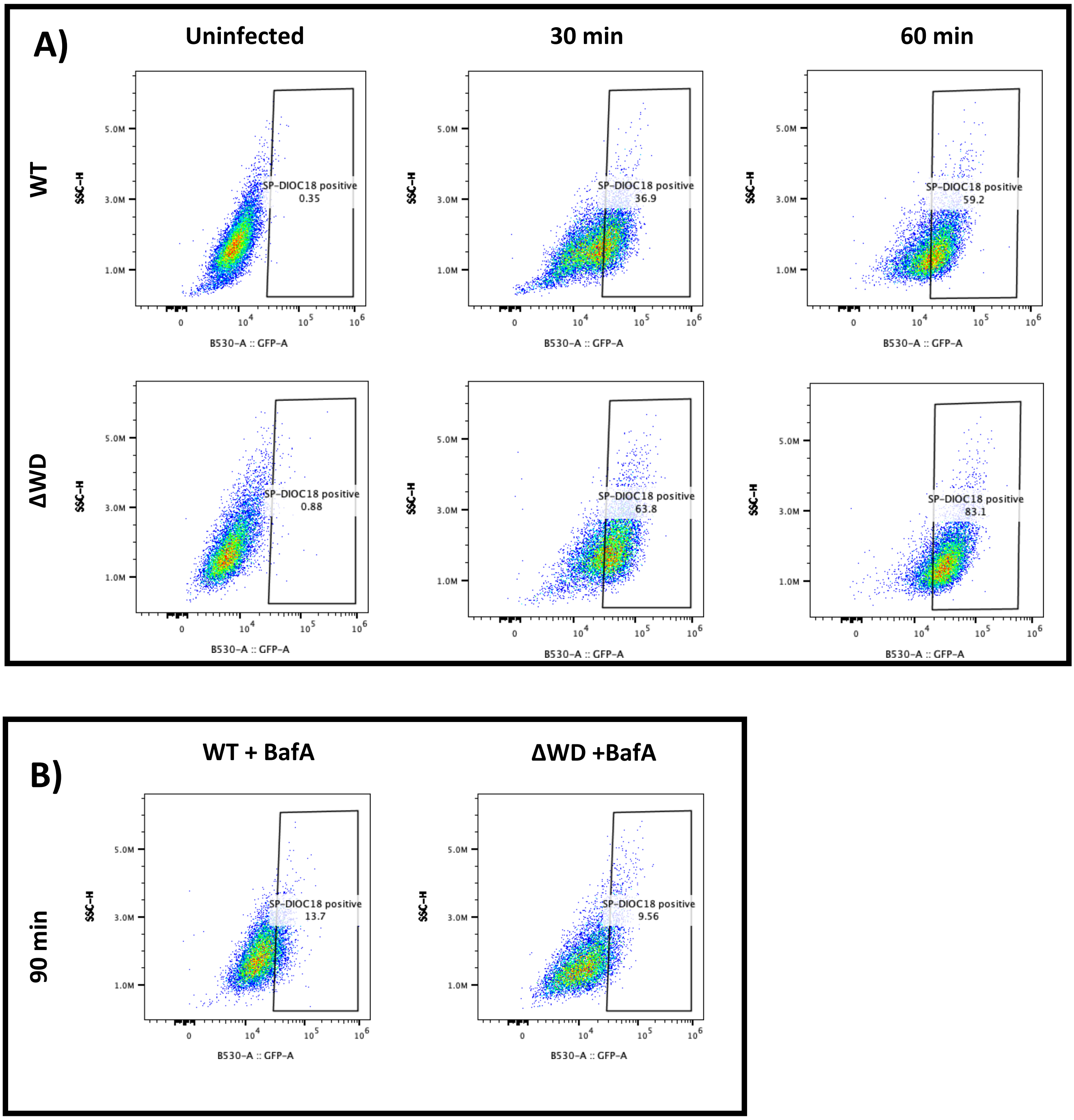

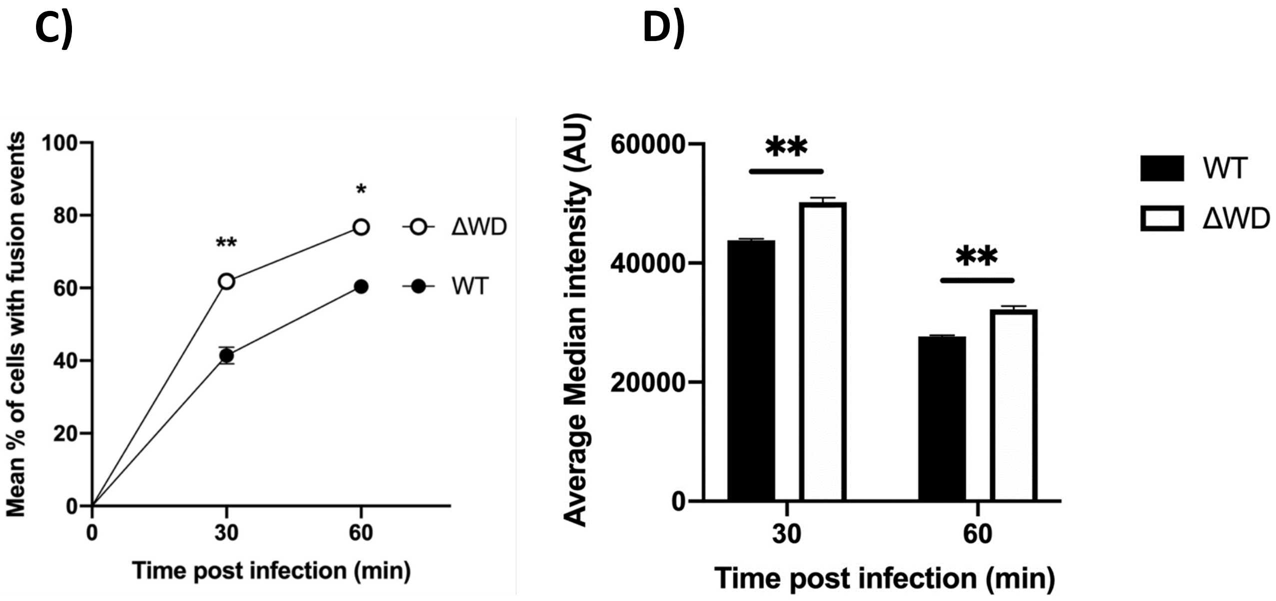

Figure 4.8: Increased fusion of IAV X31 was measured by fluorescence-activated cell sorting (FACs) in ΔWD MEFs at 30 and 60 min post infection. [1]

A) WT and ΔWD MEFs were infected with X31 labelled with a lipophilic dye that fluoresces green when viral-endosomal fusion occurs. FACs was used to measure the side scatter fluorescence of the cells and the number of cells that fluoresce green. Cells were either not infected, or infected for 30 and 60 min. FACs graphs present the increasing population of cells that fluoresce green.

B) WT and ΔWD MEFs were pre-treated with the fusion inhibitor bafilomycin A (50 nM) and then infected for 90 min before a fusion assay was carried out.

C) The mean average percentage (%) of WT and ΔWD cells with fusion events is presented for the 30 and 60 min time points (±SEM). An independent samples t-test was conducted: * = $p<0.05$ ** = $p<0.005$ n=3 experimental replicates.

D) The average median intensity of the WT and ΔWD cell fluorescence is presented for the 30 and 60 min time points (+SEM). An independent samples t-test was conducted: ** = $p<0.005$ n=3 experimental replicates.

---

[1] Data published in Figure 6 of Wang *et al.* (2021) (Appendix 1).

4.3.6 Increased IAV NP expression in ΔWD MEFs compared with WT MEFs.

Figure 4.7 and 4.8 both suggest that IAV is able to enter cells more efficiently and access the cytoplasm more efficiently. To provide further evidence towards this increased entry of IAV, I monitored IAV NP expression at the nucleus.

WT and ΔWD MEFs were infected with IAV PR8, with a bind warm-up of 60 minutes followed by an infection time course of 5 hours. Coverslips were fixed at 2, 3, 4 and 5 hours post infection and stained with an anti-NP antibody. An Alexa Fluor 488 antibody was used to view this (Figure 4.9A). The corrected total nuclear fluorescence (CTNF) was determined from the fluorescence of the nuclei corrected against the auto-fluorescence of the cell and the nuclei (Figure 4.9B). At 2 and 3 hours post infection the CTNF was higher in the ΔWD MEFs compared with the WT MEFs. For the 2 hour time point, the difference was very clear, with the WT MEF average CTNF no different to the uninfected controls, with the ΔWD MEF average CTNF being 4064.4. For the 3 hour time point, the ΔWD MEF’s average CTNF was 45.2% higher than the WT CTNF, with the values being 10405.3 and 7161.9 respectively. At 4 hours post infection, the WT average CTNF was 51.8% higher than the ΔWD MEF average CTNF, with their values being 5863.7 and 2824.9 respectfully. At 5 hours post infection both values were not statistically significant from one another. This data implies that IAV NP is translated and accumulates at the nucleus for vRNP production sooner in ΔWD MEFs compared to WT MEFs due to the increased CTNF at earlier time points. At 4 hpi there was more IAV NP in the WT nuclei than ΔWD nuclei however; with similar amounts of NP being present in both cell lines’ nuclei at 5 hpi. This data supports the data in figures 4.7 and 4.8 which show that IAV is able to enter ΔWD MEFs at earlier time points compared with WT MEFs.

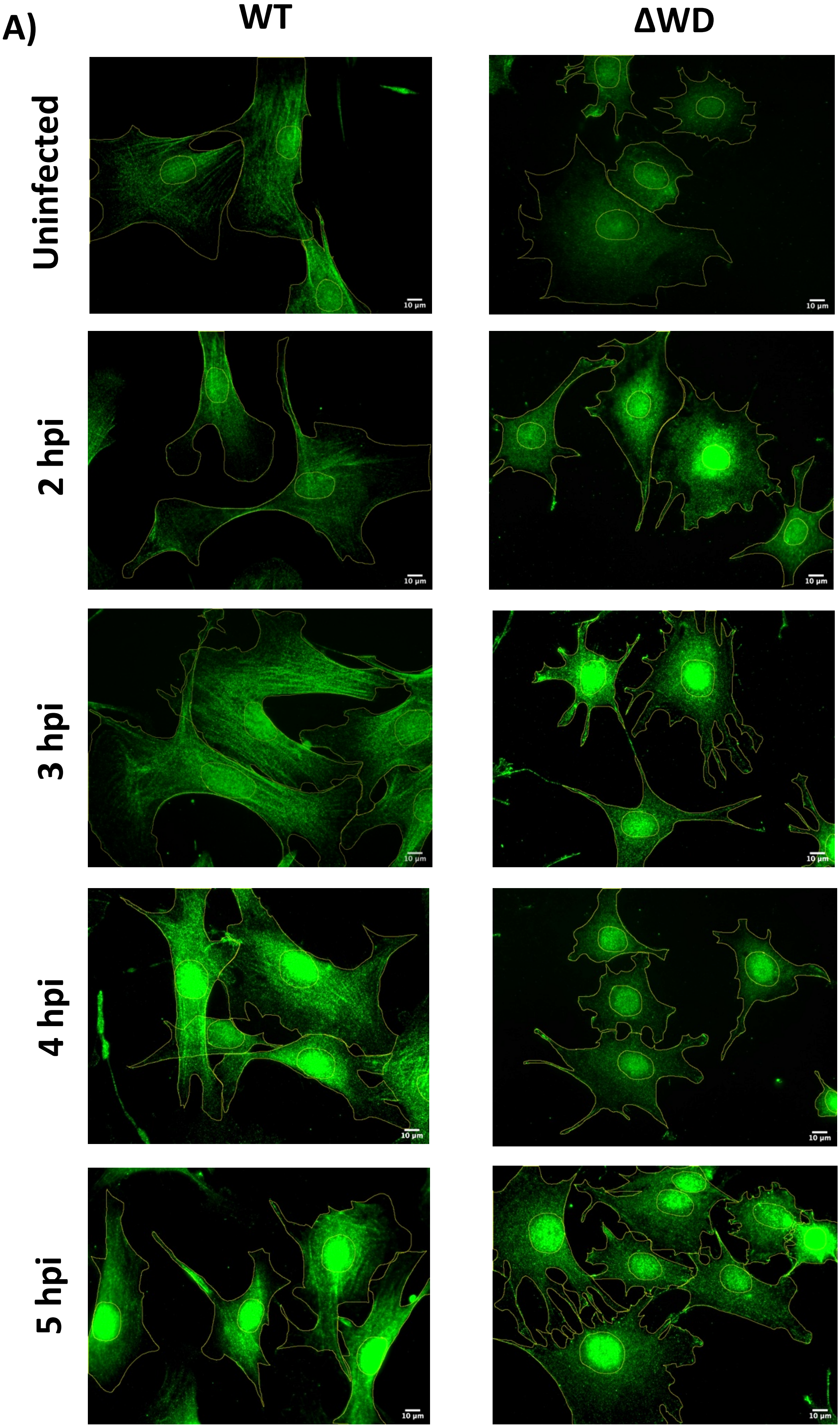
A)
WT
ΔWD
Uninfected
2 hpi
3 hpi
4 hpi
5 hpi
10 µm

B)

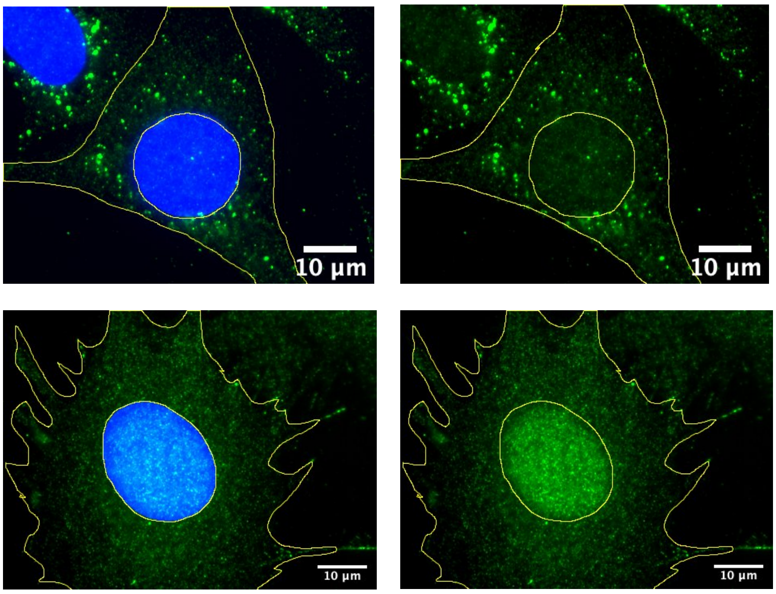

Negative NP nuclei co-localisation.
488 nm corrected total nuclear fluorescence: 327.7

Positive NP nuclei co-localisation.
488 nm corrected total nuclear fluorescence: 14698.7

Figure 4.9: Increased IAV PR8 NP expression in ΔWD MEFs at 2 and 3 hours post infection.

A) WT and ΔWD MEFs were infected with PR8 for a time course with end points of 2, 3, 4 and 5 hours post infection. Cells were stained with an anti-NP antibody and stained with an Alexa Fluor 488 antibody. Cells were also stained with DAPI and WGA647. Cells were visualised using an Zeiss M2 imager. Cell outlines and nuclei outlines are shown for microscopy images.

B) The average corrected total nuclei fluorescence was determined for all nuclei and presented (+SEM). A Mann-Whitney U test was conducted: ** = $p<0.005$ *** = $p<0.001$ n=53; three coverslips.

4.4 Discussion

The previous chapter showed that cholesterol homeostasis is altered in cells lacking the WD domain. Cholesterol accumulates in late endosomes and lysosomes in ΔWD MEFs with a reduction of cholesterol in the ΔWD plasma membrane (PM). The work in this chapter aimed at determining whether IAV enters ΔWD MEFs due to this cholesterol reduction at the PM.

IAV enters the cell via endocytosis at the PM, therefore the IAV-containing endosome membrane would have a similar constitution to the PM (106). ΔWD MEFs possess less cholesterol in their PMs. The experiments here have shown that this has an effect on the fusion of the virus. Fusion of IAV was forced at the PM through a process known as acid bypass. Firstly, the IFN response to incoming vRNP was assessed using qPCR, with increased IFN signalling following IAV fusion at the plasma membrane in ΔWD MEFs (Figure 4.4). This suggested that more IAV is able to enter ΔWD MEFs through fusion. This was followed up by monitoring viral nucleoprotein in cells infected with IAV by acid bypass. An increased frequency of IAV NP was seen in ΔWD MEFs compared with WT MEFs over a 50 minute time course (Figure 4.5). This suggests that IAV fuses more efficiently with ΔWD MEF PMs due to the reduced cholesterol within the membrane. This was further investigated by modulating the cholesterol within the PM using three drug treatments: U18666A (which inhibits the NPC1 cholesterol transporter resulting in less cholesterol reaching the PM), cholesterol and 25HC (Figure 4.6). There was an increased frequency of NP in WT and ΔWD MEFs treated with U18666A, which shows that reducing membrane cholesterol promotes IAV fusion. Cholesterol supplementation reduced NP in ΔWD MEFs. Interestingly, 25HC reduced NP in both WT and ΔWD MEFs, which supports its antiviral role in membranes. Overall, this demonstrates that reducing cholesterol at the PM promotes viral fusion. Supplementing ΔWD MEFs with cholesterol reduces the amount of IAV NP that enters cells, demonstrating that cholesterol has an antiviral role and suppresses fusion.

Three assays were then used to measure the entry of IAV during its normal infection cycle: an endocytosis assay, a fusion assay and a nuclear entry assay. Both the endocytosis and fusion assay measure how well the virus enters the cell. More internalised virus after 30 minutes indicates more endocytosis of the virus in those cells. More cells fluorescing green indicates more IAV fusion events in that cell population. As can be seen in figure 4.7, more IAV was internalised by endocytosis in ∆WD MEFs compared with WT MEFs. This difference is small however, but significant. Figure 4.8 presented the fusion assay results, with more IAV fusion events in ∆WD MEFs at 30 and 60 minutes compared with WT MEFs. More IAV is therefore able to enter the cytoplasm in ∆WD MEFs. Both of these assays are supported by the nuclear entry assay, which found that more reached the nuclei of ∆WD MEFs than WT MEFs (Figure 4.9), which occurs if the virus was able to access the cytoplasm more efficiently beforehand.

∆WD MEFs possess less cholesterol in their PMs. Cholesterol accumulates in the late endosomes and lysosomes of ∆WD MEFs, with these organelles being enlarged in ∆WD MEFs. These experiments show that IAV fusion is enhanced with PMs possessing reduced cholesterol levels. Reducing cholesterol in WT plasma membranes through drug treatment increases IAV fusion with it, suggesting that cholesterol levels in host cell membranes affect IAV fusion. The data from this chapter begin to provide a mechanism as to why the ∆WD mouse is more susceptible to IAV, with IAV replicating to higher levels within the E230 mouse (79). IAV enters ∆WD cells more efficiently than WT cells, with more entering via endocytosis and fusion in ∆WD. This increased fusion is explained through the difference in cholesterol within the membrane. The membrane composition of the IAV-containing endosome is similar to the plasma membrane composition due to it being derived from it. In ∆WD MEFs this membrane would therefore have reduced cholesterol levels. This chapter demonstrates that IAV is able to fuse more efficiently in ∆WD MEFs which could be due to this biochemical reason.

Unlike with fusion, the cholesterol content of the plasma membrane is unlikely to be the explanation behind the endocytosis assay results seen in figure 4.3. Cholesterol removal by methyl-β-cyclodextrin has not been shown to affect the endocytosis of IAV (104). ATG16L1 has been shown to interact with heavy-chain clathrin (82); however this interaction is thought to occur between the N-terminus of the protein and clathrin, far upstream of the C-terminal WD domain which appears to inhibit endocytosis of influenza.

To summarise the findings of this chapter, the WD domain has a role in suppressing viral entry. The WD domain is responsible for cholesterol transportation to the PM, through a mechanism which could be lysosomal exocytosis. In cells lacking the WD domain, PM cholesterol is reduced. IAV was shown to fuse more efficiently to PMs with reduced cholesterol and as the endosome originates from the plasma membrane, fusion in the endosome may well be enhanced. Indeed when entry by fusion was investigated, there was increased fusion in the endosome in ΔWD cells. As well as that I saw increased endocytosis of IAV and increased migration of IAV NP to the nucleus.

However, the inability of ΔWD MEFs to undergo LAP/LANDO and destroy the virus upon entry may explain the increased amount of fusion seen. My experiments show that it is more likely the decreased endosomal membrane cholesterol levels enhance fusion and entry of IAV. ΔWD mice suffer lethal cytokine storms, with IAV replicating to higher titres in mice lacking the WD domain (78). In the next chapter I investigated whether this reduction in membrane cholesterol and increased viral entry cause elevated IFN/cytokine or increased IAV replication.

CHAPTER 5

The WD domain attenuates IAV replication and cytokine signalling

5.1 Introduction

The previous chapters have demonstrated that the WD domain of ATG16L1 has a role in cholesterol homeostasis and suppressing IAV entry. It is thought that the WD domain of ATG16L1 is needed to facilitate lysosomal fusion to the plasma membrane, to deposit cholesterol into the plasma membrane (84). The previous chapters have shown that when the WD domain is absent, cholesterol is retained in late endosomes and lysosomes and there is reduced cholesterol in the plasma membrane. Less cholesterol present in the plasma membrane also results in less cholesterol in the endosomal membrane, which then promotes viral entry by fusion. Indeed, increased fusion of IAV, as well as increased endocytosis and increased migration to the nucleus has been observed in WD deficient MEFs.

Our lab showed that deletion of the WD domain results in increased susceptibility to IAV (78). IAV infected ΔWD mice presented elevated cytokine levels, increased infiltration of the lungs with neutrophils, decreased weight, increased IAV replication and death. In this chapter I investigated whether increased IAV replication and cytokine storm could be reconstituted *in vitro* and *ex vivo*. Viral replication was measured by $TCID_{50}$ and plaque assay of viral supernatants from infected cells MEFs and from precision cut lung slices. Precision cut lung slices provide an opportunity to assess the role of the WD domain in suppressing viral replication in a functional 3D organ model. Lung slices include the diverse population of cells in the lungs, including resident macrophages (320). I investigated whether infection of precision cut lung slices from ΔWD mice resulted in greater IAV replication.

The host innate immune defence determines the severity of disease. Complications with IAV in humans and mice generally result from a breakdown in innate immune homeostasis, which leads to cytokine storms. A cytokine storm is a term used to describe severe immune dysregulation which is characterised by systemic inflammation and multiple organ damage and dysfunction, resulting in a poor prognosis (251,336). Another characteristic is elevated inflammatory cytokine levels, such as interleukin-6, type I IFNs (such as IFNβ) and type III IFNs. The expression of IFNβ leads to the expression of hundreds of antiviral interferon-stimulated genes (ISGs), including IFIT1 and ISG15.

ISG15 is a ubiquitin-like protein that is rapidly produced following interferon expression (337,338). Interferon activates the JAK STAT signalling pathway following binding to Interferon alpha and beta receptor 2 (IFNAR2). This leads to subsequent phosphorylation of IRF9 that upregulates ISG15 expression. Following translation of ISG15, the protein is conjugated to the target protein via a three step enzymatic cascade that involves E1, E2 and E3 enzymes, as ubiquitination does. This results in ISG15 conjugation (ISGylation). ISG15 also exists as an unconjugated protein that can regulate viral replication and host responses through both non-covalent protein interactions and its action as a cytokine. *In vivo* study in mice lacking *isg15* have found that they are more susceptible to IAV, Sindbis virus and herpes virus (339); with a further study demonstrating that the Influenza B virus could replicate better in mice lacking the ISG15 E1 enzyme (340). Evidence indicates that ISGylation targets newly synthesised viral proteins, which suggests it may interfere with the activity of those proteins (341).

IFIT1 (previously known as ISG56) belongs to the IFIT family of antiviral cytokine proteins, all of which inhibit viral replication through their shared recognition of certain RNAs. How this RNA recognition inhibits viral replication is poorly understood however. IFIT1 possesses another characterised antiviral function: to inhibit eIF3. Eukaryotic translation factor 3 (eIF3) contributes to successful protein translation based on its roles in keeping the 40S and 60S subunits apart and maintaining the fidelity of start codon selection (342). IFIT1 binds to eIF3, inhibiting translation initiation, subsequently inhibiting viral replication in the cell (343). Additionally, IFIT1 has been shown to bind to the 5' triphosphate of viral RNA, a biochemical feature found on the transcripts of IAV (344).

This chapter aimed to compare the replication of the virus and cytokine expression and potential for cytokine storms in ∆WD cell lines and in ∆WD precision cut lung slices. Since more IAV enters by endocytosis and accesses the cytoplasm in ∆WD cells, this should lead to greater activation of toll-like receptors such as TLR3 in the endosome, as well as Rig-I in the cytoplasm. A greater activation would lead to increased cytokine levels, such as IFNβ, with the interferon stimulated genes IFIT1 and ISG15 being then upregulated. These could then be measured.

5.2 Aims

The previous chapters have demonstrated that the WD domain has a role in the transport of cholesterol to the plasma membrane. This results in IAV being able to more efficiently enter cells by fusion. This chapter aims to investigate the effects of this increased entry, namely the replication of IAV and the cytokine levels of WD deficient cells.

- To Investigate the role of the WD domain in suppressing viral replication and cytokine storms in MEFs and a 3D lung organ model.
  - By titrating IAV secreted from MEFs and lung slices by $TCID_{50}$, qPCR and plaque assay.
  - By measuring IFN and ISG expression by qPCR.
  - By inhibiting IFN signal transduction through TLR3 inhibition.
  - By inhibiting IFN signal transduction through Rig-I knock out.

5.3 Results

5.3.1 Increased IAV replication in ∆WD MEFs compared with WT MEFs*.*

WT and ∆WD MEFs were infected with IAV PR8 (MOI: 0.1) for 48 hpi. The cell media was collected and used to infect MDCK indicator cells. Supernatants were titrated by serial dilution from 10^{-1} to 10^{-5} before infecting MDCK cells seeded in a 6-well plate (Figure 5.1). The virus was detected by immunostaining for nucleoprotein (NP) with an anti-NP and visualised with secondary antibody labelled with Alexa Fluor 488. The $TCID_{50}$ was calculated as the end point dilution at which 50% of the cells were infected. The $TCID_{50}$ was calculated by the Spearman-Karber method. For WT MEFs the mean average titre was 5.4×10^5 $TCID_{50}$/mL. For ∆WD MEFs the mean average titre was 3.04×10^6 $TCID_{50}$/mL. The viral titre of supernatants collected from ∆WD MEFs was higher than WT supernatants. Approximately, six times more IAV was secreted from ∆WD MEFs than WT MEFs, as can be seen figure 5.1.

Two different IAV isolates (PR8 and X31) were used to quantify virus secretion over a 72 hour time course (MOI: 0.1). Supernatants from WT and mutant MEFs were collected at 24, 48 and 72 hpi and quantified using a plaque assay. For IAV PR8, there was significantly more virus secreted from ∆WD MEFs, with more PR8 secreted at 24, 48 and 72 hpi (Figure 5.2 PR8). For IAV X31 (Figure 5.2 X31), more virus was secreted from WT MEFs than from ∆WD MEFs at 24 hpi, and similar amounts for both cell types secreted at 48 hpi between WT and ∆WD MEFs. Significantly more IAV X31 was secreted from ∆WD MEFs at 72 hpi compared with WT however this difference is small compared with the increased replication of PR8 in ∆WD MEFs and the result not as definite (Figure 5.3). These results show differences in replication or host responses between the two IAV strains. In ∆WD MEFs the PR8 strain replicated more efficiently over all time points by a considerable amount, whereas X31 only weakly increased from ∆WD MEFs at 72 hpi.

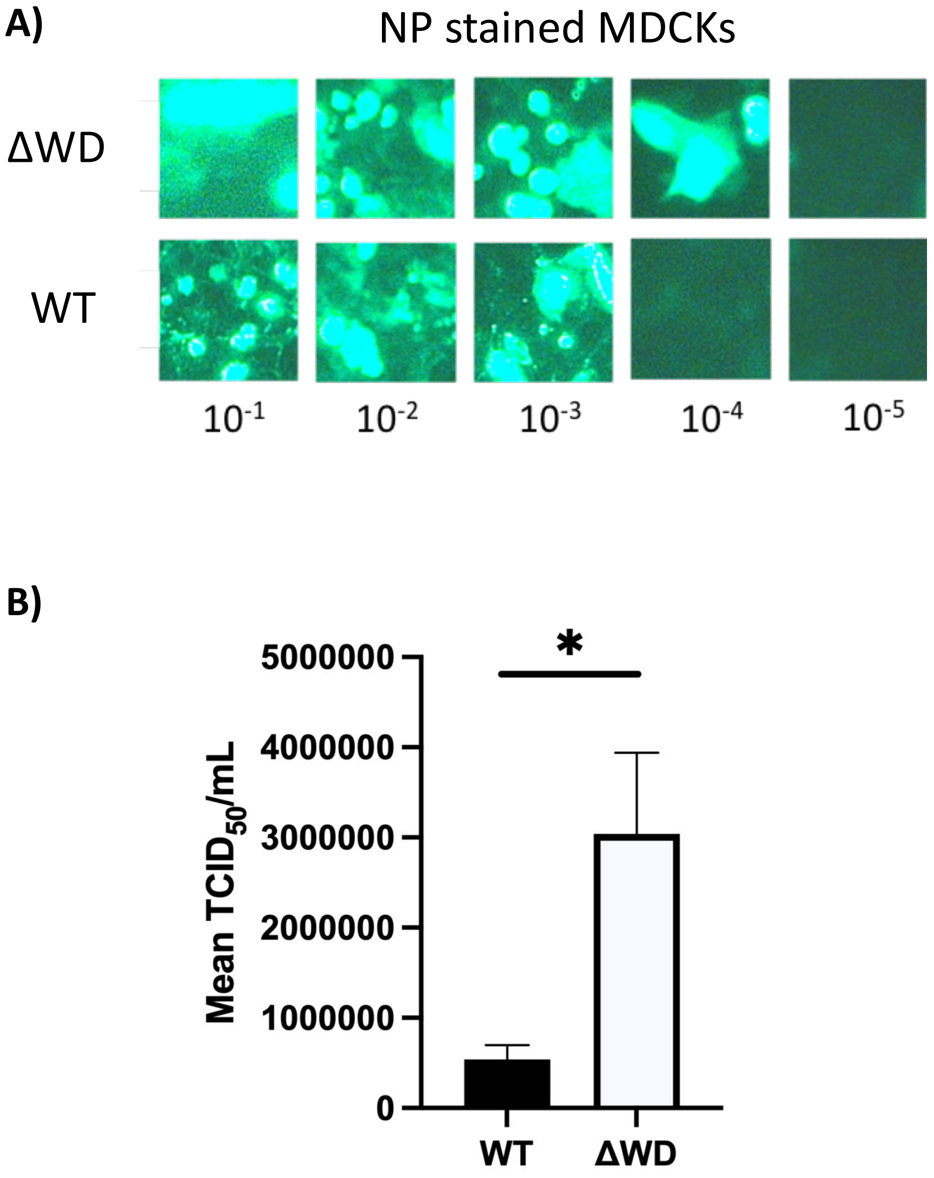

Figure: 5.1: Increased secretion of IAV PR8 from ΔWD MEFs compared with WT MEFs at 48 hpi.

A) WT and ΔWD MEFs were infected and incubated with IAV PR8 for 48 hours before supernatants were harvested. Supernatants were titrated by serial dilution on MDCK cells from 10^{-1} to 10^{-5} using the $TCID_{50}$ assay. MDCKs were stained using an anti-NP antibody and stained with Alexa 488.

B) Mean $TCID_{50}$ virus titres for IAV PR8 secreted from WT and ΔWD MEFs were determined using the Spearman Kärber calculation (+SD) (see methods). An Independent samples t-test was conducted: * = $p<0.05$ n=3 technical replicates.

PR8

A)

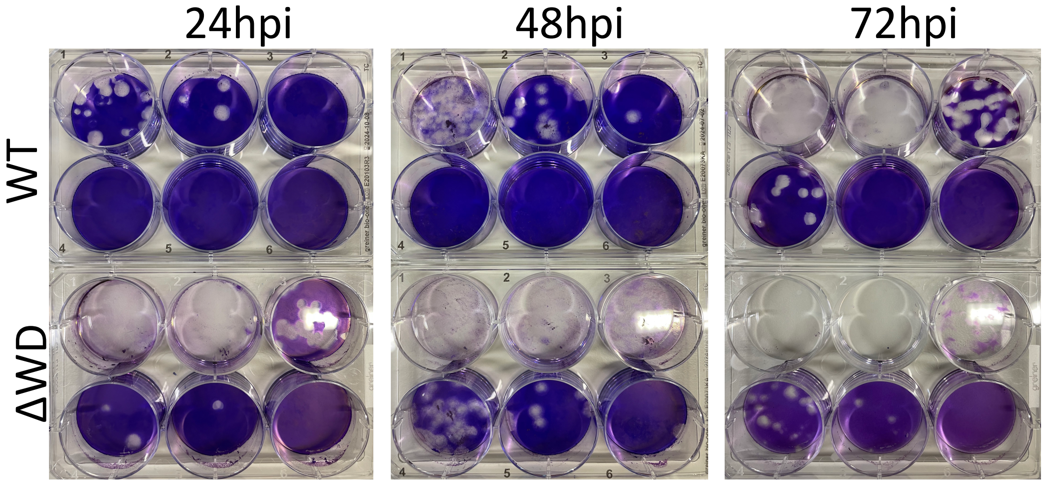
24hpi
48hpi
72hpi
WT
ΔWD

B)

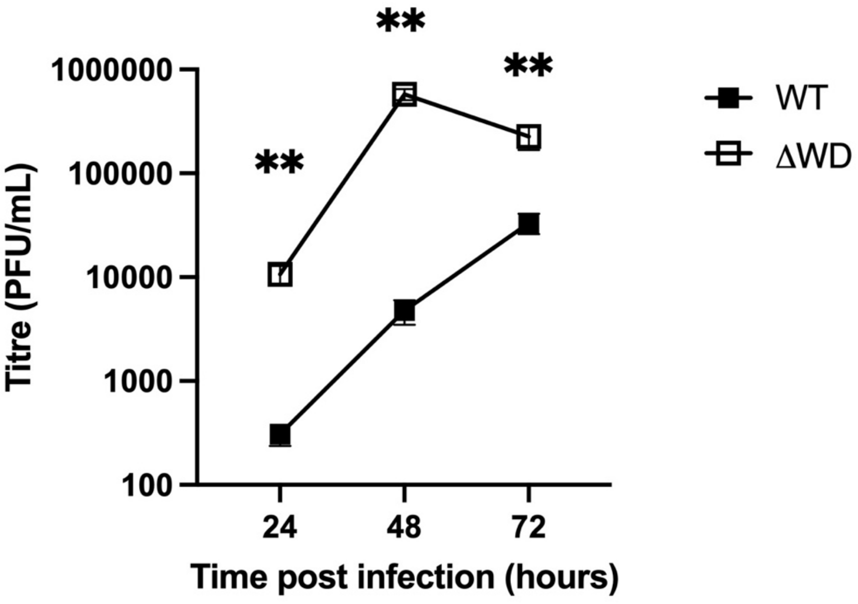
**
**
**
1000000
100000
10000
1000
100
Titre (PFU/mL)
24
48
72
Time post infection (hours)
WT
ΔWD

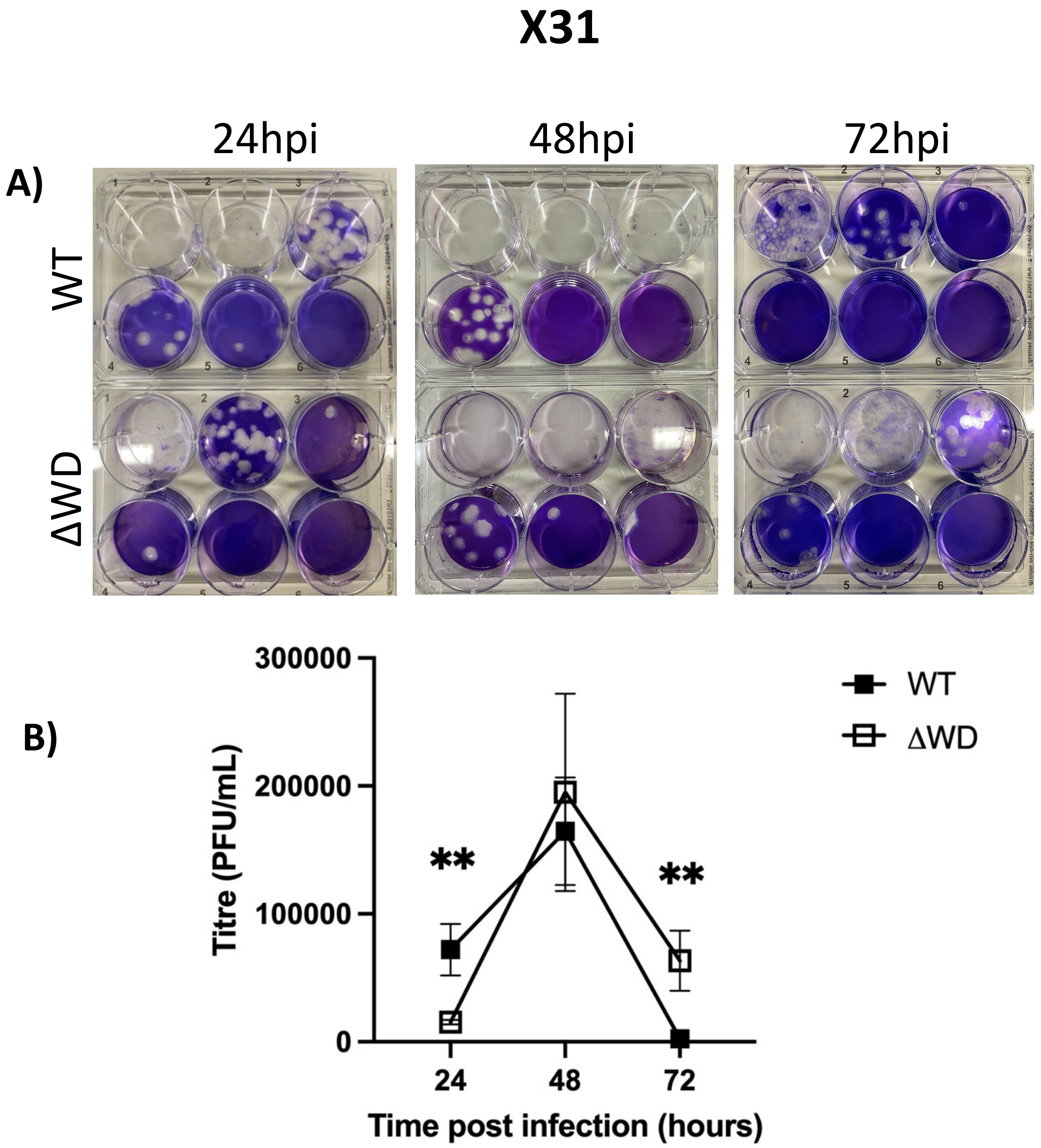

Figure 5.2: Increased IAV PR8 was detected by plaque assay in ∆WD MEF compared to WT supernatants at 24, 48 and 72 hpi. Increased IAV X31 was detected by plaque assay in ∆WD MEF supernatants at 72 hpi.

A) WT and ∆WD MEFs were infected and incubated with IAV PR8 or X31 for 24, 48 and 72 hours after which supernatants were harvested and titrated on MDCK cells. Serial dilutions of plaques from 10^{-1} to 10^{-6} were stained with crystal violet. The PFU/mL was determined by counting plaques in the lowest dilution plaques were present in.

B) The plaque number was used to calculate a virus concentration (PFU/mL), average concentrations are presented (+SEM). A Mann Whitney U test was conducted: ** = $p<0.005$ n=6 experimental replicates.

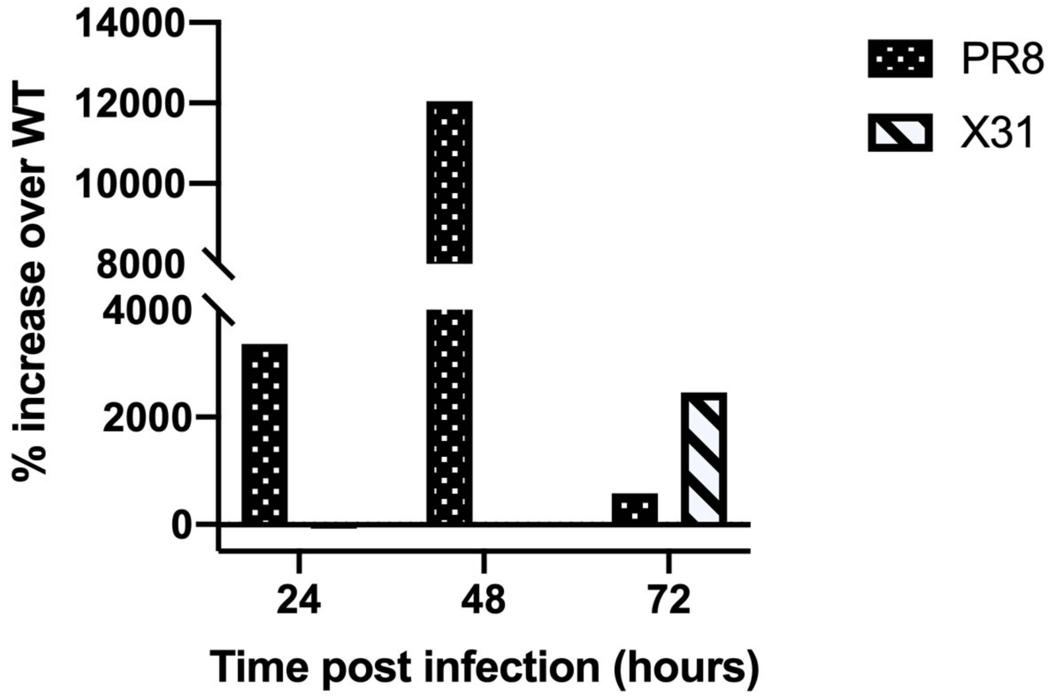

Figure 5.3: Increased IAV PR8 secretion peaks at 48 hpi in ∆WD MEFs whereas IAV X31 secretion increased at 72 hpi. The percentage increase shown is percentage (%) ∆WD PR8 and X31 plaque assay titres over WT.

5.3.2 Decreased IAV X31 M2 RNA whereas increased IAV PR8 M2 RNA in ATG16L1 ΔWD MEFs at early times in infection.

WT and ΔWD MEFs were seeded and infected with X31 and PR8 at an MOI of 2 for 4, 6, 8 and 12 hours. RNA was extracted and analysed by qPCR using IAV primers complimentary to the M2 gene of H1N1 (Table 2.5). Decreased IAV X31 M2 gene RNA was detected in ΔWD MEFs compared to WT MEFs across all time points with significantly more at 6 and 12 hours (Figure 5.4 A). In contrast, more IAV PR8 M2 gene RNA was seen in ΔWD MEFs compared with WT MEFs, with significantly more at 8 and 12 hpi (Figure 5.4 B). These results show increased IAV PR8 M2 RNA in ΔWD MEFs at 12 hpi, which support the plaque assay results that show increased PR8 replication in ΔWD MEFs. For IAV X31, the qPCR results confirm the plaque assay results that there was less virus produced from ΔWD MEFs before 48 hpi.

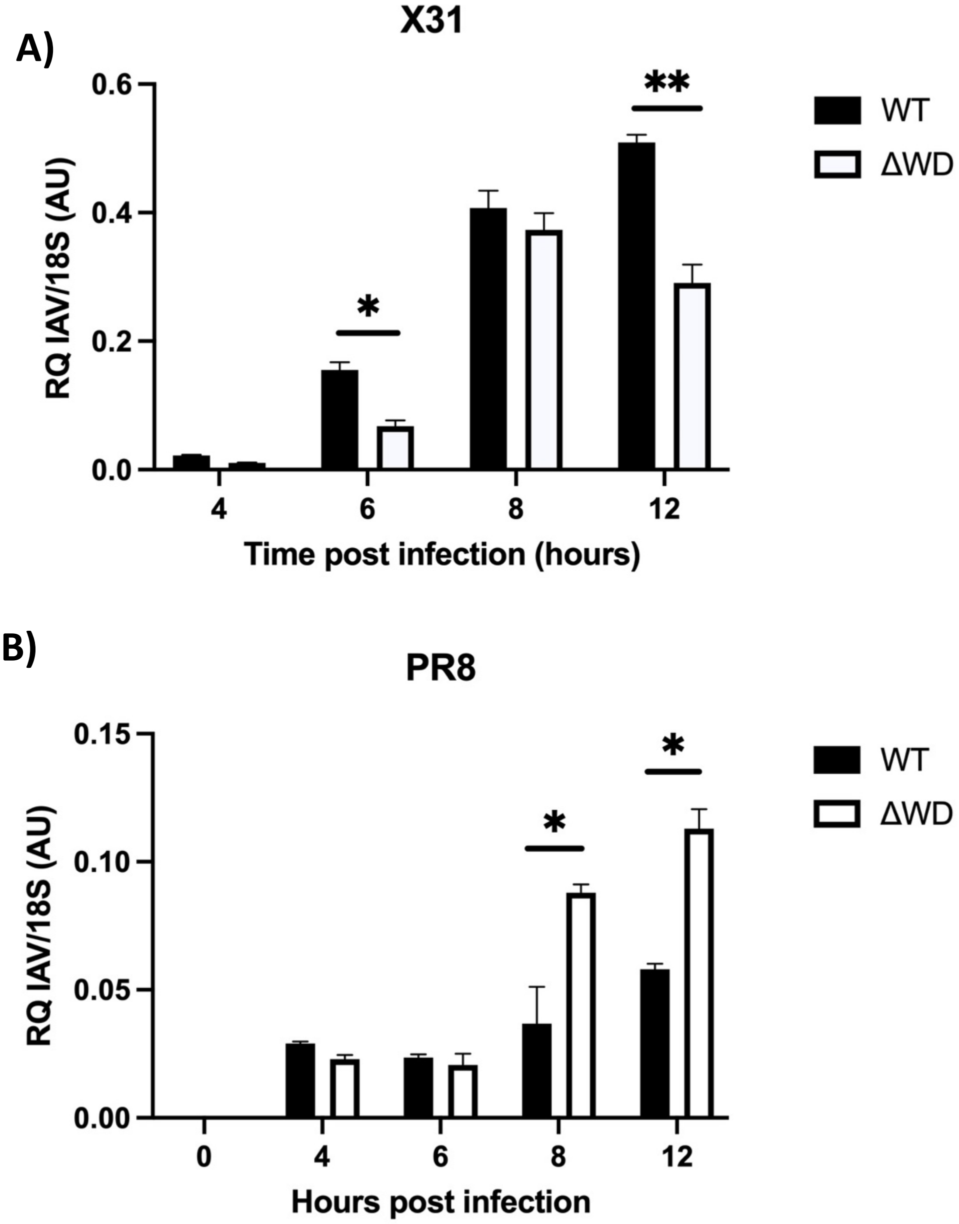

Figure 5.4: Decreased IAV X31 but increased IAV PR8 M2 RNA in ΔWD MEF lysates compared with WT MEF lysates. WT and ΔWD MEFs were infected with X31 (A) or PR8 (B) and incubated for 4, 6, 8 and 12 hours before lysing and isolating the RNA. IAV M2 gene RNA was quantified by qPCR, normalised to 18S, and (+SD). An independent samples t-test was conducted: * = $p<0.05$ ** = $p<0.005$ n=3 technical replicates.

5.3.3 Ex vivo lung explants show increased IAV X31 replication in ΔWD lung tissue compared to WT lung slices.

With Figures 5.1-5.4 suggesting increased IAV replication in ΔWD MEFs although this is strain-dependent, I investigated viral replication in a 3D organ model. I generated precision cut lung slices from WT and ΔWD mice. Slices contain diverse populations of cells therefore IAV replication would be representative of replication in epithelial and other cell types eg: fibroblasts, vascular cells and resident alveolar macrophages. WT and ΔWD lung slices were cultured and infected with IAV X31 (5×10^4 particles per slice) for 24, 48 and 72 hours with TPCK-treated trypsin. Supernatants were harvested and titrated by plaque assay to quantify the viral concentration. At 24, 48 and 72 hpi, more X31 virus was detected in the supernatants in ΔWD than WT lung slices (Figure 5.5), with this difference being statistically significant at 48 and 72 hpi. X31 virus concentrations also increased across the time course in each genotype.

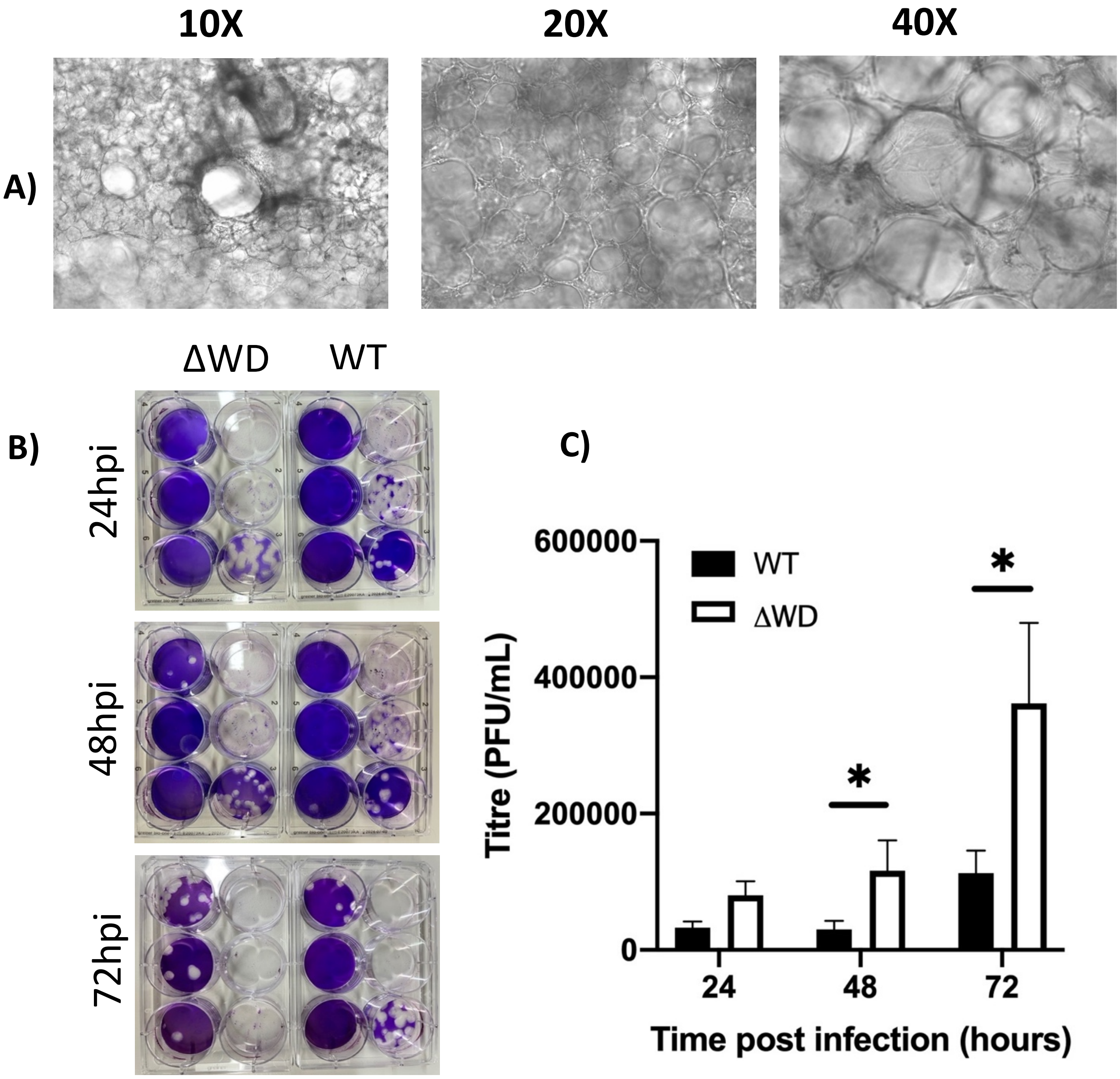

Figure 5.5: Increased IAV X31 by plaque assay in ΔWD lung slice supernatants at 24, 48 and 72 hpi.

A) Brightfield images of lung slice tissue (live cells imaged with Zeiss aviovert).

B) WT and ΔWD lung slices were infected and incubated with IAV X31 for 24, 48 and 72 hours. Virus secreted from explants were titrated using a plaque assay with the number of plaques being counted in the final successfully infected well.

B) The plaque number was used to calculate a virus concentration (PFU/mL), average concentrations are presented (+SEM). A Mann Whitney U test was conducted: * = $p<0.05$ n=6 biological replicates.

5.3.4 WT and ΔWD bone marrow derived macrophages do not support IAV replication.

Bone marrow derived macrophages (BMDMs) are crucial antigen presenting cells and produce an array of cytokines to combat IAV infection (345). With a deficiency in the WD domain increasing IAV replication, as seen in Figures 5.1-5.5, I investigated whether IAV was able to replicate to higher levels in WT and ΔWD BMDMs.

BMDMs were isolated from legs of mice as described in methods. Cells were differentiated over 7 days in M-CSF. At day 7, BMDMs were infected with IAV X31 and RNA was harvested at t=0 and t=48 hours. As shown in figure 5.6, there was no significant difference between the IAV X31 M2 RNA at 48 hpi for wild type and mutant cells. Additionally, there was no significant difference between the M2 RNA levels at 0 hpi and 48 hpi. This shows that there was no significant X31 replication in BMDMs, and that there was no difference in the absence of WD domain of ATG16L1.

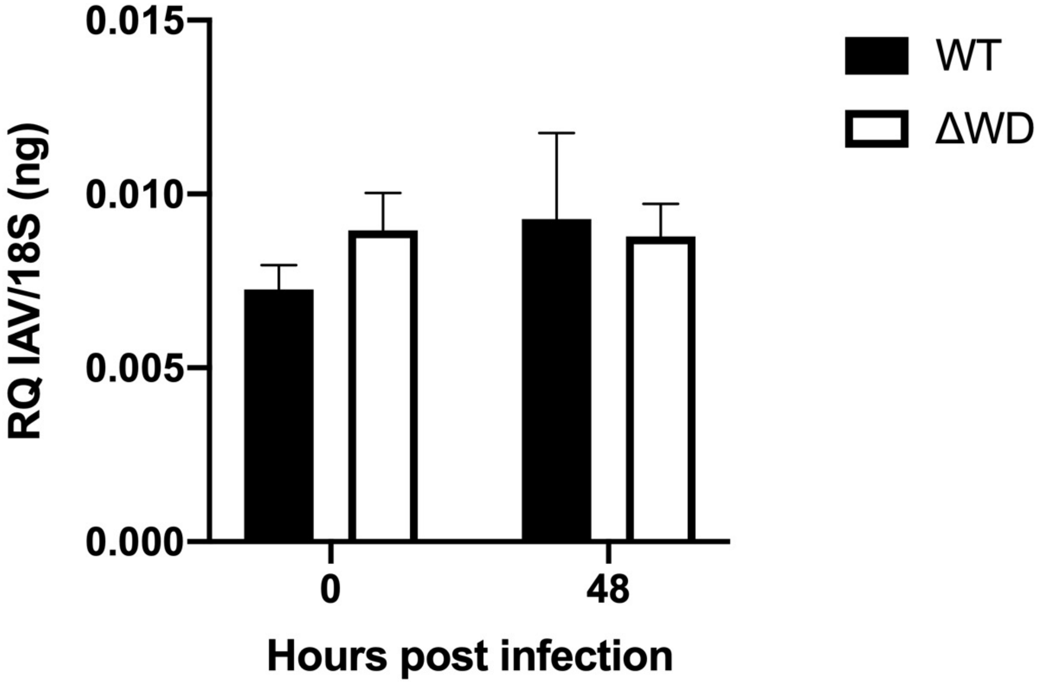

Figure 5.6: BMDMs do not support IAV X31 replication over 48 hpi with no difference between WT and ΔWD BMDMs. WT and ΔWD BMDMs were infected with IAV X31 (MOI: 5) and incubated for 48 hours before cells were lysed and RNA isolated. IAV X31 M2 gene RNA was quantified using qPCR. The relative quantity of M2 RNA at 0 hpi and 48 hpi, normalised to 18S, is presented (+SEM). An independent samples t-test was conducted: Not significant $p>0.05$ $n=3$ biological replicates.

5.3.5 Increased ISG mRNA expression in ∆WD MEFs compared with WT MEFs infected with IAV X31.

In the previous section, it has been demonstrated that IAV replicates better in ∆WD MEFs and precision cut lung slices from ∆WD mice, although this is dependent on the strain of IAV. In the next experiments I investigated if this correlated with elevated cytokine expression. I set out to measure the type I interferon IFNβ as well as two ISGs: IFIT1 and ISG15. These three cytokines are known to be expressed by MEFs in response to IAV (346,347).

WT and ∆WD MEFs were infected with X31 (MOI: 2) for a time course of 12 hours and cells were lysed at 4, 6, 8 and 12 hpi. RNA was extracted, reverse transcribed into cDNA and ISG expression levels measured by qPCR using primers to the mouse IFIT1 and ISG15 genes. Figure 5.7 A displays the relative quantity of IFIT1 and ISG15 transcripts at each time point. Approximately 5-fold more IFIT1 and ISG15 mRNA was expressed in ∆WD cells compared with WT at 12 hpi. Both IFIT1 and ISG15 mRNA levels have increased in WT and ∆WD by the 12 hour time point, which was higher than at 4 and 8 hpi.

This experiment was repeated with IAV PR8 infection, with the results shown in figure 5.7 B. The differences for ISG15 mRNA levels in a time course of 0-12 hours between WT and ∆WD MEFs showed that in contrast to the X31 strain shown in figure 4.1 A, ISG15 mRNA levels were higher for each time point in WT cells compared with ΔWD cells. For IFIT1, however, mRNA expression levels were higher in ∆WD MEFs. Overall, the values are considerably smaller than values generated from X31 infection, (note 100-fold difference in y-axis) indicating that there was less ISG mRNA expression following PR8 infection.

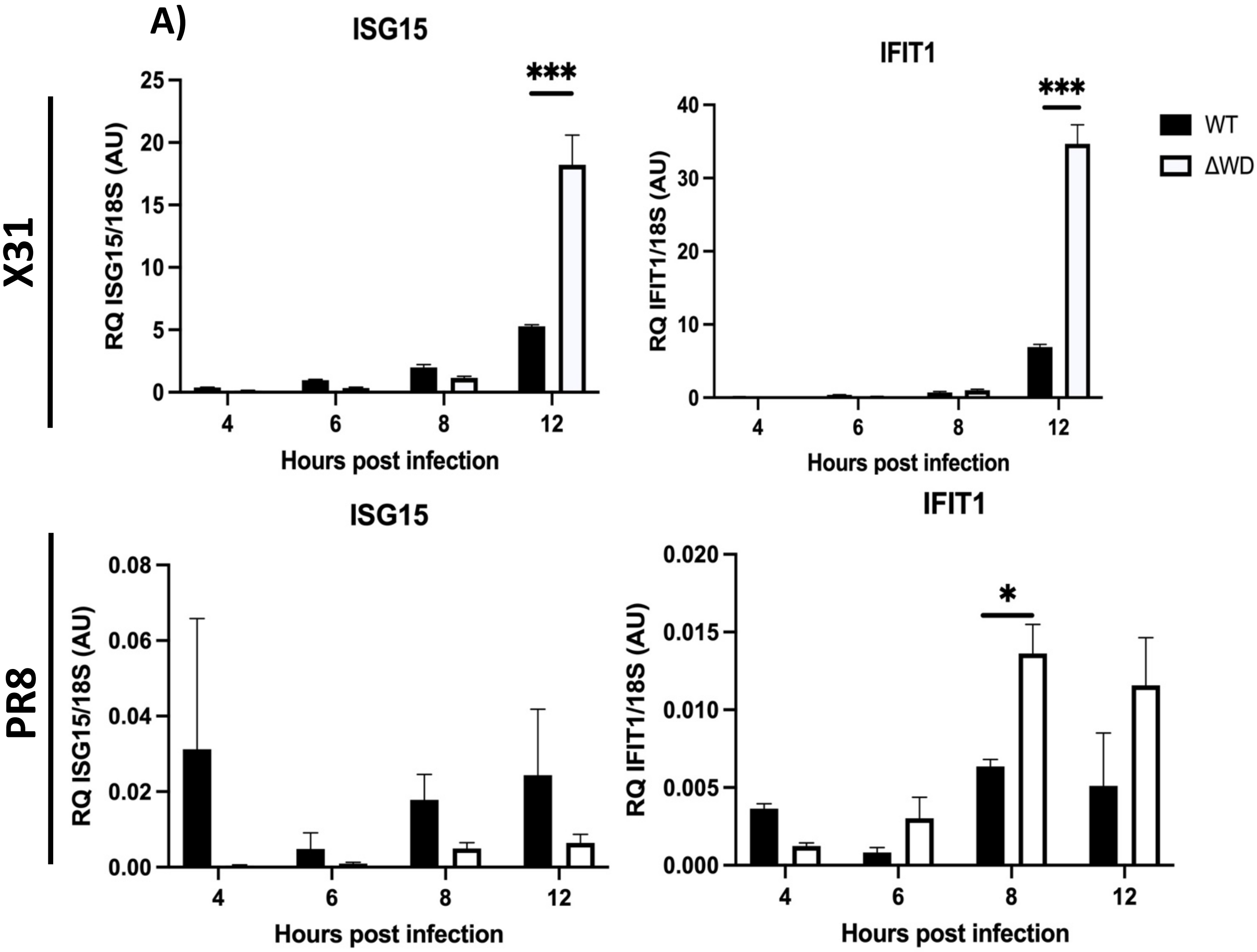

Figure 5.7: Increased ISG15 and IFIT1 expression in IAV X31-infected, but not PR8-infected ΔWD MEFs. WT and ΔWD MEFs were infected with IAV for a time course of 12 hours, with cells lysed and RNA extracted at 4, 6, 8 and 12 hpi.

A) ISG15 and IFIT1 mRNA transcripts from cells infected with X31 were quantified by qPCR. The relative quantity of ISG15 and IFIT1 transcripts at 4, 6, 8 and 12 hpi were normalised to 18S and a negative control (+SD). Time points were statistically tested by an independent samples t-test: *** = $p<0.001$ n=3 technical replicates. [2]

B) ISG15 and IFIT1 transcripts from cells infected with PR8 were quantified by qPCR. The relative quantity of ISG15 and IFIT1 transcripts at 4, 6, 8 and 12 hpi, normalised to 18S, are presented (+SD). An independent samples t-test was conducted: * = $p<0.05$ n=3 technical replicates.

---

[2] Data published in Figure 6 of Wang *et al.* (2021) (Appendix 1).

5.3.6 Increased levels of IFNβ mRNA expression detected in ∆WD MEFs constitutively and after infection with X31.

With the data in Figure 5.7 showing that WD deficient IAV infected MEFs express higher levels of the ISGs IFIT1 and ISG15 than WT, I investigated whether the expression levels of IFNβ were altered. IFNβ mRNA is rapidly turned over (348), so I used very early time points following infection.

WT and ∆WD MEFs were infected with X31 (MOI: 2) for a time course of 120 min and cells were lysed at 60, 90 and 120 min post infection and the RNA extracted. RNA was reverse transcribed to cDNA before measuring mRNA levels by qPCR for IFNβ transcripts. Uninfected cells were used to measure basal IFNβ levels. Basal IFNβ levels were subtracted from infected IFNβ condition values to give the change in transcript levels in response to infection. Only X31 was investigated due to X31 eliciting strong ISG responses as seen in Figure 5.7.

Increased IFNβ transcripts were detected in uninfected ∆WD MEFs over WT MEFs, demonstrating that they have a higher basal level of IFNβ compared with WT MEFs (Figure 5.8A).

Figure 5.8 B demonstrates that at 120 min post infection there is significantly more IFNβ1 mRNA in ∆WD MEFs compared with WT MEFs. No significant difference is seen at 60 or 90 min post infection.

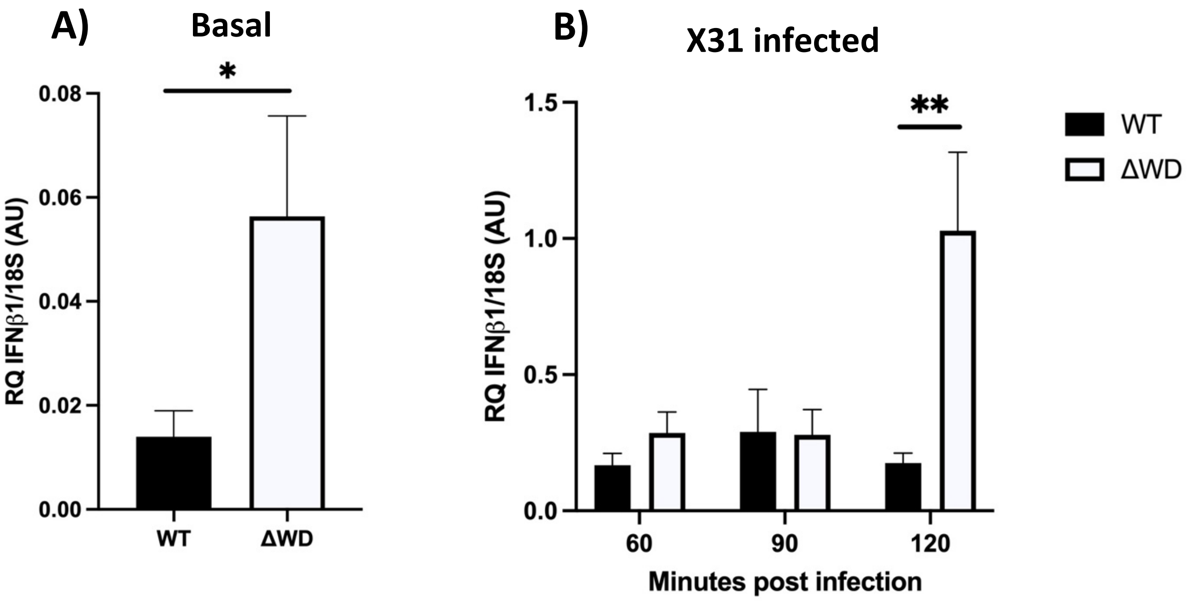

Figure 5.8: Increased IFNβ expression in uninfected and IAV infected ΔWD MEFs by 120 min post infection, compared with WT. WT and ΔWD MEFs were infected with IAV X31 and incubated for 60, 90 and 120 min post infection. Cells were lysed and RNA extracted for qPCR.

A) IFNβ transcripts from uninfected cells were quantified by qPCR. The relative quantities of IFNβ transcripts, normalised to 18S, are presented (+SEM). A Mann Whitney U test was conducted: * = $p<0.05$ n=5 experimental replicates.

B) IFNβ transcripts from X31 infected cells were quantified by qPCR. The relative quantities of IFNβ transcripts at 60, 90 and 120 min post infection, normalised to 18S and to the basal levels are presented (+SEM). A Mann Whitney U test was conducted: ** = $p<0.005$ n=5 experimental replicates.

5.3.7 Significantly less IFNβ expression when TLR3 but not Rig-I is inhibited.

In order to measure the role different RNA signalling pathways in early IAV infection events, a TLR3 competitive inhibitor ($C_{18}H_{13}ClFNO_3S$ - Sigma Aldrich) (349) was used to block TLR3. Additionally, I generated Rig-I knock out cell lines to block signalling through this pathway. Rig-I knock out MEFs were generated using custom CRISPR-cas lentivirus particles and validated by Western blot. The TLR3 inhibitor was validated using qPCR, with the inhibitor successfully attenuating IFNβ, ISG15 and IFIT1 expression following treatment with Poly I:C (a dsRNA TLR3 ligand) (Figure 5.9 A).

Successful knock out of Rig-I in both WT and ∆WD MEFs was validated by both Western blot of Rig-I protein and qPCR. For the Western blot, there was an absence of the 107 kDa Rig-I band in both of the second knock experiments. There was a reduction in Rig-I mRNA transcript expression in WT MEFs by qPCR, however the reduction was not as clear in ∆WD due to a very low basal expression level (Figure 5.10 B).

WT and ∆WD MEFs were treated with the TLR3 inhibitor one hour prior to infection. All cells were infected with X31 (MOI: 2) and incubated for 60, 90 and 120 minutes. Cells were then lysed and RNA extracted. cDNA was prepared via reverse transcription before the samples were interrogated for IFNβ levels by qPCR. In addition, WT and ∆WD MEFs and Rig-I KO MEFs were also infected with IAV X31.

Figure 5.11 A demonstrates increased IFNβ1 mRNA expression detected in ∆WD MEFs, confirming the results in Figure 5.8. Figure 5.11 B represents only the Rig-I KO construct transcript levels in comparison to the WT and ∆WD MEFs. Increased expression of IFNβ is seen in the Rig-I KO constructs compared to WT and ∆WD Rig-I$^+$ MEFs, at 60 and 120 min post infection however this increase is not significant, except between the WT and its KO construct at 120 time point. At 90 min post infection the construct transcript levels were not significantly higher or lower than the Rig-I$^+$ MEFs. This shows that the IAV-induced IFNβ expression demonstrated in Figure 5.8 is reliant on TLR3 activation and not Rig-I activation. However, this experiment has not rules out the involvement of other receptors such as TLR7 or MDA5. Regardless, this experiment suggests that the activation is taking place in the endosome and not the cytoplasm.

Figure 5.11 C represents only the TLR3 inhibited cell IFNβ expression levels in comparison to uninhibited WT and ∆WD MEFs IFNβ expression. Significantly less expression of IFNβ is seen in all TLR3 inhibited MEFs compared to either their untreated counterparts.

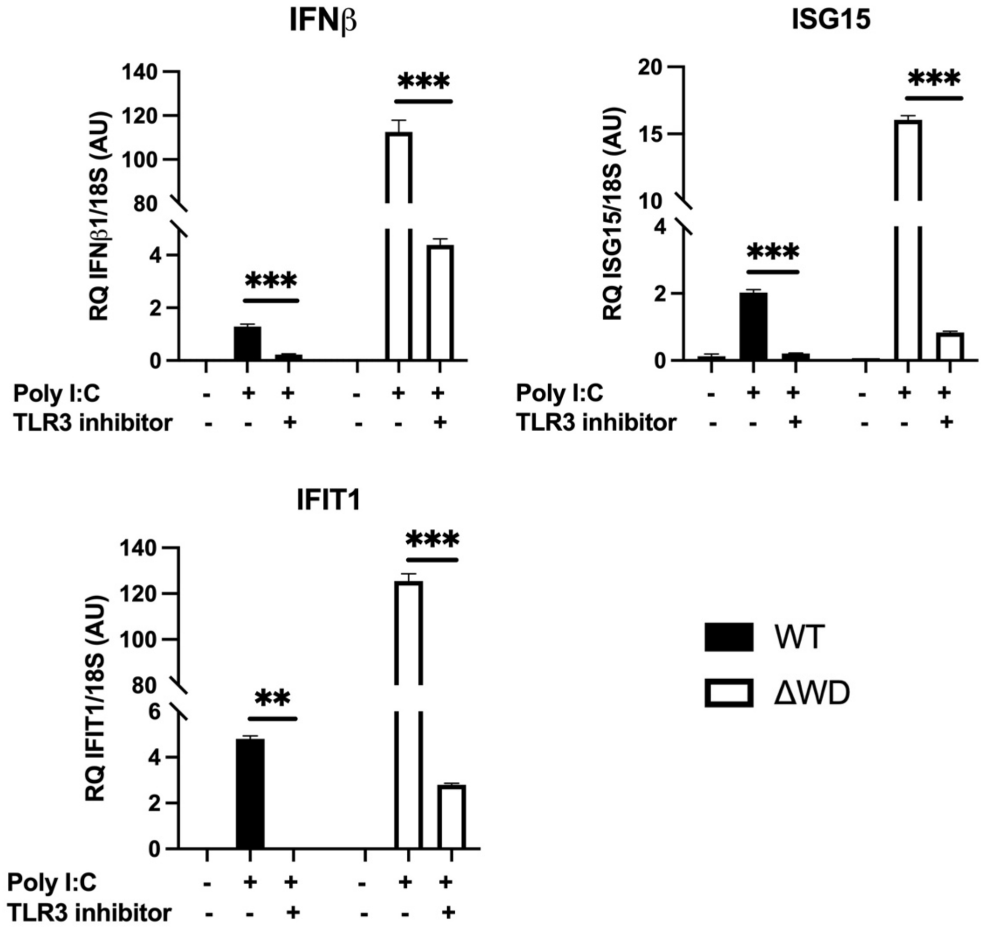

Figure 5.9: WT and ∆WD MEF treatment with TLR3 inhibitor attenuates IFNβ, ISG15 and IFIT1 expression following Poly I:C treatment. WT and ∆WD MEFs were treated with TLR3 inhibitor for one hour prior to transfection with Poly I:C. Cells were then incubated for 4 hours before RNA extracted and IFNβ1, ISG15 and IFIT1 transcripts were quantified by qPCR and presented normalised to 18S (+SD). A two-way ANOVA with Šidák correction was performed: ** = p<0.01 *** = p<0.001, n=3 technical replicates.

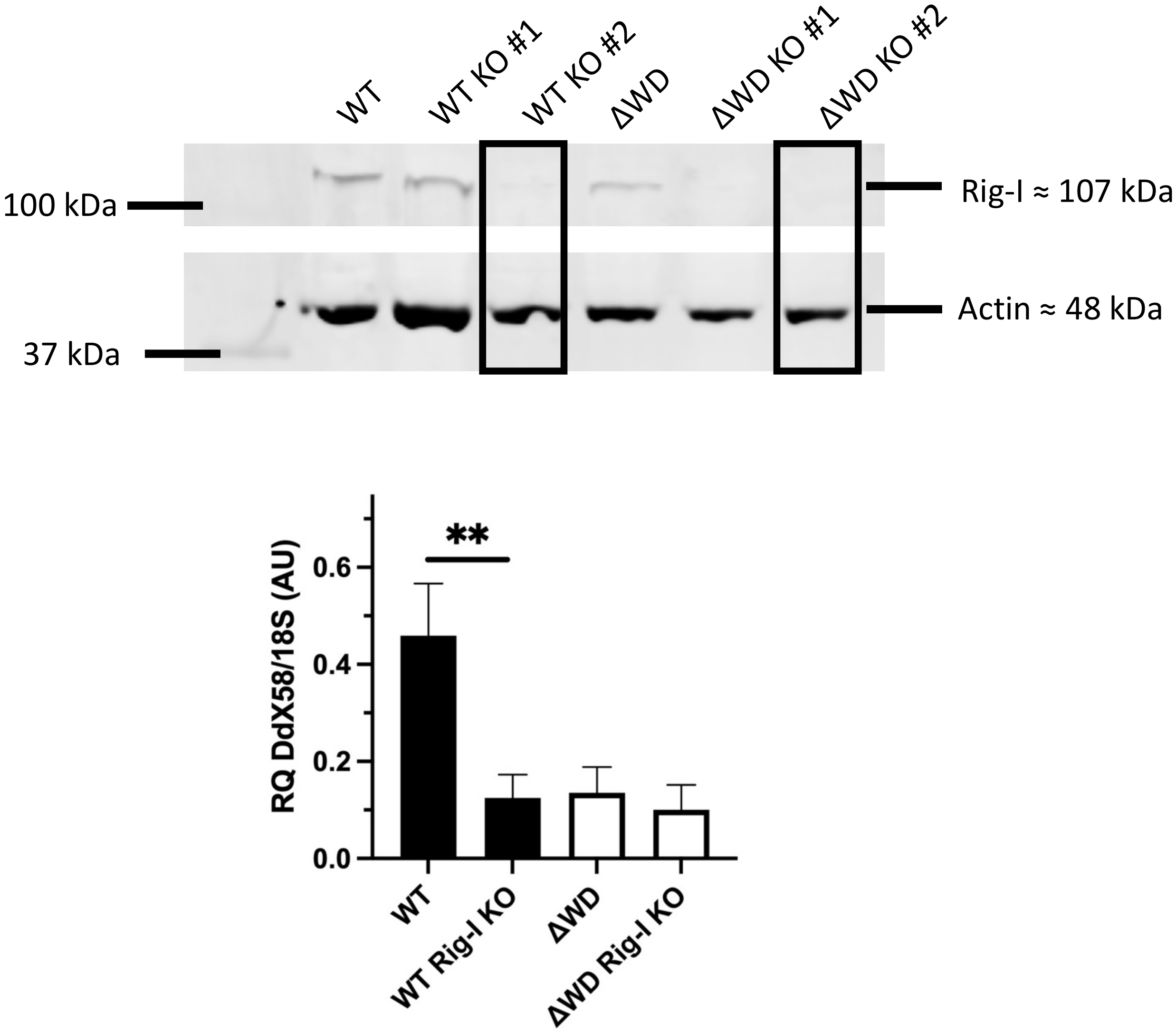

Figure 5.10: WT and ΔWD MEF Rig-I protein expression knocked down in WT and ΔWD MEFs. Cells were transformed using custom CRISPR-cas lentivirus particles to knockout of Rig-I. Rig-I protein expression was validated by Western blot using anti-DdX58 (Rig-I). Rig-I transcript expression was quantified by qPCR and normalised to 18S (+SD). An independent samples t-test was conducted: ** = $p<0.01$, n=3 technical replicates.

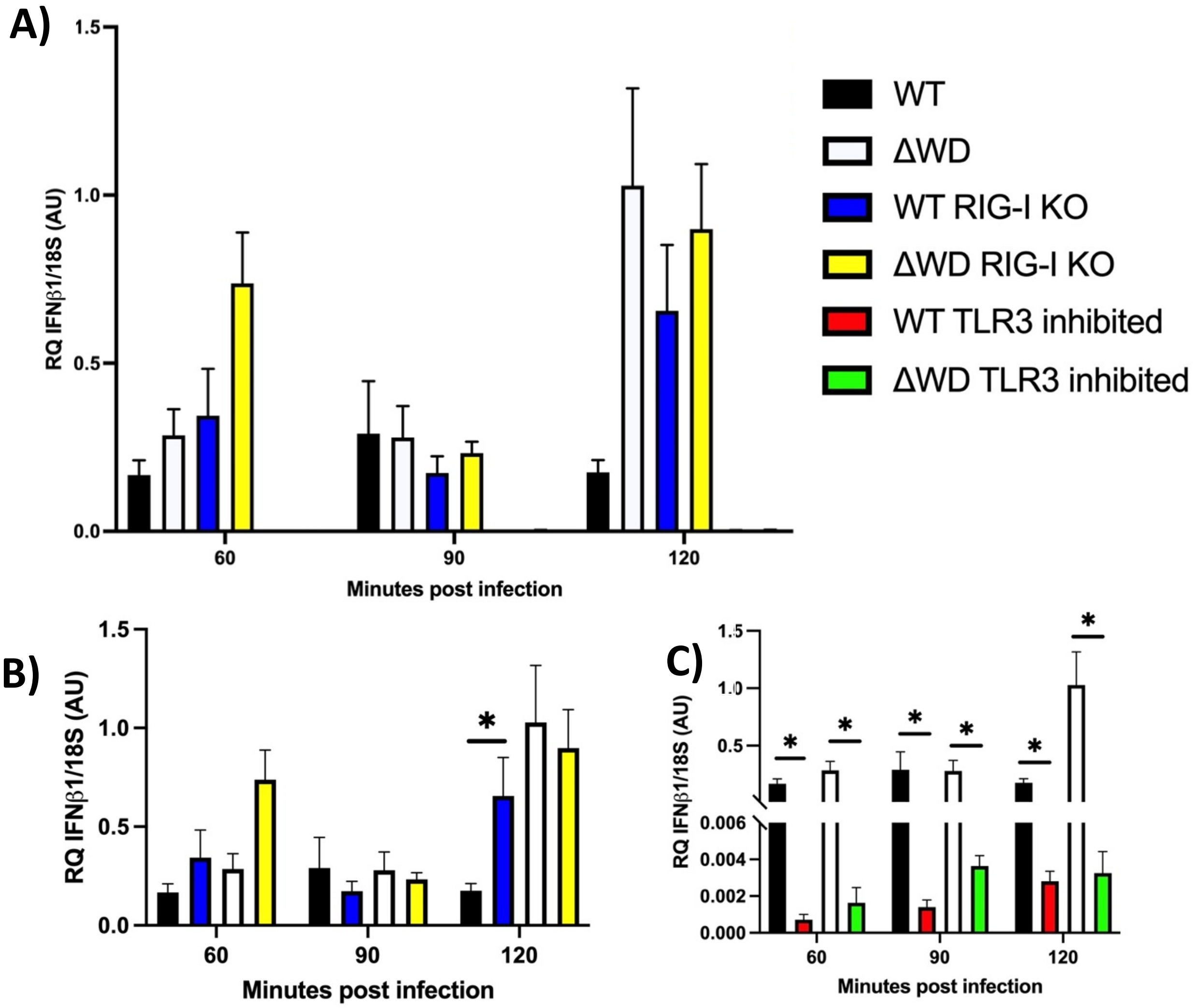

Figure 5.11: TLR3 inhibition of WT and ΔWD MEFs decreased IFNβ expression.

Control WT and ΔWD MEFs were infected with X31 together with MEFs treated with a TLR3 inhibitor and WT and ΔWD MEFs where Rig-I was knocked down. Cells were incubated for 60, 90 and 120 min post infection before lysis and extraction of RNA. The IFNβ transcript levels of each sample was analysed by qPCR and normalised to the 18S levels.

A) All samples are presented (+SEM). No significance values shown.
B) Rig-I^{+} cells vs Rig-I KO constructs are presented for each time point. A Mann Whitney U test was conducted between Rig-I KO and Rig-I^{+} MEFs * = $p<0.05$ n=6 experimental replicates.
C) Untreated cells vs TLR3 inhibited cells are presented for each time point. A Mann Whitney U test was conducted between untreated and treated cells * = $p<0.05$ n=6 experimental replicates.

5.3.8 Increased ISG15 and IFNβ1 expression were detected in ΔWD MEFs after stimulation with dsRNA.

The data in Figure 5.11 indicate that TLR3 is a key signalling protein sensing IAV infection. To further test and support this, I challenged WT and ΔWD MEFs with Poly I:C, a dsRNA mimic capable of activating TLR3. WT and ΔWD MEFs were transfected with Poly I:C using Lipofectamine LTX PLUS reagent. Cells were transfected with Poly I:C for four hours before they were lysed and RNA extracted and isolated. RNA was reverse transcribed to cDNA before the quantities of ISG15, IFIT1 and IFNβ1 mRNA transcripts were analysed by qPCR. These data are presented in Figure 5.12. Poly I:C upregulates ISG15, IFIT1 and IFNβ in both WT and ΔWD MEFs. This response is approximately 2-fold greater for ISG15 and 3-fold greater for IFNβ in ΔWD MEFs compared to WT. The IFIT1 mRNA response was not significantly greater for either WT or ΔWD MEFs following Poly I:C treatment. These data show that IFNβ and ISG expression following TLR3 activation is upregulated in ΔWD MEFs.

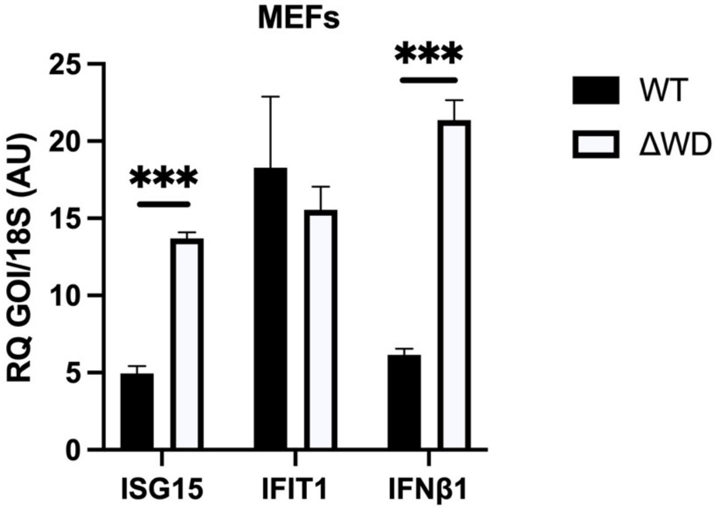

Figure 5.12: Increased ISG15 and IFNβ expression in Poly I:C treated ΔWD MEFs, compared with WT.

WT and ΔWD MEFs were transfected with Poly I:C in Lipofectamine LTX PLUS reagent for 4 hours. ISG15, IFIT1 and IFNβ transcripts from transfected cells were quantified by qPCR. The relative quantities of RNA transcripts, normalised to 18S, are presented (+SEM). An independent samples t-test was conducted *** = p<0.001 n=3 experimental replicates.

5.3.9 Increased IFNβ and ISG mRNA in ΔWD BMDMs following TLR activation.

In the previous section, I demonstrated that my BMDMs do not support IAV replication and that the WD domain neither promotes or attenuates replication. In order to see if there is an elevated cytokine response to IAV in BMDMs, I investigated IFNβ and ISG responses to BMDMs treated with a range of TLR ligands.

BMDMs were infected with either X31 or PR8 (MOI: 2) for four hours. Alternatively, cells were treated with TLR9 ligands (unmethylated CpG DNA oligonucleotides - 5 μM) or treated with TLR3 ligand dsRNA for four hours. Cells were then lysed and RNA extracted before RNA was reverse transcribed to cDNA and the mRNA levels for IFIT1, ISG15 and IFNβ were determined by qPCR.

Increased IFNβ and ISG mRNA were seen in ΔWD BMDMs compared with WT (Figure 5.13) following stimulation with TLR3 ligand, TLR9 ligand and with X31 and PR8 IAV. The standard error of the mean is high for many of these BMDM samples, probably because of the heterogenicity of the cells. In the case of IFNβ mRNA, this difference was significant following X31 exposure and exposure to the TLR9 ligands (Figure 5.13 C).

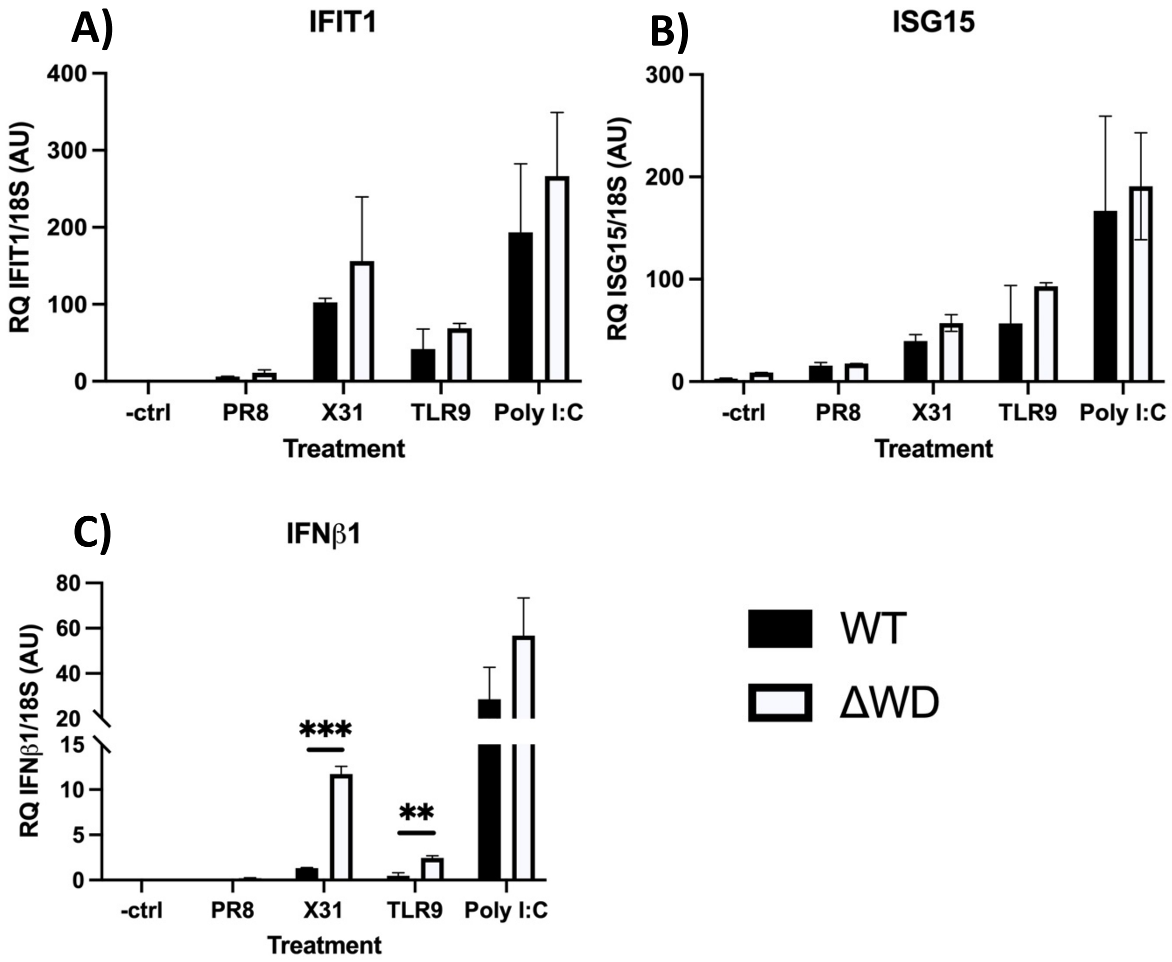

Figure 5.13: Greater expression of IFIT1, ISG15 and IFNβ were seen in response to stimulation with X31, PR8, TLR9 ligands and Poly I:C, in BMDMs.

WT and ΔWD BMDMs were exposed to a variety of stimuli before lysing and extracting RNA. The cDNA of the transcripts was then analysed and IFIT1 (A), ISG15 (B) and IFNβ1 (C) transcripts quantified by qPCR. The relative quantity of cytokine transcripts, normalised to 18S, are presented here. An independent samples t-test was conducted ** = $p<0.005$ *** = $p<0.001$ n = 3 biological replicates.

5.3.10 Precision cut lung slices from ΔWD mice infected with IAV show Increased ISG and IL-6 mRNA.

In order to examine whether the effect on cytokine expression was reproduced in tissues from mutant mice, I produced precision cut lung slices from WT and ΔWD lungs to culture a 3D organ model. Lung slices would contain resident macrophages as well as epithelial cells, therefore would respond to infection with an array of pro-inflammatory cytokines.

Lungs were inflated with low melting point agarose, cast in agarose blocks and sliced using a vibrating microtome. Slices were infected with IAV X31 (5×10^4 particles) for 16 hours before cells were dissociated from the agarose and tissue using collagenase and dispase, then the RNA was extracted. RNA was reverse transcribed to cDNA and the mRNA levels for IFNβ, IFIT, ISG15, IFITM3 and IL-6 were determined by qPCR. Targets were normalised to 18S and also normalised to the negative control.

There was significant increase in IFIT1, ISG15, IFITM3 and IL-6 mRNA expression in ΔWD lung tissue (Figure 5.14). IFIT1 levels were 4.7 fold higher and ISG15 levels were 11 fold higher in ΔWD lung slices. For IFITM3 and IL-6, WT lung slices had no expression detected in response to IAV X31. Overall ISG and inflammatory cytokine levels appeared significantly higher in in IAV infected ΔWD lung slice tissue. There was a significant increase in IFNβ mRNA expression in WT lung tissue following IAV X31 infection, with no expression seen in the ΔWD tissue. This may be due to IFNβ having been expressed earlier in the infection time course.

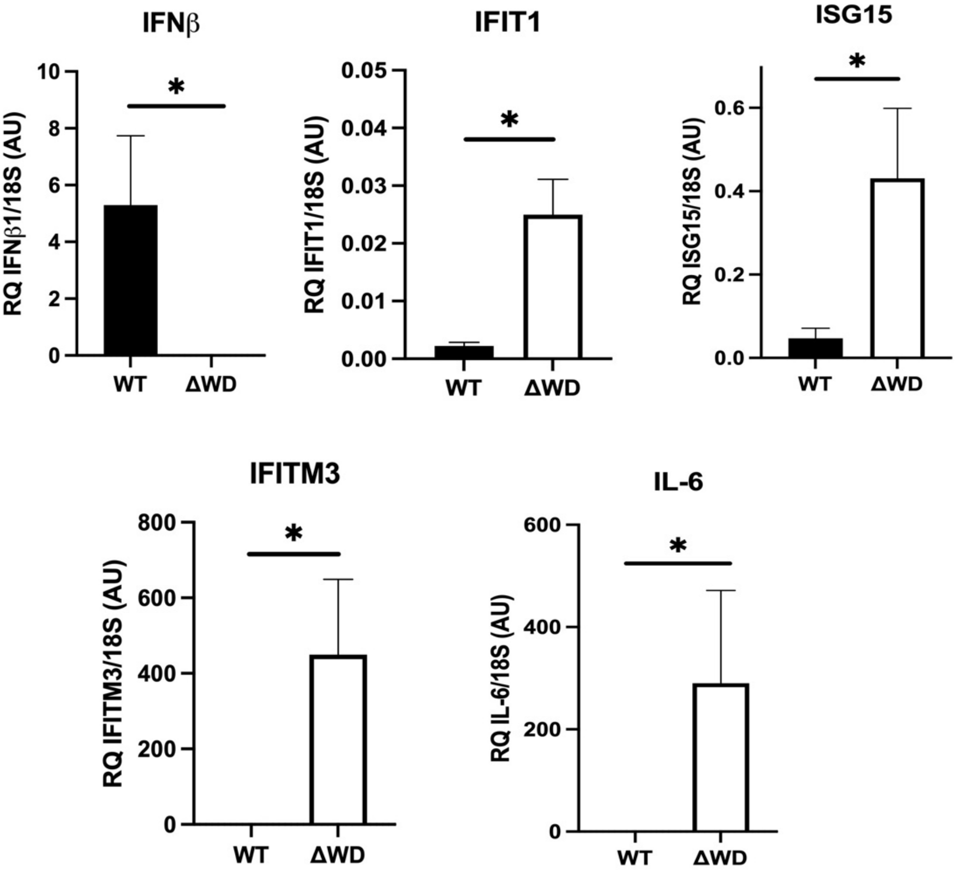

Figure 5.14: Increased expression of IFIT1, ISG15, IFITM3 and IL-6 in ΔWD lung slices when infected with IAV X31. WT and ΔWD lungs were inflated with LMP agarose and sliced using a vibrating microtome. Slices were cultured and infected with IAV X31 for 16 hours. RNA was extracted following cell dissociation with collagenase III and dispase II and IFNβ, IFIT1, ISG15, IFITM3 and IL-6 mRNA transcripts were quantified by qPCR. Values were normalised to 18S and negative controls and are presented (+SEM). A Mann Whitney U test was conducted: * = $p<0.05$, n=7 biological replicates.

5.4 Discussion

In this chapter I have demonstrated that the WD domain of ATG16L1 has a role in the suppression of IAV replication and IAV-induced cytokine storms. IAV replication was measured over a 72 hour time course with two IAV strains: X31 and PR8. IAV PR8 replication was greater in ΔWD MEFs at 24, 48 and 72 hpi as measured by $TCID_{50}$ and plaque assay whereas for IAV X31, virus replication was greater in WT MEFs over 48 hpi, and then virus replication in ΔWD became greater at 72 hpi (Figure 5.2). Both viruses replicated more efficiently in ΔWD MEFs than WT MEFs at 72 hpi, although for X31 this increase was weak. These differences in replication appear to be strain-dependent.

Replication was measured over an earlier (0-12 hour) time course using qPCR for IAV M2 expression (Figure 5.4). Here, IAV PR8 replication was also greater in ΔWD MEFs over the earlier time course, with replication in ΔWD MEFs being greater than WT at 8 and 12 hpi. IAV X31 replicated to higher levels in WT MEFs than ΔWD MEFs over the 12 hour time course.

An *ex vivo* model was used to investigate virus replication in lung tissue. These 3D organ models comprise of the heterogenous population of cells found in the lung, including epithelial cells, goblet cells, endothelial cells and resident alveolar macrophages. WT and ΔWD mouse lung slices were infected with X31 and increased virus was released over a 72 hour time course in ΔWD lung slices compared with WT (Figure 5.5). These results demonstrate that lung slices supported the replication of IAV and that the loss of the WD domain enhances virus replication in *ex vivo* lung tissue.

Professional phagocytic cells were used to investigate the loss of the WD domain on virus replication. BMDMs clear pathogens and apoptotic cells through the LAP pathway. Our group has shown that the WD domain is essential for LAP in macrophages (66). In my work I show that IAV does not replicate in BMDMs Figure 5.6).

Interferon signal transduction induced by IAV infection was measured by ISG induction in WT and ΔWD MEFs by qPCR over a 12 hour time course. When IAV X31 and PR8 were used to infect MEFs, IFIT1 and ISG15 were expressed to higher levels in ΔWD MEFs at 12 hpi with X31. However with PR8, the ISG expression was higher in WT MEFs

(Figure 5.7). Furthermore, when IFNβ was measured over a 120 minute time course in IAV X31 infected WT and ΔWD MEFs, constitutive baseline IFNβ levels were higher in ΔWD MEFs compared with WT. Following IAV infection IFNβ expression was greater in ΔWD at 2 hpi (Figure 5.8).

To identify whether interferon signalling was due to IAV signalling in the endosome or after delivery of the genome to the cytoplasm, the IAV receptors TLR3 and Rig-I were inhibited. TLR3 inhibition was achieved using the drug $C_{18}H_{13}ClFNO_3S$. Interferon production inhibited in poly I:C transfected MEFs (Figure 5.9). CRISPR-cas was used to inhibit Rig-I signalling in MEFs. This was verified by Western blot (Figure 5.10). Overall, IFNβ was severely reduced to almost zero in TLR3 inhibited cells but not in the Rig-I knock out cells (Figure 5.11). This suggests that TLR3 is the main sensor of IAV leading up to the IFNβ and ISG production in IAV infected cells.

The response of WT and ΔWD MEFs to various TLR ligands was investigated. The ISG and IFNβ response to the dsRNA ligand (poly I:C) was measured using qPCR and greater ISG and IFNβ expression was detected in ΔWD MEFs transfected with poly I:C (Figure 5.12). In BMDMs, the ISG and IFNβ responses to poly I:C, TLR9 ligands (DNA rich in unmethylated CpG motifs) and IAV were measured using qPCR. Greater IFN and ISG expression was seen in ΔWD for the TLR9 ligands, X31 and poly I:C but not for PR8 (Figure 5.13). One limitation to these Poly I:C controls is that the cells were immortalised, with the cytokine overreaction possibly being due to breakdowns in the cell innate immune systems. However, similar cytokine overreactions to Poly I:C were seen in macrophage cell lines which were primary cells that shouldn’t have any attenuations in their innate immune systems.

Finally this chapter aimed to investigate in cell culture the IAV-induced cytokine storm demonstrated by our lab *in vivo* in the ΔWD mouse. When precision cut lung slices were infected with X31, there was far greater expression of IFIT1, ISG15, IFITM3 and the inflammatory interleukin IL-6 in ΔWD compared with WT lung slices (Figure 5.14).

BMDMs are professional phagocytic cells that utilise LAP to remove pathogens. The data here shows there was very little replication of IAV in WT and ΔWD BMDMs. IAV initially binds to the expressed sialic acid and is then taken into the cell by endocytosis, these endosomes may then be decorated with LC3 and targeted for degradation. If the loss of the WD domain (ΔWD) results in a LANDO deficiency, more IAV would survive in endosomes and explain the higher replication in ΔWD MEFs. However the novel findings I have demonstrated here show that the WD domain has a role in cholesterol homeostasis, with a WD deficiency resulting in reduced cholesterol at the plasma membrane. I have shown that this results in more fusion at the endosomal membrane and therefore more virus is able to reach the nucleus and replicate to higher levels.

While both IAV strains showed increased replication in ΔWD MEFs, PR8 showed consistently higher replication from 8 hpi to 72 hpi, whereas X31 only replicated more in ΔWD MEFs at 72 hpi. This difference could be due to the different strains of influenza virus exhibiting substantially different pathogenicity, with different host interactions between the two strains. The PR8 strain used was the PR8 Mount Sinai strain and it is an attenuated H1N1 lab strain that has been selected for its ability to infect cells *in vitro.* The X31 strain is A/X-31 and is constructed from PR8 with H2N3 glycoproteins. (350,351). It is interesting that both PR8 and X31 share the same genome, differing only in their expressed glycoproteins and that this can drastically alter viral replication in MEFs. The host innate immune response to virus infection can significantly alter pathogenicity. IFN expression activates signalling pathways which cause antiviral ISG expression (352) and differences between IFN and ISG expression were observed between X31 and PR8. PR8 induced less cytokine responses compared with X31 over 12 hour infection time courses. Since there was increased antiviral response following X31 infection, it is not surprising that X31 replication was attenuated compared to PR8. PR8 is described in the literature as being a more pathogenic IAV strain, lethal in mice at smaller doses. X31, on the other hand, is described as less pathogenic and responsible for a more self-limiting infection (353). Mice infected with PR8 and X31 have been shown to respond differently depending on the strain. PR8 has been shown to generate overlapping pro and anti-inflammatory responses, whereas X31 has been shown to respond to infection with a distinct proinflammatory response, followed by a distinct anti-inflammatory response (353). In contrast to my data though, PR8 has been shown to trigger significant antiviral and inflammatory cytokine responses (354,355). This could be due to the cell line used, fibroblasts may respond and signal differently to the different glycoproteins expressed between the two strains. Additionally, there may be unidentified viral factors that drive this difference between the two IAV strains and suppress the IFNβ response.

To investigate the expression of IFNβ and ISGs following infection with X31 and PR8, I used qPCR to show that ISGs and IFNβ were expressed in cells following infection, rapidly in the case of IFNβ, and to higher levels in ∆WD MEFs. Furthermore, there appears to be higher levels of IFNβ in uninfected ∆WD MEFs compared with the WT MEFs. This higher basal level of IFNβ in ∆WD MEFs could be a consequence of the cells lacking LAP. LAP deficient models have been shown to be autoinflammatory (15) and IFNβ has a pro-inflammatory role in fibroblasts (356) suggesting that could be the reason for this increased basal level.

One possible limitation of these experiments is that the immortalised MEFs used were generated through spontaneous immortalisation. Spontaneously immortalised cells can have attenuated innate immune systems. The tumour suppressor gene p53, which is lost during immortalisation, regulates type I IFN expression. Without this gene, ISG responses to virus infection can be reduced (357). The results of this chapter demonstrate increased ISG expression in X31 infected ∆WD MEFs, which could have been influenced by the caveat of using spontaneously immortalised MEFs. However, very similar results were seen with lung slices, which wouldn't suffer from this limitation, which suggests this result is true.

Through inhibition of Rig-I and TLR3 signalling pathways, I have demonstrated that the IFNβ response to IAV could be induced by TLR3 activation. These data are supported by the increased endocytosis of IAV into ∆WD MEFs. Increased IAV in cells was due to increased virus within endosomes and since TLR3 is an endosomal receptor it would be activated by the IAV genome. TLR3 recognises dsRNA, and yet is widely understood to detect IAV (which is a ssRNA virus). TLR3 detects IAV's ssRNA genome during viral replication when dsRNA replication intermediates are produced (358). While the exact nature of how TLR3 recognises incoming IAV is not published, TLR3 may be able to recognise the ssRNA genome of IAV due to its conformation within the IAV vRNP. Viral RNA is wrapped into a double helical configuration within vRNPs (359), which could enable it to be detected by TLR3.

Interestingly, TLR3 has been implicated in deleterious proinflammatory cytokine responses to IAV infection. Mice lacking TLR3 were found to have reduced proinflammatory cytokine responses to IAV as opposed to mice expressing the receptor (360).

Increased TLR3 activation from incoming IAV would therefore lead to greater IFNβ expression. This over-induction of IFNβ has deleterious effects in tissues. I showed that when precision cut lung slices were infected with X31 not only did they have elevated ISG expression but also elevated IL-6 expression. IL-6 is a pro-inflammatory cytokine produced by macrophages, dendritic cells and other innate immune cells. Clinical studies have shown that over expression of the cytokine increases the likelihood of hospitalisation of the influenza infected patient (361). As well as in IAV infection, IL-6 has also been implicated in the progression of severe COVID-19, with it contributing to cytokine storms (362,363). Therefore IL-6 is a significant factor in the development of cytokine storms and certainly contributes to IAV-induced cytokine storms (364). In this thesis I have created a model in lung slices for the events that occur in the ∆WD mice as seen in Wang *et al.* (2021).

To summarise the findings of this chapter, I have shown that the WD domain does indeed play a role in suppressing IAV replication and IAV-induced cytokine storms *in vitro*. IAV replicates more efficiently in ∆WD MEFs and precision cut lung slices. Additionally, IAV induces greater cytokine expression in ∆WD MEFs, BMDMs and precision cut lung slices. I have shown that in BMDMs this is not based on viral replication. My work has shown that increased IAV infects the cells and activates the TLR3 pathway to induce more interferon expression in MEFs.

CHAPTER 6

Discussion

6.1 The WD domain has a role in cholesterol transport to the plasma membrane.

Our lab has shown that mice lacking the WD domain of ATG16L1, a domain shown to be vital for the non-canonical mechanism LAP, were susceptible to IAV. IAV replicated to higher levels in these WD deficient mice, resulting in a lethal cytokine storm and death. The ATG16L1 protein has many non-canonical functions, with Tan *et al.* (2018) demonstrating that ATG16L1 facilitates lysosomal fusion to the plasma membrane (PM). This role allows for the movement of cholesterol from lysosomal/late endosomal membranes to the PM, aiding lysosomal/PM fusion and subsequent cholesterol transport to the PM. The T300A mutation, which introduces a caspase 3 cleavage site in the linker region of ATG16L1, has been postulated to cause cleavage of the protein and loss of the WD domain. This mutation has also been shown to inhibit cholesterol homeostasis and plasma membrane repair (84).

This mutation implicates the WD domain in cholesterol transport therefore I investigated whether the WD domain has a role in the transport of cholesterol within cells. Unlike in Tan *et al.* (2018) I specifically investigated the cholesterol content of the PM to see if there was an altered content, in WD deficient tissue and MEFs. I hypothesised that a reduced PM cholesterol content would affect the ability of IAV to gain access to the cell and tested this using three assays for endocytosis, fusion and nuclear entry. Our lab's *in vivo* data demonstrated susceptibility to IAV in ΔWD mice therefore I investigated IAV replication and interferon signalling in WD deficient cells.

I developed a primary MEF cell line from WT and ΔWD mice to investigate cholesterol homeostasis in membranes, as well as using brain and lung tissue. Total and unesterified cholesterol content of WD deficient PMs were reduced compared with WT PMs. Furthermore, the cholesterol localisation within ΔWD cells was altered. Increased cholesterol was found to co-localise to late endosomes and lysosomes, more so than early endosomes with an increased cholesterol localisation to late endosomes and lysosomes in ΔWD cells. This indicates that cholesterol is held up in late endosomes/lysosomes, a similar finding to Tan *et al.* (2018) who found the same result in ATG16L1 KO cells (84). This suggests the WD domain has a role in lysosomal fusion to the PM and without it, lysosomes cannot fuse and cholesterol egress to the PM is halted.

A further D4H cholesterol probe: D4H-GFP, is used to visualise cholesterol in the exofacial leaflet (329). I attempted to purify this probe using GST purification however was unsuccessful. Further to my experiments, the D4H-GFP probe would be used to visualise cholesterol in PM, which would give a further indication of cholesterol localisation in cells and on the PM. Fluorescence activated cell sorting would then be used measure the fluorescence of these cells to quantify cholesterol in the PM.

With it established that there is a cholesterol reduction in the PM of WD deficient cells, Chapter 4 aimed to examine whether IAV is able to enter WD deficient cells more efficiently. Initially, I set out to investigate whether IAV can fuse to the PM of WD deficient cells more efficiently, what with them possessing a reduction in cholesterol. This was accomplished via acid bypass infection, a method that forces fusion at the PM. Higher frequencies of IAV nucleoprotein (NP) was detected in ΔWD cells compared with WT cells early after infection. Cholesterol modulation of the PM using the drugs U18666A, 25-hydroxycholesterol (25HC) and cholesterol changed the frequencies of NP entry. U18666A, which inhibits Niemann Pick carrier protein 1 (NPC1), restricts cholesterol transport to the PM. Treatment with this increased IAV NP frequency in WT and ΔWD cells. In contrast, 25HC and cholesterol treatment reduced IAV NP frequency in WT and ΔWD cells. This suggests that cholesterol in the PM has an antiviral role, with a fine balance needed for efficient viral entry. A reduced PM cholesterol content is optimum for virus entry, with WD deficient MEFs providing this.

When IAV enters cells via endocytosis, the endosomal membrane is donated through invagination of the PM. This means the IAV-containing endosomal membrane would have a similar constitution to the PM, with reduced cholesterol in the endosomal membrane in WD deficient cells. My data has shown that reduced membrane cholesterol enhances viral fusion therefore this reduced endosomal cholesterol would enhance viral fusion to it. I examined viral entry using three entry assays outlined by Banerjee *et al.* (2013). The first was an endocytosis assay, using two antibodies to distinguish internal and external influenza. A higher percentage of internalised IAV was detected in WD deficient cells. The second was a fusion assay, using IAV labelled with a lipophilic dye that fluoresces green when fusion occurs. A higher frequency of fusion events was seen in WD deficient cells. The third assay was a nuclear migration assay, relying on monitoring IAV NP migration to the nucleus. Increased NP was detected in WD deficient cells at earlier time points compared with WT. The results of these assays indicate that IAV is able to enter WD deficient MEFs more efficiently. This data fits my hypothesis that IAV would be able to enter WD deficient cells more efficiently due to reduced cholesterol in the IAV-containing endosomal membrane.

In mice, a higher level of IAV replication was detected in WD deficient mice as well as elevated cytokine levels. I generated precision cut lung slices and used my primary MEF cell line to investigate the cytokine levels in a 3D-organ model and *in vitro*. Higher titres of IAV were secreted from WD deficient MEFs as well as WD deficient precision cut lung slices. ΔWD MEFs and BMDMs infected with IAV responded with a higher expression of cytokines than compared with WT MEFs. Furthermore, increased inflammatory cytokine expression was induced in WD deficient lung tissue, replicating the *in vivo* data demonstrated by Wang *et al.* (2021). These two effects in ΔWD: higher replication and cytokine storms, are caused through increased IAV entering cells (Figure 6.1). More endocytosis of IAV results in more virus interacting with TLR3, causing TLR3 activation and subsequent downstream signalling. Increased fusion of the virus results in an increased virus payload reaching the nucleus earlier, increasing the replication of the virus. Further work would be needed to prove that the IAV-containing endosomal membrane contains reduced cholesterol. Co-staining using the endocytosis assay antibodies (PINDA and HA1) and filipin III or transfecting with D4H-mCherry would allow for visualisation of cholesterol at IAV-containing endosomes.

ATG16L1 is involved in a number of fusion events, including lysosomal-autophagosome fusion during autophagy and lysosomal-phagosome fusion during LAP. LC3 is conjugated to single membranes during LAP and these single membraned vesicles then fuse, this being facilitated by the ATG5-ATG12+ATG16L1 complex. ATG16L1 binds to the single membraned LAPosomes via the WD domain, with this domain binding to the membrane following the production of ROS by the NOX2 complex. Following the binding of the WD domain, the ATG5-ATG12+ATG16L1 complex can then conjugate LC3 to the

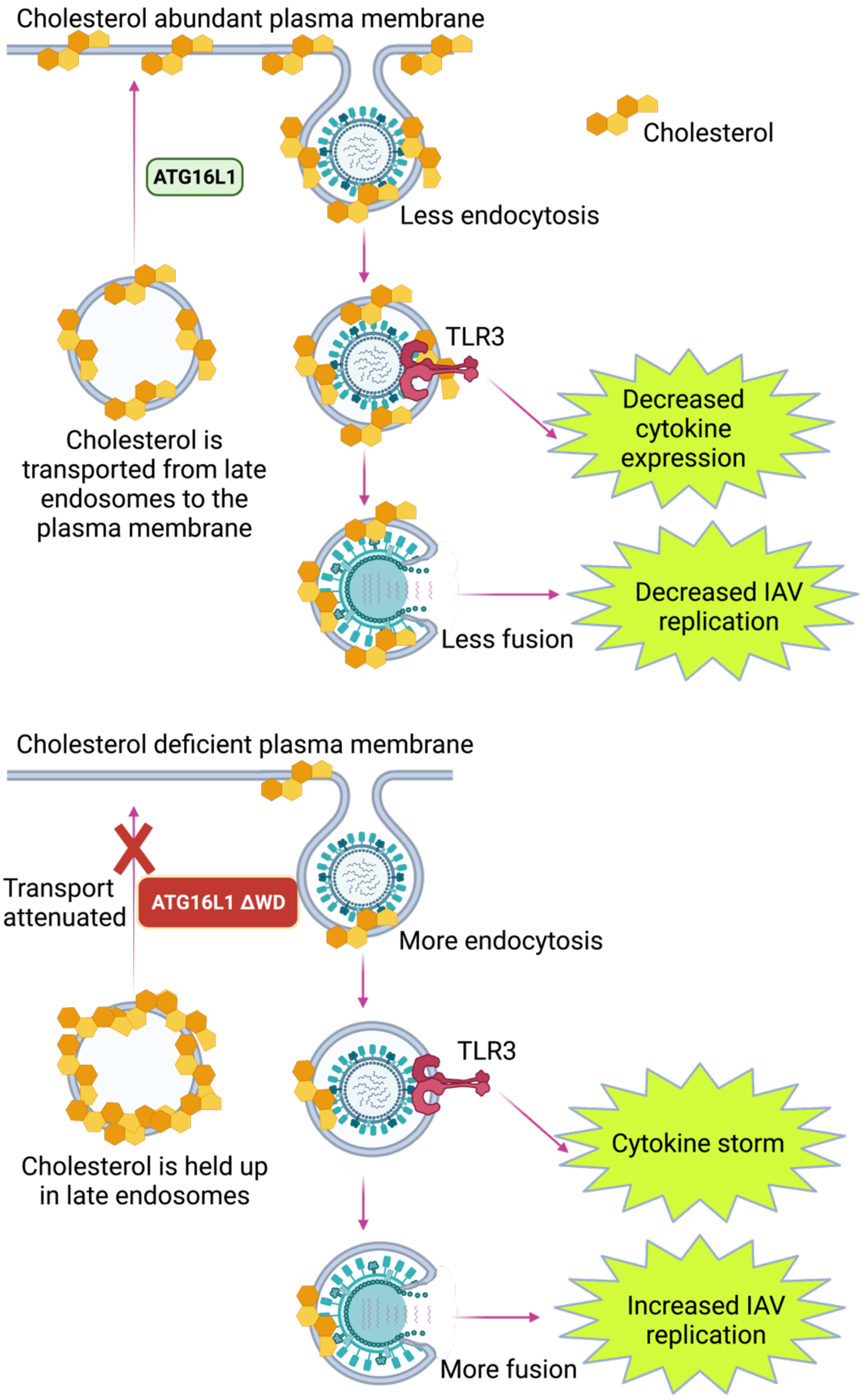

Figure 6.1: The WD domain of ATG16L1 has a role in the transport of cholesterol to the plasma membrane. Without the WD domain, late endosomal/lysosomal fusion cannot occur, preventing cholesterol egress to the plasma membrane. This results in increased endocytosis and fusion of IAV. In turn, this causes increased TLR3 activation causing cytokine storms and increased IAV replication. Produced using Biorender.

endo-lysosome membrane, a subsequent step in vesicle membrane fusion (78). Recently Sønder *et al.* (2021) demonstrated that plasma membrane damage initiates recruitment of actin and an accumulation of LC3 around the injury site. Like LAP, the process is dependent on rubicon. Macropinocytosis then internalises the damaged plasma membrane for fusion to lysosomes (80). Should ATG16L1 bind to the PM or lysosomal membrane via its WD domain then it may be involved in conjugating LC3, promoting the fusion of the PM and lysosomal membrane. Alternatively, ATG16L1 may be involved in another pathway that allows it promote lysosomal-PM fusion. Tan *et al.* (2018) did not find significant co-localisation between ATG16L1 and LAMP1 (lysosomes) suggesting that the protein was not directly involved in lysosomal-PM fusion (84). Exactly how the ATG16L1 protein facilitates this lysosomal-PM fusion would provide an exciting avenue for further research.

The results of this thesis have broad application with other viruses. IAV is a membrane enveloped virus that causes elevated cytokine levels that lead to inflammation and tissue damage. Other membraned viruses that cause cytokine storms include SARS-CoV, MERS-CoV and SARS-CoV-2 (365). The entry of these viruses is similar to IAV, entering by endocytosis and fusing to the endosomal membrane. The cholesterol content of endosomal membranes may affect their release into the cytoplasm. IFITM3 has been shown to cause cholesterol accumulation in the late endosome (138) with this protein also having been shown to inhibit the fusion of SARS-CoV-2 (366). This implicates cholesterol as being limiting in SARS-CoV-2 infection when it accumulates in endosomal membranes. Disruption in cholesterol homeostasis could promote infection if cholesterol was reduced in the endosomal membrane. My results demonstrate that the WD domain of ATG16L1 has a role in cholesterol homeostasis with reduced cholesterol at the PM. Investigation into the sterol content of the PM is warranted. 25-hydroxycholesterol (25HC) has antiviral properties, reducing the accessibility of cholesterol in membranes. 25HC treatment of the PM in WD deficient MEFs was seen to restrict IAV NP access to the cytoplasm implicating it in reducing viral fusion. Further work using high pressure gas or liquid chromatography would be used to analyse the sterol content of the subcellular fractions isolated in Chapter 3.

Tan *et al.* (2018) showed that the T300A mutation in ATG16L1, which could cause cleavage and loss of the WD domain, impairs cholesterol homeostasis. The T300A mutation is a risk allele for Crohn's disease and occurs naturally in the human population. The findings of this thesis have an important application to this mutation. Humans carrying this mutation would express an ATG16L1 protein prone to cleavage. Should the WD domain be lost this would impair cholesterol homeostasis within cells. These individuals could be more susceptible to IAV. Furthermore, what with cholesterol having a role in other viral infections, the T300A mutation in humans could increase susceptibility to other viruses, such as SARS-CoV-2. Our lab has generated a T300A mouse model and I very recently generated a MEF cell line from these mice. This mouse and cell line provide another avenue for further work. I would hypothesise that the T300A mutation in MEFs impairs cholesterol homeostasis due to the loss of the WD domain. I would also hypothesise that mice expressing this mutation would be more susceptible to IAV. The PM of T300A MEFs and tissue would be isolated and cholesterol content measured. The entry assays described in Chapter 4 could also be used to monitor IAV entry into T300A cells. Furthermore, to demonstrate the role of the WD domain in the limiting the infection by other viruses: the E230 (ΔWD) and the T300A mouse model could be crossed with a mouse expressing human ACE2, to see whether the loss of the WD domain or the T300A mutation enhances the infection of SARS-CoV-2.

As well as analysing the membrane cholesterol content of T300A mice, human cell lines expressing T300A could be used to investigate their susceptibility to IAV. Crohn's disease is characterised by severe intestinal inflammation and it has been recently shown that the WD domain of ATG16L1 interacts with the IL-10 receptor (IL-10R) and this interaction promotes endocytosis and trafficking of the receptor. This interaction may explain the pro-inflammatory phenotype seen in ATG16L1 deficient models (367). It is possible that the T300A mutation prevents this interaction with IL-10R and this could lead to a pro-inflammatory environment within the patient. This would be the subject of future study.

To conclude, the WD domain of ATG16L1 has a role in limiting lethal influenza infection. The WD domain has a role cholesterol transport from late endosomes/lysosomes to the PM. Cholesterol is transported to the PM via lysosomal exocytosis and while the exact nature of ATG16L1's role is unclear, the WD domain is needed to facilitate this process. Without the WD domain cholesterol accumulates within lysosomes and late endosomes and cholesterol in the PM is reduced. I showed that IAV fusion is enhanced to membranes with reduced cholesterol content. The WD domain has a role in limiting IAV endocytosis and fusion, with these mechanisms promoted in WD deficient cells. Finally, I showed that IAV is able to replicate to higher levels in WD deficient cells and that there is elevated cytokine signalling in WD deficient cells and tissue. These results open up further avenues of research, with the T300A mutation of ATG16L1 possibly impairing cholesterol homeostasis. Humans expressing the T300A mutation may also be more susceptible to IAV therefore further research into this is warranted.

Acknowledgements

There are two types of people currently reading this. Those that have read this thesis and finally reached this section, and those that have skipped to the end to see whether I've mentioned their name. To those that have read it, I'm sorry for having put you through this. While I have enjoyed writing this, even I have to admit, it's not the sort of reading you want to do reclined on an armchair. To the cheeky ones that haven't read it, I damn well hope I've acknowledged you.

Ten years ago, in 2011, I would have been starting my A-levels (AS levels to be precise) and more specifically, my extended project question. This was a small essay based project that you could focus on anything you fancied reading around. I decided to read into HIV and learn about virology. This topic led me to my undergraduate degree in Microbiology and subsequently to spend 4 years of my life researching the innate immune system and the influenza virus for a PhD. But the origin of all that was the fantastic supervision I got from two inspiring biology teachers Dr Sarah O'Connor and Dr Kevin Geall. Without them I would never have pursued science, at least not as far as I have done. Additionally, I've got to acknowledge my physics teacher, Mr Peter Hurry. He taught me to apply myself and work hard in environments where other people are more advantaged, aka are studying maths as well as physics, because who in their right mind just studies physics (me).

I would never have made it onto a PhD if it weren't for two people, one of those being Dr Gabriella Kelemen. Gabriella was a fantastic mentor in my undergraduate project and Masters year, teaching me the foundations of working in a lab and more importantly how to write scientifically (something which I'm still not perfect at yet, but getting there). I've also got to thank the members of that lab: Dr Gemma Cassettari, Dr Emily Alcock, Dr Elena Tan, Dr Sundeep Kau and Dr Michael Gillespie, all of whom I hope have been successful with their projects.

The other person I've got to thank, and still thank to this day is my dear friend Dr Rob Johnson. Rob has helped me with a number of either academic or fencing related favours over the course of my time here at UEA and has always been someone who I can rely on. Our coffee/hot chocolate breaks and quiz nights have been great respites from difficult days in the lab and he deserves all the praise in the world for the work he has done for me and others.

I have of course now got to thank the fantastic lab I work for. Team members old and new have all played a significant role in me being where I am today, whether it be through me supervising them or them helping me. A massive thank you to Dr Shashank Rai, Dr Weijiao Zhang, Maria Ramos, Charlotte Dixon, Luke Griffith and Dr Tim Pearson. Two members who deserve extra praise are Dr Yingxue Wang and Dr Matthew (the guru) Jefferson. Yingxue and I worked together almost immediately after me joining the lab and without her careful supervision I would not be the scientist I am today, so thank you. I don't think there are enough good things to say about Matt. He has helped me through so many protocols where I haven't had a clue and has had to put up with my oversized ordering lists. A massive thank you to him for helping me navigate myself around the DMU, and of course for being an excellent source of banter at the lab bench.

I am very privileged to have received great supervision during my PhD, and this supervision has come from two brilliant scientists: Prof. Tom Wileman and Dr Penny Powell. Tom has been an excellent source of criticism over the years without which I would not have honed my presentations and writing down to the critical points. I have come to appreciate how he presents science over the years and 'sell' his research, something which has inspired me and I hope will carry through to my future work. As for Penny, I don't think there are enough pages to praise you. She has been an absolute idol and an inspiration and if I become half the scientist she is over the course of my career I will be one very happy person. Her supervision has been next to none, working tirelessly on my manuscripts and drafts and helping me at the bench with difficult experiments. Thank you so much for making my PhD such a pleasure to work on. I wish them both all the best with their careers and hope they will keep in touch.

Other scientists and groups who I must thank are the Morris group and Chris Morris himself for allowing me to pinch reagents every now and then. With their/his permission of course. Also a big thank you to Dr Yohei Yamauchi and his lab over in Bristol for having me for a few weeks to work on the IAV entry assays. I learned a lot of fascinating virology techniques while over there that I know are going to play a role in future research. Thank you to Dr John McCauley for the influenza virus and thank you to Dr Gregory Fairn for the

D4H plasmid. Thank you to Prof. Paul Digard for agreeing to be my external examiner and for being able to examine me after such a short period of time following completion. I also would like to thank Andrew Loveday for being a fantastic tech for the BMRC. As well as that I would like to thank the team at the Norwich Research Park who facilitate the DTP. A thanks to Dr Sarah Eglington for helping me organise my PIPS placement and to Michael Corley at the British Society for Antimicrobial Chemotherapy for supervising my PIPS placement. I would also like to thank and recognise the funding received from the UKRI-BBSRC Norwich Research park Biosciences Doctoral training partnership to achieve my research (grant code: 100040071-R).

A massive thank you to friends and family as well. To Nathan Kelly and Tom Burke for the fantastic board game evenings. To Luke Daniels for the cheeky nights out. To all the amazing people from fencing: Nathan Gull, Caitlin Arthur, Otto Billström, Dr Kris Sales, Dr Martin Walters, Peter Gallop and Paul Stimpson. To Jade Eyles who has been so supportive over the course of the last couple of years, from feeding me to chauffeuring me about the county. I would definitely not be at the stage in my career that I am without you. Finally, a big thank you to my family: to my Mum and step-dad Andrew and to my Dad and step-mum Michelle, thank you for supporting me over the course of my degree and PhD. To my sisters Lucy, Lily and Emily, thank you for being available for a chat when I needed it and for brightening my days when I visited.

One thing I am not thanking though is the COVID-19 pandemic.

‘The future belongs to those who believe in the beauty of their dreams.’
Eleanor Roosevelt.

References

1. Yang Z, Klionsky DJ. Mammalian autophagy: core molecular machinery and signaling regulation. Curr Opin Cell Biol. 2010 Apr 1;22(2):124–31.

2. Romao S, Münz C. LC3-associated phagocytosis. Autophagy. 2014 Mar 3;10(3):526–8.

3. Xu Y, Eissa NT. Autophagy in Innate and Adaptive Immunity. Proc Am Thorac Soc. 2010 Feb 15;7(1):22–8.

4. Ohsumi Y. Molecular dissection of autophagy: two ubiquitin-like systems. Nat Rev Mol Cell Biol. 2001 Mar;2(3):211–6.

5. Martinez J, Malireddi RKS, Lu Q, Cunha LD, Pelletier S, Gingras S, et al. Molecular characterization of LC3-associated phagocytosis reveals distinct roles for Rubicon, NOX2 and autophagy proteins. Nat Cell Biol. 2015 Jul;17(7):893–906.

6. Martinez J, Almendinger J, Oberst A, Ness R, Dillon CP, Fitzgerald P, et al. Microtubule-associated protein 1 light chain 3 alpha (LC3)-associated phagocytosis is required for the efficient clearance of dead cells. Proc Natl Acad Sci. 2011 Oct 18;108(42):17396–401.

7. Wild P, McEwan DG, Dikic I. The LC3 interactome at a glance. J Cell Sci. 2014 Jan 1;127(1):3–9.

8. Mann SS, Hammarback JA. Molecular characterization of light chain 3. A microtubule binding subunit of MAP1A and MAP1B. J Biol Chem. 1994 Apr 15;269(15):11492–7.

9. Mehta P, Henault J, Kolbeck R, Sanjuan MA. Noncanonical autophagy: one small step for LC3, one giant leap for immunity. Curr Opin Immunol. 2014 Feb;26:69–75.

10. Shintani T, Klionsky DJ. Autophagy in Health and Disease: A Double-Edged Sword. Science. 2004 Nov 5;306(5698):990–5.

11. Sanjuan MA, Milasta S, Green DR. Toll-like receptor signaling in the lysosomal pathways. Immunol Rev. 2009;227(1):203–20.

12. Martinez J. LAP it up, fuzz ball: a short history of LC3-associated phagocytosis. Curr Opin Immunol. 2018 Dec 1;55:54–61.

13. Tam JM, Mansour MK, Khan NS, Seward M, Puranam S, Tanne A, et al. Dectin-1–Dependent LC3 Recruitment to Phagosomes Enhances Fungicidal Activity in Macrophages. J Infect Dis. 2014 Dec 1;210(11):1844–54.

14. Martinez J, Cunha LD, Park S, Yang M, Lu Q, Orchard R, et al. Noncanonical autophagy inhibits the autoinflammatory, lupus-like response to dying cells. Nature. 2016 May;533(7601):115–9.

15. Heckmann BL, Boada-Romero E, Cunha LD, Magne J, Green DR. LC3-Associated Phagocytosis and Inflammation. J Mol Biol. 2017 Nov 24;429(23):3561–76.

16. Itakura E, Kishi C, Inoue K, Mizushima N. Beclin 1 Forms Two Distinct Phosphatidylinositol 3-Kinase Complexes with Mammalian Atg14 and UVRAG. Mol Biol Cell. 2008 Oct 8;19(12):5360–72.

17. Matsunaga K, Saitoh T, Tabata K, Omori H, Satoh T, Kurotori N, et al. Two Beclin 1-binding proteins, Atg14L and Rubicon, reciprocally regulate autophagy at different stages. Nat Cell Biol. 2009 Apr;11(4):385–96.

18. Matsunaga K, Noda T, Yoshimori T. Binding Rubicon to cross the Rubicon. Autophagy. 2009 Aug 16;5(6):876–7.

19. Tanaka S, Hikita H, Tatsumi T, Sakamori R, Nozaki Y, Sakane S, et al. Rubicon inhibits autophagy and accelerates hepatocyte apoptosis and lipid accumulation in nonalcoholic fatty liver disease in mice. Hepatology. 2016;64(6):1994–2014.

20. Yang C-S, Lee J-S, Rodgers M, Min C-K, Lee J-Y, Kim HJ, et al. Autophagy Protein Rubicon Mediates Phagocytic NADPH Oxidase Activation in Response to Microbial Infection or TLR Stimulation. Cell Host Microbe. 2012 Mar 15;11(3):264–76.

21. Kim Y-R, Kim J-S, Gu S-J, Jo S, Kim S, Young Kim S, et al. Identification of highly potent and selective inhibitor, TIPTP, of the p22phox-Rubicon axis as a therapeutic agent for rheumatoid arthritis. Sci Rep [Internet]. 2020 Mar 12 [cited 2020 Apr 7];10.

22. Boyle KB, Randow F. Rubicon swaps autophagy for LAP. Nat Cell Biol. 2015 Jul;17(7):843–5.

23. Heckmann BL, Green DR. LC3-associated phagocytosis at a glance. J Cell Sci. 2019 20;132(5).

24. Wong S-W, Sil P, Martinez J. Rubicon: LC3-associated phagocytosis and beyond. FEBS J. 2017 Nov 20;1379–88.

25. Smith WL, Murphy RC. Oxidized Lipids Formed Non-enzymatically by Reactive Oxygen Species. J Biol Chem. 2008 Jun 6;283(23):15513–4.

26. Bochkov VN, Oskolkova OV, Birukov KG, Levonen A-L, Binder CJ, Stöckl J. Generation and Biological Activities of Oxidized Phospholipids. Antioxid Redox Signal. 2009 Aug 17;12(8):1009–59.

27. Tanida I, Mizushima N, Kiyooka M, Ohsumi M, Ueno T, Ohsumi Y, et al. Apg7p/Cvt2p: A Novel Protein-activating Enzyme Essential for Autophagy. Mol Biol Cell. 1999 May 1;10(5):1367–79.

28. Kaiser SE, Qiu Y, Coats JE, Mao K, Klionsky DJ, Schulman BA. Structures of Atg7-Atg3 and Atg7-Atg10 reveal noncanonical mechanisms of E2 recruitment by the autophagy E1. Autophagy. 2013 May 6;9(5):778–80.

29. Shintani T, Mizushima N, Ogawa Y, Matsuura A, Noda T, Ohsumi Y. Apg10p, a novel protein-conjugating enzyme essential for autophagy in yeast. EMBO J. 1999 Oct 1;18(19):5234–41.

30. Varshavsky A. The ubiquitin system. Trends Biochem Sci. 1997 Oct 1;22(10):383–7.

31. Codogno P, Meijer AJ. Atg5: more than an autophagy factor. Nat Cell Biol. 2006 Oct;8(10):1045–7.

32. Mizushima N, Noda T, Ohsumi Y. Apg16p is required for the function of the Apg12p–Apg5p conjugate in the yeast autophagy pathway. EMBO J. 1999 Jul 15;18(14):3888–96.

33. Xiong Q, Li W, Li P, Yang M, Wu C, Eichinger L. The Role of ATG16 in Autophagy and The Ubiquitin Proteasome System. Cells. 2018 20;8(1).

34. Kuma A, Mizushima N, Ishihara N, Ohsumi Y. Formation of the ~350-kDa Apg12-Apg5·Apg16 Multimeric Complex, Mediated by Apg16 Oligomerization, Is Essential for Autophagy in Yeast. J Biol Chem. 2002 May 24;277(21):18619–25.

35. Rockenfeller P, Koska M, Pietrocola F, Minois N, Knittelfelder O, Sica V, et al. Phosphatidylethanolamine positively regulates autophagy and longevity. Cell Death Differ. 2015 Mar;22(3):499–508.

36. Fujita N, Hayashi-Nishino M, Fukumoto H, Omori H, Yamamoto A, Noda T, et al. An Atg4B Mutant Hampers the Lipidation of LC3 Paralogues and Causes Defects in Autophagosome Closure. Mol Biol Cell. 2008 Sep 3;19(11):4651–9.

37. Klionsky DJ, Schulman BA. Dynamic regulation of macroautophagy by distinctive ubiquitin-like proteins. Nat Struct Mol Biol. 2014 Apr;21(4):336–45.

38. Scherz-Shouval R, Shvets E, Fass E, Shorer H, Gil L, Elazar Z. Reactive oxygen species are essential for autophagy and specifically regulate the activity of Atg4. EMBO J. 2007 Apr 4;26(7):1749–60.

39. Ichimura Y, Kirisako T, Takao T, Satomi Y, Shimonishi Y, Ishihara N, et al. A ubiquitin-like system mediates protein lipidation. Nature. 2000 Nov;408(6811):488–92.

40. Kim J, Dalton VM, Eggerton KP, Scott SV, Klionsky DJ. Apg7p/Cvt2p Is Required for the Cytoplasm-to-Vacuole Targeting, Macroautophagy, and Peroxisome Degradation Pathways. Mol Biol Cell. 1999 May 1;10(5):1337–51.

41. Yamada Y, Suzuki NN, Hanada T, Ichimura Y, Kumeta H, Fujioka Y, et al. The Crystal Structure of Atg3, an Autophagy-related Ubiquitin Carrier Protein (E2) Enzyme that Mediates Atg8 Lipidation. J Biol Chem. 2007 Mar 16;282(11):8036–43.

42. Geng J, Baba M, Nair U, Klionsky DJ. Quantitative analysis of autophagy-related protein stoichiometry by fluorescence microscopy. J Cell Biol. 2008 Jul 14;182(1):129–40.

43. Zhao YG, Zhang H. Autophagosome maturation: An epic journey from the ER to lysosomes. J Cell Biol. 2019 Mar 4;218(3):757–70.

44. Heckmann BL, Teubner BJW, Tummers B, Boada-Romero E, Harris L, Yang M, et al. LC3-Associated Endocytosis Facilitates β-Amyloid Clearance and Mitigates Neurodegeneration in Murine Alzheimer's Disease. Cell. 2019 Jul 25;178(3):536-551.e14.

45. Gluschko A, Herb M, Wiegmann K, Krut O, Neiss WF, Utermöhlen O, et al. The β2 Integrin Mac-1 Induces Protective LC3-Associated Phagocytosis of Listeria monocytogenes. Cell Host Microbe. 2018 Mar 14;23(3):324-337.e5.

46. Hubber A, Kubori T, Coban C, Matsuzawa T, Ogawa M, Kawabata T, et al. Bacterial secretion system skews the fate of Legionella -containing vacuoles towards LC3-associated phagocytosis. Sci Rep. 2017 Mar 20;7(1):1–17.

47. Sprenkeler EGG, Gresnigt MS, van de Veerdonk FL. LC3-associated phagocytosis: a crucial mechanism for antifungal host defence against Aspergillus fumigatus. Cell Microbiol. 2016 Sep 1;18(9):1208–16.

48. Chu H, Khosravi A, Kusumawardhani IP, Kwon AHK, Vasconcelos AC, Cunha LD, et al. Gene-microbiota interactions contribute to the pathogenesis of inflammatory bowel disease. Science. 2016 May 27;352(6289):1116–20.

49. Martin CJ, Peters KN, Behar SM. Macrophages clean up: efferocytosis and microbial control. Curr Opin Microbiol. 2014 Feb 1;17:17–23.

50. Korns DRP, Frasch SCP, Fernandez-Boyanapalli RP, Henson PMP, Bratton DLM. Modulation of Macrophage Efferocytosis in Inflammation. Front Immunol [Internet]. 2011 [cited 2020 Apr 17];2.

51. Elliott MR, Koster KM, Murphy PS. Efferocytosis Signaling in the Regulation of Macrophage Inflammatory Responses. J Immunol. 2017 Feb 15;198(4):1387–94.

52. Muñoz LE, Lauber K, Schiller M, Manfredi AA, Herrmann M. The role of defective clearance of apoptotic cells in systemic autoimmunity. Nat Rev Rheumatol. 2010 May;6(5):280–9.

53. Brown GD. Dectin-1: a signalling non-TLR pattern-recognition receptor. Nat Rev Immunol. 2006 Jan;6(1):33–43.

54. Ma J, Becker C, Lowell CA, Underhill DM. Dectin-1-triggered Recruitment of Light Chain 3 Protein to Phagosomes Facilitates Major Histocompatibility Complex Class II Presentation of Fungal-derived Antigens. J Biol Chem. 2012 May 10;287(41):34149–56.

55. Deen NS, Gong L, Naderer T, Devenish RJ, Kwok T. Analysis of the Relative Contribution of Phagocytosis, LC3-Associated Phagocytosis, and Canonical

Autophagy During Helicobacter pylori Infection of Macrophages. Helicobacter. 2015;20(6):449–59.

56. Oikonomou V, Renga G, De Luca A, Borghi M, Pariano M, Puccetti M, et al. Autophagy and LAP in the Fight against Fungal Infections: Regulation and Therapeutics [Internet]. Mediators of Inflammation. 2018 [cited 2020 Apr 18].

57. Mehta P, Henault J, Martinez J, Riggs J, Tian J, Clarke L, et al. LC3-associated phagocytosis mediates IFN-alpha secretion in response to DNA-immune complexes. (BA3P.207). J Immunol. 2014 May 1;192(1 Supplement):44.13-44.13.

58. Hayashi K, Taura M, Iwasaki A. The interaction between IKKα and LC3 promotes type I interferon production through the TLR9-containing LAPosome. Sci Signal [Internet]. 2018 May 1 [cited 2020 Apr 23];11(528).

59. Levy DE, García-Sastre A. The virus battles: IFN induction of the antiviral state and mechanisms of viral evasion. Cytokine Growth Factor Rev. 2001 Jun 1;12(2):143–56.

60. Henault J, Martinez J, Riggs JM, Tian J, Mehta P, Clarke L, et al. Noncanonical Autophagy Is Required for Type I Interferon Secretion in Response to DNA-Immune Complexes. Immunity. 2012 Dec 14;37(6):986–97.

61. Raso F, Sagadiev S, Du S, Gage E, Arkatkar T, Metzler G, et al. $\boldsymbol{\alpha}_v$ Integrins regulate germinal center B cell responses through noncanonical autophagy. J Clin Invest. 2018 Aug 31;128(9):4163–78.

62. Kim J-Y, Zhao H, Martinez J, Doggett TA, Kolesnikov AV, Tang PH, et al. Noncanonical Autophagy Promotes the Visual Cycle. Cell. 2013 Jul 18;154(2):365–76.

63. Rai S, Arasteh M, Jefferson M, Pearson T, Wang Y, Zhang W, et al. The ATG5-binding and coiled coil domains of ATG16L1 maintain autophagy and tissue homeostasis in mice independently of the WD domain required for LC3-associated phagocytosis. Autophagy. 2019;15(4):599–612.

64. Gammoh N, Florey O, Overholtzer M, Jiang X. Interaction between FIP200 and ATG16L1 distinguishes ULK1 complex–dependent and –independent autophagy. Nat Struct Mol Biol. 2013 Feb;20(2):144–9.

65. Dooley HC, Razi M, Polson HEJ, Girardin SE, Wilson MI, Tooze SA. WIPI2 links LC3 conjugation with PI3P, autophagosome formation, and pathogen clearance by recruiting Atg12-5-16L1. Mol Cell. 2014 Jul 17;55(2):238–52.

66. Fletcher K, Ulferts R, Jacquin E, Veith T, Gammoh N, Arasteh JM, et al. The WD40 domain of ATG16L1 is required for its non-canonical role in lipidation of LC3 at single membranes. EMBO J. 2018 Jan 9;e97840.

67. Dudley LJ, Cabodevilla AG, Makar AN, Sztacho M, Michelberger T, Marsh JA, et al. Intrinsic lipid binding activity of ATG16L1 supports efficient membrane anchoring and autophagy. EMBO J. 2019 May 2;38(9):e100554.

68. Mizushima N, Kuma A, Kobayashi Y, Yamamoto A, Matsubae M, Takao T, et al. Mouse Apg16L, a novel WD-repeat protein, targets to the autophagic isolation membrane with the Apg12-Apg5 conjugate. J Cell Sci. 2003 May 1;116(9):1679–88.

69. Lystad AH, Carlsson SR, Simonsen A. Toward the function of mammalian ATG12-ATG5-ATG16L1 complex in autophagy and related processes. Autophagy. 2019;15(8):1485–6.

70. Boada-Romero E, Letek M, Fleischer A, Pallauf K, Ramón-Barros C, Pimentel-Muiños FX. TMEM59 defines a novel ATG16L1-binding motif that promotes local activation of LC3. EMBO J. 2013 Feb 20;32(4):566–82.

71. Hu J, Li G, Qu L, Li N, Liu W, Xia D, et al. TMEM166/EVA1A interacts with ATG16L1 and induces autophagosome formation and cell death. Cell Death Dis. 2016 Aug;7(8):e2323–e2323.

72. Ullrich S, Münch A, Neumann S, Kremmer E, Tatzelt J, Lichtenthaler SF. The Novel Membrane Protein TMEM59 Modulates Complex Glycosylation, Cell Surface Expression, and Secretion of the Amyloid Precursor Protein. J Biol Chem. 2010 Feb 7;285(27):20664–74.

73. Gerlach JP, Jordens I, Tauriello DVF, Land-Kuper I van ‘t, Bugter JM, Noordstra I, et al. TMEM59 potentiates Wnt signaling by promoting signalosome formation. Proc Natl Acad Sci. 2018 Apr 24;115(17):E3996–4005.

74. Lystad AH, Carlsson SR, Ballina LR de la, Kauffman KJ, Nag S, Yoshimori T, et al. Distinct functions of ATG16L1 isoforms in membrane binding and LC3B lipidation in autophagy-related processes. Nat Cell Biol. 2019 Mar;21(3):372–83.

75. Boada-Romero E, Serramito-Gómez I, Sacristán MP, Boone DL, Xavier RJ, Pimentel-Muiños FX. The T300A Crohn’s disease risk polymorphism impairs function of the WD40 domain of ATG16L1. Nat Commun. 2016 Jun 8;7(1):1–13.

76. Lassen KG, Kuballa P, Conway KL, Patel KK, Becker CE, Peloquin JM, et al. Atg16L1 T300A variant decreases selective autophagy resulting in altered cytokine signaling and decreased antibacterial defense. Proc Natl Acad Sci. 2014 May 27;111(21):7741–6.

77. Kuballa P, Huett A, Rioux JD, Daly MJ, Xavier RJ. Impaired Autophagy of an Intracellular Pathogen Induced by a Crohn’s Disease Associated ATG16L1 Variant. Gay N, editor. PLoS ONE. 2008 Oct 13;3(10):e3391.

78. Wang Y, Sharma P, Jefferson M, Zhang W, Bone B, Kipar A, et al. Non-canonical autophagy functions of ATG16L1 in epithelial cells limit lethal infection by influenza A virus. EMBO J. 2021 Mar 15;40(6):e105543.

79. Wang Y, Sharma P, Jefferson M, Zhang W, Bone B, Kipar A, et al. Non-canonical autophagy functions of ATG16L1 in epithelial cells limit lethal infection by influenza A virus. EMBO J. 2021 Feb 15;n/a(n/a):e105543.

80. Sønder SL, Häger SC, Heitmann ASB, Frankel LB, Dias C, Simonsen AC, et al. Restructuring of the plasma membrane upon damage by LC3-associated macropinocytosis. Sci Adv. 2021 Jul 1;7(27):eabg1969.

81. Goodwin JM, Walkup WG, Hooper K, Li T, Kishi-Itakura C, Ng A, et al. GABARAP membrane conjugation sequesters the FLCN-FNIP tumor suppressor complex to activate TFEB and lysosomal biogenesis [Internet]. 2021 Feb [cited 2021 Aug 21] p. 2021.02.22.432209.

82. Ravikumar B, Moreau K, Jahreiss L, Puri C, Rubinsztein DC. Plasma membrane contributes to the formation of pre-autophagosomal structures. Nat Cell Biol. 2010 Aug;12(8):747–57.

83. Jefferson M, Bone B, Buck JL, Powell PP. The Autophagy Protein ATG16L1 Is Required for Sindbis Virus-Induced eIF2α Phosphorylation and Stress Granule Formation. Viruses. 2019 Dec 29;12(1):39.

84. Tan JMJ, Mellouk N, Osborne SE, Ammendolia DA, Dyer DN, Li R, et al. An ATG16L1-dependent pathway promotes plasma membrane repair and limits Listeria monocytogenes cell-to-cell spread. Nat Microbiol. 2018 Dec;3(12):1472–85.

85. Tan JMJ, Mellouk N, Brumell JH. An autophagy-independent role for ATG16L1: promoting lysosome-mediated plasma membrane repair. Autophagy. 2019 May 4;15(5):932–3.

86. Mouritsen OG. The liquid-ordered state comes of age. Biochim Biophys Acta BBA - Biomembr. 2010 Jul 1;1798(7):1286–8.

87. Nelson DL, Cox MM. Lehninger principles of biochemistry / David L. Nelson, Michael M. Cox. sixth. New York, NY : W.H. Freeman and Company ; Houndmills, Basingstoke : Macmillan Higher Education; 2013. 1198 p.

88. Simons K, Ikonen E. Functional rafts in cell membranes. Nature. 1997 Jun 5;387(6633):569–72.

89. Simons K, Ikonen E. How Cells Handle Cholesterol. Science. 2000 Dec 1;290(5497):1721–6.

90. Simons K, Ehehalt R. Cholesterol, lipid rafts, and disease. J Clin Invest. 2002 Sep 1;110(5):597–603.

91. Gaus K, Le Lay S, Balasubramanian N, Schwartz MA. Integrin-mediated adhesion regulates membrane order. J Cell Biol. 2006 Aug 28;174(5):725–34.

92. Toppozini L, Meinhardt S, Armstrong CL, Yamani Z, Kučerka N, Schmid F, et al. Structure of Cholesterol in Lipid Rafts. Phys Rev Lett. 2014 Nov 25;113(22):228101.

93. Simons K, Toomre D. Lipid rafts and signal transduction. Nat Rev Mol Cell Biol. 2000 Oct;1(1):31–9.

94. Zhang J, Pekosz A, Lamb RA. Influenza Virus Assembly and Lipid Raft Microdomains: a Role for the Cytoplasmic Tails of the Spike Glycoproteins. J Virol. 2000 May 15;74(10):4634–44.

95. Scheiffele P, Rietveld A, Wilk T, Simons K. Influenza Viruses Select Ordered Lipid Domains during Budding from the Plasma Membrane. J Biol Chem. 1999 Jan 22;274(4):2038–44.

96. Rossman JS, Lamb RA. Influenza virus assembly and budding. Virology. 2011 Mar 15;411(2):229–36.

97. Nayak DP, Balogun RA, Yamada H, Zhou ZH, Barman S. Influenza virus morphogenesis and budding. Virus Res. 2009 Aug 1;143(2):147–61.

98. Mahammad S, Parmryd I. Cholesterol Depletion Using Methyl-β-cyclodextrin. In: Owen DM, editor. Methods in Membrane Lipids [Internet]. New York, NY: Springer; 2015 [cited 2019 Dec 19]. p. 91–102. (Methods in Molecular Biology).

99. Barman S, Nayak DP. Lipid Raft Disruption by Cholesterol Depletion Enhances Influenza A Virus Budding from MDCK Cells. J Virol. 2007 Nov 15;81(22):12169–78.

100. Fitzgerald KA. The Interferon Inducible Gene: Viperin. J Interferon Cytokine Res. 2011 Jan;31(1):131–5.

101. Chin K-C, Cresswell P. Viperin (cig5), an IFN-inducible antiviral protein directly induced by human cytomegalovirus. Proc Natl Acad Sci. 2001 Dec 18;98(26):15125–30.

102. Wang X, Hinson ER, Cresswell P. The Interferon-Inducible Protein Viperin Inhibits Influenza Virus Release by Perturbing Lipid Rafts. Cell Host Microbe. 2007 Aug 16;2(2):96–105.

103. Imelli N, Meier O, Boucke K, Hemmi S, Greber UF. Cholesterol Is Required for Endocytosis and Endosomal Escape of Adenovirus Type 2. J Virol. 2004 Mar 15;78(6):3089–98.

104. Sieczkarski SB, Whittaker GR. Influenza Virus Can Enter and Infect Cells in the Absence of Clathrin-Mediated Endocytosis. J Virol. 2002 Oct 15;76(20):10455–64.

105. Sun X, Whittaker GR. Role for Influenza Virus Envelope Cholesterol in Virus Entry and Infection. J Virol. 2003 Dec;77(23):12543–51.

106. Alberts B, Johnson A, Lewis J, Raff M, Roberts K, Walter P. Transport into the Cell from the Plasma Membrane: Endocytosis. Mol Biol Cell 4th Ed [Internet]. 2002 [cited 2020 Jan 9];

107. Goldstein JL, Brown MS. The Cholesterol Quartet. Science. 2001 May 18;292(5520):1310–2.

108. Go G, Mani A. Low-Density Lipoprotein Receptor (LDLR) Family Orchestrates Cholesterol Homeostasis. Yale J Biol Med. 2012 Mar 29;85(1):19–28.

109. Abi-Mosleh L, Infante RE, Radhakrishnan A, Goldstein JL, Brown MS. Cyclodextrin overcomes deficient lysosome-to-endoplasmic reticulum transport of cholesterol in Niemann-Pick type C cells. Proc Natl Acad Sci. 2009 Nov 17;106(46):19316–21.

110. Maxfield FR, van Meer G. Cholesterol, the central lipid of mammalian cells. Curr Opin Cell Biol. 2010 Aug;22(4):422–9.

111. Vance JE, Peake KB. Function of the Niemann–Pick type C proteins and their bypass by cyclodextrin. Curr Opin Lipidol. 2011 Jun;22(3):204–9.

112. Naslavsky N, Rahajeng J, Rapaport D, Horowitz M, Caplan S. EHD1 regulates cholesterol homeostasis and lipid droplet storage. Biochem Biophys Res Commun. 2007 Jun 8;357(3):792–9.

113. Hao M, Lin SX, Karylowski OJ, Wüstner D, McGraw TE, Maxfield FR. Vesicular and Non-vesicular Sterol Transport in Living Cells the endocytic recycling compartment is a major sterol storage organelle. J Biol Chem. 2002 Apr 1;277(1):609–17.

114. Strauss JF, Kallen CB, Christenson LK, Watari H, Devoto L, Arakane F, et al. The steroidogenic acute regulatory protein (StAR): a window into the complexities of intracellular cholesterol trafficking. Recent Prog Horm Res. 1999;54:369–94; discussion 394-395.

115. Murphy D. The biogenesis and functions of lipid bodies in animals, plants and microorganisms. Prog Lipid Res. 2001 Sep;40(5):325–438.

116. Knævelsrud H, Simonsen A. Lipids in autophagy: Constituents, signaling molecules and cargo with relevance to disease. Biochim Biophys Acta BBA - Mol Cell Biol Lipids. 2012 Aug 1;1821(8):1133–45.

117. Gao Q, Goodman JM. The lipid droplet—a well-connected organelle. Front Cell Dev Biol [Internet]. 2015 Aug 12 [cited 2020 Jan 21];3.

118. Feng B, Xu L, Wang H, Yan X, Xue J, Liu F, et al. Atorvastatin exerts its anti-atherosclerotic effects by targeting the receptor for advanced glycation end products. Biochim Biophys Acta BBA - Mol Basis Dis. 2011 Sep 1;1812(9):1130–7.

119. Episcopio D, Aminov S, Benjamin S, Germain G, Datan E, Landazuri J, et al. Atorvastatin restricts the ability of influenza virus to generate lipid droplets and severely suppresses the replication of the virus. FASEB J. 2019 May 24;33(8):9516–25.

120. Kreutzberger AJB, Kiessling V, Tamm LK. High Cholesterol Obviates a Prolonged Hemifusion Intermediate in Fast SNARE-Mediated Membrane Fusion. Biophys J. 2015 Jul 21;109(2):319–29.

121. Chlanda P, Mekhedov E, Waters H, Schwartz CL, Fischer ER, Ryham RJ, et al. The hemifusion structure induced by influenza virus haemagglutinin is determined by physical properties of the target membranes. Nat Microbiol. 2016 Apr 18;1(6):1–8.

122. Nussbaum O, Rott R, Loyter A. Fusion of influenza virus particles with liposomes: requirement for cholesterol and virus receptors to allow fusion with and lysis of neutral but not of negatively charged liposomes. J Gen Virol. 1992 Nov;73 (Pt 11):2831–7.

123. Chernomordik LV, Leikina E, Frolov V, Bronk P, Zimmerberg J. An early stage of membrane fusion mediated by the low pH conformation of influenza hemagglutinin depends upon membrane lipids. J Cell Biol. 1997 Jan 13;136(1):81–93.

124. Lee C-J, Lin H-R, Liao C-L, Lin Y-L. Cholesterol Effectively Blocks Entry of Flavivirus. J Virol. 2008 Jul;82(13):6470–80.

125. Yu J, Li M, Wilkins J, Ding S, Swartz TH, Esposito AM, et al. IFITM Proteins Restrict HIV-1 Infection by Antagonizing the Envelope Glycoprotein. Cell Rep. 2015 Oct 6;13(1):145–56.

126. Savidis G, Perreira JM, Portmann JM, Meraner P, Guo Z, Green S, et al. The IFITMs Inhibit Zika Virus Replication. Cell Rep. 2016 Jun 14;15(11):2323–30.

127. Weidner JM, Jiang D, Pan X-B, Chang J, Block TM, Guo J-T. Interferon-Induced Cell Membrane Proteins, IFITM3 and Tetherin, Inhibit Vesicular Stomatitis Virus Infection via Distinct Mechanisms. J Virol. 2010 Dec 15;84(24):12646–57.

128. Brass AL, Huang I-C, Benita Y, John SP, Krishnan MN, Feeley EM, et al. The IFITM proteins mediate cellular resistance to influenza A H1N1 virus, West Nile virus, and dengue virus. Cell. 2009 Dec 24;139(7):1243–54.

129. Jaffe EA, Armellino D, Lam G, Cordon-Cardo C, Murray HW, Evans RL. IFN-gamma and IFN-alpha induce the expression and synthesis of Leu 13 antigen by cultured human endothelial cells. J Immunol. 1989 Dec 15;143(12):3961–6.

130. Feeley EM, Sims JS, John SP, Chin CR, Pertel T, Chen L-M, et al. IFITM3 Inhibits Influenza A Virus Infection by Preventing Cytosolic Entry. PLOS Pathog. 2011 Oct 27;7(10):e1002337.

131. Bailey CC, Huang I-C, Kam C, Farzan M. Ifitm3 Limits the Severity of Acute Influenza in Mice. PLoS Pathog [Internet]. 2012 Sep 6 [cited 2020 Jan 30];8(9).

132. Sohn M, Korzeniowski M, Zewe JP, Wills RC, Hammond GRV, Humpolickova J, et al. PI(4,5)P2 controls plasma membrane PI4P and PS levels via ORP5/8 recruitment to ER–PM contact sites. J Cell Biol. 2018 Feb 22;217(5):1797–813.

133. Vance JE, Tasseva G. Formation and function of phosphatidylserine and phosphatidylethanolamine in mammalian cells. Biochim Biophys Acta BBA - Mol Cell Biol Lipids. 2013 Mar 1;1831(3):543–54.

134. Levine TP, Munro S. The pleckstrin homology domain of oxysterol-binding protein recognises a determinant specific to Golgi membranes. Curr Biol. 1998 Jun 18;8(13):729–39.

135. Raychaudhuri S, Prinz WA. The Diverse Functions of Oxysterol-Binding Proteins. Annu Rev Cell Dev Biol. 2010;26(1):157–77.

136. Neefjes J, Cabukusta B. What the VAP: The Expanded VAP Family of Proteins Interacting With FFAT and FFAT-Related Motifs for Interorganellar Contact. Contact. 2021 Jan 1;4:25152564211012250.

137. Levine T. Short-range intracellular trafficking of small molecules across endoplasmic reticulum junctions. Trends Cell Biol. 2004 Sep 1;14(9):483–90.

138. Amini-Bavil-Olyaee S, Choi YJ, Lee JH, Shi M, Huang I-C, Farzan M, et al. The Antiviral Effector IFITM3 Disrupts Intracellular Cholesterol Homeostasis to Block Viral Entry. Cell Host Microbe. 2013 Apr 17;13(4):452–64.

139. Lu F, Liang Q, Abi-Mosleh L, Das A, De Brabander JK, Goldstein JL, et al. Identification of NPC1 as the target of U18666A, an inhibitor of lysosomal cholesterol export and Ebola infection. eLife. 2015 Dec 8;4:e12177.

140. Olsen BN, Schlesinger PH, Ory DS, Baker NA. 25-Hydroxycholesterol Increases the Availability of Cholesterol in Phospholipid Membranes. Biophys J. 2011 Feb 16;100(4):948–56.

141. Liu S-Y, Aliyari R, Chikere K, Li G, Marsden MD, Smith JK, et al. Interferon-Inducible Cholesterol-25-Hydroxylase Broadly Inhibits Viral Entry by Production of 25-Hydroxycholesterol. Immunity. 2013 Jan 24;38(1):92–105.

142. Sobo K, Blanc IL, Luyet P-P, Fivaz M, Ferguson C, Parton RG, et al. Late Endosomal Cholesterol Accumulation Leads to Impaired Intra-Endosomal Trafficking. PLoS ONE [Internet]. 2007 [cited 2020 Feb 6];2(9).

143. Yang S-T, Kreutzberger AJB, Lee J, Kiessling V, Tamm LK. The Role of Cholesterol in Membrane Fusion. Chem Phys Lipids. 2016 Sep;199:136–43.

144. Domanska MK, Wrona D, Kasson PM. Multiphasic Effects of Cholesterol on Influenza Fusion Kinetics Reflect Multiple Mechanistic Roles. Biophys J. 2013 Sep 17;105(6):1383–7.

145. Avula K, Singh B, Kumar PV, Syed GH. Role of Lipid Transfer Proteins (LTPs) in the Viral Life Cycle. Front Microbiol. 2021;12:1493.

146. Influenza (Seasonal) [Internet]. [cited 2020 Feb 18].

147. Thompson MG, Shay DK, Zhou H, Bridges CB, Cheng PY, Burns E, et al. Estimates of deaths associated with seasonal influenza - United States, 1976-2007. Morb Mortal Wkly Rep. 2010;59(33):1057–62.

148. Arriola CS, Anderson EJ, Baumbach J, Bennett N, Bohm S, Hill M, et al. Does Influenza Vaccination Modify Influenza Severity? Data on Older Adults Hospitalized With Influenza During the 2012−2013 Season in the United States. J Infect Dis. 2015 Oct 15;212(8):1200–8.

149. Peasah SK, Azziz-Baumgartner E, Breese J, Meltzer MI, Widdowson M-A. Influenza cost and cost-effectiveness studies globally--a review. Vaccine. 2013 Nov 4;31(46):5339–48.

150. Slonczewski JL, Foster JW. Microbiology : an evolving science / Joan L. Slonczewski, John W. Foster. Fourth edition. International student edition. New York: W.W. Norton & Company; 2017. 1174 p.

151. Fiers W, De Filette M, Birkett A, Neirynck S, Min Jou W. A “universal” human influenza A vaccine. Virus Res. 2004 Jul 1;103(1):173–6.

152. Boni MF. Vaccination and antigenic drift in influenza. Vaccine. 2008 Jul 18;26(Suppl 3):C8-14.

153. Treanor J. Influenza Vaccine — Outmaneuvering Antigenic Shift and Drift. N Engl J Med. 2004 Jan 15;350(3):218–20.

154. Webster RG. The importance of animal influenza for human disease. Vaccine. 2002 May 15;20:S16–20.

155. Shoham D. Review: Molecular evolution and the feasibility of an avian influenza virus becoming a pandemic strain—a conceptual shift. Virus Genes. 2006 Oct 1;33(2):127–32.

156. Duan L, Campitelli L, Fan XH, Leung YHC, Vijaykrishna D, Zhang JX, et al. Characterization of Low-Pathogenic H5 Subtype Influenza Viruses from Eurasia: Implications for the Origin of Highly Pathogenic H5N1 Viruses. J Virol. 2007 Jul;81(14):7529–39.

157. Yin J, Liu S, Zhu Y. An overview of the highly pathogenic H5N1 influenza virus. Virol Sin. 2013 Feb 1;28(1):3–15.

158. Compans RW, Content J, Duesberg PH. Structure of the Ribonucleoprotein of Influenza Virus. J Virol. 1972 Oct 1;10(4):795–800.

159. Eisfeld AJ, Neumann G, Kawaoka Y. At the centre: influenza A virus ribonucleoproteins. Nat Rev Microbiol. 2015 Jan;13(1):28–41.

160. Hagen M, Chung TD, Butcher JA, Krystal M. Recombinant influenza virus polymerase: requirement of both 5’ and 3’ viral ends for endonuclease activity. J Virol. 1994;68(3):1509–15.

161. Detjen BM, St Angelo C, Katze MG, Krug RM. The three influenza virus polymerase (P) proteins not associated with viral nucleocapsids in the infected cell are in the form of a complex. J Virol. 1987 Jan 1;61(1):16–22.

162. Palese P, Schulman JL. Mapping of the influenza virus genome: identification of the hemagglutinin and the neuraminidase genes. Proc Natl Acad Sci. 1976 Jun 1;73(6):2142–6.

163. Portela A, Digard P. The influenza virus nucleoprotein: a multifunctional RNA-binding protein pivotal to virus replication. J Gen Virol. 2002;83(4):723–34.

164. Lamb RA, Horvath CM. Diversity of coding strategies in influenza viruses. Trends Genet. 1991 Aug 1;7(8):261–6.

165. Noda T, Sagara H, Yen A, Takada A, Kida H, Cheng RH, et al. Architecture of ribonucleoprotein complexes in influenza A virus particles. Nature. 2006 Jan;439(7075):490–2.

166. Paterson D, Fodor E. Emerging Roles for the Influenza A Virus Nuclear Export Protein (NEP). PLoS Pathog [Internet]. 2012 Dec 6 [cited 2020 Mar 10];8(12).

167. Hilsch M, Goldenbogen B, Sieben C, Höfer CT, Rabe JP, Klipp E, et al. Influenza A Matrix Protein M1 Multimerizes upon Binding to Lipid Membranes. Biophys J. 2014 Aug 19;107(4):912–23.

168. Bouvier NM, Palese P. The biology of influenza viruses. Vaccine. 2008 Sep 12;26:D49–53.

169. Matrosovich MN, Matrosovich TY, Gray T, Roberts NA, Klenk H-D. Human and avian influenza viruses target different cell types in cultures of human airway epithelium. Proc Natl Acad Sci. 2004 Mar 30;101(13):4620–4.

170. Jiang S, Li R, Du L, Liu S. Roles of the hemagglutinin of influenza A virus in viral entry and development of antiviral therapeutics and vaccines. Protein Cell. 2010 Apr;1(4):342–54.

171. Shinya K, Ebina M, Yamada S, Ono M, Kasai N, Kawaoka Y. Influenza virus receptors in the human airway. Nature. 2006 Mar;440(7083):435–6.

172. Sieczkarski SB, Whittaker GR. Dissecting virus entry via endocytosis. J Gen Virol. 2002;83(7):1535–45.

173. Lakadamyali M, Rust MJ, Zhuang X. Endocytosis of influenza viruses. Microbes Infect. 2004 Aug 1;6(10):929–36.

174. de Vries E, Tscherne DM, Wienholts MJ, Cobos-Jiménez V, Scholte F, García-Sastre A, et al. Dissection of the Influenza A Virus Endocytic Routes Reveals Macropinocytosis as an Alternative Entry Pathway. PLoS Pathog [Internet]. 2011 Mar 31 [cited 2020 Mar 11];7(3).

175. Rust MJ, Lakadamyali M, Feng Zhang, Xiaowei Zhuang. Assembly of endocytic machinery around individual influenza viruses during viral entry. Nat Struct Mol Biol. 2004 Jun;11(6):567–73.

176. Huotari J, Helenius A. Endosome maturation. EMBO J. 2011 Aug 31;30(17):3481–500.

177. Simpson C, Yamauchi Y. Microtubules in Influenza Virus Entry and Egress. Viruses. 2020 Jan;12(1):117.

178. Yoshimura A, Ohnishi S. Uncoating of influenza virus in endosomes. J Virol. 1984 Aug 1;51(2):497–504.

179. Stegmann T. Membrane Fusion Mechanisms: The Influenza Hemagglutinin Paradigm and its Implications for Intracellular Fusion. Traffic. 2000 Aug 1;1(8):598–604.

180. Harrison SC. Viral membrane fusion. Nat Struct Mol Biol. 2008 Jul;15(7):690–8.

181. Pleschka S. Overview of Influenza Viruses. In: Richt JA, Webby RJ, editors. Swine Influenza [Internet]. Berlin, Heidelberg: Springer; 2013 [cited 2020 Mar 19]. p. 1–20. (Current Topics in Microbiology and Immunology).

182. Liang R, Swanson JMJ, Madsen JJ, Hong M, DeGrado WF, Voth GA. Acid activation mechanism of the influenza A M2 proton channel. Proc Natl Acad Sci. 2016 Nov 8;113(45):E6955–64.

183. Martin K, Helenius A. Transport of Incoming Influenza Virus Nucleocapsids into the Nucleus. J. Virol. 1991;65:13.

184. Bui M, Whittaker G, Helenius A. Effect of M1 protein and low pH on nuclear transport of influenza virus ribonucleoproteins. J Virol. 1996;70(12):8391–401.

185. Fontana J, Cardone G, Heymann JB, Winkler DC, Steven AC. Structural Changes in Influenza Virus at Low pH Characterized by Cryo-Electron Tomography. J Virol. 2012 Mar 15;86(6):2919–29.

186. Li S, Sieben C, Ludwig K, Höfer CT, Chiantia S, Herrmann A, et al. pH-Controlled Two-Step Uncoating of Influenza Virus. Biophys J. 2014 Apr 1;106(7):1447–56.

187. Martin K, Helenius A. Nuclear transport of influenza virus ribonucleoproteins: The viral matrix protein (M1) promotes export and inhibits import. Cell. 1991 Oct 4;67(1):117–30.

188. Stauffer S, Feng Y, Nebioglu F, Heilig R, Picotti P, Helenius A. Stepwise Priming by Acidic pH and a High K+ Concentration Is Required for Efficient Uncoating of Influenza A Virus Cores after Penetration. J Virol. 2014 Nov 15;88(22):13029–46.

189. Chiang M-J, Musayev FN, Kosikova M, Lin Z, Gao Y, Mosier PD, et al. Maintaining pH-dependent conformational flexibility of M1 is critical for efficient influenza A virus replication. Emerg Microbes Infect. 2017 Jan;6(1):1–11.

190. Yamauchi Y. Quantum dots crack the influenza uncoating puzzle. Proc Natl Acad Sci U S A. 2019 12;116(7):2404–6.

191. Chook Y, Blobel G. Karyopherins and nuclear import. Curr Opin Struct Biol. 2001 Dec 1;11(6):703–15.

192. Cros JF, Palese P. Trafficking of viral genomic RNA into and out of the nucleus: influenza, Thogoto and Borna disease viruses. Virus Res. 2003 Sep 1;95(1):3–12.

193. Wu WW, Sun Y-HB, Panté N. Nuclear import of influenza A viral ribonucleoprotein complexes is mediated by two nuclear localization sequences on viral nucleoprotein. Virol J. 2007 Jun 4;4(1):49.

194. Kalderon D, Roberts BL, Richardson WD, Smith AE. A short amino acid sequence able to specify nuclear location. Cell. 1984 Dec 1;39(3, Part 2):499–509.

195. Pemberton LF, Blobel G, Rosenblum JS. Transport routes through the nuclear pore complex. Curr Opin Cell Biol. 1998 Jun 1;10(3):392–9.

196. Wang P, Palese P, O’Neill RE. The NPI-1/NPI-3 (karyopherin alpha) binding site on the influenza a virus nucleoprotein NP is a nonconventional nuclear localization signal. J Virol. 1997 Mar 1;71(3):1850–6.

197. Cohen S, Au S, Panté N. How viruses access the nucleus. Biochim Biophys Acta BBA - Mol Cell Res. 2011 Sep 1;1813(9):1634–45.

198. Yamada M, Tachibana T, Imamoto N, Yoneda Y. Nuclear transport factor p10/NTF2 functions as a Ran-GDP dissociation inhibitor (Ran-GDI). Curr Biol CB. 1998 Dec 3;8(24):1339–42.

199. Krug RM. Priming of Influenza Viral RNA Transcription by Capped Heterologous RNAs. In: Shatkin AJ, editor. Initiation Signals in Viral Gene Expression [Internet]. Berlin, Heidelberg: Springer; 1981 [cited 2020 Mar 26]. p. 125–49. (Current Topics in Microbiology and Immunology).

200. Shi L, Galarza JM, Summers DF. Recombinant-baculovirus-expressed PB2 subunit of the influenza A virus RNA polymerase binds cap groups as an isolated subunit. Virus Res. 1996 Jun 1;42(1):1–9.

201. Ulmanen I, Broni BA, Krug RM. Role of two of the influenza virus core P proteins in recognizing cap 1 structures (m7GpppNm) on RNAs and in initiating viral RNA transcription. Proc Natl Acad Sci. 1981 Dec 1;78(12):7355–9.

202. Xing W, Barauskas O, Kirschberg T, Niedziela-Majka A, Clarke M, Birkus G, et al. Biochemical characterization of recombinant influenza A polymerase heterotrimer complex: Endonuclease activity and evaluation of inhibitors. PLoS ONE [Internet]. 2017 Aug 15 [cited 2020 Mar 26];12(8).

203. Luo GX, Luytjes W, Enami M, Palese P. The polyadenylation signal of influenza virus RNA involves a stretch of uridines followed by the RNA duplex of the panhandle structure. J Virol. 1991 Jun 1;65(6):2861–7.

204. Dubois J, Terrier O, Rosa-Calatrava M. Influenza Viruses and mRNA Splicing: Doing More with Less. Krug R, Palese P, editors. mBio. 2014 May 13;5(3):e00070-14.

205. Shapiro GI, Gurney T, Krug RM. Influenza virus gene expression: control mechanisms at early and late times of infection and nuclear-cytoplasmic transport of virus-specific RNAs. J Virol. 1987 Mar;61(3):764–73.

206. Pereira CF, Read EKC, Wise HM, Amorim MJ, Digard P. Influenza A Virus NS1 Protein Promotes Efficient Nuclear Export of Unspliced Viral M1 mRNA. J Virol. 91(15):e00528-17.

207. Read EKC, Digard P. Individual influenza A virus mRNAs show differential dependence on cellular NXF1/TAP for their nuclear export. J Gen Virol. 2010 May;91(Pt 5):1290–301.

208. Nakielny S, Dreyfuss G. Transport of Proteins and RNAs in and out of the Nucleus. Cell. 1999 Dec 23;99(7):677–90.

209. Matthew Michael W, Choi M, Dreyfuss G. A nuclear export signal in hnRNP A1: A signal-mediated, temperature-dependent nuclear protein export pathway. Cell. 1995 Nov 3;83(3):415–22.

210. Sidorenko Y, Reichl U. Structured model of influenza virus replication in MDCK cells. Biotechnol Bioeng. 2004;88(1):1–14.

211. Cassetti MC, Noah DL, Montelione GT, Krug RM. Efficient translation of mRNAs in influenza A virus-infected cells is independent of the viral 5′ untranslated region. Virology. 2001 Oct 25;289(2):180–5.

212. Luna S de la, Fortes P, Beloso A, Ortín J. Influenza virus NS1 protein enhances the rate of translation initiation of viral mRNAs. J Virol. 1995 Apr 1;69(4):2427–33.

213. Enami K, Sato TA, Nakada S, Enami M. Influenza virus NS1 protein stimulates translation of the M1 protein. J Virol. 1994 Mar 1;68(3):1432–7.

214. Katze MG, DeCorato D, Krug RM. Cellular mRNA translation is blocked at both initiation and elongation after infection by influenza virus or adenovirus. J Virol. 1986 Dec 1;60(3):1027–39.

215. Nemeroff ME, Barabino SML, Li Y, Keller W, Krug RM. Influenza Virus NS1 Protein Interacts with the Cellular 30 kDa Subunit of CPSF and Inhibits 3′ End Formation of Cellular Pre-mRNAs. Mol Cell. 1998 Jun 1;1(7):991–1000.

216. te Velthuis AJW, Fodor E. Influenza virus RNA polymerase: insights into the mechanisms of viral RNA synthesis. Nat Rev Microbiol. 2016 Aug;14(8):479–93.

217. Perez JT, Varble A, Sachidanandam R, Zlatev I, Manoharan M, García-Sastre A, et al. Influenza A virus-generated small RNAs regulate the switch from transcription to replication. Proc Natl Acad Sci U S A. 2010 Jun 22;107(25):11525–30.

218. York A, Hengrung N, Vreede FT, Huiskonen JT, Fodor E. Isolation and characterization of the positive-sense replicative intermediate of a negative-strand RNA virus. Proc Natl Acad Sci. 2013 Nov 5;110(45):E4238–45.

219. Carrique L, Fan H, Walker AP, Keown JR, Sharps J, Staller E, et al. Host ANP32A mediates the assembly of the influenza virus replicase. Nature. 2020 Nov;587(7835):638–43.

220. Martin K, Helenius A. Nuclear transport of influenza virus ribonucleoproteins: the viral matrix protein (M1) promotes export and inhibits import. Cell. 1991 Oct 4;67(1):117–30.

221. Baudin F, Petit I, Weissenhorn W, Ruigrok RWH. In Vitro Dissection of the Membrane and RNP Binding Activities of Influenza Virus M1 Protein. Virology. 2001 Mar;281(1):102–8.

222. Huang X, Liu T, Muller J, Levandowski RA, Ye Z. Effect of Influenza Virus Matrix Protein and Viral RNA on Ribonucleoprotein Formation and Nuclear Export. Virology. 2001 Sep;287(2):405–16.

223. Ye Z, Liu T, Offringa DP, McInnis J, Levandowski RA. Association of Influenza Virus Matrix Protein with Ribonucleoproteins. J Virol. 1999 Sep 1;73(9):7467–73.

224. The influenza virus NEP (NS2 protein) mediates the nuclear export of viral ribonucleoproteins. EMBO J. 1998 Jan 1;17(1):288–96.

225. Huang S, Chen J, Chen Q, Wang H, Yao Y, Chen J, et al. A Second CRM1-Dependent Nuclear Export Signal in the Influenza A Virus NS2 Protein Contributes to the Nuclear Export of Viral Ribonucleoproteins. J Virol. 2013 Jan 15;87(2):767–78.

226. Elster C, Larsen K, Gagnon J, Ruigrok RWH, Baudin F 1997. Influenza virus M1 protein binds to RNA through its nuclear localization signal. J Gen Virol. 78(7):1589–96.

227. Shimizu T, Takizawa N, Watanabe K, Nagata K, Kobayashi N. Crucial role of the influenza virus NS2 (NEP) C-terminal domain in M1 binding and nuclear export of vRNP. FEBS Lett. 2011 Jan 3;585(1):41–6.

228. Whittaker G, Bui M, Helenius A. Nuclear trafficking of influenza virus ribonuleoproteins in heterokaryons. J Virol. 1996 May;70(5):2743–56.

229. Babcock HP, Chen C, Zhuang X. Using Single-Particle Tracking to Study Nuclear Trafficking of Viral Genes. Biophys J. 2004 Oct 1;87(4):2749–58.

230. Digard P, Elton D, Bishop K, Medcalf E, Weeds A, Pope B. Modulation of Nuclear Localization of the Influenza Virus Nucleoprotein through Interaction with Actin Filaments. J Virol. 1999;73(3):2222–31.

231. Amorim MJ, Bruce EA, Read EKC, Foeglein Á, Mahen R, Stuart AD, et al. A Rab11- and Microtubule-Dependent Mechanism for Cytoplasmic Transport of Influenza A Virus Viral RNA. J Virol. 2011 May 1;85(9):4143–56.

232. Nturibi E, Bhagwat AR, Coburn S, Myerburg MM, Lakdawala SS. Intracellular Colocalization of Influenza Viral RNA and Rab11A Is Dependent upon Microtubule Filaments. J Virol [Internet]. 2017 Oct 1 [cited 2020 Mar 30];91(19).

233. Momose F, Kikuchi Y, Komase K, Morikawa Y. Visualization of microtubule-mediated transport of influenza viral progeny ribonucleoprotein. Microbes Infect. 2007 Oct 1;9(12):1422–33.

234. Bruce EA, Stuart A, McCaffrey MW, Digard P. Role of the Rab11 pathway in negative-strand virus assembly. Biochem Soc Trans. 2012 Dec 1;40(6):1409–15.

235. Vale-Costa S, Alenquer M, Sousa AL, Kellen B, Ramalho J, Tranfield EM, et al. Influenza A virus ribonucleoproteins modulate host recycling by competing with Rab11 effectors. J Cell Sci. 2016 Apr 15;129(8):1697–710.

236. Alenquer M, Vale-Costa S, Sousa AL, Etibor TA, Ferreira F, Amorim MJ. Influenza A Virus Ribonucleoproteins Form Liquid Organelles at Endoplasmic Reticulum Exit Sites. Nat Commun. 2019 Apr 9;10(1):1629. doi: 10.1038/s41467-019-09549-4.

237. Giese S, Bolte H, Schwemmle M. The Feat of Packaging Eight Unique Genome Segments. Viruses. 2016 Jun;8(6):165.

238. Barman S, Adhikary L, Chakrabarti AK, Bernas C, Kawaoka Y, Nayak DP. Role of Transmembrane Domain and Cytoplasmic Tail Amino Acid Sequences of Influenza A Virus Neuraminidase in Raft Association and Virus Budding. J Virol. 2004 May 15;78(10):5258–69.

239. Kordyukova LV, Serebryakova MV, Baratova LA, Veit M. S Acylation of the Hemagglutinin of Influenza Viruses: Mass Spectrometry Reveals Site-Specific Attachment of Stearic Acid to a Transmembrane Cysteine. J Virol. 2008 Sep;82(18):9288–92.

240. Bajimaya S, Frankl T, Hayashi T, Takimoto T. Cholesterol is required for stability and infectivity of influenza A and respiratory syncytial viruses. Virology. 2017 Oct 1;510:234–41.

241. Takeda M, Leser GP, Russell CJ, Lamb RA. Influenza virus hemagglutinin concentrates in lipid raft microdomains for efficient viral fusion. Proc Natl Acad Sci U S A. 2003 Dec 9;100(25):14610–7.

242. Chen BJ, Leser GP, Morita E, Lamb RA. Influenza Virus Hemagglutinin and Neuraminidase, but Not the Matrix Protein, Are Required for Assembly and Budding of Plasmid-Derived Virus-Like Particles. J Virol. 2007 Jul 1;81(13):7111–23.

243. Lai JCC, Chan WWL, Kien F, Nicholls JM, Peiris JSM, Garcia J-M. Formation of virus-like particles from human cell lines exclusively expressing influenza neuraminidase. J Gen Virol. 2010;91(9):2322–30.

244. Jin H, Leser GP, Zhang J, Lamb RA. Influenza virus hemagglutinin and neuraminidase cytoplasmic tails control particle shape. EMBO J. 1997 Mar 15;16(6):1236–47.

245. Elleman CJ, Barclay WS. The M1 matrix protein controls the filamentous phenotype of influenza A virus. Virology. 2004 Mar 30;321(1):144–53.

246. Chen BJ, Leser GP, Jackson D, Lamb RA. The Influenza Virus M2 Protein Cytoplasmic Tail Interacts with the M1 Protein and Influences Virus Assembly at the Site of Virus Budding. J Virol. 2008 Oct 15;82(20):10059–70.

247. Rossman JS, Jing X, Leser GP, Lamb RA. Influenza virus M2 protein mediates ESCRT-independent membrane scission. Cell. 2010 Sep 17;142(6):902–13.

248. Rossman JS, Lamb RA. Viral Membrane Scission. Annu Rev Cell Dev Biol. 2013;29(1):551–69.

249. Air GM, Laver WG. The neuraminidase of influenza virus. Proteins. 1989;6(4):341–56.

250. Russell CJ, Hu M, Okda FA. Influenza Hemagglutinin Protein Stability, Activation, and Pandemic Risk. Trends Microbiol. 2018 Oct 1;26(10):841–53.

251. Liu Q, Zhou Y, Yang Z. The cytokine storm of severe influenza and development of immunomodulatory therapy. Cell Mol Immunol. 2016 Jan;13(1):3–10.

252. Hashimoto C, Hudson KL, Anderson KV. The Toll gene of drosophila, required for dorsal-ventral embryonic polarity, appears to encode a transmembrane protein. Cell. 1988 Jan 29;52(2):269–79.

253. Takeda K, Akira S. TLR signaling pathways. Semin Immunol. 2004 Feb 1;16(1):3–9.

254. Akira S. TLR Signaling. In: Pulendran B, Ahmed R, editors. From Innate Immunity to Immunological Memory [Internet]. Berlin, Heidelberg: Springer; 2006 [cited 2020 May 3]. p. 1–16. (Current Topics in Microbiology and Immunology).

255. Akira S, Uematsu S, Takeuchi O. Pathogen Recognition and Innate Immunity. Cell. 2006 Feb 24;124(4):783–801.

256. Kawai T, Akira S. TLR signaling. Semin Immunol. 2007 Feb 1;19(1):24–32.

257. Greene CM, Carroll TP, Smith SGJ, Taggart CC, Devaney J, Griffin S, et al. TLR-Induced Inflammation in Cystic Fibrosis and Non-Cystic Fibrosis Airway Epithelial Cells. J Immunol. 2005 Feb 1;174(3):1638–46.

258. Schaefer TM, Desouza K, Fahey JV, Beagley KW, Wira CR. Toll-like receptor (TLR) expression and TLR-mediated cytokine/chemokine production by human uterine epithelial cells. Immunology. 2004;112(3):428–36.

259. Seibl R, Birchler T, Loeliger S, Hossle JP, Gay RE, Saurenmann T, et al. Expression and Regulation of Toll-Like Receptor 2 in Rheumatoid Arthritis Synovium. Am J Pathol. 2003 Apr 1;162(4):1221–7.

260. Kim Y-M, Brinkmann MM, Paquet M-E, Ploegh HL. UNC93B1 delivers nucleotide-sensing toll-like receptors to endolysosomes. Nature. 2008 Mar;452(7184):234–8.

261. Toscano F, Estornes Y, Virard F, Garcia-Cattaneo A, Pierrot A, Vanbervliet B, et al. Cleaved/Associated TLR3 Represents the Primary Form of the Signaling Receptor. J Immunol. 2013 Jan 15;190(2):764–73.

262. Ewald SE, Lee BL, Lau L, Wickliffe KE, Shi G-P, Chapman HA, et al. The ectodomain of Toll-like receptor 9 is cleaved to generate a functional receptor. Nature. 2008 Dec;456(7222):658–62.

263. Schille S, Crauwels P, Bohn R, Bagola K, Walther P, van Zandbergen G. LC3-associated phagocytosis in microbial pathogenesis. Int J Med Microbiol. 2018 Jan 1;308(1):228–36.

264. Kawasaki T, Kawai T. Toll-Like Receptor Signaling Pathways. Front Immunol [Internet]. 2014 [cited 2020 May 3];5.

265. Kawai T, Akira S. Toll-like receptors and their crosstalk with other innate receptors in infection and immunity. Immunity. 2011 May 27;34(5):637–50.

266. Blasius AL, Beutler B. Intracellular Toll-like Receptors. Immunity. 2010 Mar 26;32(3):305–15.

267. Wang T, Town T, Alexopoulou L, Anderson JF, Fikrig E, Flavell RA. Toll-like receptor 3 mediates West Nile virus entry into the brain causing lethal encephalitis. Nat Med. 2004 Dec;10(12):1366–73.

268. Tabeta K, Georgel P, Janssen E, Du X, Hoebe K, Crozat K, et al. Toll-like receptors 9 and 3 as essential components of innate immune defense against mouse cytomegalovirus infection. Proc Natl Acad Sci. 2004 Mar 9;101(10):3516–21.

269. Wu W, Zhang W, Duggan ES, Booth JL, Zou M-H, Metcalf JP. RIG-I and TLR3 are both required for maximum interferon induction by influenza virus in human lung alveolar epithelial cells. Virology. 2015 Aug 1;482:181–8.

270. Majde JA, Kapás L, Bohnet SG, De A, Krueger JM. Attenuation of the influenza virus sickness behavior in mice deficient in Toll-like receptor 3. Brain Behav Immun. 2010 Feb 1;24(2):306–15.

271. Könner AC, Brüning JC. Toll-like receptors: linking inflammation to metabolism. Trends Endocrinol Metab. 2011 Jan 1;22(1):16–23.

272. Vijay K. Toll-like receptors in immunity and inflammatory diseases: Past, present, and future. Int Immunopharmacol. 2018 Jun 1;59:391–412.

273. Bekeredjian-Ding IB, Wagner M, Hornung V, Giese T, Schnurr M, Endres S, et al. Plasmacytoid Dendritic Cells Control TLR7 Sensitivity of Naive B Cells via Type I IFN. J Immunol. 2005 Apr 1;174(7):4043–50.

274. Saitoh T, Satoh T, Yamamoto N, Uematsu S, Takeuchi O, Kawai T, et al. Antiviral Protein Viperin Promotes Toll-like Receptor 7- and Toll-like Receptor 9-Mediated Type I Interferon Production in Plasmacytoid Dendritic Cells. Immunity. 2011 Mar 25;34(3):352–63.

275. Honda K, Yanai H, Mizutani T, Negishi H, Shimada N, Suzuki N, et al. Role of a transductional-transcriptional processor complex involving MyD88 and IRF-7 in Toll-like receptor signaling. Proc Natl Acad Sci. 2004 Oct 26;101(43):15416–21.

276. Fuchsberger M, Hochrein H, O'Keeffe M. Activation of plasmacytoid dendritic cells. Immunol Cell Biol. 2005;83(5):571–7.

277. Jiang X, Chen ZJ. The role of ubiquitylation in immune defence and pathogen evasion. Nat Rev Immunol. 2012 Jan;12(1):35–48.

278. Chang M, Jin W, Sun S-C. Peli1 facilitates TRIF-dependent Toll-like receptor signaling and proinflammatory cytokine production. Nat Immunol. 2009 Oct;10(10):1089–95.

279. Smith H, Liu X-Y, Dai L, Goh ETH, Chan A-T, Xi J, et al. The role of TBK1 and IKKϵ in the expression and activation of Pellino 1. Biochem J. 2011 Mar 15;434(3):537–48.

280. Kollewe C, Mackensen A-C, Neumann D, Knop J, Cao P, Li S, et al. Sequential Autophosphorylation Steps in the Interleukin-1 Receptor-associated Kinase-1 Regulate its Availability as an Adapter in Interleukin-1 Signaling. J Biol Chem. 2004 Feb 13;279(7):5227–36.

281. Génin P, Vaccaro A, Civas A. The role of differential expression of human interferon-A genes in antiviral immunity. Cytokine Growth Factor Rev. 2009 Aug 1;20(4):283–95.

282. Randall RE, Goodbourn S. Interferons and viruses: an interplay between induction, signalling, antiviral responses and virus countermeasures. J Gen Virol. 2008;89(1):1–47.

283. Morales DJ, Lenschow DJ. The Antiviral Activities of ISG15. J Mol Biol. 2013 Dec 13;425(24):4995–5008.

284. Habjan M, Hubel P, Lacerda L, Benda C, Holze C, Eberl CH, et al. Sequestration by IFIT1 Impairs Translation of 2′O-unmethylated Capped RNA. PLoS Pathog [Internet]. 2013 Oct 3 [cited 2020 May 5];9(10).

285. Ablasser A, Chen ZJ. cGAS in action: Expanding roles in immunity and inflammation. Science [Internet]. 2019 Mar 8 [cited 2021 Sep 2];

286. Decout A, Katz JD, Venkatraman S, Ablasser A. The cGAS–STING pathway as a therapeutic target in inflammatory diseases. Nat Rev Immunol. 2021 Sep;21(9):548–69.

287. Cunha LD, Yang M, Carter R, Guy C, Harris L, Crawford JC, et al. LC3-associated phagocytosis in myeloid cells promotes tumor immune tolerance. Cell. 2018 Oct 4;175(2):429-441.e16.

288. Karpus ON, Heutinck KM, Wijnker PJM, Tak PP, Hamann J. Triggering of the dsRNA Sensors TLR3, MDA5, and RIG-I Induces CD55 Expression in Synovial Fibroblasts. PLoS ONE [Internet]. 2012 May 10 [cited 2020 May 6];7(5).

289. Mikkelsen SS, Jensen SB, Chiliveru S, Melchjorsen J, Julkunen I, Gaestel M, et al. RIG-I-mediated Activation of p38 MAPK Is Essential for Viral Induction of Interferon and Activation of Dendritic Cells dependence on TRAF2 and TAK1. J Biol Chem. 2009 Apr 17;284(16):10774–82.

290. Schlee M, Hartmann G. The Chase for the RIG-I Ligand—Recent Advances. Mol Ther. 2010 Jul 1;18(7):1254–62.

291. Uzri D, Gehrke L. Nucleotide Sequences and Modifications That Determine RIG-I/RNA Binding and Signaling Activities. J Virol. 2009 May 1;83(9):4174–84.

292. Rehwinkel J, Tan CP, Goubau D, Schulz O, Pichlmair A, Bier K, et al. RIG-I Detects Viral Genomic RNA during Negative-Strand RNA Virus Infection. Cell. 2010 Feb 5;140(3):397–408.

293. Kato H, Takeuchi O, Sato S, Yoneyama M, Yamamoto M, Matsui K, et al. Differential roles of MDA5 and RIG-I helicases in the recognition of RNA viruses. Nature. 2006 May;441(7089):101–5.

294. Chen X, Yang X, Zheng Y, Yang Y, Xing Y, Chen Z. SARS coronavirus papain-like protease inhibits the type I interferon signaling pathway through interaction with the STING-TRAF3-TBK1 complex. Protein Cell. 2014 May 1;5(5):369–81.

295. Siu K-L, Yeung ML, Kok K-H, Yuen K-S, Kew C, Lui P-Y, et al. Middle East Respiratory Syndrome Coronavirus 4a Protein Is a Double-Stranded RNA-Binding Protein That Suppresses PACT-Induced Activation of RIG-I and MDA5 in the Innate Antiviral Response. J Virol. 2014 May 1;88(9):4866–76.

296. Zou J, Chang M, Nie P, Secombes CJ. Origin and evolution of the RIG-I like RNA helicase gene family. BMC Evol Biol. 2009 Apr 28;9(1):85.

297. Yoneyama M, Kikuchi M, Natsukawa T, Shinobu N, Imaizumi T, Miyagishi M, et al. The RNA helicase RIG-I has an essential function in double-stranded RNA-induced innate antiviral responses. Nat Immunol. 2004 Jul;5(7):730–7.

298. Saito T, Hirai R, Loo Y-M, Owen D, Johnson CL, Sinha SC, et al. Regulation of innate antiviral defenses through a shared repressor domain in RIG-I and LGP2. Proc Natl Acad Sci. 2007 Jan 9;104(2):582–7.

299. Kageyama M, Takahasi K, Narita R, Hirai R, Yoneyama M, Kato H, et al. 55 Amino acid linker between helicase and carboxyl terminal domains of RIG-I functions as a critical repression domain and determines inter-domain conformation. Biochem Biophys Res Commun. 2011 Nov 11;415(1):75–81.

300. Jiang F, Ramanathan A, Miller MT, Tang G-Q, Gale M, Patel SS, et al. Structural basis of RNA recognition and activation by innate immune receptor RIG-I. Nature. 2011 Nov;479(7373):423–7.

301. Civril F, Bennett M, Moldt M, Deimling T, Witte G, Schiesser S, et al. The RIG-I ATPase domain structure reveals insights into ATP-dependent antiviral signalling. EMBO Rep. 2011 Nov 1;12(11):1127–34.

302. Takahasi K, Yoneyama M, Nishihori T, Hirai R, Kumeta H, Narita R, et al. Nonself RNA-Sensing Mechanism of RIG-I Helicase and Activation of Antiviral Immune Responses. Mol Cell. 2008 Feb 29;29(4):428–40.

303. Zeng W, Sun L, Jiang X, Chen X, Hou F, Adhikari A, et al. Reconstitution of the RIG-I Pathway Reveals a Signaling Role of Unanchored Polyubiquitin Chains in Innate Immunity. Cell. 2010 Apr 16;141(2):315–30.

304. Jiang X, Kinch LN, Brautigam CA, Chen X, Du F, Grishin NV, et al. Ubiquitin-Induced Oligomerization of the RNA Sensors RIG-I and MDA5 Activates Antiviral Innate Immune Response. Immunity. 2012 Jun 29;36(6):959–73.

305. Okazaki T, Higuchi M, Gotoh Y. Mitochondrial localization of the antiviral signaling adaptor IPS-1 is important for its induction of caspase activation. Genes Cells. 2013;18(6):493–501.

306. Seth RB, Sun L, Ea C-K, Chen ZJ. Identification and Characterization of MAVS, a Mitochondrial Antiviral Signaling Protein that Activates NF-κB and IRF3. Cell. 2005 Sep 9;122(5):669–82.

307. Wu B, Hur S. How RIG-I like receptors activate MAVS. Curr Opin Virol. 2015 Jun 1;12:91–8.

308. Saha SK, Pietras EM, He JQ, Kang JR, Liu S-Y, Oganesyan G, et al. Regulation of antiviral responses by a direct and specific interaction between TRAF3 and Cardif. EMBO J. 2006 Jul 26;25(14):3257–63.

309. Li L, Yang R, Feng M, Guo Y, Wang Y, Guo J, et al. Rig-I is involved in inflammation through the IPS-1/TRAF6 pathway in astrocytes under chemical hypoxia. Neurosci Lett. 2018 Apr 13;672:46–52.

310. Guo B, Cheng G. Modulation of the Interferon Antiviral Response by the TBK1/IKKi Adaptor Protein TANK. J Biol Chem. 2007 Apr 20;282(16):11817–26.

311. Sasai M, Shingai M, Funami K, Yoneyama M, Fujita T, Matsumoto M, et al. NAK-Associated Protein 1 Participates in Both the TLR3 and the Cytoplasmic Pathways in Type I IFN Induction. J Immunol. 2006 Dec 15;177(12):8676–83.

312. Zhao T, Yang L, Sun Q, Arguello M, Ballard DW, Hiscott J, et al. The NEMO adaptor bridges the nuclear factor-κB and interferon regulatory factor signaling pathways. Nat Immunol. 2007 Jun;8(6):592–600.

313. Kolakofsky D, Kowalinski E, Cusack S. A structure-based model of RIG-I activation. RNA. 2012 Jan 12;18(12):2118–27.

314. Yoneyama M, Fujita T. RNA recognition and signal transduction by RIG-I-like receptors. Immunol Rev. 2009 Jan 1;227(1):54–65.

315. Liu R, An L, Liu G, Li X, Tang W, Chen X. Mouse lung slices: An ex vivo model for the evaluation of antiviral and anti-inflammatory agents against influenza viruses. Antiviral Res. 2015 Aug;120:101–11.

316. Thomas F, Magill TP. Vaccination of Human Subjects with Virus of Human Influenza. Proc Soc Exp Biol Med. 1936 Jan 1;33(4):604–6.

317. Influenza Research Database - Strain A/X-31(H3N2) [Internet]. [cited 2020 Jun 22].

318. Universitätsklinikum Heidelberg: Downloads [Internet]. [cited 2020 Dec 26].

319. Baer A, Kehn-Hall K. Viral Concentration Determination Through Plaque Assays: Using Traditional and Novel Overlay Systems. JoVE J Vis Exp. 2014 Nov 4;(93):e52065.

320. Niehof M, Hildebrandt T, Danov O, Arndt K, Koschmann J, Dahlmann F, et al. RNA isolation from precision-cut lung slices (PCLS) from different species. BMC Res Notes. 2017 Mar 9;10:121.

321. Pfaffl MW. A new mathematical model for relative quantification in real-time RT–PCR. Nucleic Acids Res. 2001 May 1;29(9):e45.

322. Sakai T, Ohuchi M, Imai M, Mizuno T, Kawasaki K, Kuroda K, et al. Dual Wavelength Imaging Allows Analysis of Membrane Fusion of Influenza Virus inside Cells. J Virol. 2006 Feb;80(4):2013–8.

323. Banerjee I, Miyake Y, Nobs SP, Schneider C, Horvath P, Kopf M, et al. Influenza A virus uses the aggresome processing machinery for host cell entry. Science. 2014 Oct 24;346(6208):473–7.

324. Miyake Y, Keusch JJ, Decamps L, Ho-Xuan H, Iketani S, Gut H, et al. Influenza virus uses transportin 1 for vRNP debundling during cell entry. Nat Microbiol. 2019 Apr;4(4):578–86.

325. Saha P, Shumate JL, Caldwell JG, Elghobashi-Meinhardt N, Lu A, Zhang L, et al. Inter-domain dynamics drive cholesterol transport by NPC1 and NPC1L1 proteins. eLife. 9:e57089.

326. Myant NB. Cholesterol metabolism. J Clin Pathol. 1973 Jan 1;s1-5(1):1–4.

327. Kruth HS, Fry DL. Histochemical detection and differentiation of free and esterified cholesterol in swine atherosclerosis using filipin. Exp Mol Pathol. 1984 Jun 1;40(3):288–94.

328. Trinh MN, Brown MS, Goldstein JL, Han J, Vale G, McDonald JG, et al. Last step in the path of LDL cholesterol from lysosome to plasma membrane to ER is governed by phosphatidylserine. Proc Natl Acad Sci. 2020 Aug 4;117(31):18521–9.

329. Maekawa M. Domain 4 (D4) of Perfringolysin O to Visualize Cholesterol in Cellular Membranes—The Update. Sensors. 2017 Mar 3;17(3):504.

330. Shatursky O, Heuck AP, Shepard LA, Rossjohn J, Parker MW, Johnson AE, et al. The Mechanism of Membrane Insertion for a Cholesterol-Dependent Cytolysin: A Novel Paradigm for Pore-Forming Toxins. Cell. 1999 Oct 29;99(3):293–9.

331. Banerjee I, Yamauchi Y, Helenius A, Horvath P. High-Content Analysis of Sequential Events during the Early Phase of Influenza A Virus Infection. PLOS ONE. 2013 Jul 12;8(7):e68450.

332. Hamilton BS, Whittaker GR, Daniel S. Influenza Virus-Mediated Membrane Fusion: Determinants of Hemagglutinin Fusogenic Activity and Experimental Approaches for Assessing Virus Fusion. Viruses. 2012 Jul 24;4(7):1144–68.

333. Härmälä A-S, Pörn MI, Mattjus P, Slotte JP. Cholesterol transport from plasma membranes to intracellular membranes is inhibited by 3β-[2-(diethylamino) ethoxy]androst-5-en-17-one. Biochim Biophys Acta BBA - Lipids Lipid Metab. 1994 Mar 24;1211(3):317–25.

334. Zhao J, Chen J, Li M, Chen M, Sun C. Multifaceted Functions of CH25H and 25HC to Modulate the Lipid Metabolism, Immune Responses, and Broadly Antiviral Activities. Viruses. 2020 Jul;12(7):727.

335. Macia E, Ehrlich M, Massol R, Boucrot E, Brunner C, Kirchhausen T. Dynasore, a Cell-Permeable Inhibitor of Dynamin. Dev Cell. 2006 Jun 1;10(6):839–50.

336. Fajgenbaum DC, June CH. Cytokine Storm. N Engl J Med. 2020 Dec 3;383(23):2255–73.

337. Farrell PJ, Broeze RJ, Lengyel P. Accumulation of an mRNA and protein in interferon-treated Ehrlich ascites tumour cells. Nature. 1979 Jun;279(5713):523–5.

338. Loeb KR, Haas AL. The interferon-inducible 15-kDa ubiquitin homolog conjugates to intracellular proteins. J Biol Chem. 1992 Apr 15;267(11):7806–13.

339. Lenschow DJ, Lai C, Frias-Staheli N, Giannakopoulos NV, Lutz A, Wolff T, et al. IFN-stimulated gene 15 functions as a critical antiviral molecule against influenza, herpes, and Sindbis viruses. Proc Natl Acad Sci. 2007 Jan 23;104(4):1371–6.

340. Lai C, Struckhoff JJ, Schneider J, Martinez-Sobrido L, Wolff T, García-Sastre A, et al. Mice Lacking the ISG15 E1 Enzyme UbE1L Demonstrate Increased Susceptibility to both Mouse-Adapted and Non-Mouse-Adapted Influenza B Virus Infection. J Virol. 2009 Jan 15;83(2):1147–51.

341. Durfee LA, Lyon N, Seo K, Huibregtse JM. The ISG15 Conjugation System Broadly Targets Newly Synthesized Proteins: Implications for the Antiviral Function of ISG15. Mol Cell. 2010 Jun 11;38(5):722–32.

342. Valášek LS, Zeman J, Wagner S, Beznosková P, Pavlíková Z, Mohammad MP, et al. Embraced by eIF3: structural and functional insights into the roles of eIF3 across the translation cycle. Nucleic Acids Res. 2017 Nov 2;45(19):10948–68.

343. Fensterl V, Sen GC. The ISG56/IFIT1 Gene Family. J Interferon Cytokine Res. 2011 Jan;31(1):71–8.

344. Pichlmair A, Lassnig C, Eberle C-A, Górna MW, Baumann CL, Burkard TR, et al. IFIT1 is an antiviral protein that recognizes 5′-triphosphate RNA. Nat Immunol. 2011 Jul;12(7):624–30.

345. Cline TD, Beck D, Bianchini E. Influenza virus replication in macrophages: balancing protection and pathogenesis. J Gen Virol. 2017 Oct;98(10):2401–12.

346. Zhao M, Zhang J, Phatnani H, Scheu S, Maniatis T. Stochastic Expression of the Interferon-β Gene. PLOS Biol. 2012 Jan 24;10(1):e1001249.

347. Reynaud JM, Kim DY, Atasheva S, Rasalouskaya A, White JP, Diamond MS, et al. IFIT1 Differentially Interferes with Translation and Replication of Alphavirus Genomes and Promotes Induction of Type I Interferon. PLOS Pathog. 2015 Apr 30;11(4):e1004863.

348. Ivashkiv LB, Donlin LT. Regulation of type I interferon responses. Nat Rev Immunol. 2014 Jan;14(1):36–49.

349. Cheng K, Wang X, Yin H. Small-Molecule Inhibitors of the TLR3/dsRNA Complex. J Am Chem Soc. 2011 Mar 23;133(11):3764–7.

350. Slepushkin VA, Staber PD, Wang G, McCray PB, Davidson BL. Infection of Human Airway Epithelia with H1N1, H2N2, and H3N2 Influenza A Virus Strains. Mol Ther. 2001 Mar 1;3(3):395–402.

351. Kenney AD, McMichael TM, Imas A, Chesarino NM, Zhang L, Dorn LE, et al. IFITM3 protects the heart during influenza virus infection. Proc Natl Acad Sci U S A. 2019 Sep 10;116(37):18607–12.

352. Wu W, Metcalf JP. The Role of Type I IFNs in Influenza: Antiviral Superheroes or Immunopathogenic Villains? J Innate Immun. 2020;12(6):437–47.

353. Tam VC, Quehenberger O, Oshansky CM, Suen R, Armando AM, Treuting PM, et al. Lipidomic Profiling of Influenza Infection Identifies Mediators that Induce and Resolve Inflammation. Cell. 2013 Jul 3;154(1):213–27.

354. Vogel AJ, Harris S, Marsteller N, Condon SA, Brown DM. Early Cytokine Dysregulation and Viral Replication Are Associated with Mortality During Lethal Influenza Infection. Viral Immunol. 2014 Jun 1;27(5):214–24.

355. Rutigliano JA, Sharma S, Morris MY, Oguin TH, McClaren JL, Doherty PC, et al. Highly Pathological Influenza A Virus Infection Is Associated with Augmented Expression of PD-1 by Functionally Compromised Virus-Specific CD8+ T Cells. J Virol. 2014 Feb 1;88(3):1636–51.

356. Bolívar S, Anfossi R, Humeres C, Vivar R, Boza P, Muñoz C, et al. IFN-β Plays Both Pro- and Anti-inflammatory Roles in the Rat Cardiac Fibroblast Through Differential STAT Protein Activation. Front Pharmacol [Internet]. 2018 [cited 2021 Mar 29];9.

357. Hare D, Collins S, Cuddington B, Mossman K. The Importance of Physiologically Relevant Cell Lines for Studying Virus–Host Interactions. Viruses. 2016 Nov 1;8(11):297.

358. Matsumoto M, Seya T. TLR3: interferon induction by double-stranded RNA including poly(I:C). Adv Drug Deliv Rev. 2008 Apr 29;60(7):805–12.

359. Dawson WK, Lazniewski M, Plewczynski D. RNA structure interactions and ribonucleoprotein processes of the influenza A virus. Brief Funct Genomics. 2017 Oct 10;17(6):402–14.

360. Goffic RL, Balloy V, Lagranderie M, Alexopoulou L, Escriou N, Flavell R, et al. Detrimental Contribution of the Toll-Like Receptor (TLR)3 to Influenza A Virus–Induced Acute Pneumonia. PLOS Pathog. 2006 Jun 9;2(6):e53.

361. Oshansky CM, Gartland AJ, Wong S-S, Jeevan T, Wang D, Roddam PL, et al. Mucosal Immune Responses Predict Clinical Outcomes during Influenza Infection

Independently of Age and Viral Load. Am J Respir Crit Care Med. 2014 Feb 15;189(4):449–62.

362. Zhang C, Wu Z, Li J-W, Zhao H, Wang G-Q. Cytokine release syndrome in severe COVID-19: interleukin-6 receptor antagonist tocilizumab may be the key to reduce mortality. Int J Antimicrob Agents. 2020 May;55(5):105954.

363. Chen LYC, Hoiland RL, Stukas S, Wellington CL, Sekhon MS. Confronting the controversy: Interleukin-6 and the COVID-19 cytokine storm syndrome. Eur Respir J [Internet]. 2020 Jan 1 [cited 2021 Sep 3].

364. Gu Y, Zuo X, Zhang S, Ouyang Z, Jiang S, Wang F, et al. The Mechanism behind Influenza Virus Cytokine Storm. Viruses. 2021 Jul;13(7):1362.

365. Olbei M, Hautefort I, Modos D, Treveil A, Poletti M, Gul L, et al. SARS-CoV-2 Causes a Different Cytokine Response Compared to Other Cytokine Storm-Causing Respiratory Viruses in Severely Ill Patients. Front Immunol. 2021;12:381.

366. Opposing activities of IFITM proteins in SARS-CoV-2 infection. EMBO J. 2021 Feb 1;40(3):e106501.

367. Serramito-Gómez I, Boada-Romero E, Villamuera R, Fernández-Cabrera Á, Cedillo JL, Martín-Regalado Á, et al. Regulation of cytokine signaling through direct interaction between cytokine receptors and the ATG16L1 WD40 domain. Nat Commun. 2020 Nov 20;11(1):1–15.

Appendices

Appendix 1

Non-canonical autophagy functions of ATG16L1 in epithelial cells limit lethal infection by influenza A virus

Yingxue Wang, Parul Sharma, Matthew Jefferson, Weijiao Zhang, Ben Bone, Anja Kipar, David Bitto, Janine L Coombes, Timothy Pearson, Angela Man, Alex Zhekova, Yongping Bao, Ralph A Tripp, Simon R Carding, Yohei Yamauchi, Ulrike Mayer, Penny P Powell, James P Stewart & Thomas Wileman.

Abstract

Influenza A virus (IAV) and SARS-CoV-2 (COVID-19) cause pandemic infections where cytokine storm syndrome and lung inflammation lead to high mortality. Given the high social and economic cost of respiratory viruses, there is an urgent need to understand how the airways defend against virus infection. Here we use mice lacking the WD and linker domains of ATG16L1 to demonstrate that ATG16L1-dependent targeting of LC3 to single-membrane, non-autophagosome compartments – referred to as non-canonical autophagy – protects mice from lethal IAV infection. Mice with systemic loss of non-canonical autophagy are exquisitely sensitive to low-pathogenicity IAV where extensive viral replication throughout the lungs, coupled with cytokine amplification mediated by plasmacytoid dendritic cells, leads to fulminant pneumonia, lung inflammation and high mortality. IAV was controlled within epithelial barriers where non-canonical autophagy reduced IAV fusion with endosomes and activation of interferon signalling. Conditional mouse models and ex vivo analysis showed that protection against IAV infection of lung was independent of phagocytes and other leucocytes. This establishes non-canonical autophagy in airway epithelial cells as a novel innate defence that restricts IAV infection and lethal inflammation at respiratory surfaces.

Introduction

Influenza A virus (IAV) is a respiratory pathogen of major global public health concern (Yamayoshi & Kawaoka, 2019). As with SARS-CoV-2, animal reservoirs of IAV can contribute to zoonotic infection leading to pandemics with a high incidence of viral pneumonia, morbidity and mortality. IAV infects airway and alveolar epithelium and damage results from a combination of the intrinsic pathogenicity of individual virus strains as well as the strength and timing of the host innate/inflammatory responses. Optimal cytokine levels protect from IAV replication and disease but excessive cytokine production and inflammation worsens the severity of lung injury (Davidson *et al*, 2014; Iwasaki & Pillai, 2014; Teijaro *et al*, 2014; Herold *et al*, 2015; Ramos & Fernandez-Sesma, 2015). Even though infection of the lower respiratory tract can result in inflammation, flooding of alveolar spaces, acute respiratory distress syndrome and respiratory failure, the factors that control IAV replication at epithelial surfaces and limit lethal lung inflammation remain largely unknown.

The transport of viruses to lysosomes for degradation provides an important barrier against infection. Transport to lysosomes can be enhanced by non-canonical autophagy pathways which conjugate autophagy marker protein LC3 to endo-lysosome compartments to increase lysosome fusion. In phagocytes, LC3-associated phagocytosis (LAP) conjugates LC3 to phagosomes and enhances phagosome maturation (Sanjuan *et al*, 2007; Delgado *et al*, 2008; Martinez *et al*, 2015; Lamprinaki *et al*, 2017; Fletcher *et al*, 2018). In non-phagocytic cells, LC3 is conjugated to endo-lysosome compartments during the uptake of particulate material such as apoptotic cells and aggregated β-amyloid, and following membrane damage during pathogen entry or osmotic imbalance induced by lysosomotropic drugs (Florey *et al*, 2011, 2015; Roberts *et al*, 2013; Tan *et al*, 2018; Heckmann *et al*, 2019). It is known from *in vitro* studies that LC3 can be recruited to endo-lysosome compartments during the uptake of pathogens, but the roles played by non-canonical autophagy during viral infection *in vivo* are largely unknown.

A role for non-canonical autophagy in host defence has been implied from *in vitro* studies of LAP in phagocytes infected with free living microbes with a tropism for macrophages such as bacteria (*Listeria monocytogenes* (Gluschko *et al*, 2018), *Legionella dumoffii* (Hubber *et al*, 2017)), protozoa (*Leishmania major*) and fungi (*Aspergillus fumigatus* (Akoumianaki *et al*, 2016, Kyrmizi *et al*, 2018, Matte *et al*, 2016)). It is also known that IAV induces non-canonical autophagy during infection of cells in culture (Fletcher *et al*, 2018); however, the role played by non-canonical autophagy in controlling IAV infection and lung inflammation *in vivo* is currently unknown. It is not known, for example, whether non-canonical autophagy is important in the control of IAV infection by epithelial cells at sites of infection or whether it plays a predominant role within phagocytes and antigen-presenting cells during development of an immune response. Herein we use mice with specific loss of non-canonical autophagy to determine the role played by non-canonical autophagy in host defence against IAV infection of the respiratory tract. The mice (δWD) lack the WD and linker domains of ATG16L1 that are required for conjugation of LC3 to endo-lysosome membranes (Rai *et al*, 2019) but express the N-terminal ATG5-binding domain and the coiled coil domain (CCD) and linker residues up to glutamate at position 230 (E230) of ATG16L1 that are required for WIPI2 binding and autophagy (Dooley *et al*, 2014). Importantly, the δWD mice grow normally and maintain tissue homeostasis (Rai *et al*, 2019), and unlike mice with LysMcre-mediated deletion of autophagy genes from myeloid cells (Lu *et al*, 2016), or disruption of ATG16L1 through loss of the CCD (Saitoh *et al*, 2008), the δWD mice do not have a pro-inflammatory phenotype.

We show that loss of non-canonical autophagy from all tissues renders mice highly sensitive to low-pathogenicity murine-adapted IAV (A/X-31) leading to extensive viral replication throughout the lungs, cytokine dysregulation and high mortality typically seen after infection with highly pathogenic IAV. Conditional mouse models and *ex vivo* analysis showed that protection against IAV infection of lung was independent of phagocytes and other leucocytes, and that infection was controlled within epithelial barriers where non-canonical autophagy slowed fusion of IAV with endosomes and reduced interferon signalling. This establishes non-canonical autophagy pathways in airway epithelial cells as a novel innate defence mechanism that restricts IAV infection at respiratory surfaces.

Results

Mice with systemic loss of the WD and linker domains of ATG16L1 are highly sensitive to IAV infection

Panels A and B of Fig EV1 show the rationale for removing the WD and linker domains from ATG16L1 to generate mice (δWD) with a specific loss of non-canonical autophagy (E230 mice described in Rai *et al,* 2019). The consequences of loss of the WD and linker domains of ATG16L1 on conventional autophagy and non-canonical autophagy were confirmed using cell lines taken from controls and δWD mice. Figure 1A shows that mouse embryo fibroblasts (MEFs) from littermate control mice recruited LC3 to small puncta indicative of autophagosomes when they were starved in HBSS to induce conventional autophagy and recruited LC3 to large endo-lysosomal vacuoles when non-canonical autophagy was induced by chloroquine or monensin. HBSS induced LC3 puncta in MEFs from δWD mice, but the MEFs were unable to recruit LC3 to large vacuoles induced by chloroquine or monensin. LC3 recruitment was quantified by imaging LC3-positive puncta and vacuoles. The graphs (Fig 1B) show that numbers of autophagosomes induced by HBSS were the same in each cell type but MEFs from δWD were unable to recruit LC3 to large vacuoles when incubated with chloroquine or monensin. The results indicated a selective loss of non-canonical autophagy. LC3 recruitment was quantified by Western blot to detect LC3II, the lipidated form of LC3 that binds membranes. Figure 1C shows that control MEFs expressed the full-length α and β forms of ATG16L1 at 70 kDa and generated increased levels of LC3II following starvation in HBSS or incubation with monensin or chloroquine. MEFs from δWD mice expressed a truncated ATG16L1 at 30 kDa (Fig 1C). The LC3II signal in δWD cells increased after starvation to levels that were similar to starvation controls. LC3II also increased in δWD MEFs incubated with monensin and chloroquine. Monensin and chloroquine raise lysosomal pH, and the consequent inhibition of proteolysis slows the efflux of amino acids from the lysosome. This in turn inhibits the Ragulator-Rag:MTORC1 complex and induces autophagy. Previous work (Fletcher *et al*, 2018) has shown that monensin activates conventional autophagy and at the same time raised lysosomal pH slows fusion of autophagosomes with lysosomes. This explains the accumulation of small LC3 puncta and increased LC3II observed in δWD cells incubated with monensin or chloroquine. Quantification of Western blots (Fig 1D) showed that there was no significant difference between LC3II signals in control and δWD MEFs after starvation suggesting that autophagy was equally active in the two cell types. The LC3II signal in δWD MEFs incubated with monensin or chloroquine was however lower than controls but not significantly different. Studies in phagocytic cells have shown that non-canonical autophagy/LAP is downstream of Rubicon and PHOX:NOX2 ROS signalling (Martinez *et al*, 2015). Addition of diphenyliodonium (DPI), an inhibitor of NOX2, to cells incubated with monensin or chloroquine inhibited recruitment of LC3 to large vacuoles (Figure EV1C) indicating that WD domain-dependent non-canonical autophagy is also downstream of ROS signalling in non-phagocytic cells. Microscopy and line profile analysis were used to determine whether recruitment of LC3 to phagosomes in bone marrow-derived macrophages (BMDM) induced by Zymosan also required the WD domain of ATG16L1. Figure 1E-H shows that LC3 was recruited to phagosomes in control BMDM, but was not recruited to phagosomes in BMDM from δWD mice. Taken together, the results show that the δWD mice have specific loss of non-canonical autophagy in both myeloid and non-myeloid cells.

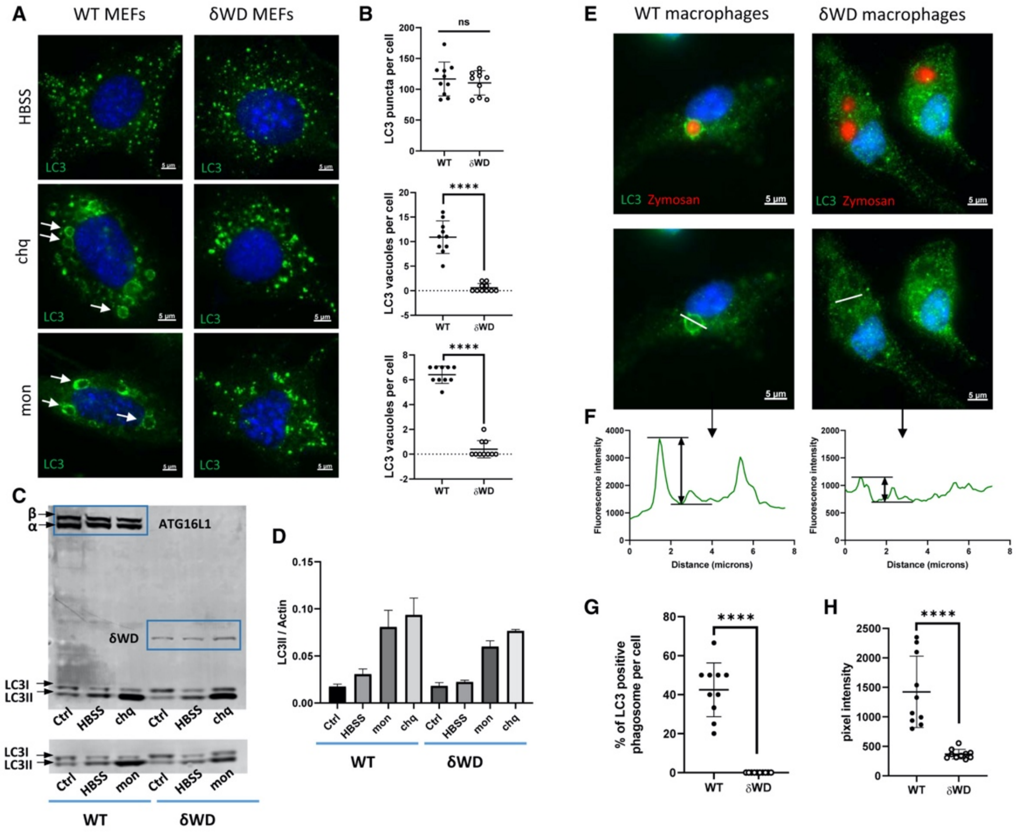

Figure 1. Deletion of the WD and linker domains of ATG16L1 leads to selective loss of non-canonical autophagy

- A. MEFs from δWD and littermate control mice were incubated with HBSS, chloroquine or monensin for 2 h as indicated. Cells were fixed and permeabilised and stained for LC3. Arrows indicate LC3 vacuoles where a ring of LC3 signal surrounds vacuoles ranging between 2 and 8 µm diameter.
- B. Numbers of fluorescent LC3 puncta and LC3 vacuoles in each cell were quantified by fluorescence microscopy. LC3 puncta were identified using spot function software to locate puncta ranging from 0.5 to 1.0 µm diameter. LC3

vacuoles were identified by eye as rings of fluorescence ranging between 2 and 8 µm diameter. Data from 10 cells are shown, and bars represent the mean ± SD and were compared by Student’s *t*-test (**P* < 0.05, *****P* < 0.0001).

- C–E. MEFs from δWD and littermate control mice were incubated with HBSS, chloroquine or monensin for 2 h as indicated and cell lysates analysed by Western blot for ATG16L1, δWD and LC3 as indicated. Control MEFs express α and β isoforms of ATG16L1 at 70 kDa, and MEFs from δWD mice express a truncated ATG16L1 at 30kDa. (D) shows the level of conversion of LC3 to LC3II estimated by densitometry from a mean (±SD) of three replicate blots. (E) shows fluorescence images of phagosomes following engulfment of Zymosan (red) by bone marrow-derived macrophages (BMDM) from control and δWD mice. White line indicates track used for line profile analysis to compare the LC3 signal on the limiting membrane of the phagosome with the centre.
- F. Shows examples of line profile analysis
- G, H. (G) shows the percentage of LC3-positive phagosomes per cell, and (H) shows line profile analysis of data from 10 cells, and bars represent the mean ± SD and were compared by Student’s *t*-test (*****P* < 0.0001).

IAV enters airway and lung epithelial cells by endocytosis, and in tissue culture IAV induces non-canonical autophagy leading to ATG16L1-WD domain-dependent conjugation of LC3 to the plasma membrane and peri-nuclear structures (Fletcher *et al*, 2018). To test whether non-canonical autophagy has a host defence function *in vivo*, δWD mice were infected with IAV. We used a low-pathogenicity murine-adapted IAV (A/X31) that does not normally lead to extensive viral replication throughout the lungs, or cause the cytokine storm syndrome and death typically seen after infection with highly pathogenic viral strains. The results (Fig 2) showed that δWD mice became moribund and showed severe signs of clinical illness (rapid breathing, piloerection). They also displayed rapid weight loss compared to littermate controls (Fig 2A) and had increased mortality with survivors recovering more slowly from infection (Fig 2B). Virus titres in the lungs of both mice increased with time (Fig 2C) and increased weight loss in δWD mice was associated with an approx. log increase in lung virus titre at 5 days post-infection (d.p.i). Furthermore, histopathology and immunohistochemistry (IH) analysis of lungs from δWD mice showed fulminant viral pneumonia with large numbers of IAV-positive cells (Fig 2D). Lungs from control and δWD mice did not show signs of inflammation before infection (Fig EV2).

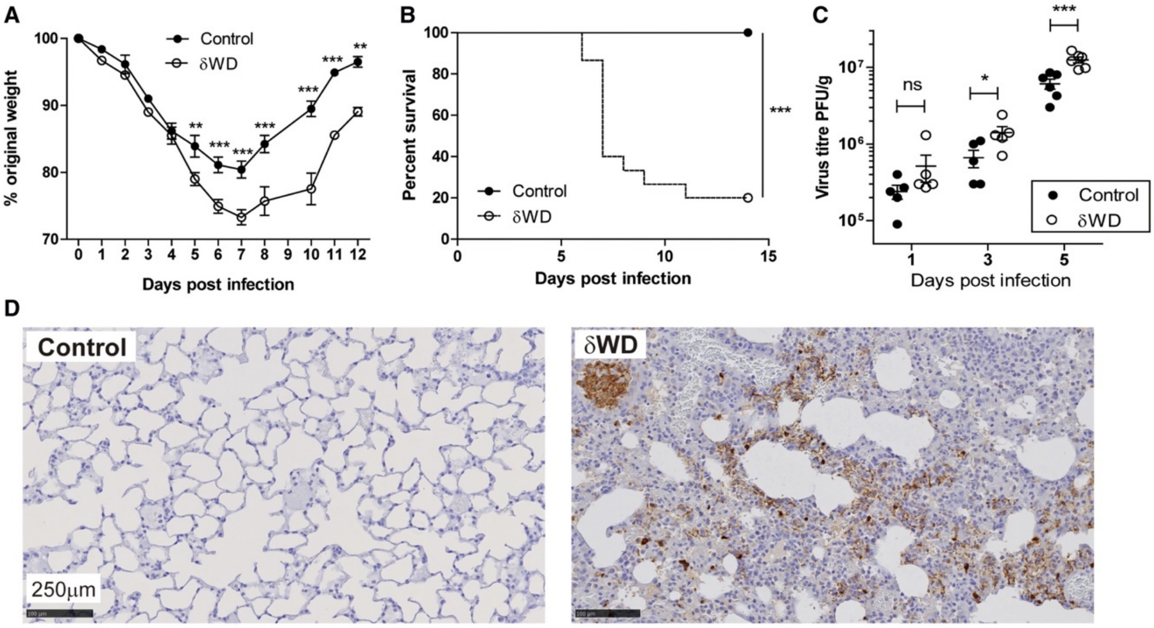

Figure 2. Systemic loss of non-canonical autophagy increases susceptibility to IAV infection

- A–D. Littermate control and δWD mice were challenged intranasally with IAV strain X31 (10^3 pfu). (A) Mice were monitored for weight loss at indicated time points. ($n = 8$). Data represent the mean value ± SEM. Comparisons were made using a repeated-measures two-way ANOVA (Bonferroni post-test (**$P < 0.01$, ***$P < 0.001$)). (B) Survival was assessed at indicated time points ($n = 15$). Comparisons were made using log-rank (Mantel–Cox) test ***$P < 0.001$. (C) IAV titre in lungs was determined by plaque assay at 5 d.p.i. ($n = 6$). Data for individual animals are shown, and bars represent the mean ± SD. Mann–Whitney *U*-test was used to determine significance (**$P < 0.01$. (D) The presence of IAV antigen was assessed by IH at 7 d.p.i. (representative images from $n = 6$).

Non-canonical autophagy controls lung inflammation after IAV infection

Innate protection against IAV is provided by type 1 (α, β) and III (λ) interferon (IFN) with severe IAV infection causing excessive airway inflammation and pulmonary changes attributable in part to IFNαβ and TNF-α (Szretter *et al*, 2007; Davidson *et al*, 2014). Measurement of cytokine expression at 2 d.p.i showed that IAV induced a transient increase in transcripts for interferon-stimulated genes (ISGs), ISG15 and IFIT1 (Iwasaki & Pillai, 2014) and pro-inflammatory cytokines (IL-1β, TNF-α and CCL2 [MCP-1]) in the lungs of both control and δWD mice (Fig 3A). This increase in cytokine expression was resolved by 3 d.p.i. before a second wave of increased cytokine expression at 5 d.p.i. This second wave of cytokine expression was resolved by 7 d.p.i in control mice, but δWD mice showed sustained increases in ISG15, IFIT1, IL-1β, TNF-α and CCL2 transcripts, coincident with exacerbated weight loss. At 3 d.p.i, lungs of δWD mice showed increased expression of neutrophil chemotaxis factor CXCL1 mRNA (Fig 3A), coincident with increased neutrophil infiltration of airways and parenchyma, and extensive neutrophil extracellular traps (NETs) as a consequence of neutrophil degeneration as shown by IH (Fig 3B and Appendix Fig S1). Increased neutrophil infiltration of airways in δWD mice at 2 d.p.i. was confirmed and quantified using flow cytometric analysis of bronchoalveolar lavage (BAL; Fig 3C). At 5–7 d.p.i., increased expression of CCL2 mRNA in δWD mice was coincident with extensive macrophage/monocyte infiltration into lung parenchyma observed by IH (Fig 3B and Appendix Fig S2) which was not seen in controls or the lungs of δWD mice before infection with virus (EV2). This increased macrophage/monocyte infiltration in δWD mice was confirmed and quantified using flow cytometric analysis of single-cell suspensions from lung tissue (Fig 3D). It is known that, in severe IAV infection, a cytokine storm occurs that is amplified by plasmacytoid dendritic cells (pDCs) (Davidson *et al*, 2014). pDCs detect virus-infected cells and produce large amounts of cytokines, in particular IFNαβ, that in severe infections can enhance disease. In these cases, depletion of pDCs can decrease morbidity (Davidson *et al*, 2014). Depletion of pDCs in IAV-infected δWD mice using anti-PDCA-1 led to markedly decreased weight loss as compared with isotype control-treated mice and that was similar to that seen in littermate controls (Fig 3E). This indicates that excessive cytokine production amplified by pDCs is responsible for the increased morbidity seen in the δWD mice.

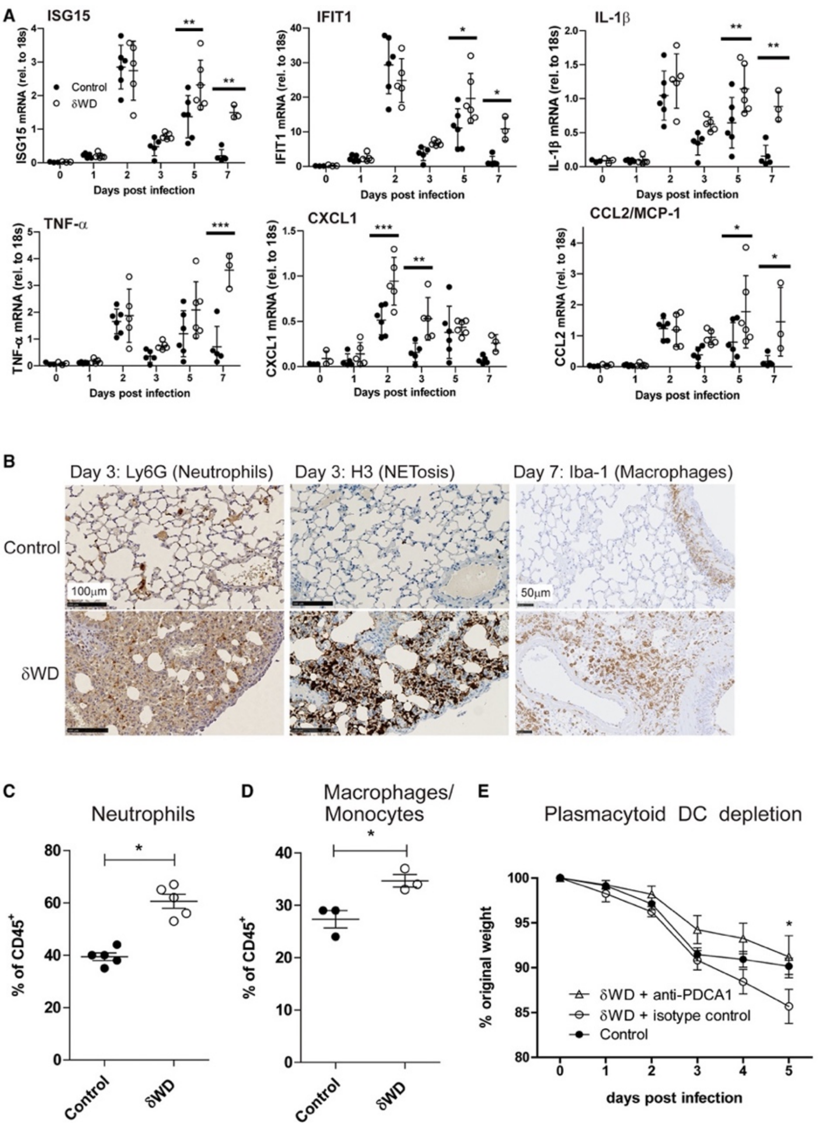

Figure 3. Systemic loss of non-canonical autophagy leads to extensive lung inflammation and damage

- A–E. Littermate control and δWD mice (*n* = 5) were challenged with IAV X31 (10^3 pfu). (A) At the indicated time points, cytokine mRNA transcripts in lung tissue (*n* = 5) were evaluated by qPCR. Data for individual animals are shown, and bars represent the mean ± SD and were compared by 2-way ANOVA with Bonferroni post-tests (**P* < 0.05, ***P* < 0.01, ****P* < 0.001). (B) Representative lung sections from animals (*n* = 6) taken at 3 d.p.i. were stained by IH for neutrophils (Ly6G) or neutrophil extracellular traps (NET; anti-H3). Sections at 7 d.p.i. were stained for macrophages (Iba-1). Further micrographs are shown in Appendix Figs S1 and S2. (C) BAL (*n* = 5) was taken at 2 d.p.i and evaluated by flow cytometry, with pre-gating on $CD45^+$. The percentage of neutrophils ($CD11b^+$, $Ly6G^+$) cells is shown ± SEM and was compared using Mann–Whitney *U*-test (**P* < 0.05). (D) Single-cell suspensions were prepared from lungs taken at 5 d.p.i and evaluated by flow cytometry, with pre-gating on CD45$^+$. The percentage of macrophage/monocytes (CD11b$^+$, F4/80$^+$) cells is shown ± SEM and was compared using Mann–Whitney *U*-test ($^*P < 0.05$). (E) δWD mice were treated with either anti-PCDA-1 (to deplete plasmacytoid DC) or an isotype-matched control. Littermate control mice were used as comparator. Weight loss was measured at the indicated days p.i. ($n = 5$). Comparisons were made using a repeated-measures two-way ANOVA (Bonferroni post-test, $^*P < 0.05$).

Thus, mice with systemic loss of non-canonical autophagy failed to control lung virus replication and inflammation, leading to increased cytokine production, morbidity and mortality.

Systemic loss of the WD and linker domains of ATG16L1 does not lead to gross changes in inflammatory threshold or immunological homeostasis

Macrophages cultured from embryonic livers from mice with loss of the coiled coil domain of ATG16L1 are unable to activate canonical autophagy and secrete high levels of IL1-β (Saitoh *et al*, 2008). Similarly, LysMcre-mediated deletion of genes essential for conventional autophagy (e.g. Atg5, Atg7, Atg14, Atg16L1, FIP200) in mice leads to raised pro-inflammatory cytokine expression in the lung. This has been reported to increase resistance to IAV infection (Lu *et al*, 2016), and this was also observed in mice used in our study (Appendix Fig S3) where LysMcre-mediated loss of Atg16L1 resulted in weight loss similar to controls (Appendix Fig S3A) and reduced overall virus titre (Appendix Fig S3B). This led us to test the possibility that the δWD mutation to ATG16L1 could also increase IL-1β secretion and cause the increased inflammation observed during IAV infection. This was tested by incubating BMDM with LPS and purine receptor agonist, BzATP (Appendix Fig S4A), or by challenging mice with LPS (Appendix Fig S4B). Mice with a complete loss of ATG16L1 in myeloid cells (Atg16L1$^{fl/fl}$-lysMcre) showed threefold increases in IL-1β in serum and increased secretion IL-1β from BMDM *in vitro*. In contrast IL-1β secretion in δWD mice did not differ significantly from littermate controls (Appendix Fig S4A and B). This was consistent with lack of elevated cytokines in lungs prior to infection (see day 0 in Fig 3A), and our previous work shows that serum levels of IL-1β, IL-12p70, IL-13 and TNF-α in δWD mice are the same as in littermate controls at 8-12 and 20-24 weeks (Rai *et al*, 2019). The exaggerated inflammatory response to IAV in δWD mice did not therefore result from a raised pro-inflammatory threshold or dysregulated IL-1β responses in the lung. Also, the frequencies of T cells, B cells and macrophages were similar in δWD mice to littermate controls (Appendix Fig S5). These data suggest that the exaggerated responses of δWD mice to IAV do not occur because the mice have a raised inflammatory threshold or abnormal immunological homeostasis.

Non-canonical autophagy limits IAV infection independently of phagocytic cells

The link between non-canonical autophagy, TLR signalling, NADPH oxidase activation and ROS production (Sanjuan *et al*, 2007; Delgado *et al*, 2008; Martinez *et al*, 2015) provides phagocytes with a powerful mechanism to limit infections *in vivo*. To test whether wild-type bone marrow-derived cells could protect susceptible δWD mice from lethal IAV infection, we generated radiation chimaeras (Fig EV3). When challenged with IAV, δWD mice reconstituted with either wild-type or δWD bone marrow remained highly sensitive to IAV (Fig 4A and B) with body weight reduced by up to 25% and decreased survival by 5 d.p.i. As seen for δWD mice, weight loss was associated with a 10-fold increase in lung viral titre (Fig 4C), fulminant pneumonia and inflammatory infiltration into the lung (Fig 4D). This increased susceptibility to IAV was not observed for control mice reconstituted with wild-type bone marrow, showing that non-canonical autophagy pathways in phagocytes and other leucocytes from control mice were not able to protect δWD mice against lethal IAV infection. In a reciprocal experiment (Fig 5), mice expressing Cre recombinase in myeloid cells (LysMcre) were used to generate mice (called δWD^{phag}), where the truncated *Atg16*L1δWD gene was restricted to phagocytic cells (Appendix Fig S6). In these mice, non-canonical autophagy was absent in cultured phagocytes (BMDM) but it was present in skin fibroblasts (Appendix Fig S6E). After infection with IAV, δWD^{phag} mice showed comparable weight loss and virus titres to those seen in littermate control mice (Fig 5A and B). Likewise, the raised IL-1β levels (Fig 5C) and profuse macrophage and neutrophil lung infiltration observed in δWD mice were absent (Fig EV4) and similar to littermate controls. The ability of the WD and linker domains of ATG16L1 to protect epithelial cells against IAV infection was tested *ex vivo* to further exclude any contribution from recruited leucocytes. Virus titres in precision-cut lung slices (Fig 5D) increased over 3 days and similar to the kinetics seen in vivo titres from δWD mice rose to 10-fold greater than controls. Thus, the sensitivity of δWD mice to IAV was not due to the loss of non-canonical autophagy from myeloid cells, making it likely that non-canonical autophagy mediated by the WD and linker domains of ATG16L1 protects against lethal IAV infection in non-myeloid tissue.

Non-canonical autophagy slows IAV fusion with endosomes and reduces interferon signalling

IAV enters cells by receptor-mediated endocytosis where acidification of late endosomes results in fusion with the endosomal membrane and delivery of viral ribonuclear proteins (RNPs) into the cytoplasm (Wharton *et al*, 1994; Skehel & Wiley, 2000). RNPs are then imported into the nucleus for genome replication (Boulo *et al*, 2007). Figure 6A shows that the generation of infectious virus was greater in δWD MEFs compared to control. IAV binding was analysed using fluorescent virus, and Fig 6B shows that binding was similar between control and δWD MEFs suggesting that subsequent steps of endocytosis and viral fusion may be increased in δWD MEFs. The possibility that the WD domain of ATG16L1 affected replication of IAV independently of endocytosis was tested using an acid bypass assay. IAV was bound to cells at 4° and warmed to 37°C for 2 min at pH 6.8 (control) or pH 5 to induce direct fusion with the plasma membrane. When early stages of replication were assessed by staining for nuclear protein, there was no difference between δWD MEFs and control (Fig 6C). This made it unlikely that the WD domain has a direct role in facilitating IAV replication. The effect of non-canonical autophagy on IAV entry was tested using fluorescence de-quenching assay where the envelope of purified IAV was labelled with green (DiOC18) and red (R18) lipophilic dyes. Individual fusion events in cells estimated by automated confocal microscopy (Fig 6D) show that the number of fusion events per cell was increased after 60 min at 37°C in δWD MEFs compared to control. Similarly, FACS analysis (see also Fig EV5) of the percentage of cells with de-quenched signal showed greater fusion in δWD MEFs (60%) compared to controls (40%) at 30 min and this increased at 60 min (73% versus 56% for controls; Fig 6E), as did mean fluorescence intensity (Fig 6F). Endocytosed viruses were also estimated by automated

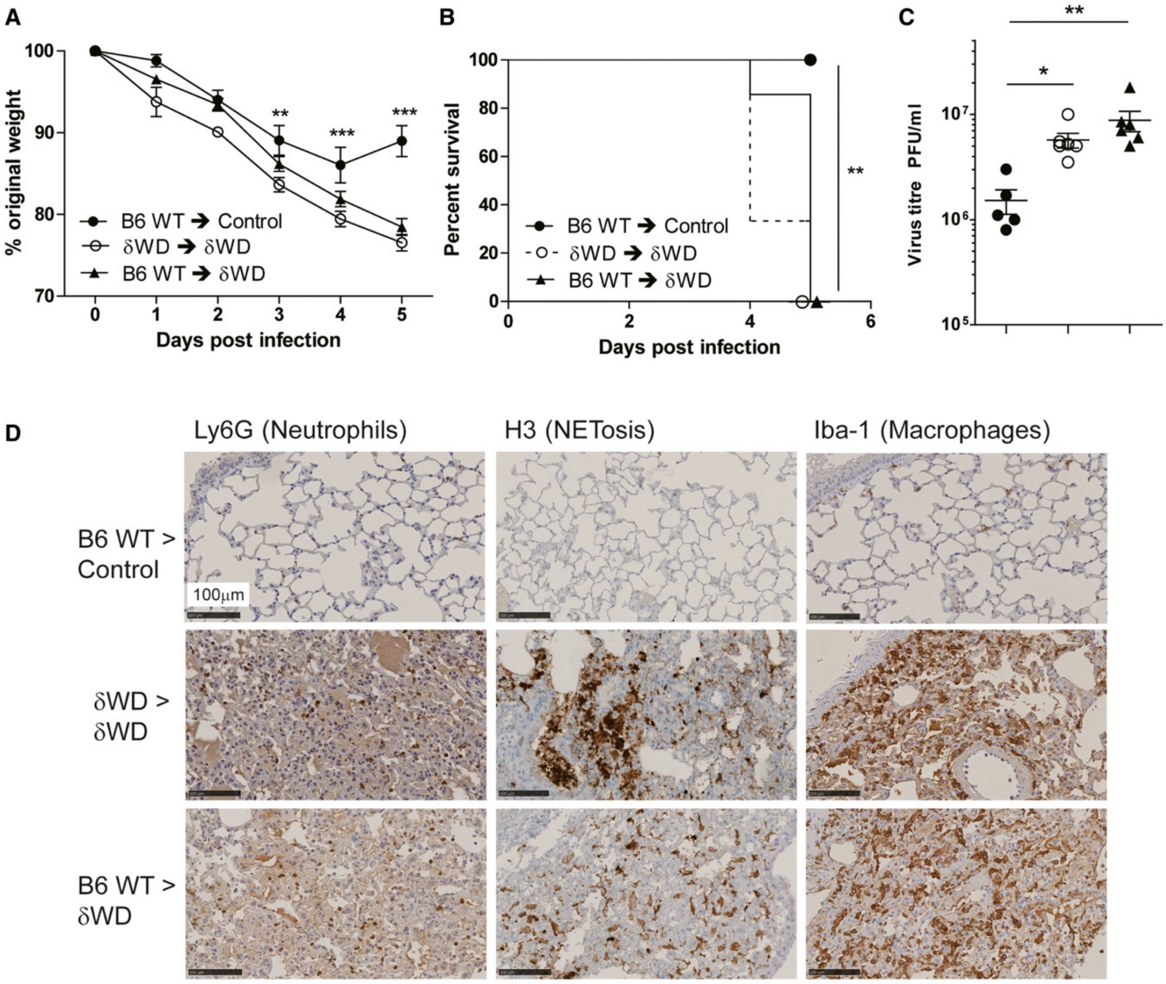

Figure 4. Bone marrow-derived lymphoid tissue cannot reverse sensitivity to IAV infection

- A–D. Bone marrow from wild-type (*Atg16*L1$^{+/+}$) was used to reconstitute irradiated littermate control mice (B6 WT → control [●]) or δWD mice (B6 WT → δWD [○]). Bone marrow from δWD mice was used to reconstitute irradiated δWD mice (δWD → δWD [▲]). After 12 weeks, mice (*n* = 5 per group) were challenged with IAV X31 (10^3 pfu). (A) Mice were monitored for weight loss at indicated time points. Data represent the mean value ± SEM. Comparisons were made using a repeated-measures two-way ANOVA (Bonferroni post-test, $**P < 0.01$, $***P < 0.001$). (B) Survival was assessed at indicated time points. Comparisons were made using log-rank (Mantel–Cox) test $**P < 0.01$). (C) IAV titre in lungs was determined by plaque assay at 5 d.p.i. (*n* = 6). Data for individual animals are shown using symbols described in (A) and (B), and bars represent the mean ± SD. A one-way ANOVA with Tukey's post hoc analysis was used to determine significance (**P* < 0.05, ***P* < 0.01). (D) Lungs taken at 5 d.p.i. were analysed for neutrophils (Ly6G), neutrophil extracellular traps (NET; anti-H3) and macrophages (Iba-1).

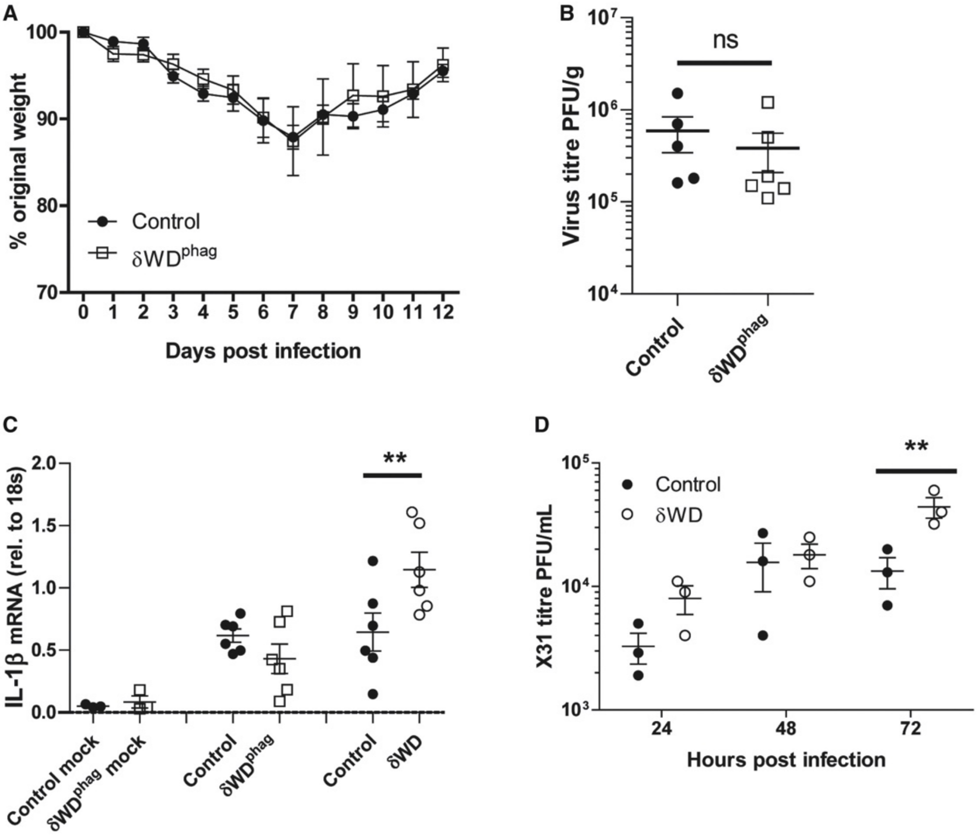

Figure 5. Loss of non-canonical autophagy from phagocytes does not increase sensitivity to IAV infection

- A–C. δWD^{phag} mice lack non-canonical autophagy in myeloid (LysMcre) cells (for construction see Appendix Fig S6A). Offspring negative for LysMcre were used as littermate controls. Mice (*n* = 6 per group) were challenged intranasally with IAV X31 (10^3 pfu). (A) Mice were monitored for weight loss at indicated time points. Data represent the mean value ± SEM. Comparisons were made using a repeated-measures two-way ANOVA (Bonferroni post-test). (B) IAV titre in lungs was determined by plaque assay at 5 d.p.i. (*n* = 6). Data for individual animals are shown, and bars represent the mean ± SD. Mann–Whitney *U*-test was used to determine significance. (C) IL-1β mRNA transcripts in lung at 5 d.p.i. were determined by qPCR. Mann–Whitney *U*-test was used to determine significance (***P* < 0.01).
- D. Precision-cut lung slices from control and δWD mice were infected with IAV. Virus titres were determined at indicated time points. Comparisons were made using two-way ANOVA with Bonferroni post-tests (***P* < 0.01).

confocal microscopy (Fig 6 G and H) of permeabilised cells and again there was a significant increase in endocytosis of IAV in δWD MEFs at 30 min. Taken together, the results showed that the WD domain of ATG16L1 slowed fusion of IAV with endosome membranes. The recognition of viral RNA by interferon sensors following delivery of RNPs into the cytoplasm was used as a second assay for IAV entry. MEFs from δWD mice showed between three- and fivefold increases in expression of IFN responsive genes, ISG15 and IFIT1 (Fig 6I and J), and this was also observed in the lung *in vivo* (Fig 3A). Taken together, the results demonstrate for the first time that the WD and linker domains of ATG16L1 allow non-canonical autophagy to provide a novel innate defence mechanism against lethal IAV infection within the epithelial barrier *in vivo*.

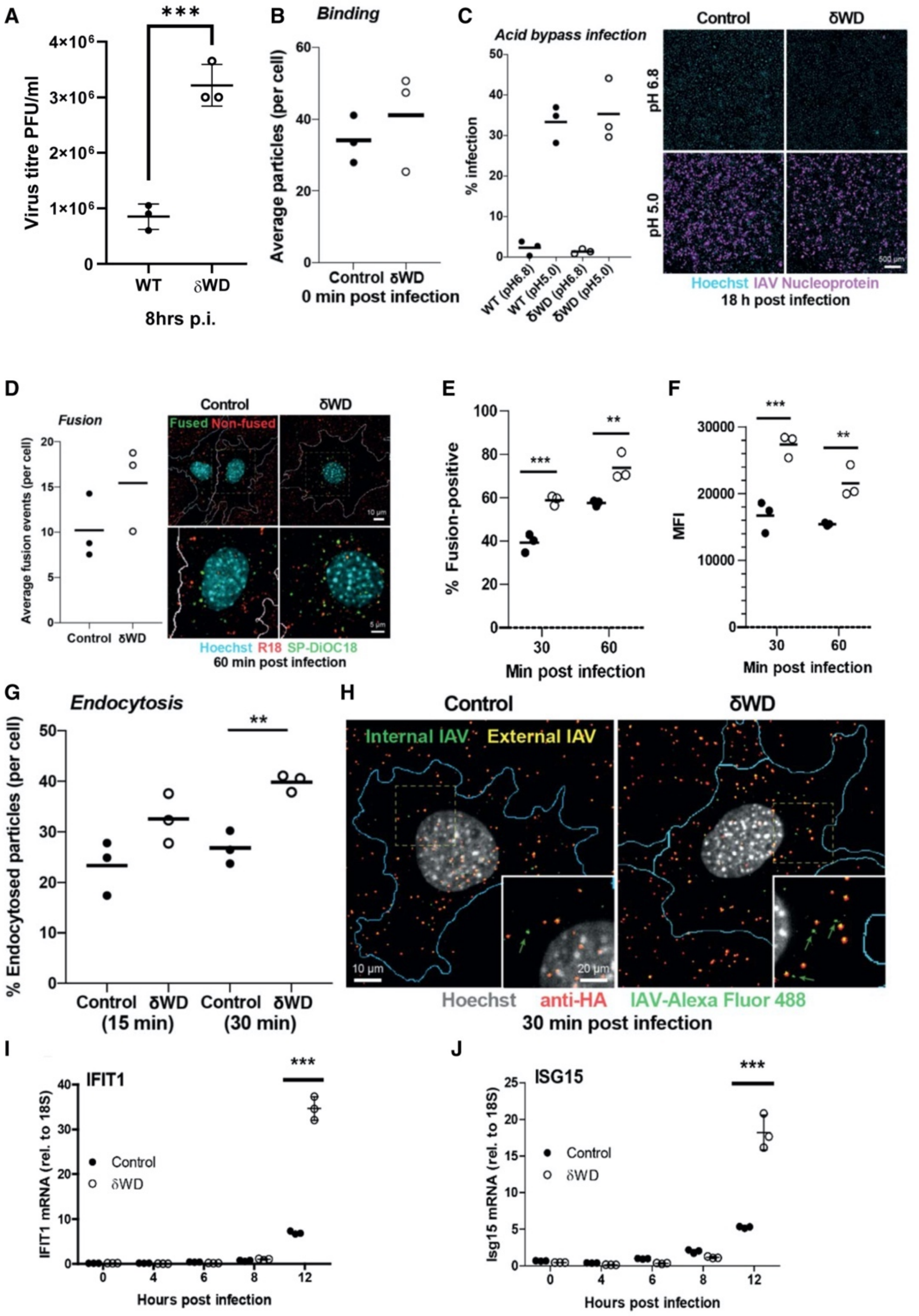

Figure 6. Non-canonical autophagy reduces virus replication, endosome fusion and interferon signalling

- A. The WD domain of ATG16L1 reduces IAV replication in MEFs. Cells were infected with IAV, and virus titres were estimated at 8 h post-infection by plaque assay. Graphs show three individual experiments with a bar (± SD) at the mean and were compared using two-way ANOVA with Bonferroni post-tests ***$P < 0.001$).
- B. IAV binding is similar between control and δWD MEFs. Cells were bound with IAV X31 labelled with AF488 on ice for 1 h and fixed immediately. The cells were stained with anti-HA (H3SKE, red) without permeabilisation to visualise extracellular IAV particles and counterstained with Hoechst (nuclei) and WGA-AF647 to label the cell membrane. Cells were imaged by automated confocal microscopy using a 40x objective, and the maximum intensity projection images were analysed to quantify the number of bound IAV particles per cell. The results and means (horizontal line) of $n = 3$ independent experiments (50-100 cells per experiment) are shown.
- C. IAV infection following acid bypass is comparable between control and δWD MEFs. IAV was bound on ice for 1 h and warmed at either neutral pH (6.8) or low pH (pH 5.0) for 2 min, followed by incubation in STOP medium containing NH_4Cl for 18 h. Cells were fixed and stained for NP and Hoechst, imaged by automated confocal microscopy and maximum intensity projection images analysed to quantify viral infectivity. The results from N = 3 independent experiments (5,000-10,000 cells quantified per experiment), and the means are shown. Scale bar; 500 µm.
- D. IAV fusion with endosomes is increased in δWD MEFs. Cells were infected with dual-labelled (R18/SP-DiOC18) IAV for 1 h, fixed and counterstained with Hoechst (nuclei blue) and WGA-AF647 (cell perimeter in white). Cells were imaged by automated confocal microscopy, and the number of fusion events per cell (represented by number of SP-DiOC18 puncta) was quantified. Fused and non-fused viral particles are shown as green and red spots, respectively. The results and means (horizontal lines) of $n = 3$ independent experiments (30-60 cells per experiment) are shown. Representative cells overlayed with the cell boundary segmented from the WGA staining are shown on the right.
- E, F. Numbers of fusion-positive cells are increased for δWD MEFs. MEFs from δWD (white circles) or littermate control mice (black circles) were incubated with dual-labelled (SP-DiOC18/R18) IAV at 4°C for 45 min and warmed to 37°C for 30 ad 60 min. Cells were harvested by trypsinisation, fixed in PFA and analysed by flow cytometry to determine to determine percentage of cells positive for fusion (E) and median fluorescence intensity (MFI) of de-quenched SP-DiOC18 signa (F). Graphs show individual replicates ($n = 3$) with a horizontal line at the mean and were compared using two-way ANOVA with Bonferroni post-tests **$P < 0.01$, ***$P < 0.001$). pH-dependent fusion was assessed by adding bafilomycin A1 to the infection assay (Fig EV5).
- G, H. Endocytosis of IAV increases in δWD MEFs. MEFs from δWD or littermate control mice were incubated with Alexa Fluor 488-labelled IAV at 4°C for 1hr and warmed to 37°C for 15. Cells were fixed and permeabilised and stained with

antibody against HA (red). The blue line indicates the plasma membrane of the cell. Green arrows indicate examples of viruses only labelled with green fluorescence. Double-labelled virus particles (green-red) represent non-endocytosed particles bound at the cell surface, whereas green particles represent endocytosed particles. The results and means of *n* = 3 independent experiments (50-100 cells per experiment) are shown. Student's *t*-test; *P* < 0.01. The dotted square in the top row panels is enlarged in the bottom row. Scale bars; 10 µm (top row) and 5 µm (bottom row).

- I, J. Interferon signalling increases in δWD MEFs. MEFs from δWD or littermate control mice were infected with IAV. At the indicated time points, mRNA transcripts were evaluated by qPCR for IFIT1 (I) and ISG15 (J). Data from 3 replicates are shown, and bars represent the mean ± SD and were compared by two-way ANOVA with Bonferroni post-tests (****P* < 0.001)

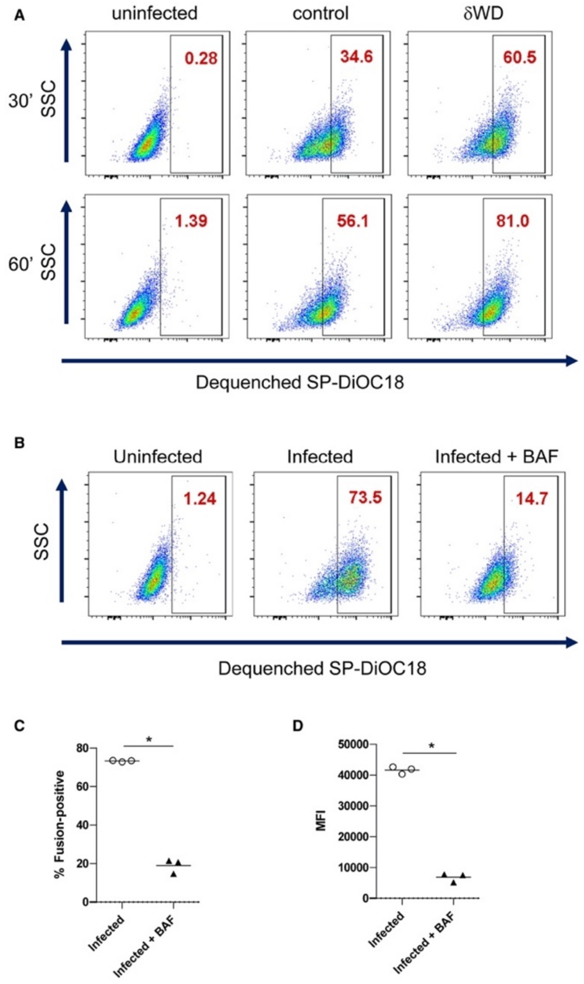

Figure EV5. Non-canonical autophagy reduces endosome fusion *in vitro*

- Sub-confluent monolayers of MEFs were incubated with dual-labelled (SP-DiOC18/R18) IAV at 4°C for 45 min. Cells were harvested by trypsinisation, fixed in PFA and analysed by flow cytometry.

Discussion

Respiratory viruses such as influenza A virus (IAV) and SARS-CoV-2 can move from animal reservoirs to create human pandemics with high morbidity and mortality. The danger posed by pandemic spread of respiratory viruses underlines an urgent need to understand how the airways defend against viral infection. In this study, we have analysed the role played by non-canonical autophagy in defending the respiratory tract against infection by IAV *in vivo*. Mice with systemic loss of non-canonical autophagy (δWD) showed profound sensitivity to infection by a low-pathogenicity murine-adapted IAV (A/X31) leading to extensive viral replication throughout the lungs, dysregulated cytokine production and fulminant pneumonia leading to high mortality and death usually seen after infection with virulent strains (Belser *et al*, 2011). These signs mirror the cytokine storms and mortality seen in humans infected with highly pathogenic strains of IAV such as the 1918 “Spanish” Influenza (Belser *et al*, 2011).

The observation that bone marrow transfers from wild-type mice were unable to protect δWD mice from IAV suggested that protection against IAV infection *in vivo* was independent of leucocytes and did not require non-canonical autophagy in leucocyte populations (e.g. macrophages, dendritic cells, neutrophils, granulocytes, lymphocytes). In a reciprocal experiment, the linker and WD domains of ATG16L1 were deleted specifically from myeloid cells. These mice, which lack non-canonical autophagy in phagocytic cells (LAP), but maintain non-canonical autophagy in other tissues, failed to show increased sensitivity to IAV infection. Thus, protection against severe IAV-associated disease in the respiratory tract of the host relies heavily on non-canonical autophagy in non-leucocyte populations.

Activation of non-canonical autophagy in phagocytic cells leads to LC3-associated phagocytosis (LAP) where TLR signalling and reactive oxygen species (ROS) recruit LC3 to phagosomes. A lack of involvement of non-canonical autophagy/LAP in protection against IAV disease *in vivo* was surprising because the activation of LAP in phagocytic cells such as macrophages, dendritic cells and neutrophils would provide a powerful means of recognising and controlling microbial infection *in vivo*. *In vitro* studies show that activation of acid sphingomyelinase by *Listeria monocytogenes* (Gluschko *et al*, 2018) and subsequent ROS production by NOX2 recruit LC3 to phagosomes. Similarly, activation of TLR2 and NOX2 by *Legionella dumoffii in vitro* signals ULK1-independent translocation of LC3 to single-membraned vacuoles containing Legionella (Hubber *et al*, 2017). In both cases, LC3 promotes fusion with lysosomes. The observation that virulence factors such as the GP63 metalloprotease of *Leishmania major* and melanin of *Aspergillus fumigatus* prevent recruitment of NOX2 to phagosomes to prevent LAP (Akoumianaki *et al*, 2016; Matte *et al*, 2016; Kyrmizi *et al*, 2018) further suggests that non-canonical autophagy in phagocytes should provide a defence against infection. One reason for the discrepancy may be that the studies cited above have focused on *in vitro* experiments using microbes with a tropism for macrophages, rather than *in vivo* studies where pathogens encounter epithelial barriers.

Intranasal infection of mice with IAV results in rapid infection of principally airway and pulmonary epithelial cells (Akram *et al*, 2018). The results of *in vivo* challenge of radiation chimaeras and δWD^{phag} mice strongly suggest that non-canonical autophagy in the epithelium rather than leucocytes is responsible for restricting IAV infection. This was supported by *ex vivo* experiments where virus titres and interferon responses were five- to 10-fold greater in precision-cut lung slices and MEFs from δWD mice. Furthermore, loss of non-canonical autophagy increased fusion of IAV envelope with endosomes and increased activation of interferon signalling pathways. Both assays suggest that non-canonical autophagy reduces IAV entry and delivery of viral RNA to the cytoplasm. This would explain reduced interferon signalling, and at the same time the delayed escape of IAV into the cytoplasm would increase the transfer of endocytosed virus to lysosomes for degradation. The precise mechanisms employed by non-canonical autophagy to reduce virus entry from endosomes are unknown. This may involve recruitment of LC3 to endosomes by TMEM59 (Boada-Romero *et al*, 2016) to increase fusion with lysosomes, or by maintaining membrane repair during virus entry, as observed for bacteria such as *S*. Typhimurium and *Listeria monocytogenes* (Kreibich *et al*, 2015; Tan *et al*, 2018). A p22^{phox}-NOX2 pathway that recruits LC3 to vacuoles containing *S*. Typhimurium in epithelial cells (Huang *et al*, 2009) may also be activated during IAV entry and hamper lethal infection.

δWD mice infected with IAV appeared to be unable to resolve inflammatory responses resulting in sustained expression of pro-inflammatory cytokines, morbidity and a striking lung changes characterised by profuse migration of neutrophils into the airway at day 3 followed by macrophages on day 7. pDCs detect IAV-infected cells and produce large amounts of cytokines, in particular IFNαβ, that in severe infections can enhance disease (Davidson *et al*, 2014). The fact that morbidity in δWD mice could be decreased by depleting pDCs indicates that excessive cytokine production, amplified by pDCs, was a major factor. This is not due to a lack of non-canonical autophagy/LAP in pDC as bone marrow chimaeras of δWD mice with wild-type leucocytes have the same phenotype as δWD mice. IAV is recognised by endosomal TLR3 in respiratory epithelial cells and RIG-I detects virus replicating in the cytosol leading to activation of IRF3 and NFkB with subsequent induction of interferon, ISG and pro-inflammatory cytokine production (Iwasaki & Pillai, 2014). Increased inflammation may result directly from increased virus in the lungs, but the increased fusion of IAV envelope with endosomes in δWD mice may increase delivery of viral RNA to the cytoplasm resulting in the sustained pro-inflammatory cytokine signalling. A similar pro-inflammatory phenotype resulting from decreased trafficking of inflammatory cargoes is observed following disruption of non-canonical autophagy by LysMcre-mediated loss of Rubicon from macrophages or microglia (Martinez *et al*, 2016; Heckmann *et al*, 2019). Studies also show that the WD domain of ATG16L1 can modulate endocytosis of cytokine receptors (Serramito-Gómez *et al*, 2020). Interaction of the WD domain with the IL10 receptor (IL10-R), for example, promotes formation of endosomes containing IL-10/IL-10 receptor complexes leading to an enhanced anti-inflammatory signalling, that would be lost in δWD mice. Impaired recycling of Toll-like receptor 4, CD36 and the β-amyloid receptor TREM2 is also observed in microglia lacking the WD domain of ATG16L1 leading to neuroinflammation (Heckmann *et al*, 2020). Inhibition of receptor recycling results from slowed return of receptors to the plasma membrane, rather than increased endocytosis (Heckmann *et al*, 2019). This makes it unlikely that the increased fusion of IAV with endosomes we see in δWD cells results from upregulation of endocytosis following loss of the ATG16L1 WD domain.

We have dissected the roles played by conventional autophagy and non-canonical autophagy *in vivo* by removing the linker and WD domain from ATG16L1 to prevent conjugation of LC3 to single-membraned endo-lysosome compartments (Rai *et al*, 2019). Quantitative analysis of conventional autophagy by fluorescence microscopy of LC3 puncta (Fig 1B) and Western blot of LC3II (Fig 1C&D) did not reveal a loss of canonical autophagy in cells from δWD mice compared to controls. Nevertheless, it is not possible to exclude the possibility that removal of the WD and linker domains of ATG16L1 has a minor effect on canonical autophagy that might affect infection "in vivo". There are however examples where the WD domain of ATG16L1 has roles during infection that are separate from conventional autophagy, and this may be true also for control of IAV. The WD domain of ATG16L1 maintains membrane repair during Listeria infection independently of conventional autophagy (Tan *et al*, 2018). The Salmonella T3SS effector protein SopF reduces recruitment of LC3 to vacuoles containing *S.* Typhimurium by inhibiting the interaction between the WD domain of ATG16L1 and the vacuolar ATPase recruited to sites of vacuole damage (Xu *et al*, 2019). This promotes growth and virulence of *S.* Typhimurium, but is independent of FIP200, an essential component of conventional autophagy. An alternative approach to studying non-canonical autophagy "in vivo" has been to target pathways upstream of LC3 conjugation where deletion of Rubicon produces a selective block in LAP (Martinez *et al*, 2015; Heckmann *et al*, 2019). Rubicon stabilises the PHOX:NOX2 complex (Yang *et al*, 2009) allowing reactive oxygen species (ROS) to induce binding of ATG16L1 to endo-lysosome membranes (Martinez *et al*, 2015). Mouse models relying on loss of Rubicon show defects in the clearance of bacterial and fungal pathogens and apoptotic cells (Martinez *et al*, 2015; Martinez *et al*, 2016), but have not yet been studied in the context of viral infection. Furthermore, disruption of Rubicon leads to upregulation of IL-1β, IL6 and TNF-α secretion, and the mice fail to gain weight and develop an autoimmune disease that resembles systemic lupus erythematosus (Martinez *et al*, 2016; Heckmann *et al*, 2017). This exaggerated inflammation might make it difficult to predict if any altered responses to infection observed in Rubicon-/- mice, particularly lung inflammation, resulted directly from loss of non-canonical autophagy, or from upstream changes in cytokine regulation caused by loss of Rubicon.

Several non-canonical pathways leading to recruitment of LC3 to endo-lysosomal compartments, rather than phagosomes, are beginning to emerge. Non-canonical autophagy in microglia facilitates endocytosis of β-amyloid and TLR receptors to reduce β-amyloid deposition and inflammation in mouse models of Alzheimer's disease (Heckmann *et al*, 2019). This may involve interaction between the WD domain and TMEM59 which is required for β-amyloid glycosylation (Ullrich *et al*, 2010). Lysosomotropic drugs, which stimulate direct recruitment of LC3 to endosomes, create pH and osmotic changes that may mimic the consequences of viral infections that perturb endosome membranes or deliver viroporins to endo-lysosome compartments. It will be interesting to see if the WD and linker domains of ATG16L1 limit infection by other microbes at epithelial barriers *in vivo,* particularly infection of the respiratory tract by SARS-CoV-2. This may be true for picornaviruses where LC3 is recruited to enlarged endosomes during entry of foot-and-mouth disease virus (Berryman *et al*, 2012) and following LC3 accumulation on megaphagosomes in pancreatic acinar cells during coxsackievirus B3 infection (Kemball *et al*, 2010). In the specific cases of IAV and SARS-CoV-2, non-canonical autophagy at epithelial barriers is likely important for innate control of new pathogenic strains, where acquired immunity from previous infection may be absent or less effective. It will be valuable to assess whether human allelic variants of ATG16L1 confer altered resistance/susceptibility to respiratory infections such as IAV and whether drug-based manipulation of non-canonical autophagy can increase resistance at the respiratory epithelial barrier.

Appendix 2

The Autophagy Protein ATG16L1 Is Required for Sindbis Virus-Induced eIF2α Phosphorylation and Stress Granule Formation

Matthew Jefferson, Benjamin Bone, Jasmine L. Buck, and Penny P. Powell

Abstract

Sindbis virus (SINV) infection induces eIF2α phosphorylation, which leads to stress granule (SG) assembly. SINV infection also stimulates autophagy, which has an important role in controlling the innate immune response. The importance of autophagy to virus-induced translation arrest is not well understood. In this study, we show that the autophagy protein ATG16L1 not only regulates eIF2α phosphorylation and the translation of viral and antiviral proteins, but also controls SG assembly. Early in infection (2hpi), capsids were recruited by host factors Cytotoxic Granule-Associated RNA Binding Protein (TIA1), Y-box binding protein 1 (YBX1), and vasolin-containing protein 1 (VCP), to a single perinuclear body, which co-localized with the viral pattern recognition sensors, double stranded RNA-activated protein-kinase R (PKR) and RIG-I. By 6hpi, there was increased eIF2α phosphorylation and viral protein synthesis. However, in cells lacking the autophagy protein ATG16L1, SG assembly was inhibited and capsid remained in numerous small foci in the cytoplasm containing YBX1, TIA1 with RIG-I, and these persisted for over 8hpi. In the absence of ATG16L1, there was little phosphorylation of eIF2α and low levels of viral protein synthesis. Compared to wild type cells, there was potentiated interferon protein and interferon-stimulated gene (ISG) mRNA expression. These results show that ATG16L1 is required for maximum eIF2α phosphorylation, proper SG assembly into a single perinuclear focus, and for attenuating the innate immune response. Therefore, this study shows that, in the case of SINV, ATG16L1 is pro-viral, required for SG assembly and virus replication.

Introduction

When RNA viruses infect mammalian cells, innate immune pathways including autophagy, apoptosis and the interferon signaling are induced to eliminate the virus [1]. In addition, some viruses activate PKR, leading to phosphorylation of eukaryotic initiation factor 2α (eIF2α). This halts host translation and leads to the formation of SG [2]. SG are non-membranous cytoplasmic ribonucleoprotein aggregates, typically containing mRNA and a stable core of RNA binding proteins, with a dynamic outer shell with diverse protein components, depending on the stress inducer [3]. During replication, viral double-stranded RNA (dsRNA) intermediates are recognized by pattern recognition receptors leading to the production of anti-viral cytokines such as Type 1 interferon [4]. Pattern recognition receptors include Toll-like receptor 3 (TLR3), localized in early endosomes, and the cytoplasmic RIG-like receptors (RLRs), RIG-I and MDA5, and PKR [5]. PKR, RIG-I and MDA-5 localize to SG following infection, together with other anti-viral proteins encoded by interferon sensitive genes (ISGs) such as PARP, ZAP and RNAi-binding ISGs [2,6]. In some cases, virus-induced SG are essential for efficient induction of Type I interferon. SG themselves may be either pro- or anti-viral, as they may sequester either factors needed for viral replication or innate factors required for anti-viral defenses [7].

Autophagy is another important innate response to virus infection. Autophagy is a stress response, which is activated to sequester pathogens within double-membrane vesicles called autophagosomes, to deliver them for degradation in lysosomes. Autophagy is activated during alphavirus infection [8]. Alphaviruses are a genus of the Togavirus family, and include Sindbis virus (SINV), Semliki Forest Virus (SFV) and chikugunya virus (CHIKV). They infect vertebrates and insects. They have a single-stranded, positive -sense RNA genome of approximately 12 kb with two open reading frames (ORF). The subgenomic RNA is translated into structural proteins, the capsid and envelope glycoproteins E1 and E2. The other ORF encodes the non-structural proteins nsp 1–4 [9]. Previous work has shown that autophagosomes accumulate during SFV infection due to the inhibition of autophagosome maturation by the viral glycoproteins [10]. A further study showed that SINV capsid protein binds to the autophagy cargo protein p62, an adaptor protein that targets it to the autophagosome [11]. In vitro, viral replication was independent of the autophagy protein ATG5, although in vivo, mice with disrupted neuronal Atg5 had a reduced clearance of viral proteins and increased accumulation of p62 aggregates in neurons [11]. Autophagy has been shown to enhance the replication of some viruses, such as picornaviruses and flaviviruses [12].

In this study, we investigated the effect of the autophagy protein ATG16L1 on eIF2α phosphorylation, early SG formation and modulation of viral and host protein synthesis. We showed that in wild type MEFs, SINV efficiently activated autophagy and eIF2α phosphorylation, with high levels of viral protein translation. The viral capsid protein redistributed to a single perinuclear SG comprising host RNA-binding proteins YBX1, TIA1, VCP, in addition to PKR and RIG-I. In contrast, in ATG16L1-/- cells, there was absence of eIF2α phosphorylation, and low viral protein synthesis. Host RNA-binding proteins failed to coalesce into a perinuclear SG, but were found co-localized with viral capsid in numerous small cytoplasmic puncta. Interferon synthesis and induction of ISG transcription were potentiated in ATG16L1 deficient cells, and this demonstrated that both SG assembly and autophagy were not required for interferon signaling. The results indicate that the autophagy protein ATG16L1 is important for the early phosphorylation of eIF2α and the switch from host to virus protein production. ATG16L1 is also involved in attenuation of interferon responses and the formation of perinuclear SGs after viral infection.

Results

3.1. ATG16L1 is Required for SINV-Induced Phosphorylation of eIF2α and the Switch to Viral Protein Synthesis

To investigate the effect of ATG16L1 on virus protein expression and eIF2α phoshorylation, wild type and ATG16L1-deficient MEF cells [13] were infected with SINV at an moi of 2. A time course of viral protein expression from 0–8 hpi using rabbit anti-SINV antibody showed that viral protein translation commenced by 6 hpi in both cell lines (Figure 1a). The enveloped glycoprotein p62 (E2/3) together with the capsid protein fused to mCherry fluorescent protein (ch.capsid), is seen as the major band at 62 kDa. The envelope protein E1 is detected at 45kDa and cleaved capsid protein at 30kDa. This anti-SINV antibody detected a non-specific, cross reacting band at this molecular weight at 0 hpi. The p62/capsid proteins increased 12-fold by 8 hpi in wild type cells. In contrast, there was only a 2-fold increase in p62/capsid proteins in ATG16L1 knockout cells (Figure 1a, bar chart). In wild type cells, SINV infection triggered phosphorylation of elongation factor eIF2α by 6 hpi. However, there was little phosphorylation of eIF2α detected by 6hpi in ATG16L1 knockout cells (Figure 1b). On this blot SINV virus expressing mCherry capsid is shown at 62kDa in wild type cells using an anti-dsRed antibody. There is a low intensity caspid band at 62kDa in ATG16L1 knockout cells, confirming the lower viral protein translation in these cells. The graph below shows the levels of eIF2α phosphorylation from three independent blots (+/-SE) at each time point, with 3-fold more eIF2α phosphorylated protein in wild type compared to ATG16L1 knockout cells. These results suggest that ATG16L1 is required both for eIF2α phosphorylation and for viral protein synthesis.

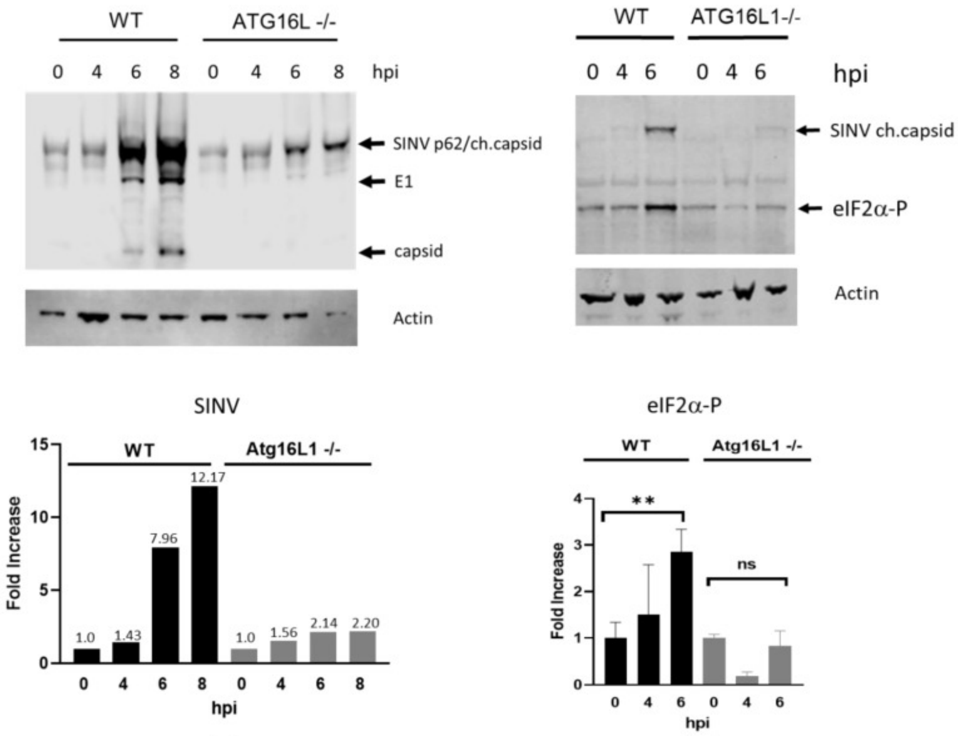

(a)

(b)

Figure 1 - eIF2α phosphorylation and virus protein production is diminished in ATG16L1-/- cells. (**a**) Western blot of SINV-infected lysates at 0–8 hpi detected with anti-SINV antibody. Bar chart below shows fold increase in p62/capsid proteins relative to actin. (**b**) SINV expressing cherry capsid detected with anti-dsRred antibody and phosphorylated eIF2α detected with rabbit monoclonal phospho-eIF2α (Ser51). Bar chart below shows the fold increase in eIF2α-P normalised to actin for 3 independent blots with +/-SE ** $p <$ 0.01, ns is non-significant.

3.2. Host Protein Rearrangements Following Entry of SINV Capsids

Canonical SG are induced by sodium arsenate and they are comprised of host proteins TIA1, G3BP1and YBX1. In MEF cells, these RNA-binding proteins redistributed from the cytoplasm and nucleus to several perinuclear bodies after treatment with sodium arsenate (Figure 2a). In contrast, SG formed after infection with SINV wild type strain AR339 condensed into a single, large perinuclear granule, which also localised with host RNA binding proteins YBX1 and TIA1 (Figure 2b). As such, these granules are defined as canonical SG. Host proteins redistributed from the nucleus and cytoplasm and formed SGs by 4–8 hpi. The SG formed after virus infection was seen as a single perinuclear body. Similarly, during infection of the recombinant SINV mCherry.capsid, the virus capsid redistributed with YBX1 and TIA1 and also with VCP and G3BP1 into a single perinuclear granule (Figure 2c).

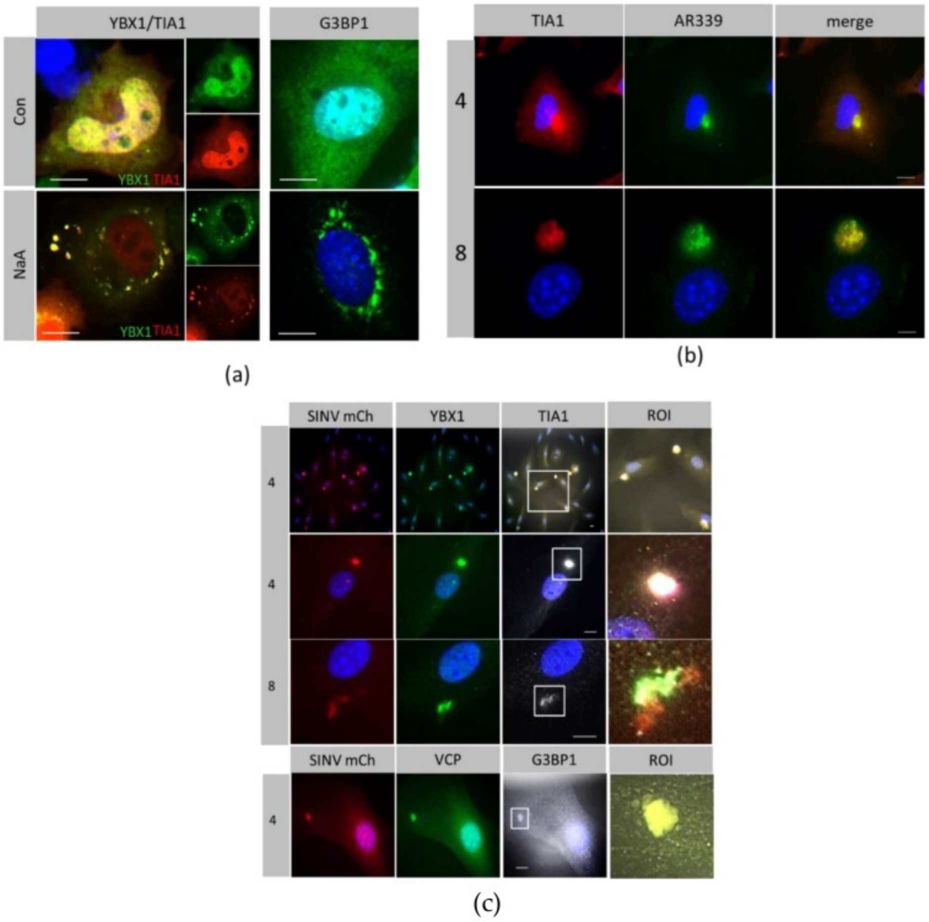

(a)

(b)

(c)

Figure 2 - RNA binding proteins redistributed with SINV capsid early in infection. Host RNA-binding proteins YBX1, TIA 1, G3BP1 and VCP were detected by immunostaining (**a**) Control MEF cells (Con) and cells treated with 100 nM sodium arsenate for 2 h (NaA) (**b**) MEFs infected with SINV strain AR339 for 4 and 8 hpi (**c**) Cells infected with SINV Cherry.capsid for 4hpi (low power x40), 4 hpi (x63) and 8 hpi (x63). Region of interest (ROI) are from merged images of white squares. Scale bar = 10 µm.

RNA-binding proteins VCP, YBX1 and TIA1 were initially found in the nucleus and cytoplasm in both WT and ATG16L1 -/- cells (Figure 3a). The capsid redistributed with the RNA-binding proteins as early as 2hpi into small cytoplasmic puncta which coalesced into a single large perinuclear body in WT cells by 8 hpi (Figure 3b, WT). In ATG16L1 -/- cells, characterised in detail in Rai et al. [13], capsid redistributed with YBX1, TIA1 and VCP in the cytoplasm by 2 hpi, however a large perinuclear granule was not formed by 8hpi (Figure 3 b, ATG16L1-/-). In ATG16L1-/- cells, host RNA-binding factors and capsid were seen as numerous small puncta throughout the cytoplasm. When the number of cells having either a large capsid-containing perinuclear SG in wild type cells, or small cytoplasmic puncta containing capsid in ATG16L1-/- were quantitated, there was a significant difference in large and small granules between both cell types. However, the same percentage of cells were infected in both cell types (Figure 3c). Therefore, although the initial infection was the same in both cell types, viral protein synthesis shown in Figure 1a was higher in wild type cells. In wild type cells, SG formation does not halt translation of viral proteins. In contrast, in ATG16L1 knockout cells, viral protein synthesis was restricted, despite low levels of eIF2α phosphorylation and absence of perinuclear SG formation. These experiments followed labelled capsid at early time points before the start of virus replication. We detected dsRNA with antibody J2 in separate replication complexes.

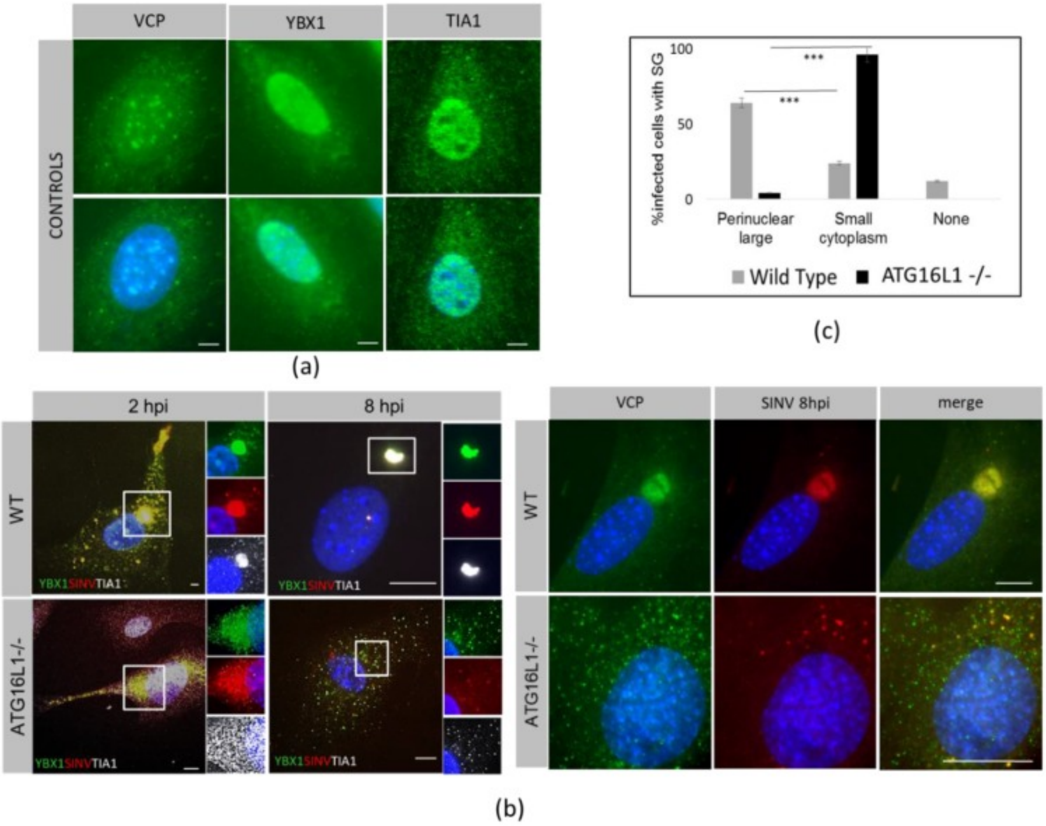

Figure 3 - Perinuclear stress granules do not form in ATG16L1-/-cells.Host proteins YBX1, TIA1 and VCP were stained in WT and ATG16L1-/- MEF cells. (**a**) distribution in ATG16L1 uninfected cells. (**b**) distribution of host proteins in WT and ATG16L1 MEFs cells infected with SINV mCh.capsid for 2 and 8 hpi. (**c**) The bar chart shows percentage of infected cells with either large perinuclear SG or small cytoplasmic puncta from 5 independent fields of view of WT and ATG16L1-/- cells at 8hpi at 40× magnification. +/- SE and ***$p < 0.001$. None indicates a small number of infected cells with no SG.

Inhibition of degradation by autophagy may explain the accumulation of the many small cytoplasmic puncta containing capsid and RNA-binding proteins seen in ATG16L1-/- cells. To investigate whether autophagy affects turnover of these host translation factors, we investigated protein levels during activation of autophagy by SINV in wild type cells (Figure 4).

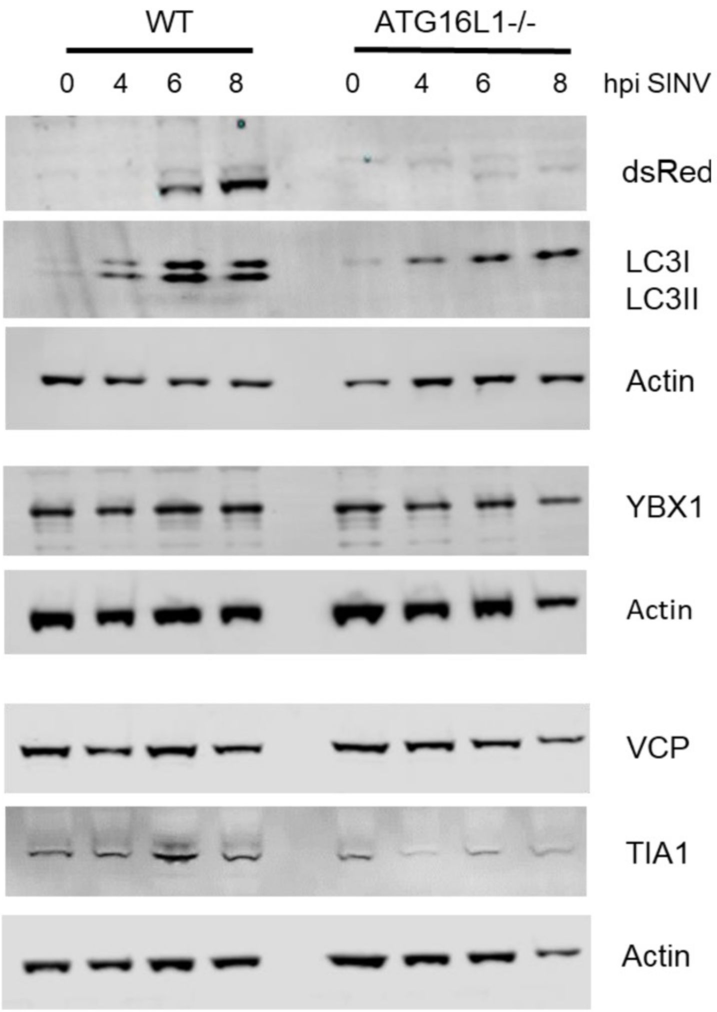

Figure 4 - Host translational RNA-binding proteins are not degraded by autophagy induced by SINV infection. A time course of SINV infection from 0–8 hpi in wild type (WT) and ATG16L1-/- MEFs (ATG16L1-/-). Western blot of protein lysates with antibodies against LC3, YBX1, TIA1 and VCP, with actin showing equal lane loading for each gel.

During autophagy, cytoplasmic LC3 (LC3I) is conjugated to phosphatidylethanolamine to form membrane-bound LC3II, by proteins, including ATG16L1, that are part of an ubqitination-like conjugation system. By 4 hpi, LC3I had been converted to the faster migrating LC3II form, demonstrating that SINV indeed activates autophagy early in infection. In ATG16LI -/- cells, LC3I was not converted to LC3 II during infection, confirming that these cells lack autophagy and also demonstrating that the puncta in Figure 3b are not autophagosomes There was no change in levels of YBX1, VCP and TIA1 over the time course of 0 to 8 hpi in wild type cells, indicating that they are not degraded by autophagy during this time period. In ATG16L1-/-, protein levels for TIA1, YBX1 and VCP also remained constant. Therefore, inhibition of autophagy does not lead to the accumulation of these host translation proteins, and the small cytoplasmic puncta seen in ATG16L1 knockout cells are not due to block in degradation of these factors.

3.3. Innate Responses to SINV in Autophagy-Deficient Cells

We examined the localisation of dsRNA viral sensors PKR and RIG-I. In wild type cells, by 2 hpi, both PKR and RIG-I had relocated from the cytoplasm (Figure 5a, CON) to a single capsid-containing perinuclear SG (Figure 5b WT), which remained for up to 8hpi. In ATG16L-/- cells, PKR and RIG-I also redistributed with capsid but there were smaller granules, less tightly packed and which became dispersed throughout the cytoplasm by 8hpi (Figure 5b, ATG16L1-/-). These small cytoplasmic puncta at 8hpi contained SINV capsid, RIG-I and TIA1 (Figure 5c), marking them as canonical SG.

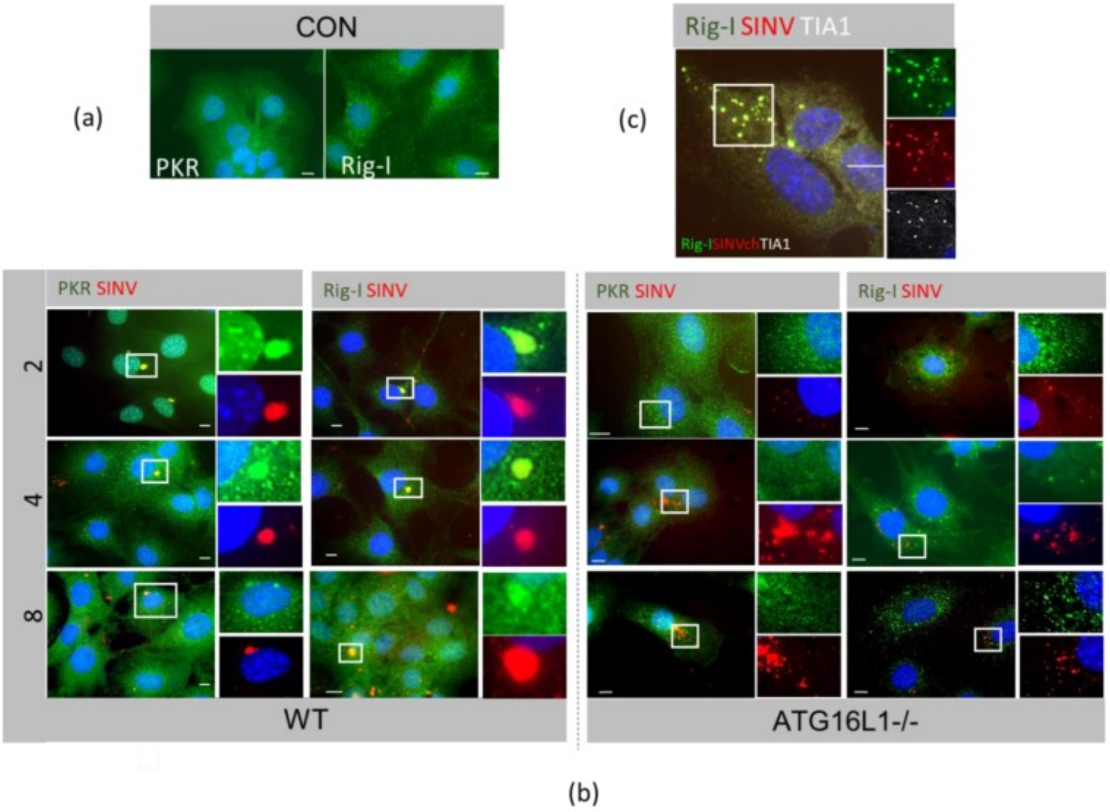

Figure 5 - Viral dsRNA sensors PKR and RIG-I redistribute with viral capsid. Cells were immunostained for PKR, RIG-I and TIA-1. (**a**) Control uninfected wild type MEFs (CON) (**b**) Wild type (WT) and ATG16L1-/- cells infected with SINV mCh.capsid for a time course of 2, 4 and 8 hpi. (**c**) ATG16L1-/- infected with SINVmCh.capsid for 8 hpi.

Interferon synthesis is required to induce several interferon stimulated genes or ISGs [14]. Type 1 interferon secretion was measured after SINV infection of wild type and ATG16L1 -/- cells for 24 hpi, using a sensitive Affymetrics Luminex IFN β assay kit. Figure 6a shows the fold increase in interferon secreted from ATG16L1-/- treated with poly IC, or infected with SINV, compared to wild type cells. We found that the assay varied with different virus preparations; therefore we treated each experiment independently for 5 biological replicates using the same virus stock in each experiment. Both dsRNA (poly I:C) treatment and SINV infection increased interferon secretion in ATG16L1 knockout cells by 1- to 4-fold over wild type cells. To examine if this was due to early induction of interferon synthesis, we investigated ISG mRNA expression, using total RNA isolated from SINV infected cells at 0, 4, 6, 8 and 24 hpi. Transcription of ISGs, MDA-5, RIG-I, PKR, ISG-15, ISG-56 and IP-10 were analysed by semi-quantitative RT-PCR with specific primers (Figure 6b). SINV infection led to a rapid increase by 4hpi in mRNA for ISGs RIG-I, PKR, MDA-5, with the greatest increase being ISG15 and ISG56 mRNA, which were undetectable before infection. This demonstrates that ISGs were induced through the production of interferon as early as 4hpi. We used IRF3 mRNA levels to represent a non-responsive gene.

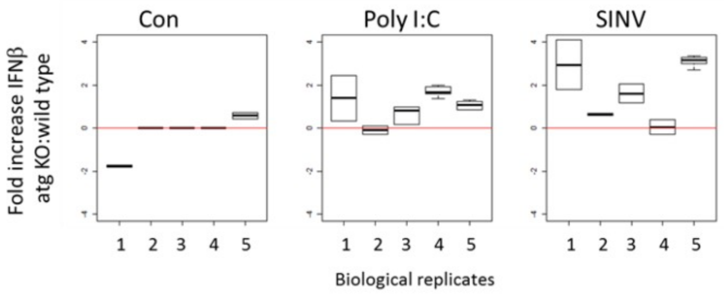

(a)

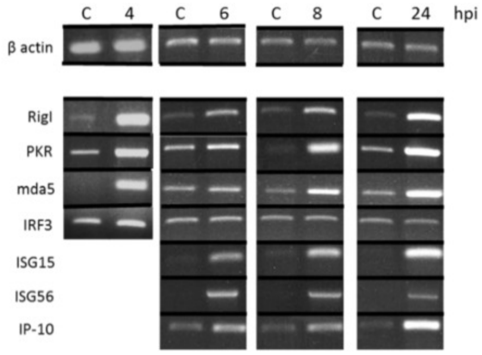

(b)

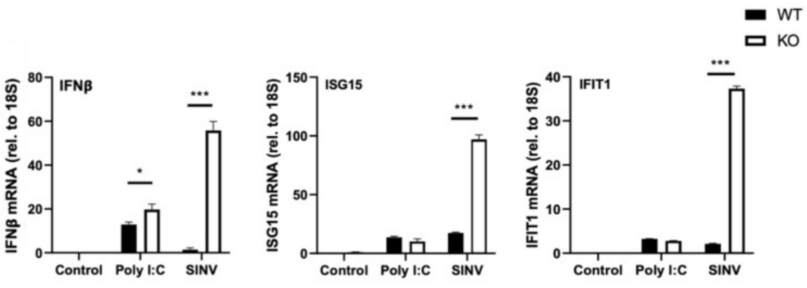

(c)

Figure 6 - ATG16L1 attenuates interferon β mRNA and protein secretion, and ISG gene expression in SINV infected cells.(**a**) Interferon β secretion from control cells cells (CON), cells treated with synthetic dsRNA (Poly I:C), or cells infected with SINV. Fold increase in interferon secretion from ATG16L1-/- cells relative to wild type cells is shown for control cells, cells transfected with poly I:C with lipofectamine and cells infected with SINV for 24 hpi. Graph shows values for 5 independent biological replicates. (**b**) MEF cells were infected with SINV for 4, 6, 8 and 24 hpi with matching controls isolated at the same time point. mRNA for ISGs RIG-I, PKR, MDA5, ISG15, ISG56 and IP-10 are shown by semi-quantitative RT-PCR. Beta actin shows equal lane loading and IRF3 is a non-responsive gene. (**c**) qPCR using primers for IFNβ, ISG15 and IFIT1 (ISG56) using total RNA from MEFs (WT) and MEFs deleted in ATG16 (ATG16L1-/-) either transfected with dsRNA (Poly I:C) or infected with SINV for 4 h. WT cells (black bars) and ATG16L1 -/- cells (white bars). ΔΔCt relative to 18S. (*) *p*-values < 0.05; (***) *p*-value < 0.001.

Real-time quantitative RT-PCR was used to measure relative differences between wild type and ATG16L1 knockout cells for IFN beta, ISG15 and IFIT1 (ISG56). When cells were treated with poly I:C for 4 h, there was a small significant difference (*p*-value < 0.5) between wild type and ATG16L1 knockout cells in interferon beta mRNA expression levels, but no difference for ISG15 or IFIT1 mRNA (Figure 6c). However, when cells were infected with SINV for 4 h, there was 100-fold greater IFN beta, ISG15 and ISG56 mRNA detected in cells lacking ATG16L1 compared to wild type cells (Figure 6c). In summary, interferon translation occurs in wild type cells in the presence of SG, at a time when eIF2a is phosphorylated and translation factors had been sequestered into SG during virus infection. However, there is a potentiation in interferon production and ISG transcription in ATG16L1 knockout cells, when RNA-binding host translation factors are scattered throughout the cytoplasm, and when there was little eIF2α phosphorylation and low viral protein synthesis.

Discussion

Here we show that, following SINV infection, ATG16L1 is required for the efficient phosphorylation of eIF2α, for high levels of viral protein synthesis and for the formation of the single perinuclear SG containing capsid seen early in infection. Generally, eIF2α phosphorylation leads to host translational arrest. It can be phosphorylated by over four different kinases, PERK, PKR, heme-regulated eIF2α kinase (HRI), and general control nonderepressible 2 (GCN2) [15]. PKR is activated mainly by dsRNA during viral infection, although GCN2 can also be activated by SINV RNA genomes [16]. For most viruses, this would also block viral replication. However, it does not affect the translation of alphavirus proteins. SINV can promote its own translation in the presence of phosphorylated eIF2α, through a translational enhancer, which is a stable hairpin loop in the 26S subgenomic promoter that stalls the ribosome on the initiation codon to enhance translation of the structural proteins [17,18]. In our study, when there was a diminished eIF2α phosphorylation in ATG16L1 deficient cell, there was a lower viral protein translation. It demonstrates that the translation enhancer requires eIF2α to be phosphorylated for virus translation to begin.

SINV infection promotes both stress and autophagy [19]. Autophagy and translation are inversely regulated, and previous work has shown that phosphorylation of eIF2α is essential for both starvation-induced and virus-induced autophagy [20]. Cells with a non-phosphorylatable mutant of eIF2α (S51A) did not induce autophagy in response to starvation [21]. We show that that autophagy protein ATG16L1 is essential for eIF2α phosphorylation and to initiate SG formation. ATG16L1 has a well-defined role in canonical and non- canonical autophagy, but it is unclear how it regulates PKR. Autophagy is initiated when stresses such as starvation and infection increase AMPK activity, which inactivates the mechanistic target of rapamycin complex (mTOR). Autophagy proteins in the ULK1 multi-protein complex phosphorylate phosphatidylinositol 3-phosphate (PI3P) to act in autophagosome nucleation. ATG16L1 interacts with ATG12-ATG5 to mediate the conjugation of LC3 to phosphatidylethanolamine (PE) on autophagosomes, leading to membrane elongation and expansion. However, this occurs in late infection, after 8hpi. ATG16L1 is also associated with non-canonical autophagy, the phagocytosis of extracellular pathogens into single membrane vesicles in a process known as LC3 associated phagocytosis (LAP). Roles of ATG16L1 in other processes, such as endocytosis, exocytosis and endosomes/lysosome repair have been described [22,23]. This study highlights another role for ATG16L1 in eIF2α kinase signaling.

SGs acted as platforms for sensing viral dsRNA, as RLR sensors, PKR and RIG-I localized to virus-induced SG very early in infection [24]. In wild type cells, RNA binding proteins TIA1, YBX1 and VCP redistributed with PKR and RIG-I into a single perinuclear body containing SINV capsid. However, in cells deficient in ATG16L1, RIG-I and PKR were scattered with TIA-1 and capsid throughout the cytoplasm, and did not coalesce into a single SG. The accumulation of cytoplasmic granules was not due to inhibition of autophagy, as we showed that host RNA binding proteins were not degraded by autophagy in wild type cells. In addition, it suggests that SG assembly is not an important anti-viral defense against SINV, as perinuclear SG formation yielded higher virus protein synthesis in wild type cells, and they were dispensable for interferon production in ATG16L1 knockout cells. The small cytoplasmic puncta containing RIG-I in ATG16L1-/- cells correlated with increased interferon and early ISG induction. The fact that ATG16L1 is important in initiating virus protein translation, and important for attenuating the anti-viral response could be linked. One mechanism by which autophagy can negatively regulate interferon signaling is through ATG5–ATG12 interacting with the CARD domain of RIG-I and MAVS to suppresses IFN induction [25]. Alphavirus can also prevent host recognition of its viral dsRNA [26] and it can inhibit synthesis of IFN and ISGs transcription and translation [27]. Interestingly, capsid proteins and nsp2 proteins can inhibit both transcription and translation [28]. In other work, SG formation by inducers such as proteasome inhibitors was inhibited when autophagy was inhibited [29].

The phosphorylation of eIF2α decreases translation of most mRNAs. However, it can increase translation of a selected number of mRNAs containing short open reading frames. We show using a sensitive ELISA that interferon translation is increased in SINV infected wild type cells compared to control cells, and this correlates with an increase in ISG mRNAs, where transcription is switched on by interferon. This transcriptional upregulation of host antiviral proteins in ATG16L1 -/- cells may help to decrease virus production. The synthesis of interferon is potentiated in ATG16L1-/- cells, at the same time as perinuclear SG formation is inhibited. This suggests that SG formation may not be required for interferon signaling, as previously suggested [30], and indeed lack of SG results in higher interferon translation. Further work using puromycin labelling of the various types of granule would determine which granule is most translationally active.

Our work here adds to the complex story of SG assembly during alphavirus infection. It has been well established that SINV disassembles SG late in infection from 8–16 hpi [31]. Different types of complexes containing viral nsP3- with G3BP1 and YBX1 have been isolated from both insect and mammalian cells [32], and sequestration of G3BP1 into replication complexes disperses SGs [31]. Similarly, CHIKV induces G3BP1 and G3BP2 – containing granules containing nsp2 and nsp3, which are not classical SG, but needed for efficient virus replication [33,34]. Our study correlates the inhibition of assembly of SGs in the absence of ATG16L1, with potentiated interferon responses and indicates that it is not the assembly of SG that enhances anti-viral responses, but the lack of eIF2α phosphorylation that decreases viral protein synthesis.